Wissenschaftlich-Technische Berichte
HZDR-003
2011

Bi-Annual Report 2009/2010

Rossendorf-Beamline at ESRF (ROBL-CRG)

Editors:
A.C. Scheinost and C. Baehtz

Print edition: ISSN 2191-8708

Electronic edition: ISSN 2191-8716

Qucosa: http://fzd.qucosa.de/startseite/

Published by Helmholtz-Zentrum Dresden-Rossendorf e.V.

2011

Herausgegeben vom

Helmholtz-Zentrum Dresden-Rossendorf e.V.

Postfach 51 01 10

D-01314 Dresden

Bundesrepublik Deutschland/Germany

Cover picture

The front cover shows an artist's impression of the reduction of selenite on pyrite surfaces, and its subsequent precipitation as elemental Se. The geochemical fate of selenium is of key importance for today's society due to its role as a highly toxic essential micronutrient and as a significant component of high level radioactive waste (HLRW) originating from the operation of nuclear reactors.

Breynaerts and coworkers of K.U. Leuven and HZDR have performed an XAS study at the Rossendorf Beamline to investigate the solid phase speciation of Se upon interaction of Se(IV) with Boom Clay, a reducing, complex sediment selected as model host rock for clay-based deep geological disposal of HLRW in Belgium and Europe. Using a combination of long-term batch sorption experiments, linear combination XANES analysis and ITFA-based EXAFS analysis allowed for the first time to identify Se^0 as the dominant solid phase speciation of Se in Boom Clay systems equilibrated with Se(IV).

Breynaert, E., Scheinost, A. C., Dom, D., Rossberg, A., Vancluysen, J., Gobechiya, E., Kirschhock, C. E. A., and Maes, A., 2010. Reduction of Se(IV) in Boom Clay: XAS solid phase speciation. *Environ. Sci. Technol.* **44**, 6649-6655.

Preface

The **Ro**ssendorf **B**eam**l**ine (**ROBL**) - located at BM20 of the European Synchrotron Radiation Facility (ESRF) in Grenoble, France - is in operation since 1998. This 7th report covers the period from January 2009 to December 2010. In these two years, 67 peer-reviewed papers have been published based on experiments done at the beamline, more than in any biannual period before. Six highlight reports have been selected for this report to demonstrate the scientific strength and diversity of the experiments performed on the two end-stations of the beamline, dedicated to Radiochemistry (RCH) and Materials Research (MRH).

The beamtime was more heavily overbooked than ever before, with an acceptance rate of only 25% experiments. We would like to thank our external proposal review members, Prof. Andre Maes (KU Leuven, Belgium), Prof. Laurent Charlet (UJF Grenoble, France), Dr. Andreas Leinweber (MPI Metallforschung, Stuttgart, Germany), Prof. David Rafaja (TU Bergakademie Freiberg, Germany), Prof. Dirk Meyer (TU Dresden, Germany), who evaluated the inhouse proposals in a thorough manner, thereby ensuring that beamtime was distributed according to scientific merit.

The period was not only characterized by very successful science, but also by intense work on the optics upgrade. In spring 2009, a workshop was held at ROBL, assembling beamline experts from German, Spanish and Swiss synchrotrons, to evaluate the best setup for the new optics. These suggestions was used to prepare the call for tender published in July 2009. From the tender acceptance in November 2009 on, a series of design review meetings and factory acceptance tests followed. Already in July 2010, the first piece of equipment was delivered, the new double-crystal, double-multilayer monochromator. The disassembly of the old optics components started end of July, 2011, followed by the installation of the new components. As of December 2011, the new optics have seen the first test beam and thorough hot commissioning will be continued until May 2012, since the ESRF shuts down for a major upgrade from December 2011 to April 2012. We expect that we will be ready for user operation from June 2012 on, with a better beamline than ever.

The beamline staff would like to thank all partners, research groups and organizations who supported the beamline during the last 24 months. Special thanks to the FZD management, the CRG office of the ESRF with Axel Kaprolat as liaison officer and Eric Dettona as lead technician, and to the ESRF safety group members, Paul Berkvens, Patrick Colomp and Yann Pira.

Andreas Scheinost and Carsten Baehtz

Contents

1. Scientific Highlights

Structural insight into californium chemistry: Experimental and theoretical approaches

G. Dupouy[1], T. Dumas[1], E. Galbis[2], D. Guillaumont[1], C. Hennig[3], J. Hernández-Cobos[2], P. Moisy[1], C. Le Naour[4], R. R. Pappalardo[2], S. Petit[1], A. C. Scheinost[3], E. Simoni[4], E. Sánchez Marcos[2], C. Den Auwer[1]

[1]CEA, Nuclear Energy Division, RadioChemistry and Processes Department, F-30207 Bagnols sur Cèze, France

[2]Departamento de Química Física, Universidad de Sevilla, 41012-Sevilla, Spain

[3]Forschungszentrum Dresden-Rossendorf (FZD), Institute of Radiochemistry, P.O. Box 510119, 01314 Dresden, Germany.

[4]Université Paris XI Orsay, IPN Orsay, 91405 Orsay, France

Introduction

The solution chemistry of actinoid ions has been a fundamental question since the beginning of the nuclear technologies, given its implication in the electronuclear fuel cycle and possible impact in environmental and toxicological transfers. From a fundamental aspect, the molecular chemistry of actinides is still a challenging issue for physical chemists because the understanding of the properties of heavy cations is still hampered by their large number of electrons. In comparison to transition metal chemistry, very little has been understood about the structural and electronic properties of actinide molecules. An additional and essential point of debate come from the comparison with parent lanthanide family with large number of electrons but very different electronic properties. From a structural point of view, transplutonium chemistry and lanthanide chemistry are often believed to yield similar molecular edifices although very few points of comparison have been reported because of the difficulty to work with weighable amounts of elements above americium. Therefore the rareness and hazardousness of the heavier actinide elements, which steeply increase with the atomic number, has prevented a complete examination of the trends along the series, beyond the middle of the series [***1***]. Curium cation, Cm(III) has often been considered as the heaviest actinide species characterized, having attracted much attention from both experimental and theoretical views in recent years [***2***].

We have focused this report on the comparison between heavy actinide(III) and parent lanthanide(III) with two examples of californium structural chemistry : the aqua ion and the hexacyanoferrate(II) adduct. Points of comparison between these two systems come from the occurrence of lanthanide analogues and possible discussion about the evolution of the cation coordination sphere across the series.

The aqua ion has always been the subject of considerable interest. Taking advantage of the EXAFS sensitivity of local structure in disordered media, the cation environment has been probed for instance in the aquo systems [3]. It has been lately discussed in full detail by Skanthakumar et al. for the curium cation in the hydrate form and in aqueous solution [4]. Also, recent work on the lanthanide series have examined using EXAFS technique if this contraction takes place in a monotone or an irregular way along the series [***5***]. In the solid state within the hydrate series, recent data available for the actinide family up to Cf(III) indicates a similar contraction [***6***]. However in solution a conclusive answer can not be given because of the uncertainty of the structural data, particularly concerning the hydration number, and the scarce information on the second half of the series. Beyond the middle of the series, there is only one study reported for berkelium [***7***], a preliminary EXAFS study for Cf(III) carried out by some of us [***8***] and the present study [***9***].

Among the quasi infinity of synthetic molecular edifices, the hexacyanometallate family is well known in transition metal chemistry to be an interesting example of building block chemistry with structurally defined subfamilies. From a structural point of view, the

$KLn^{III}/Fe^{II}(CN)_6.xH_2O$ (Ln = lanthanide element) family can be separated in three series. The first one with Ln = La to Nd presents the general formula $KLnFe^{II}(CN)_6.4H_2O$ [***10***]. These compounds crystallize in the hexagonal $P6_3/m$ space group. The second series has a unique representative, $KSmFe^{II}(CN)_6.3H_2O$, which crystallizes in a monoclinic group ($P2_1/m$) [***11***]. For these two series, the nine-coordinated lanthanide cation is bound to six $\{Fe(CN)_6\}$ motifs and to three water molecules in a distorted trigonal tricapped prism. Finally the third series involves Ln = Eu to Lu. They all occur in the orthorhombic space group: $KLnFe^{II}(CN)_6.3.5H_2O$ crystallizes in the Cmcm space group [***12***] while $KLnFe^{II}(CN)_6.3H_2O$ crystallizes in the Pnma (or Pbnm, with {a,b,c} equals {c,a,b}) space group [***13***]. The difference between the two space groups is the lanthanide coordination number: in the Cmcm group the lanthanide cation is nine-coordinated like for the La-Nd series; in the Pnma group the lanthanide cation is eight-coordinated to six nitrogen atoms and only two water molecules. In the nine-coordinated lanthanide compounds, the $LnN_6(H_2O)_3$ polyhedron forms a tri-capped trigonal prism where the lanthanide is bonded to six nitrogen atoms in prismatic sites and three water molecules in the capping positions. In the eight-coordinated lanthanide compounds, the $LnN_6(H_2O)_2$ polyhedron forms a square anti-prism or a bi-capped trigonal prism. For the actinide family, first mention of plutonium hexacyanoferrate was made in the 50's during the Manhattan project [14]. However, no structural characterization of An(III) hexacyanoferrate adduct has been reported until the present study [***15***].

Materials and methods

The ^{249}Cf(III) solution was purified from an ill-defined old solution of ^{249}Cf (~100 MBq) from IPN Orsay with a strong radiation damage of the first container. Part of the solution was evaporated to dryness and the voluminous foamy residue was taken up in concentrated HCl. The cloudy solution was centrifuged and the supernatant percolated on a column filled with an anion exchanger (Bio-Rad AG-MP 1, 100-200 mesh). Then the eluted fractions were evaporated to dryness and taken up in dilute HCl. The so obtained solution was percolated through a column filled with a cation exchanger (Bio-Rad AG-MP 50, 100-200 mesh). The purified fractions were gathered and evaporated to dryness. No deposit was visible to the naked eye. The container was then rinsed with HClO4 to obtain the stock californium solution. The gamma spectrum of a fraction of the sample used for the EXAFS measurements exhibits the main γ-rays of ^{249}Cf: 387.95, 333.44 and 252.88 keV. For the aqua sample (named Cf^{III}-aq in the following) the corresponding EXAFS sample (0.0022M) was loaded in a 200μL double layered Teflon/stainless steel cell, thus the masse of californium in the sample cell was 0.11mg. For the synthesis of the hexacyanoferrate adduct (named Cf^{III}/Fe^{II} in the following), 0. 4 μmol of Cf(III) aquo (obtained from 470 µL of a solution [Cf] = $8.7.10^{-4}$ M in $HClO_4$ 0.01 M) was mixed with a solution of 1.6 μmol of $K_4Fe^{II}(CN)_6.3H_2O$ (m = 0.675 mg in 150 µL HCl 0.2 M). Upon addition of 1.3 mL of ethanol, a pale blue precipitate appeared. The mixture was centrifuged and rinsed with pure ethanol. The compound was dried in air in the glove box and pressed in polyethylene.

Californium L_{III}-edge XAS spectra were recorded at the European Synchrotron Radiation Facility (ESRF) (6 GeV at 200 mA), Rossendorf beam line (BM20). Measurements were carried out at room temperature, in 200 µL double layered Teflon/stainless steel cells. BM20 is equipped with a water cooled double crystal Si(111) monochromator. Higher harmonics were rejected by two collimating Pt coated mirrors. A 13-element Ge solid state detector was used for data collection in the fluorescence mode. Monochromator energy calibration was carried out at Mo K-edge (20000 eV).

Results and discussion

Figure 1 shows the experimental and fitted k^2-weighted Cf L_{III}-edge EXAFS spectra of Cf^{III}-aq, using two model structures for the aqua ion: the square antiprism configuration,

SA, which represents an octahydrate and the trigonal tricapped prism, TTP, which implies an ennea-hydrate. Since no experimental estimation of the global amplitude factor S_o^2 can be obtained for the Cf case, coordination numbers were fixed to the model values of 8 (SA) fitted at 2.41 Å (σ^2 = 0.0077 Å^2) and 9 (i.e. 6+3, TTP), fitted at 2.38 Å (σ^2 = 0.0068 Å^2) and at 2.47 Å (s^2 = 0.0039 Å^2). The weighted averages of the Cf-O distances are comparable and there is no clear visible difference between the two fitted curves. Therefore, distinction between a TTP and a SA structure for the aqua ion can not be unambiguously deduced from the fittings performed. Computer simulations of Cf(III) in water represents a completely independent approach to the study of this system. Cf-H_2O intermolecular potentials based on the hydrated ion model [***16***] and combined with the polarisable and flexible MCDHO water model [***17***] have been developed. Two different quantum-mechanical (QM) potential energy surfaces have been employed, one being based on the MP2 method and the other on the DFT method by applying the BP86 functional [***18***]. Monte Carlo simulations of a system formed by 1 Cf(III) + 500 H_2O were carried out in the NVT ensemble. 2Giga configurations were generated for analysis. The MC simulation using the BP86-based intermolecular potential leads to an average CN for the first hydration shell close to 8, and the first maximum of the Cf-O RDF appears at 2.43 Å, whereas the MC simulation which uses the MP2-based potential gives a CN close to 9 with the maximum for the Cf-O RDF at 2.53 Å. The absence of experimental data other than the EXAFS spectrum which could be compared with the predicted value derived from the statistical modelisation precludes the adoption of a convincing criterion to clearly select an intermolecular potential with respect to the other.

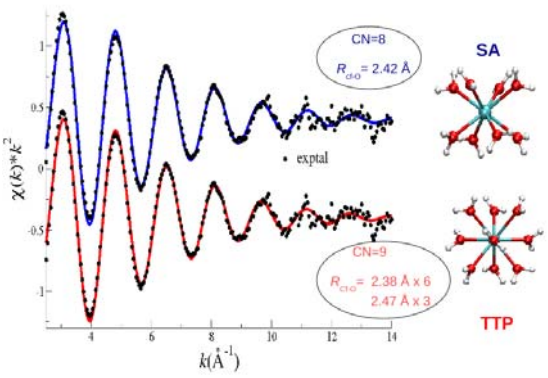

Fig. 1. Experimental (black points) and fitted (SA (CN=8) red and TTP(CN=9) blue lines) Cf L_{III}-edge EXAFS spectrum of Cf^{III}-aq.

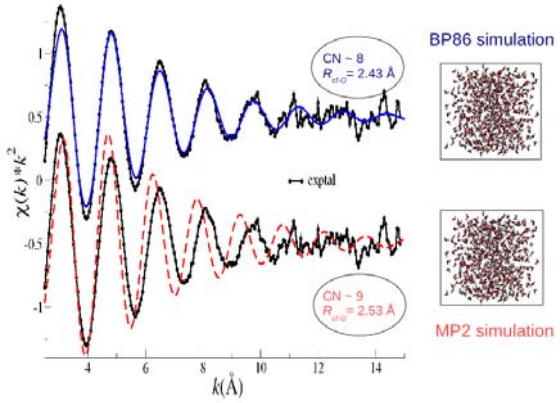

Fig. 2. Comparison of the k^2-weighted Cf-L_{III} edge EXAFS spectrum of Cf^{III}-aq (black points) with the simulated spectra obtained from the MC BP86 (blue line) or MP2 (red line) simulation.

Finally the third step has compared the simulated EXAFS spectra derived from the structural information provided by computer simulations with the experimental one of Cf^{III}-aq. A methodology already proposed for solving delicate structural problems such as the determination of the second shell has been used [***19***]. EXAFS spectra were simulated employing the FEFF code (version 8.4). Figure 2 compares the experimental EXAFS spectrum with the simulated ones obtained from the BP86 and MP2 simulations. The agreement for the case of the BP86 simulation is remarkable, where the intensity of the signal and the in-phase behavior is maintained up to where the experimental spectrum is blurred by the high noise/signal ratio. For the MP2 case the computed spectrum shows an intensity less similar to the experimental one and a progressive out-phase behavior. Bearing in mind that the first simulated spectrum is derived from the BP86 MC simulation, where n~8 and R_{Cf-O}=2.43 Å (fit = 2.41 Å), whereas the second simulated spectrum comes from the MP2 MC simulation where n~9 and R_{Cf-O}=2.53 Å, we must conclude that Cf(III) aqua ion must be mainly octacoordinated. Then, as far as Cf(III) is the heaviest actinide

aqua ion for which there is experimental information, the actinide contraction is supported by the present study. (R_{U-O}=2.56Å and CN=9±1; R_{Pu-O}=2.51Å and CN=9±1; R_{Cm-O}=2.47Å and CN=9±1).

Figure 3 shows the experimental EXAFS spectrum of Cf^{III}/Fe^{II} and Table 1 gives the metrical distances obtained with a parameterized fit (see reference [15] for fitting details). At CN = 8, the Cf^{3+} ionic radius is between that of Eu^{3+} and that of Gd^{3+} (r_{Eu} = 0.947 Å, r_{Cf} = 0.945 Å, r_{Gd} = 0.938 Å, CN = 6) [***20***,***21***]. Comparison between the californium ionic radius and the gadolinium one suggests that Cf^{III}/Fe^{II} may crystallize as the gadolinium adducts do. As described in the introduction of this paper, gadolinium adducts may occur in two different forms : $KGd^{III}Fe^{II}(CN)_6.3.5H_2O$ [12a] crystallizes in an orthorhombic space group (Cmcm) with a coordination number of nine, while $KGd^{III}Fe^{II}(CN)_6.3H_2O$ [13b] crystallizes in a orthorhombic space group (Pnma) with a coordination number of eight. The simulated EXAFS spectra (Feff8.4) of both $KGd^{III}Fe^{II}(CN)_6.3H_2O$ and $KGd^{III}Fe^{II}(CN)_6.3.5H_2O$ are compared to the experimental one of Cf^{III}/Fe^{II} in Figure 3. Simulations have been performed here by replacement of the gadolinium atomic number in the input file by the corresponding californium number.

Table 1. Bond lengths and angles reported for **Cf^{III}/Fe^{II}** (EXAFS) compared to the literature data (X-ray diffraction data) for the two Gadolinium analogues.

Distances (Å)	An-O	An-N	An--Fe	θ (°)
Cf^{III}/Fe^{II}	2 at 2.54(1) Å σ^2 = 0.0120 Å^2	6 at 2.44(1) Å σ^2 = 0.0068 Å^2	6 at 5.35(2) σ^2 = 0.0050 Å^2	159(10)
$KGd^{III}Fe^{II}(CN)_6.3.5H_2O$	2.50(1)	2.35(1)	5.34(1)	171.2(4)
$KGd^{III}Fe^{II}(CN)_6.3H_2O$	2.570(4)	2.431(5)	5.32(1)	162.1(4)

In the Figure, the e_0 value of the experimental spectrum has been adjusted in order for all the spectra to be compared. Without any adjustment of any distances in the simulation, the similarity between the EXAFS spectra of $KGd(Cf)^{III}Fe^{II}(CN)_6.3H_2O$ and of Cf^{III}/Fe^{II} is remarkable. On the contrary, strong differences in the beating modes occur after 6 Å^{-1} between the oscillations of $KGd(Cf)^{III}Fe^{II}(CN)_6.3.5H_2O$ and that of Cf^{III}/Fe^{II}. This observation strongly confirms all of the assumptions that Cf^{III}/Fe^{II} is similar to $KGd^{III}Fe^{II}(CN)_6.3H_2O$.

This conclusion is also supported by the metrical values of the EXAFS fit presented in Table 1. Although differences are small between the distances within $KGd^{III}Fe^{II}(CN)_6.3H_2O$ compared to $KGd^{III}Fe^{II}(CN)_6.3.5H_2O$, the fitted parameters of Cf^{III}/Fe^{II} clearly favor the similarity between the californium adduct and $KGd^{III}Fe^{II}(CN)_6.3H_2O$ therefore with coordination number equal to eight. As discussed in the first part of this report, additional points of discussion can be found in the comparison between the lanthanide(III) and heavy actinide(III) coordination spheres in hydrates. Generally speaking, two models of coordination spheres are most likely : a square antiprism (SA, CN = 8) and a tricapped trigonal prism (TTP, CN = 6+3). It has been exposed in the introduction that the metal coordination sphere in the hydrates is a tricapped trigonal prism for the entire Ln^{3+} series and for some of the An^{3+} series (Pu to Cf). The structure of the hydrates confirms the stability of the TTP polyhedron throughout the series from U to Cf (Bk not reported). In solution, both CN = 8 and CN = 9 are discussed and our results support the occurrence of the SA form for Cf^{III}-aq. D'Angelo et al. have also proposed that for the lanthanide(III) series a statistical deficiency of one water molecule in a capping position of the polyhedron occurs as the atomic number increases. This assumption has also been recently discussed by Duvail et al. using molecular dynamics [22]. These examples show some similarities with the hexacyanoferrate family. The Ln/An-N distances exhibit comparable

values for the actinide coordination sphere in the An^{III}/Fe^{II} compounds and in the lanthanide family.

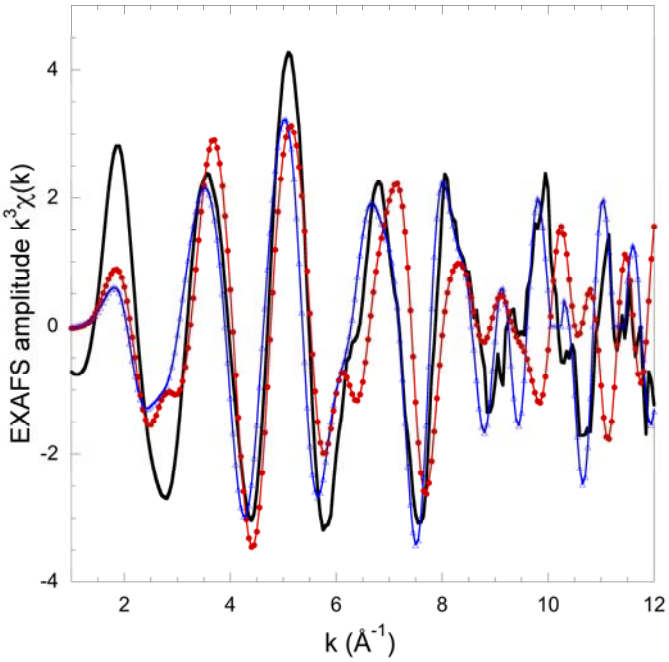

Fig. 3. Experimental EXAFS spectrum at the Cf L_3 edge of Cf^{III}/Fe^{II} (straight black line). Comparison with the simulated spectra (Feff8.4) of $KGd^{III}Fe^{II}(CN)_6.3H_2O$ (blue triangles) and $KGd^{III}Fe^{II}(CN)_6.3.5H_2O$ (red dots).

Conclusion

This work casts light to fundamental chemistry of heavy actinides by presenting data on one of the rare examples of californium molecular compounds. Summarizing, the first MC simulation of the trivalent cation of Californium, based on an exchangeable hydrated ion-water intermolecular potential, has been shown to represent an extended and improved methodology of the hydrated ion model. As far as Cf(III) is the heaviest actinoid aqua ion for which there is experimental information, the actinide contraction is supported by the present study and coordination number equals to 8 is favored. For U(III),R_{U-O}=2.56Å and CN=9±1;for Pu(III), R_{Pu-O}=2.51Å and CN=9±1; for Cm(III), R_{Cm-O}=2.47Å and CN=9±1 [1]. For the californium hexacyanoferrate adduct, EXAFS derived bond length and angle suggest that the californium cation sits in a bi-capped trigonal prism (CN = 8) as in $KGd^{III}Fe^{II}(CN)_6.3H_2O$. This arrangement differs from that in the structure of $KGd^{III}Fe^{II}(CN)_6.3.5H_2O$ in which the gadolinium is surrounded by 9 atoms. It also differs from the americium/neodymium case for which the americium hexacyanoferrate adduct has been found similar to $KNd^{III}Fe^{II}(CN)_6.4H_2O$ with coordination number equals to 9 [15]. The striking point in this comparison is the decrease of coordination number by one unit going from neodymium (americium) to gadolinium (californium), from trigonal tricapped prism for the first ones to trigonal bicapped prism for the second ones.

This work illustrates the benefits which can be achieved from the combination of the experimental XAS spectroscopies and computer simulations. We believe that this study traces out a still non-well explored combined methodology which certainly may be extremely useful for many other complex and limit chemical problems

Acknowledgements

Support for this research was provided by CEA/DEN/RBPCH program, Groupement National de Recherche PARIS, France and International Research Staff Exchange

Scheme (IRSES) HEXANE project of the European community. XAS measurements were carried out at ESRF / ROBL, a European synchrotron user facility. The authors would like to acknowledge Lester R. Morss for the former loan of 249Cf through the heavy isotopes production program of the U.S. Department of Energy.

References

[1] a) S. Skanthakumar, M. R. Antonio, R. E. Wilson, L. Soderholm, *Inorg. Chem.* 46 (2007) 3485; b) P.Lindqvist-Reis, C.Apostolidis, J. Rebizant, A. Morgenstern, R. Klenze, O. Walter, T. Fanghanel, R.G. Haire, *Angew.Chem. Int. Ed.* 46 (2007) 919; c) L. Soderholm, M.R. Antonio in *The Chemistry of the Actinide and Transactinide Elements,* Vols. 4 and 5 (Eds.:L.R.Moss,N.M.Edelstein,J.Fuger,J.J.Katz)3rd.ed. Springer, Dordrecht (2006) 3086.

[2] a) T. Yang, B. E. Bursten, *Inorg. Chem.* 45 (2006) 5291; b) N.M.Edelstein, R. Klenze, T. Fanghanel, S. Hubert, *Coord. Chem. Rev.* 250 (2006) 948; c) P. Lindqvist-Reis, C. Walther, R. Klenze, A. Eichhofer, T. Fanghanel, *J. Phys. Chem. B* 110 (2006) 5279; d) D. Hagberg, E. Bednarz, N. M. Edelstein, L. Gagliardi, *J. Am. Chem. Soc.* 129 (2007) 14136.

[3] P.G. Allen, J. J. Bucher, D. K. Shuh, N.M. Edelstein and T. Reich, *Inorg. Chem*., 36, 4676 (1997)

[4] S. Skanthakumar, M. R. Antonio, R. E. Wilson, and L. Soderholm, *Inorg. Chem.*, 46 (9), 3485 (2007)

[5] a) I. Persson, P. D'Angelo, S. de Panfilis, M. Sandström, L. Eriksson, *Chem. Eur. J.* 14 (2008) 3056; b) P. D'Angelo, S. de Panfilis, A. Filipponi, I. Persson *Chem. Eur. J.* 14 (2008) 3045.

[6] C. Apostolidis, B. Schimmelpfennig, N. Magnami, P. Lindqvist-Reis, O. Walter, R. Sykora, A. Morgenstern, E. Colineau, R. Caciuffo, R. Klenze, R. G. Haire, J. Rebizant, F. Bruchertseifer, T. Fanghänel, *Angew.Chem. Int. Ed.* 49 (2010) 6343.

[7] M. R. Antonio, C. W. Williams, L. Soderholm *Radiochim. Acta* 90 (2002) 851.

[8] R. Revel, C. Den Auwer, C. Madic, F. David, B. Fourest, S. Hubert, J.-F. Le Du, L. R. Morss, *Inorg. Chem.* 38 (1999) 4139.

[9] E. Galbis, J Hernandez-Cobos, C. Den Auwer, C. Le Naour, D. Guillaumont, E. Simoni, R. R. Pappalardo, E. Sanchez-Marcos, *Angew. Chem. Int. Ed.* 49 (2010) 3811.

[10] a) G. W. Beall, D. F. Mullica, W. O. Milligan, *Acta Cryst*, B34 (1978) 1446; b) D. F. Mullica, W. O. Milligan, J. D. Oliver, *Inorg. Nucl. Chem. Lett*., 15 (1979) 1; c) D. F. Mullica, E.L. Sappenfield, H.O. Perkins, *Journal of Solid State Chemistry*, 73 (1988) 65; d) W.O. Milligan, D. F. Mullica, H. O. Perkins, *Inorg. Chim. Acta.*, 60 (1982) 35; e) D. F. Mullica, E. L. Sappenfield, *Powder Diffraction*, 4 (1989) 101.

[11] D. F. Mullica, E. L. Sappenfield, H. O. Perkins, *J. Solid State Chem*. 78 (1989) 301.

[12] a) F. Goubard, A. Tabuteau, *J. Solid State Chem*. 167 (2002) 34; b) F. Goubard, A. Tabuteau, *Struct. Chem*. 14 (2003) 257; c) D. F. Mullica, E. L. Sappenfield, T. A. Cunningham, *J. Solid State Chem*. 91 (1991) 98.

[13] a) X. L. Xu, F. Hulliger, *Eur. J. Solid State Inorg. Chem*. 27 (1990) 443; b) D. F. Mullica, J. L. Ward, E. L. Sappenfield, *Acta Cryst*. C52 (1996) 2952.

[14] G. T. Seaborg, J. J. Katz., The Actinide Elements. Mc Graw-Hill Book Compagny, Inc. New York, Toronto, London. vol. 14B, p 427 (1954).

[15] G. Dupouy, I. Bonhoure, S. D. Conradson, T. Dumas, C. Hennig, C. Le Naour, P. Moisy, A. Scheinost, E. Simoni, C. Den Auwer, *Eur. J. Inorg. Chem.*, accepted.

[16] J. M. Martínez, R. R. Pappalardo, E. Sánchez Marcos, *J. Am. Chem. Soc.* 121 (1999) 3175.

[17] H. Saint-Martin, J. Hernández-Cobos, M. I. Bernal-Uruchurtu, I. Ortega-Blake, J. C. Berendsen, *J. Chem. Phys.* 113 (2000) 10899.

[18] A. Moritz, X. Y. Cao, M. Dolg, *Theor.Chem Acc.* 117 (2007) 473.

[19] P. J. Merkling, A. Muñoz-Páez, E. Sánchez Marcos, *J. Am. Chem. Soc.* 124 (2002) 10911.

[20] R. D. Shannon, *Acta Cryst*. A32 (1976) 751; b) A. Bilewicz, *Radiochim. Acta* 92 (2004) 69.

[21] F. David, *J. of the Less-Common Metals* 121 (1986) 27.

[22] M. Duvail, , P. D'Angelo, M-P. Gaigeot, P. Vitorge, R. Spezia, *Radiochim. Acta*, 7 (2009) 339

Sulfate coordination of Np(IV), Np(V) and Np(VI) in aqueous solution

C. Hennig, A. Ikeda-Ohno, S. Tsushima, A. C. Scheinost

Institute of Radiochemistry, Helmholtz-Zentrum Dresden-Rossendorf, 01314 Dresden, Germany

Introduction

Neptunium is considered as one of the most problematic actinide elements for waste storage due to its relatively high solubility in aqueous solution. The geochemical behavior depends strongly on the valence state. The stability of the oxidation state is affected by the acidity of the solution, i.e. the reduction potentials largely differ depending on pH. Np(V) is considered as mobile in the environment because of its relatively high solubility and low sorption capacity by minerals. In contrast, Np(IV) forms strong complexes and shows significant interactions with soil constituents. The environmental behavior of Np(VI) is characterized by high solubility in aqueous solution and high stability under oxidizing conditions. Np(III) and Np(VII) are not likely to occur under environmental conditions.

Sulfate and hydrogen sulfate anions occur in natural waters in significant concentrations and are able to form moderately strong complexes with neptunium. In consequence, sulfate complexation may play an important role in migration of neptunium from nuclear waste repositories. The current knowledge of neptunium sulfate coordination is based almost exclusively on diffraction studies in solid state. The deduction of neptunium coordination in aqueous solution from solid coordination may be misleading, because it is known that the solution species may undergo a ligand rearrangement during the crystallization process [1,2]. Therefore, the direct determination of the coordination in solution is mandatory. EXAFS is well suited for such kind of analysis, because sulfur has a strong backscattering power for the photoelectron wave. The obtained coordination numbers of sulfur represent a statistical average of coexisting neptunium sulfate complexes, and indicate the prevalent solution species. Significant differences occur between the neptunium-sulfur distances in bidentate (bid) and monodentate (mon) sulfate coordination: Sulfate in bidentate coordination shows a Np-S_{bid} distance of ~3.1 Å, whereas monodentate sulfate shows a Np-Smon distance of ~3.6 Å. This difference provides the key to separate distinct solution species. This chapter summarizes a systematic investigation of the aqueous sulfate complexes with neptunium in oxidation states IV, V and VI by Np L3-edge EXAFS spectroscopy as described detailed in reference [3].

Sample Preparation

A stock solution of 0.05 M Np(VI) in 1.0 M $HClO_4$ was prepared from ^{237}Np dioxide. Sample solutions used for electrochemical experiments (i.e. cyclic voltammetry and bulk electrolysis) were prepared by evaporating an appropriate amount of the Np stock solution, and dissolving the dried material into a desired composition of aqueous $(NH_4)_2SO_4$ solution. The pH of sample solutions was adjusted by adding $HClO_4$. The concentration of Np in the sample solutions was confirmed by UV–Vis–NIR absorption, α and γ spectroscopy.

Cyclic voltammograms in aqueous $(NH_4)_2SO_4$ solution were recorded under N_2 atmosphere. A three-electrode system consisting of a Au working electrode (surface area of 2 mm^2), a Pt-wire counter electrode, and a Ag/AgCl reference electrode in 3.0 M NaCl were employed with a Vycor glass liquid junction.

Based on redox potentials obtained from the cyclic voltammograms, the bulk electrolysis was performed to adjust the oxidation state of Np. Coulometric electrolysis of 0.05 M Np was carried out with the same potentiostat/galvanostat as for cyclic

voltammetry. The oxidation state and concentration of Np in the electrolyzed solutions were checked by UV–Vis–NIR absorption spectroscopy. Table 1 compiles the relevant preparation conditions for the EXAFS samples.

Table 1. Sample summary.

Sample ID	[Np] M	Ox. state	pH	Medium	Preparation[a]
Np^{VI}-1	0.05	VI	1.1	0.05 M $(NH_4)_2SO_4$	Dissolution.[b]
Np^{VI}-2	0.05	VI	1.2	2.0 M $(NH_4)_2SO_4$	Dissolution.[b]
Np^{V}-1	0.05	V	1.1	0.05 M $(NH_4)_2SO_4$	Reduction of Np(VI) (=**Np^{VI}-1**) at 0.0 V.
Np^{V}-2	0.05	V	2.7	2.0 M $(NH_4)_2SO_4$	Reduction of Np(VI) (=**Np^{VI}-3**) at 0.1 V.
Np^{IV}-1	0.04	IV	< 0.1	1.0 M $HClO_4$	Reduction of Np(V) at –0.3 V.
Np^{IV}-2	0.05	IV	1.1	0.5 M $(NH_4)_2SO_4$	Mixing.[c]
Np^{IV}-3	0.05	IV	1.1	1.0 M $(NH_4)_2SO_4$	Mixing.[c]
Np^{IV}-4	0.05	IV	1.1	2.0 M $(NH_4)_2SO_4$	Mixing.[c]
Np^{IV}-5	0.05	IV	1.1	3.0 M $(NH_4)_2SO_4$	Mixing.[c]

[a] Potentials for the electrolysis are referred to Ag/AgCl in 3 M NaCl.
[b] Dissolution of the dried Np(VI) stock solution.
[c] Mixing Np(IV)-$HClO_4$ solution with $(NH_4)_2SO_4$ solution.

Results and discussion

Np(VI). The L_3-edge k^3-weighted EXAFS spectra $\chi(k)$ and the corresponding FTs of Np(VI) sulfate are shown in Figure 1.

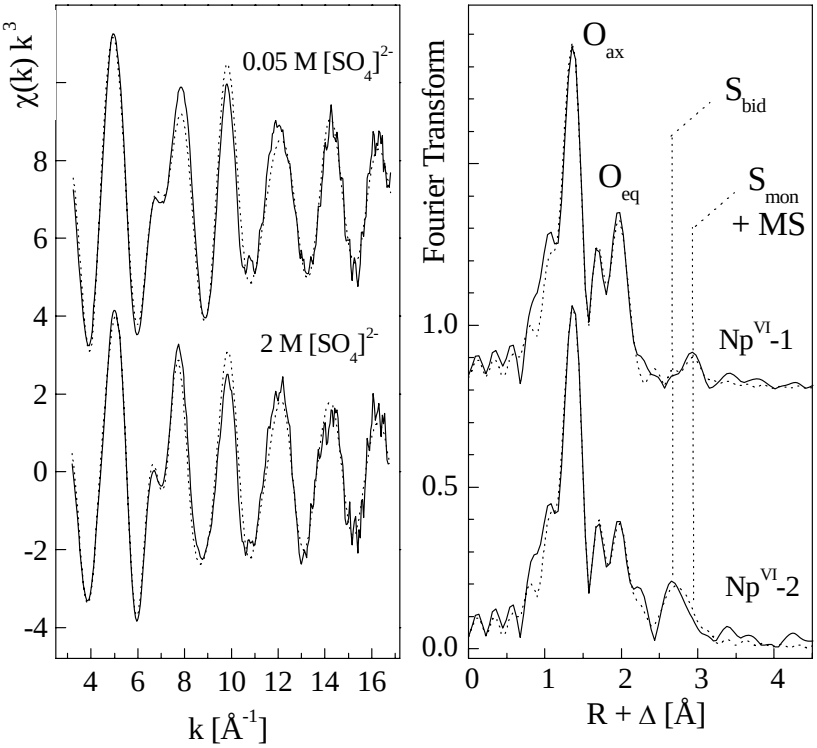

Fig. 1. Np L_3-edge k^3-weighted EXAFS spectra (left), and the corresponding Fourier transforms (right) of Np(VI) sulfate species.

The FT of the NpO_2^{2+} ion shows a dominating peak from two axial trans-oxo atoms (O_{ax}) at a Np-O distance of 1.76±0.02 Å. The equatorial shell of the sample Np^{VI}-1 exhibits 5 equatorial oxygen atoms (O_{eq}) at 2.41±0.02 Å. A third FT peak appears between the O_{ax} and O_{eq} peaks which is reproduced successfully with only the two O_{ax} and O_{eq} shells, suggesting that it arises from the superposition of these two scattering contributions. Both, the Np-O_{ax} and the Np-O_{eq} distances are close to the ones of the Np(VI) hydrate $[NpO_2(H_2O)_5]^{2+}$ which is expected to be the dominating species under these experimental conditions. A small peak at R+Δ ~ 3.0 Å occurs from multiple scattering along the $[O=Np=O]^{2+}$ moiety. This spectral feature was included in the curve fit by constraining its Debye-Waller factor and its effective path-length to twice the values of the corresponding Np-O_{ax} single-scattering path. Nevertheless, after subtracting the MS contribution there remains a peak at R+Δ ~ 3.0 Å, which could be fitted with a sulfur atom at a distance of 3.61 Å, suggesting monodentate coordinated sulfate. An additional peak could be fitted with sulfur at a distance of 3.12 Å, which would be in line with bidentate sulfate coordination. While the intensity of this peak is close to the noise level at low sulfate concentration, it increases with sulfate concentration, suggesting a real backscattering effect. In sample Np^{VI}-2 with 2.0 M SO_4^{2-}, there are approximately two sulfate atoms per neptunyl unit present. The data indicate that the coordination mode changes with increasing sulfate concentration from a prevalent monodentate to a prevalent bidentate coordination. The same tendency has been observed for U(VI) sulfate in aqueous solution. For solutions with low $[SO_4^{2-}]/[UO_2^{2+}]$ ratios, monodentate sulfate coordination has been observed [3]. In contrast, in solutions with high $[SO_4^{2-}]/[UO_2^{2+}]$ ratios the dominance of bidentate coordinated sulfate has been confirmed by HEXS and EXAFS [4]. The change in the U(VI) sulfate coordination mode is hence a function of the $[SO_4^{2-}]/[UO_2^{2+}]$ ratio. The Np(VI) sulfate species shows the same behavior.

Np(V). The L_3-edge k^3-weighted EXAFS data of Np(V) in 0.05 and 2.0 M SO_4^{2-} are shown in Figure 2.

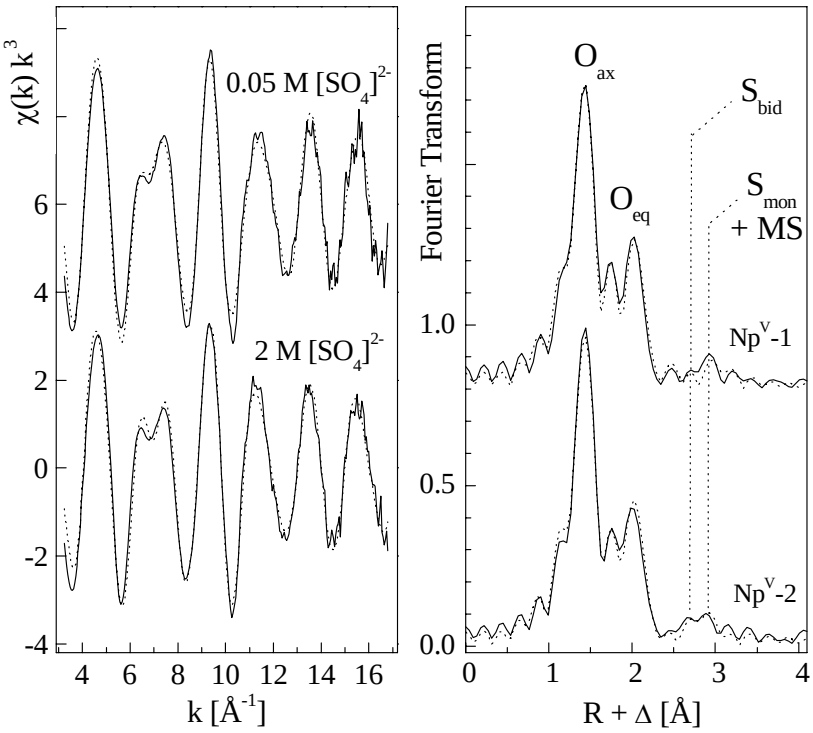

Fig. 2. Np L_3-edge k^3-weighted EXAFS spectra (left), and the corresponding Fourier transforms (right) of Np(V) sulfate species.

Np(IV). To avoid the spontaneous oxidation of Np(IV) by water the concentration of sulfate was always kept above 0.5 M. Figure 3 shows a series of Np(IV) sulfate samples at pH 1.1. The Np(IV) hydrate (**Np^{IV}-1**) is shown for comparison.

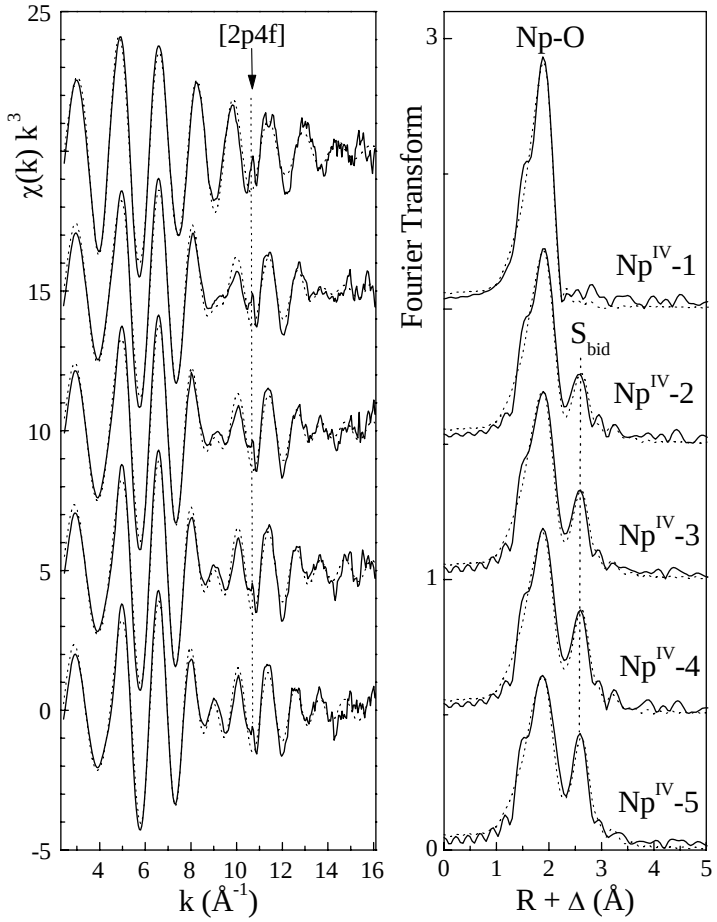

Fig. 3. Np L_3-edge k^3-weighted EXAFS spectra (left), and the corresponding Fourier transforms (right) of Np(IV) sulfate species.

Np(V) forms usually only weak complexes and the revised formation constant is reported only for the sulfate species $NpO_2SO_4^-$[5]. The trans-dioxo structure remains intact, but the charge is reduced in comparison to Np(VI). Np(VI) and Np(V) have formal electronic configurations of $5f^1$ and $5f^2$, respectively. The additional electron occupy mainly the non-bonding 5fϕ or 5fδ orbitals of Np(V), and is localized mainly on the Np atom. Therefore, the effective charge of the central atom in Np(V) is smaller compared to that of Np(VI), and both axial and equatorial Np-O distances are longer than those of Np(VI). This is confirmed by the DFT calculations indicating that the Np-O_{ax} and Np-O_{eq} distances of Np(V) are approximately 0.05 and 0.10 Å longer than those of Np(VI). Based on EXAFS spectroscopy, we derived two isomers for the species $NpO_2SO_4^-$ with sulfate either in monodentate or in bidentate coordination. The EXAFS data show a Np-O_{ax} distance of 1.83 Å in Np(V) sulfate. Within the typical error limits, this is the same distance as in Np(V) hydrate. Similarly, the equatorial oxygen distances of Np(V) sulfate and hydrate are identical. The sulfate coordination of Np(V) is less pronounced than that of Np(VI), even at high sulfate concentration. Less than 0.4 monodentate sulfate groups at a Np-S_{mon} distance of 3.67 Å were observed at 0.05 M SO_4^{2-}. The small sulfate coordination number

suggests that the hydrate remains dominant under these experimental conditions. By raising the sulfate concentration to 2.0 M, a change in the sulfate coordination can be observed: an additional small peak indicates the presence of bidentate sulfate with a Np-S_{bid} distance of 3.16 Å. The corresponding coordination number is only 0.5. The combined coordination number of monodentate and bidentate sulfate does not exceed one sulfate per Np(V) ion.

The EXAFS spectra reveal the [2p4f] double-electron excitations [6] indicated with a dotted line at k ~ 10.7 $Å^{-1}$. In the EXAFS of Np(IV) this feature appears more pronounced than in the spectra of Np(V) and Np(VI). This is related to a stronger [2p4f] resonance intensity due to a higher final state density. Furthermore, the $\chi(k)$ obtained from Np(IV) solutions show weaker scattering amplitudes at high *k* values, hence, the double-electron excitations become more obvious. The double-electron excitation may influence to a certain extent the spline approximation and may therefore bias the related coordination numbers, but will not significantly influence the interatomic distances. Most of the sulfate is coordinated in bidentate coordination with a Np-S_{bid} distance of 3.07±0.02 Å. Only a minor part is coordinated in monodentate mode with a Np-S_{mon} distance of 3.79±0.02 Å. Furthermore we found clear indication of monodentate and bidentate coordination modes. A number of species, which can be described with the general formula $[Np(SO_{4,bid})_x(SO_{4,mon})_y \cdot nH_2O]^{4-2x-2y}$, may exist in equilibrium. In the study presented here we found x = 2.0 – 3.3 and y = 1.1 – 1.4. Similar solution species have been observed for U(IV) sulfate, e.g. with a stoichiometry close to $[U(SO_{4,bid})_2(SO_{4,mon})_3 \cdot H_2O]^{6-}$ [7].

Redox chemistry and coordination. In non-complexing media the redox reaction is restricted to a fully reversible electron transfer according to $NpO_2^{2+} + e^- \leftrightarrow NpO_2^+$. In complexing media this redox reaction can be disturbed by side reactions in the equatorial plane. The latter situation occurs by the sulfate coordination: here, the cyclovoltammogram, shown in Fig. 4, indicate a non-reversible character of the Np^{5+}/Np^{6+} redox couple at ~ 0.8 V.

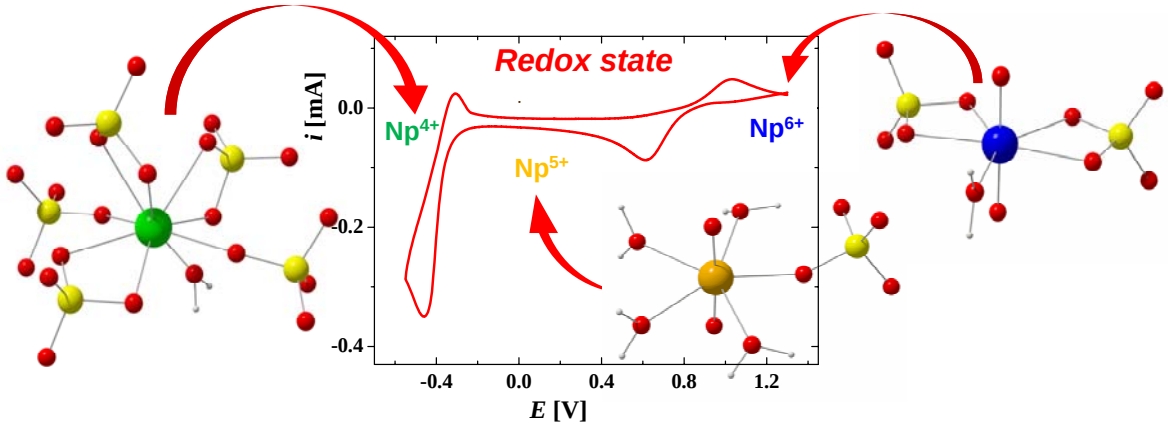

Fig. 4. Cyclic voltammograms of 0.05 M Np(VI) in an aqueous solution of 2.0 M $(NH_4)_2SO_4$ at pH 1.1, Au working electrode, start potential 1.3 V, initial scan direction: cathodic, scan rate: 400 mV/s. The sulfate coordination of the Np^{4+}, $Np^{5+}$and Np^{6+} solution species is shown as schematic structure drawing.

The EXAFS measurements reveal that bidentate sulfate coordination prevails at the hexavalent oxidation state, whereas for Np^{5+} the complexation is weaker and forms both mono- and bidentate sulfate complexes as depicted in the schematic structure drawings of Fig. 4, which were obtained from DFT calculations. The cyclovoltammogram shows also,

that the Np^{4+}/Np^{5+} redox couple, occurring at ~ -0.4 V, is fully irreversible. The EXAFS spectrum of Np^{4+} indicates the loss of the axial oxygens and the formation of a quasi-spherical shell of oxygen atoms. These oxygen atoms belong to sulfate groups which are again predominantly bidentately coordinated.

References

[1] C. Hennig, K. Servaes, P. Nockemann,K. Van Hecke, L. Van Meervelt, J. Wouters, L. Fluyt, C. Görrler-Walrand, R. Van Deun Inorg. Chem. **47** (2008) 2987.

[2] C. Hennig, A. Ikeda-Ohno, S. Tsushima, A.C. Scheinost, Inorg. Chem. **48** (2009) 5350.

[3] C. Hennig, K. Schmeide, V. Brendler, H. Moll, S. Tsushima, A.C. Scheinost, A.C.; Inorg. Chem. **46** (2007) 5882.

[4] C. Hennig, A. Ikeda, K. Schmeide, V. Brendler, H. Moll, S. Tsushima, A.C. Scheinost, S. Skanthakumar, R. Wilson, L. Soderholm, K. Servaes, C. Görrler-Walrand, R. Van Deun, Radiochim. Acta **96** (2008) 607.

[5] R. Guillaumont et al. *Update on the chemical thermodynamics of uranium, neptunium, plutonium, americium and technetium* Ed. Mompean, F. J., Illemassene, M., Domenech-Orti, C., Ben Said, K. Elsevier Science Publishers, Amsterdam, 2003.

[6] C. Hennig *Phys. Rev. B* **75** (2007) 035120.

[7] C. Hennig,W. Kraus, F. Emmerling, A. Ikeda, A.C. Scheinost *Inorg. Chem.* 47 (2008) 1634.

Oxidation state and local structure of Pu reacted with magnetite, mackinawite and siderite

R. Kirsch[1,2], D. Fellhauer[3], M. Altmaier[4], V. Neck[4], A. Rossberg[1], T. Fanghänel[3], L. Charlet[2], A. C. Scheinost[1]

[1]Institut für Radiochemie, Helmholtz-Zentrum Dresden-Rossendorf, 01314 Dresden, Germany

[2]Institut des Sciences de la Terre, Université Joseph Fourier, CNRS, 38041 Grenoble, France

[3]EC-JRC, Institute for Transuranium Elements, 76125 Karlsruhe, Germany

[4]Institut für Nukleare Entsorgung, Karlsruhe Institute of Technology, 76021 Karlsruhe, Germany

Introduction

Plutonium, the major transuranium actinide in civil and military nuclear waste, is of environmental concern due to its high chemical and radiotoxicity and the long half-life of relevant nuclides (^{239}Pu: 24 100 a, ^{242}Pu: 375 000 a, ^{244}Pu: $8.0 \cdot 10^7$ a) [1]. The solubility and complexation behavior of plutonium in aqueous systems and therefore its environmental fate are highly oxidation state dependent [2]. Due to its predominance over a wide pe-pH range and the possibility of colloid formation [3], tetravalent PuO_2 is considered one of the most important solids for Pu risk assessment. While colloid formation can enhance plutonium migration in the subsurface [4,5], the low solubility of PuO_2(am,hyd) limits dissolved Pu concentrations over a wide pe-pH range. However, under reducing conditions in the acidic to neutral pH range and particularly in presence of dissolved Fe(II) or Fe(II)-bearing minerals, Pu(III) is relevant and compared to Pu(IV) forms more soluble species [6]. Generally, contaminant migration is to a large extent controlled by sorption on minerals and redox reaction with them [4,5]. Since iron minerals form as corrosion products of steel, the first engineered physical barrier to Pu mobilization in most nuclear waste repository concepts, and are present in many "far field" barriers (clay or granite), their reactions with plutonium are of particular importance. Depending on redox conditions, ground water composition and microbial activity, Fe(II), Fe(III) or mixed Fe(II)-Fe(III) iron(hydr)oxides or sulfides such as magnetite ($Fe^{II}Fe^{III}_2O_4$), maghemite (γ-Fe_2O_3), green rusts, siderite ($FeCO_3$), and mackinawite (FeS) have been observed as corrosion products of steel. Magnetite, mackinawite and siderite are also widespread in natural aquifers. Sorption of plutonium to iron minerals can be accompanied by redox processes, leading to reduction (or possible oxidation) of the initial Pu oxidation state. For example, sorption of Pu(V) to hematite, goethite and magnetite was found to be accompanied by surface mediated reduction to Pu(IV) [7-11]. While the reductive capacity of the Fe(II)-Fe(III) mixed valence spinel magnetite is well known, the reduction of Pu(V) with iron(III) minerals hematite and goethite was attributed to the presence of traces of Fe(II) or to a stabilization of solid-state Pu(IV) [9]. Due to a lack of measured redox potentials and Fe(II) concentrations, it is not possible to clearly link these observations with thermodynamic predictions on Pu oxidation states. To investigate redox reactions of Pu with Fe(II)-bearing minerals under anoxic conditions, we chose magnetite, mackinawite and siderite as common, but chemically and structurally differing minerals. Cryogenic X-ray absorption spectroscopy (XAS) was used to assess in-situ oxidation states and local structures of resulting Pu-solid phases or surface complexes.

Materials and methods

Generally, all sample manipulations, including mineral synthesis and washing, UV-VIS measurements and preparation of samples for XAS measurements, were carried out under anoxic conditions in nitrogen or argon glove-boxes with 0-10 ppmv O_2. Experiments were carried out at RT (23 ± 3°C); de-ionized (18.2 MΩ MilliQ), degassed (O_2 and CO_2 free) water was used for all purposes. Magnetite (Fe_3O_4), mackinawite (FeS) and siderite ($FeCO_3$) were synthesized as detailed in [12]. A well characterized $2.2 \cdot 10^{-2}$ mol/L Pu(VI)

stock solution was obtained after purification and electrochemical oxidation (99.4wt. % Pu-242). Stock solutions of $8.6 \cdot 10^{-4}$ M Pu(V) and $7.3 \cdot 10^{-4}$ M Pu(III) were then prepared electrolytically in 0.5 M NaCl and 0.1 M $NaClO_4$, respectively. Prior to addition of Pu(V) or Pu(III) to mineral suspensions, the initial oxidation state was confirmed by UV-VIS spectroscopy. Total [Pu] in the stock solutions was determined using liquid scintillation counting (LSC). Similar [Pu] before and after 10 kD (~2 nm) ultrafiltration indicated the absence of significant amounts of PuO_2 colloids in the stock solutions. Pu(V) or Pu(III) plutonium stock solutions were added to the mineral suspensions to obtain [Pu(tot)] of $1.3 \pm 0.1 \cdot 10^{-5}$ M. Samples were allowed to react in the dark for 41 (Pu(V)) and 39 days (Pu(III)) (Table 1). [Fe(II)], [Fe(total)] concentrations were determined using the Ferrozine method [13] and [Pu] with LSC after 10kD ultra-filtration of aliquots of the mineral suspensions. pH and pe were determined in two ways: in suspension and in the clear supernatant after centrifugation of an aliquot of the sample, with the solid present at the bottom of the centrifuge tube.

Table 1. Experimental conditions at the end of the 40 ± 1 d reaction period for Pu(III) and Pu(V) ($[Pu(tot)]_{initial}$ $1.3 \pm 0.1 \cdot 10^{-5}$ M) reacted with magnetite (Mg), mackinawite (Mack) and siderite (Sid). $[Pu(tot)]_{final}$ for all samples ≤ 1×10^{-9} mol/L.

sample	surface area [m²/L]	pH_{sus} †	pH_{cen} ‡	pe_{sus}	pe_{cen}	[Fe(II)] [µmol/l]
Pu(III)+Mg, pH6	416	6.1	5.5	-1.3	2.9	3130
Pu(III)+Mg, pH8	416	7.9	7.4	-4.9	2.1	21.8
Pu(V)+Mg, pH8	416	7.9	7.2	-5.0	2.4	19.3
Pu(V)+Mack, pH8	183	8.0	8.4	-4.9	-2.1	8.0
Pu(V)+Sid, pH8	221	8.4	8.0	-5.8	-3.3	69.2

†sus – pH or pe measured in suspension
‡cen – pH or pe measured after centrifugation in the clear supernatant in contact with the solid phase

XANES and EXAFS spectra were acquired in fluorescence mode at the Pu-L_{III} edge (18.057 keV) at the Rossendorf Beamline (BM20) at the ESRF, France. During the measurement, samples were kept at 15 K using a closed-cycle He cryostat, thereby reducing thermal disorder in the samples and avoiding beam-induced oxidation state changes. Details of experimental setup and treatment of spectra are given in [12]. Reference spectra of acidic $(Pu^{III})_{aq}$, $(Pu^{IV})_{aq}$ and $(Pu^{V})_{aq}$ (measured at RT, courtesy of Ch. Den Auwer, CEA, Marcoule, France) and of crystalline PuO_2(cr) (measured at 15 K, courtesy of Ph. Martin, CEA, Cadarache, France) [14] had all been measured in transmission mode and at the same beamline. Details on data treatment and fitting procedures are given in [12].

Results and discussion

For all five samples (Table 1), aqueous Pu concentrations dropped within 30 minutes and for the whole duration of the experiment to values near or below the detection limit of LSC (≤ 1×10^{-9} mol/L), thereby reaching uptake levels of ≥ 99.95 %.

Reaction of Pu(III) and Pu(V) with magnetite

Figure 1a shows Pu-L_{III}-edge XANES spectra of the Pu-magnetite samples along with $(Pu^{III})_{aq}$, $(Pu^{IV})_{aq}$, and $(Pu^{V})_{aq}$ references. The three Pu-magnetite samples are characterized by very similar edge and peak positions and strongly resemble the $(Pu^{III})_{aq}$ spectrum in position and shape. To quantify the oxidation state composition, the XANES region was analyzed using an Iterative Target Test (ITT) [15] with $(Pu^{III})_{aq}$, $(Pu^{IV})_{aq}$, $(Pu^{V})_{aq}$ references. With this technique Pu(III) contents higher than 90% are found for all three Pu-

magnetite samples. To extend oxidation state analysis to the EXAFS region, ITT was also applied to EXAFS-spectra obtained by back transform (BT) of the first peak in the Fourier Transform (FT) (oxygen coordination shell) and confirms the prevalence of trivalent Pu. Shell fitting of the first FT peak yields Pu-O distances of 2.48 Å to 2.49 Å, characteristic of aqueous Pu(III) complexes [16-18]. Therefore spectral shape and position (ITT of the XANES region) and analysis of the oxygen coordination environment (ITT of the oxygen BT spectra and shell fitting of the first FT peak) all suggest Pu(III) as the predominant oxidation state. The oxidation state of Pu after reaction with magnetite was therefore independent of the initial oxidation state (III or V), suggesting that thermodynamic equilibrium has been attained.

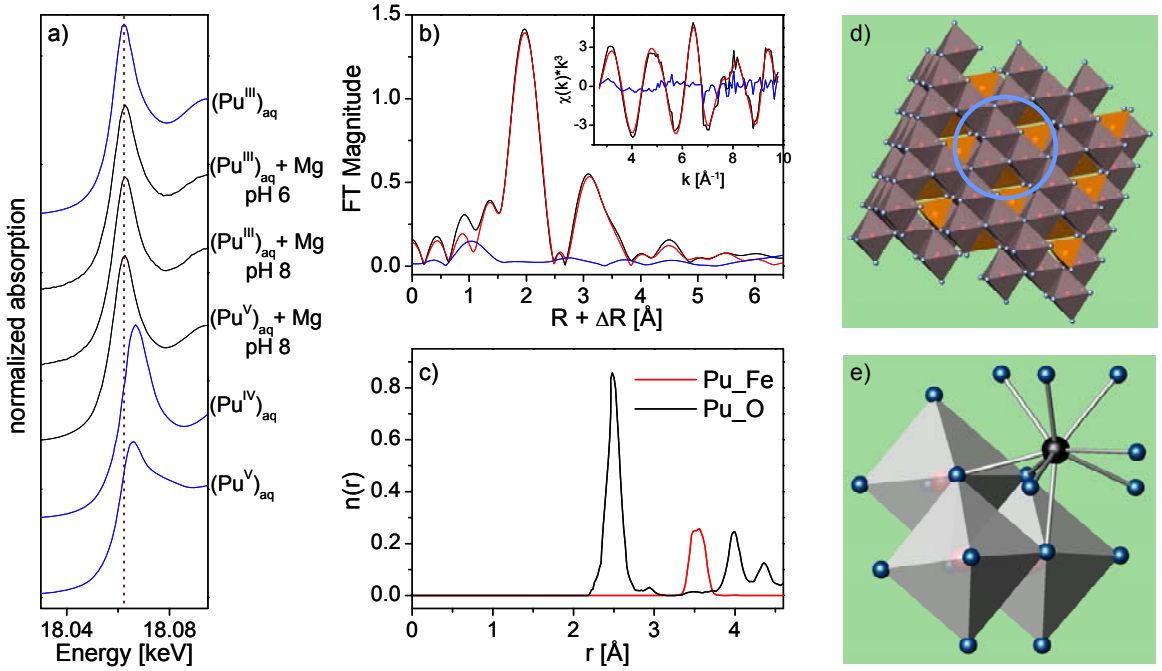

Fig. 1. a) Experimental Pu-L_{III} XANES spectra of Pu reacted with magnetite (black) and (Pu^{III})$_{aq}$, (Pu^{IV})$_{aq}$ and (Pu^{V})$_{aq}$ for reference (blue). b) Experimental Pu-L_{III} EXAFS spectrum of (Pu^{V})$_{aq}$+Mg, pH8 sample (black) and theoretical spectrum (red) resulting from radial refinement by MC simulation, FT and chi-spectrum (inset) (blue - residual). c) Pu-O and Pu-Fe radial pair distribution functions resulting from radial refinement. d) Octahedrally terminated (111) face of magnetite with one out of 7 possible positions for Pu(III) sorption marked by blue circle. e) Sorption complex structure of Pu(III) on edge-sharing FeO_6-octahedra (Pu – black, O – blue, Fe – red).

To elucidate the structure of the Pu(III) species on magnetite, shell fitting was extended to the FT peaks beyond the oxygen coordination sphere. As a second shell could be fitted with backscattering from three to five Fe atoms at a distance of 3.54 Å, suggesting either a sorption complex or formation of a solid phase, FEFF-Monte Carlo (MC) modeling [19] was applied to the EXAFS spectrum of the Pu(V)-Mg-pH8 sample to find a possible sorption complex structure (for modeling details see [12]). This MC procedure let to the identification of one specific geometric position in relation to magnetite, situated on (111) surfaces with octahedral termination (Fig. 1d). In the corresponding surface complex, one Pu atom is linked via three oxygen atoms to three edge-sharing FeO_6-octahedra (Fig. 1e). The radial Pu-atom distances found in the "raw" structure of the sorption complex were refined by reverse Monte Carlo (RMC) simulation [20,21]. As can be seen in Figure 1b, the resulting refined (theoretical) and the experimental spectra are in excellent agreement. The refinement also yields the Pu-O and Pu-Fe radial pair distribution functions (RPDF) (Fig. 1c): in the first Pu-O peak corresponds to 9 oxygen atoms at 2.49 Å and the first Pu-Fe peak to three iron atoms at 3.54 Å. The identified tridentate, trinuclear, triple edge-

sharing Pu(III) surface complex is likely to be very stable and play an important role in controlling Pu-magnetite reactions and Pu mobility.

Reaction of Pu(V) with mackinawite and siderite

XANES and EXAFS spectra of Pu(V) reacted with mackinawite (Pu(V)-Mack) and siderite (Pu(V)-Sid) are similar to those of crystalline PuO_2(cr), suggesting the prevalence of tetravalent Pu in the samples and structural similarities with PuO_2(cr) (Fig. 2). However, a higher white line (WL) intensity of the Pu(V)-Mack and a slight low-energy shift of the Pu(V)-Sid spectrum compared to PuO_2(cr) are apparent (Fig. 2a).

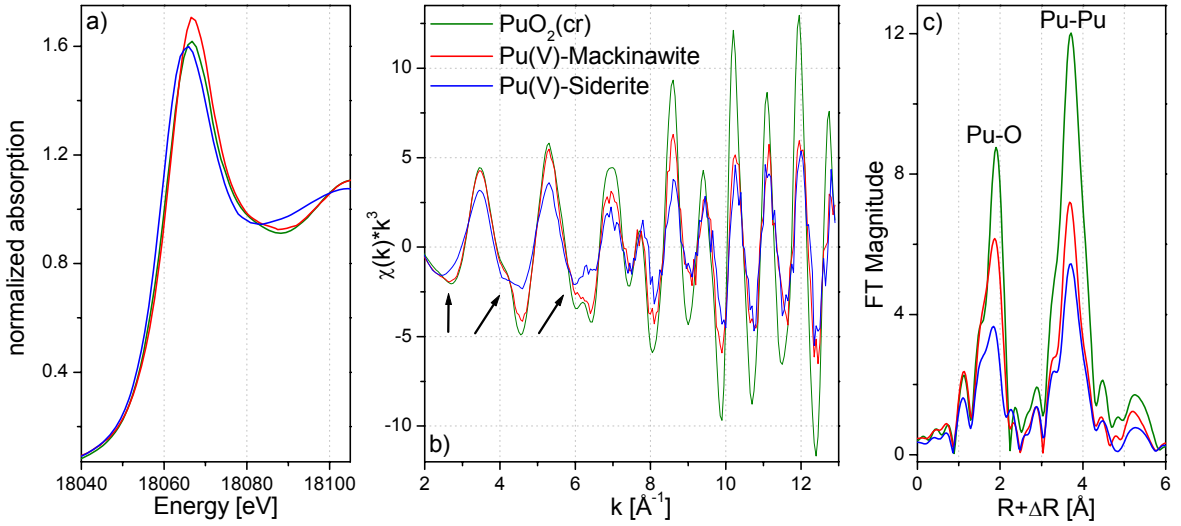

Fig. 2. Experimental Pu-L_{III} spectra of Pu(V)-Mack (red), Pu(V)-Sid (blue) and PuO_2(cr) (green). a) XANES b) $\chi(k) \times k^3$ c) Fourier Transform ($3.0 < k < 12.6$ Å^{-1}).

Apart from reduced EXAFS and FT amplitudes for Pu(V)-Mack and Pu(V)-Sid compared to PuO_2(cr) the Pu(V)-Sid spectrum shows significant additional differences in the lower k-range (arrows in Fig. 2b). For the Pu(V)-Mack sample, the XANES region gives no indication for the presence of either tri- or pentavalent plutonium species. We therefore fitted the Pu(V)-Mack and the PuO_2(cr) reference spectra with a PuO_2(cr) model in similar k-ranges (3.0-12.2 Å^{-1}) and with coordination numbers fixed to their crystallographic values.

Table 2. Shell fit of Pu(V)-Mack and PuO_2(cr) samples with fixed coordination numbers. Fit carried out in R-space, for details see SI, section 2.3, Table S9).

	Pu(V)-Mack			PuO2(cr)		
path	CN	R [Å]	σ^2 [Å^2]	CN	R [Å]	σ^2 [Å^2]
Pu - O	8	2.32	0.0081[d]	8	2.33	0.0054[d]
Pu - Pu	12	3.81	0.0059	12	3.83	0.0032
Pu - O	24	4.40	0.0088	24	4.43	0.0061
Pu-O MS	8	4.64[f]	0.0081[d]	8	4.66[f]	0.0054[d]
Pu - Pu	6	5.36	0.0084	6	5.37	0.0068
Pu - Pu	24	6.69	0.0142	24	6.68	0.0087
	E0-shift*	5.83		E0-shift*	6.81	
	Res**	7.94		Res**	8.34	
	f - fixed, d - correlated					
S_0^2 = 0.95, *E0-shift – [eV], **Res – Residual in %,						

The goodness of fit obtained is similar for both spectra, suggesting that a PuO_2 solid phase formed in the Pu(V)-Mack sample (Table 2). The higher Debye-Waller factors (σ^2), corresponding to a higher mean square radial displacement of the backscattering atoms, indicate that the PuO_2 formed in the Pu(V)-Mack sample is characterized by higher structural disorder in the coordination and all further shells compared to the reference compound,

calcinated PuO_2(cr). No indication for the presence of Pu(V) could be derived from shell fitting. By fitting the Pu(V)-Mack and PuO_2(cr) reference sample with adjustable coordination numbers, we also find similar Pu-Pu coordination numbers for both (for details see [12]). The low energy shift in the absorption edge and the low k-range differences between Pu(V)-Sid and PuO_2(cr) spectra can be explained as resulting from contribution of both Pu(III) and PuO_2 to the spectrum and the resulting interference between their corresponding backscattering waves. Tentative quantification with ITT using $(Pu^{III})_{aq}$ and PuO_2(cr) or the Pu(V)-Mack sample (≈ non-calcinated PuO_2) as references results for the XANES and EXAFS region in a Pu(III) content of 33 %.

Impact of mineral phases on reaction products

The differences in magnetite and mackinawite reaction products may appear surprising as both are (semi)conductors and have proved capable of providing electrons for multi-electron reductions of metals/metalloids at their surfaces (e.g. reduction of Se(IV) to Se(-II), Cr(VI) to Cr(III), Sb(V) to Sb(III)). However, for early actinides, that are hard Lewis acids and therefore oxyphilic, the sulfur terminated mackinawite surface, should not be attractive. If, for this reason, surface complexation does not occur, electrons for a two-electron reduction from Pu(V) to Pu(III) cannot be provided directly by the mineral. The one electron necessary for the reduction from Pu(V) to Pu(IV) might be transferred from a Fe(II) aquo-ion or co-adsorbed surface species. This behavior of Pu is in line with the partial reduction of U(VI) and precipitation of a mixed U(VI) / U(IV) oxide in presence of mackinawite [22,23] but contradicts the coordination of Np(IV) to sulfur atoms at the mackinawite surface [24]. In contrast to magnetite and mackinawite, electrons cannot move freely among the carbonate separated $Fe(O,OH)_6$ octahedra of siderite, that has a bandgap of 4.4 eV [25]. Electrons from the siderite structure can therefore not easily participate in surface reactions. The partial reduction of Pu(V) to Pu(III) in siderite but not in mackinawite suspensions may therefore be due to the complexation behavior of Pu, prefering oxygen over sulfur terminated surfaces, and thus be related to the thermodynamic stability of the respective surface complexes. Also the high solubility of siderite, resulting in a higher Fe(II) concentration (Table 1), might play a role. Only partial reduction to Pu(III) with siderite, as opposed to magnetite, might then be explained as being due to the fact that only dissolved and surface (co-adsorbed or structural) Fe(II) can participate in reducing adsorbed Pu.

Implications for environmental studies

Implications from our results for the risk assessments of Pu in contaminated sites and nuclear waste repositories are:
(1) Pu(III) is an important oxidation state in reducing anoxic environments and thermodynamic models based entirely on tetravalent Pu(IV) species are inadequate. Consequently, sorption of Pu(III) to relevant mineral surfaces should be investigated in more detail, also to lower the uncertainty of present predictions based upon analogy with other trivalent actinides, e.g. Am(III) and Cm(III). Relevant Pu(III) complexation and solubility constants should be determined to obtain more reliable quantitative transport models for Pu.
(2) Based upon our XAS investigation, we have identified and structurally characterized a tridentate Pu(III) surface complex on magnetite. Following the structural information obtained, we expect this complex to be highly stable and to play an important role in Pu-magnetite interactions and Pu retention.
(3) Thermodynamic calculations provide a useful tool to predict redox reactions and the prevalence of occurring oxidation states under equilibrium conditions; however, more specific input parameters are needed to correctly model the (geo)chemical behavior of Pu in complex natural environments. In-situ spectroscopic investigations and wet chemical data are necessary to understand actinide surface complexation and supplement predictions based upon thermodynamic modeling. Finally, it should become possible to

derive geochemical models coupling thermodynamic equilibrium calculations and quantitative description of sorption.
(4) The investigated systems, magnetite, mackinawite and siderite, represent a wide range of geochemical conditions and are known corrosion products of steel containers under anoxic groundwater conditions. They are key phases contributing to Pu sorption and redox processes under near- and far-field conditions. Regarding the applicability of our results to natural settings it should be considered that other factors (i.e. sorption of Pu on additional mineral surfaces, interaction of Pu with dissolved ligands, variation of Pu / surface ratio or competitive sorption effects) can impact reaction outcomes and should be further investigated.

Acknowledgements

This work has been financially supported by HZDR, KIT-INE, ISTerre (UJF/CNRS/INSU), Actinet-I3 (grant JRP-05), RECOSY and PACHEM-Paris. We are most grateful to Christophe Den Auwer (CEA, Marcoule) and Philippe Martin (CEA, Cadarache) for providing reference spectra for aqueous Pu species and PuO_2(cr), respectively.

References

[1] J. Magill; G. Pfennig and J. Galy *Chart of the nuclides*; 7th ed.; European Commission - DG Joint Research Centre - Institute of Transuranium Elements: Karlsruhe, 2006.
[2] W. Runde, *Los Alamos Science* (2000) 392-411.
[3] J. Rothe; C. Walther; M. A. Denecke and T. Fanghanel, *Inorg. Chem.* ***43*** (2004) 4708-4718.
[4] A. B. Kersting; D. W. Efurd; D. L. Finnegan; D. J. Rokop; D. K. Smith and J. L. Thompson, *Nature* ***397*** (1999) 56-59.
[5] A. P. Novikov; S. N. Kalmykov; S. Utsunomiya; R. C. Ewing; F. Horreard; A. Merkulov; S. B. Clark; V. V. Tkachev and B. F. Myasoedov, *Science* ***314*** (2006) 638-641.
[6] D. Rai; Y. A. Gorby; J. K. Fredrickson; D. A. Moore and M. Yui, *J. Solution Chem.* ***31*** (2002) 433-453.
[7] W. L. Keeney-Kennicutt and J. W. Morse, *Geochim. Cosmochim. Acta* ***49*** (1985) 2577-2588.
[8] B. A. Powell; R. A. Fjeld; D. I. Kaplan; J. T. Coates and S. M. Serkiz, *Environ. Sci. Technol.* ***38*** (2004) 6016-6024.
[9] B. A. Powell; R. A. Fjeld; D. I. Kaplan; J. T. Coates and S. M. Serkiz, *Environ. Sci. Technol.* ***39*** (2005) 2107-2114.
[10] A. L. Sanchez; J. W. Murray and T. H. Sibley, *Geochim. Cosmochim. Acta* ***49*** (1985) 2297-2307.
[11] A. B. Kersting; P. Zhao; M. Zavarin; E. R. Sylwester; P. G. Allen and R. W. Williams In *Colloidal-Facilitated Transport of Low-Solubility Radionuclides: A Field, Experimental, and Modeling Investigation; Report UCRL-ID-149688*; Kersting A. B., R., P. W., Ed.; Lawrence Livermore National Laboratory, Livermore, CA, 2003.
[12] R. Kirsch; D. Fellhauer; M. Altmaier; V. Neck; A. Rossberg; T. Fanghänel; L. Charlet and A. C. Scheinost, *Environ. Sci. Technol.****45*** (2011) 7267–7274.
[13] E. Viollier; P. W. Inglett; K. Hunter; A. N. Roychoudhury and P. Van Cappellen, *Appl. Geochem.* ***15*** (2000) 785-790.
[14] P. Martin; S. Grandjean; C. Valot; G. Carlot; M. Ripert; P. Blanc and C. Hennig, *J. Alloys Compd.* ***444*** (2007) 410-414.
[15] A. Rossberg; T. Reich and G. Bernhard, *Anal Bioanal Chem* ***376*** (2003) 631-638.
[16] P. G. Allen; J. J. Bucher; D. K. Shuh; N. M. Edelstein and T. Reich, *Inorg. Chem.* ***36*** (1997) 4676-4683.
[17] S. D. Conradson; D. L. Clark; M. P. Neu; W. H. Runde and C. D. Tait, *Los Alamos Science* (2000) 418-421.
[18] J. H. Matonic; B. L. Scott and M. P. Neu, *Inorg. Chem.* ***40*** (2001) 2638-2639.
[19] A. Rossberg and A. C. Scheinost, *Anal Bioanal Chem* ***383*** (2005) 56-66.
[20] S. J. Gurman and R. L. McGreevy, *J. Phys.: Condens. Matter* ***2*** (1990) 9463-9473.
[21] M. Winterer, *J. Appl. Phys.* ***88*** (2000) 5635-5644.
[22] L. N. Moyes; R. H. Parkman; J. M. Charnock; D. J. Vaughan; F. R. Livens; C. R. Hughes and A. Braithwaite, *Environ. Sci. Technol.* ***34*** (2000) 1062-1068.
[23] B. Hua and B. Deng, *Environ Sci Technol* ***42*** (2008) 8703-8708.
[24] L. N. Moyes; M. J. Jones; W. A. Reed; F. R. Livens; J. M. Charnock; J. F. W. Mosselmans; C. Hennig; D. J. Vaughan and R. A. D. Pattrick, *Environ. Sci. Technol.* ***36*** (2002) 179-183.
[25] D. M. Sherman, *Am. Mineral.* ***94*** (2009) 166-171.

Sculpting multiphase carbon-transition metal films by means of ionized physical vapour deposition: a GISAXS study

G. Abrasonis[1,2], T. W. H. Oates[3], G. J. Kovács[1], M. Tucker[2], J. Grenzer[1], P. O. Å. Persson[3], K. H. H. Heinig[1], A. Martinavičius[1], N. Jeutter[1], C. Baehtz[1], M. M. M. Bilek[2], W. Möller[1]

[1] Institute of Ion Beam Physics and Materials Research, Helmholtz-Zentrum Dresden-Rossendorf, 01314 Dresden, Germany.

[2] University of Sydney, New South Wales, 2006, Australia.

[3] Linköpings Universitet, 58183 Linköping, Sweden.

Introduction

Nanostructure determines macroscale properties, and thus is one of the key issues in thin film materials science. For multiphase films, this is of particular importance due to their multifunctionality and the combination of properties which cannot be predicted from the constituents alone [1]. Top-down approaches are affected by the production time and price issues. Alternatively, bottom-up approaches rely on self-assembly and self-organization phenomena, and their control by external parameters [2]. Film growth represents a large set of kinetic processes (surface/ bulk diffusion, nucleation&growth, phase transformation, shadowing, etc.) which can be governed by external factors such as temperature, growth rate, ion irradiation, etc…[3]. Among those, energetic ions bombardment can deliver the largest amount of energy per atom [4]. Thus it can potentially bring the structure in the far-from-equilibrium state where self-organization processes can occur.

In combination with the presence of thermodynamic forces towards phase separation, thin film growth and ion irradiation result in self-organized vertical super-lattices [5-9]. This is due to the interplay of the ion irradiation caused ballistic collision random walks of atoms in the near surface layer defined by the ion range and the thin film growth kinetics [5]. A constant supply of ions results in a steady-state movement of the surface. The phase separation kinetics is confined to the moving surface layer, leaving the bulk 'frozen'. The depth of this 'active' layer may be adjusted by changing the ion energies and masses, which controls the super-lattice periodicity [5]. It must be emphasized that the presence of energetic ions is necessary to induce such vertical self-organization process [10]. The ion directionality, which is not available in the other mechanisms involved in thin film growth, may be also exploited [4]. Using two fundamental ion irradiation properties – ion energy and direction - would allow an independent control of the nanopattern periodicity and orientation. This is the main focus of this study [4].

Materials and methods

Our group in cooperation with the University of Sydney, Australia, and the University of Linköping, Sweden, has performed studies concerning the oblique incidence ionized physical vapour deposition (iPVD) of C:Ni films. iPVD in the form of pulsed filtered cathodic vacuum arc was used. Each arc pulse deposits less than one monolayer of one kind of ions, resulting in composites from sequentially pulsed cathodes. For the former system, an arc current of ~1.5 kA was used with pulse lengths of 0.3 ms for Ni and 0.8 ms for C at the pulsing frequency of 3 HzA curved magnetic filter was used to remove the droplets and neutrals from the depositing flux, with a magnetic field strength of ~15 mT and ~ 47 mT for the C and Ni cathodes, respectively. The influence of film composition, the energy and incidence angle of incoming species on the film morphology is investigated. For more detail on the sample growth see Ref. [11].

The morphology of the films was studied by cross-sectional transmission electron microscopy (XTEM) and grazing incidence small angle x-ray scattering (GISAXS). 2D

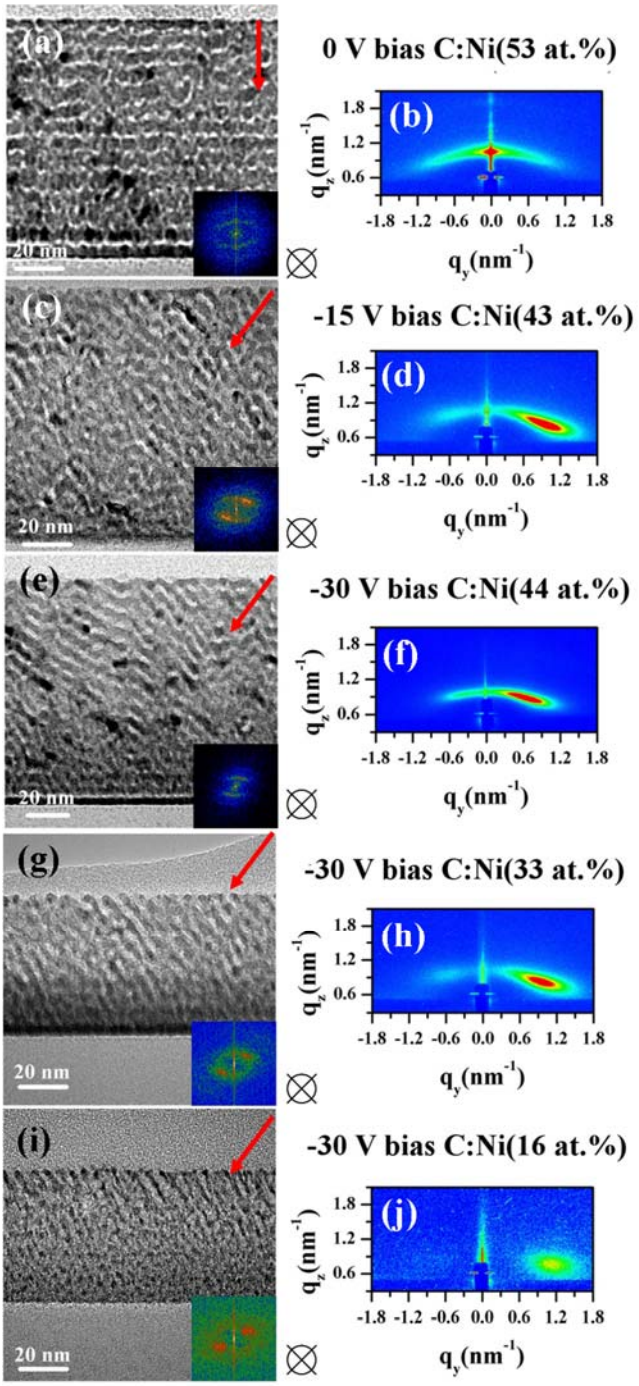

Fig. 1.
C:Ni film morphologies by XTEM (left column) and GISAXS (right column). Growth parameters are indicated on the corresponding panels. The arrows in right up corners of the XTEM images schematically indicate the incoming ion direction. The insets are FFTs of the corresponding XTEM images. The crossed circles indicate the direction of the x-ray beam for the corresponding GISAXS measurements. The azimuthal angle $\phi \approx 0$, thus $q_x \approx 0$ (taken from Ref. [11]).†

GISAXS measurements were recorded by means of a charge coupled detector at the Rossendorf Beamline ROBL BM 20, at the ESRF, Grenoble, France. The x-ray beam with wavelength λ=0.1051 nm arrives at the sample with an incidence angle α_i which was kept above the critical angle of total external reflection at 0.3° or 0.35° in order to probe all of the C:Ni precipitate layers. The reported GISAXS features can be observed only when the angle of incidence is larger than the critical angle. The in-plane scans were carried out at the beamline ID01 at the ESRF, Grenoble, France, using x-ray radiation of wavelength λ=0.1127 nm and a position sensitive detector (PSD). The PSD wire was aligned parallel with the sample surface so that the in-plane information could be measured with one shot. For more details on the thin film characterization see Ref. [11].

2D GISAXS images represent the Fourier transformation of the density contrast autocorrelation function weighted by the transmission function. Taking into account that the incidence and scattering angles are small, the horizontal and vertical components of the scattering vector $\mathbf{q}(q_x,q_y,q_z)$ are expressed as

$$\mathbf{q} = \frac{2\pi}{\lambda}\begin{bmatrix} \sin\phi \sin 2\theta_{sc} \cos\alpha_f \\ \cos\phi \sin 2\theta_{sc} \cos\alpha_f \\ \sin\alpha_i + \sin\alpha_f \end{bmatrix}$$

where α_i is the x-ray angle of incidence, α_f is the out-of-plane exit angle, θ_{sc} is the in-plane scattering angle, and ϕ is the in-plane rotation angle.

Results and discussion

Figure 1 (a)-(b) shows that ion impacts normal to the surface result in a symmetric structure consisting of alternating carbon-rich and nickel-rich layers. The nickel rich layers consist of nickel carbide nanoparticles.

Ion impacts off-normal to the surface tilt the alternating carbon rich and nickel layers (see Fig. 1 (c)-(j)): the Ni precipitate layers do not align with the film surface anymore but with the incoming ions. At the initial deposition stages a few precipitate layers form parallel to the substrate surface before the layers tilt. An increase in both Ni content and ion energy reduces the tilt angle while increases the period. The fast Fourier transform (FFT) of the XTEM images exhibit rotational rather than mirror symmetry observed for perpendicular incidence. The orientations of the most intense lobes match the direction of the incoming ions. 2D GISAXS images from a macroscopic sample region (in the order of several mm^2) closely resemble the upper part of the FFT patterns of the local area probed by XTEM. This confirms that the observed asymmetries are a global property of the material. No ordered structures have been observed for the Ni content of ~7at.% by XTEM and 2D GISAXS shows no detectable density contrast.

Frequency-filtered XTEM images of a C:Ni(~32 at.%) sample reveal that periodic composition modulations observed in the original image are enhanced when the Fourier components in the quadrants containing the incident ion direction are retained (Fig. 2). When the FFT quadrants in ion direction are removed, a weak periodic structure is revealed again but with much weaker amplitude. Thus the composition nanopattern consists of two composition waves with different amplitudes 'moving' toward the incoming and roughly perpendicular to them. This is reflected in the 2D GISAXS pattern (Fig. 2 (d)) where two intensity lobes with different intensities at positive and negative q_r values are observed. A weak intensity lobe is observed in all asymmetric GISAXS patterns except for the C:Ni film with the lowest metal to carbon ratio of ~15 at.%. Therefore the intensity lobes in 2D GISAXS patterns are attributed to the distribution of the composition modulation waves within the films.

GISAXS images for different in-plane

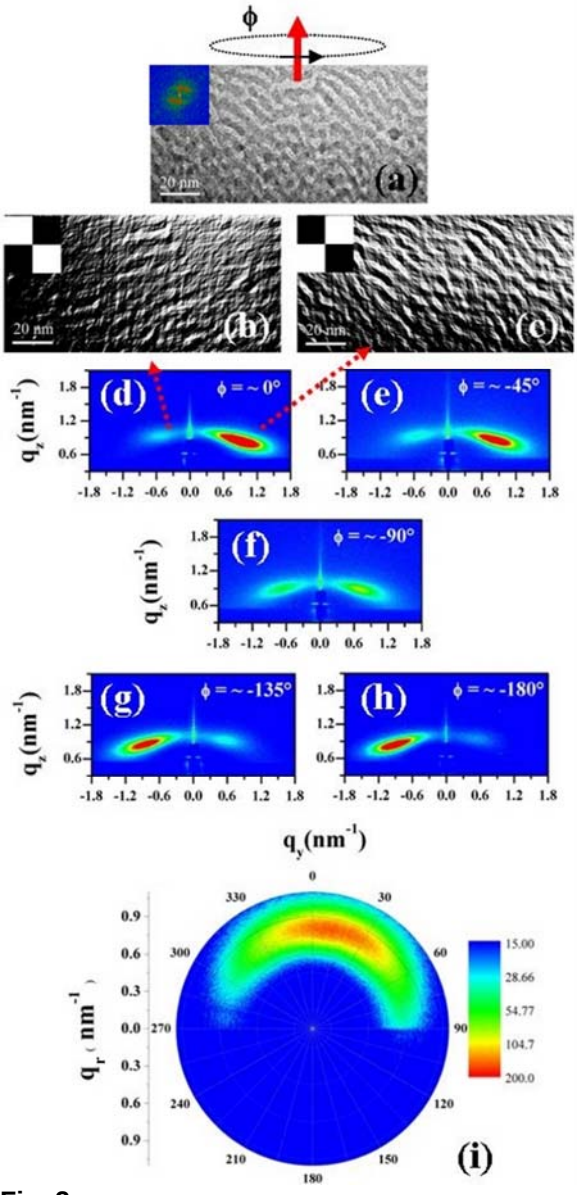

Fig. 2.
Detailed morphology of a C:Ni(~32 at.%) sample (ion incidence ~15° incidence, bias -30 V). (a) is the X-TEM image and the FFT of the C:Ni layer (inset); (b) and (c) are Fourier-filtered X-TEM images (frequency masks in the insets); (d)-(h) are GISAXS images obtained at x-ray incidence angle of α_{in}=0.30° (λ=0.1051 nm) after rotating the sample around its normal by an angle ϕ (Note that $|q_r| = \sqrt{q_x^2 + q_y^2}$); (i) is a ϕ scan at fixed values of α_{in}=0.26° and q_z=0.83 nm^{-1} (λ=0.1127 nm). The negative q_r values in (d)-(h) correspond to the positive values q_r in (i) for $\phi \geq 180°$. (taken from Ref. [11]).†

rotation ϕ angles are shown in Fig. 2 (d)-(h). The information in these images may correspond to FFTs of film cross-sections cut at corresponding angles ϕ weighted by a transmission function. At $\phi \approx$ -90° (i.e. perpendicular to the plane containing the surface normal and incoming ion direction) the two lobes equilibrate. This shows that in this direction the composition is not stratified along the film growth direction, but consists of oblique density modulations with similar periods, off-set angles and amplitudes. The latter observation strongly indicates that the metal rich layers observed by XTEM consist of individual nanoparticles and not continuous layers. Therefore the layer appearance in XTEM must be attributed to projection effects (see also Ref. [5]). The GISAXS pattern inverts under further rotation of the sample to $\phi \approx$-180°. An in-plane scan at a fixed q_z shows that the intensity is concentrated in the azimuthal angle range of ~-10°<ϕ<~45° with the maximum at ϕ=~23° (Fig. 2 (i)). The fact that the maximum is not at ϕ = 0° possibly relates to the fact that the incident ion flux comes at a certain azimuthal angle.

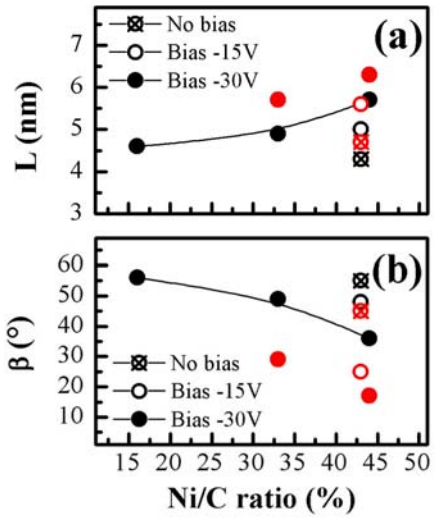

Fig. 3.
Characteristic period L (a) and layer tilting angle β (b) as determined from GISAXS (ion incidence ~15°) . Values in black (red) correspond to the more (less) intense lobe (taken from Ref. [11]).†

The pattern periodicity L and tilt angle β were estimated as the reciprocal of the vector joining the maximum of the lobe with the center of the reciprocal space and its angle with the central specular rod, respectively represents the tilting angle of the layers (Fig. 4). It can be seen that L increases concomitantly with the metal content and ion energy, while β shows the opposite tendency. The period is greater for the weak density modulation component, and the opposite is true for β.

Conclusions

The results of this study show that the directionality of the incoming ions is transferred to the periodic precipitation process during iPVD resulting in the tilt of the precipitation nanopatterns under oblique ion incidence. The periodicity and tilt are caused by ion induced ballistic effects and, consequently, depend on the ion energy and incidence angle. The findings suggest that iPVD offers means for the external control of the pattern periodicity and tilt via incoming ion energy, material supply rate and incidence angle. While the atomistic mechanisms for such a behaviour remain unclear, our recent study shows that the sub-plantation is one of the key factors governing such ion induced compositional self-organization [12]. As the underlying driving mechanism is of physical origin, we believe that the results of this study are applicable to other immiscible systems, and present an alternative approach to sculpting the nanostructure of multifunctional materials.

Acknowledgements

G.A. acknowledges the financial support of the Department of Education, Employment and Workplace Relations, Canberra, Australia, in the Framework of Endeavor Research Fellowship, under Contract No. 837_2008. We thank ESRF, Grenoble, France, for providing synchrotron radiation facilities and would like to acknowledge the support of the ID01 beamline staff T.W. Cornelius and H.T. Metzger.

References

† Reprinted with permission from G. Abrasonis, T.W.H. Oates, G.J. Kovacs, J. Grenzer, P.O.A. Persson, K.H.H. Heinig, A. Martinavicius, N. Jeutter, C. Baehtz, M. Tucker, M.M.M. Bilek, W. Moeller, J. Appl. Phys. 108, 043503 (2010). Copyright 2010, American Institute of Physics.

[1] P.M. Ajayan, L.S. Schadler, P.V. Braun, Nanocomposite Science and Technology, Wiley-VCH, Weinheim, 2003.

[2] J.D. Halley, D.A. Winkler, Complexity 14/2 (2008) 10.

[3] M. Ohring, Materials Science of Thin Films, Academic Press, San Diego, 2002.

[4] J.M.E. Harper, K.P. Rodbell, Journal of Vacuum Science & Technology B 15/4 (1997) 763.

[5] I. Gerhards, H. Stillrich, C. Ronning, H. Hofsass, M. Seibt, Phys. Rev. B 70/24 (2004) 8.

[6] W.Y. Wu, J.M. Ting, Chem. Phys. Lett. 388/4-6 (2004) 312.

[7] C. Corbella, B. Echebarria, L. Ramirez-Piscina, E. Pascual, J.L. Andujar, E. Bertran, Appl. Phys. Lett. 87/21 (2005) 3.

[8] C.Q. Chen, Y.T. Pei, K.P. Shaha, J.T.M. De Hosson, Applied Physics Letters 96/7 (2010).

[9] J.H. He, C.A. Carosella, G.K. Hubler, S.B. Qadri, J.A. Sprague, Phys. Rev. Lett. 96/5 (2006) 4.

[10] G. Abrasonis, G.J. Kovacs, L. Ryves, M. Krause, A. Mucklich, F. Munnik, T.W.H. Oates, M.M.M. Bilek, W. Moller, J. Appl. Phys. 105/8 (2009) 083518.

[11] G. Abrasonis, T.W.H. Oates, G.J. Kovacs, J. Grenzer, P.O.A. Persson, K.H.H. Heinig, A. Martinavicius, N. Jeutter, C. Baehtz, M. Tucker, M.M.M. Bilek, W. Moeller, J. Appl. Phys. 108 (2010) 043503.

[12] G. Abrasonis, G.J. Kovacs, M.D. Tucker, R. Heller, M. Krause, M.C. Guenette, F. Munnik, J. Lehmann, A. Tadich, B.C.C. Cowie, L. Thomsen, M.M.M. Bilek, W. Moller, Appl. Phys. Lett. 97/16 (2010).

In-situ X-ray diffraction studies during dehydrogenation of melt-spun and hydrogenated Mg-Ni alloys

S. Kalinichenka[1], L. Röntzsch[2], C. Baehtz[3], Th. Weißgärber[2], B. Kieback[1,2]

[1] Institute of Materials Science, Dresden University of Technology, Helmholtzstr. 7, 01069 Dresden, Germany

[2] Fraunhofer Institute for Manufacturing Technology and Advanced Materials IFAM, Winterbergstr. 28, 01277 Dresden, Germany

[3] Institute of Ion Beam Physics and Materials Research, Helmholtz Center Dresden-Rossendorf, 01314 Dresden, Germany

Introduction

Hydrogen is a powerful, versatile and carbon-free energy carrier [1]. In particular for mobile and small stationary applications, where hydrogen can serve as fuel for internal combustion engines or fuel cells, the safe and efficient storage of hydrogen has been recognized as one of the key technological challenges in the transition towards a hydrogen-based economy [2, 3]. The state-of-the-art storage methods such as high-pressure gas or liquid hydrogen cannot fulfil the targets set for storage density, safety and efficiency. Chemical or physically combined storage of hydrogen in other materials has potential advantages over other storage methods [1, 4].

It is well known that Mg-rich alloys are attractive materials for solid-state hydrogen storage applications because of their high gravimetric hydrogen storage densities of up to 7.6 wt.%-H in the case of MgH_2, good reversibility, low specific weight, a comparatively high availability in the earth's crust and low cost [2]. However, the major problem of magnesium as a reversible hydrogen storage material is the slow reaction kinetics of hydrogenation and dehydrogenation. A nanocrystalline structure and the use of catalytic elements provide a way to overcome these kinetic limitations of conventional cast magnesium materials [4, 5]. For achieving nanocrystallinity, mechanical milling has been extensively investigated [6]. Alternatively, rapid solidification processes such as melt spinning with cooling rates in the range between 10^5 and 10^6 K/s [7] can also be used to produce nanocrystalline magnesium alloys containing catalytic elements like transition metals or rare earth metals [8]. Such melt-spun Mg alloys exhibit good hydrogen storage properties based on the reaction of gaseous hydrogen with the solid material [9]. However, structural phase transformations during the hydrogen sorption reactions and the role of catalyst phases still need to be investigated in detail to elucidate the complex reaction pathways.

The aim of the in-situ diffraction study at the Rossendorf Beamline at ESRF was to investigate the phase transformations during desorption of three melt-spun, activated and hydrogenated Mg-rich alloys $Mg_{90}Ni_{10}$, $Mg_{80}Ni_{10}Y_{10}$ and $Mg_{85}Cu_5Ni_5Y_5$ whose hydrogen storage characteristics were studied recently [10, 11, 12]. It was found that the kinetics of hydrogen desorption is controlled by different mechanisms. During the dehydrogenation of $Mg_{90}Ni_{10}$ two separate processes were identified: desorption of Mg_2NiH_4 to $Mg_2NiH_{0.3}$ and desorption of MgH_2 in the presence of $Mg_2NiH_{0.3}$. Evidently, $Mg_2NiH_{0.3}$ plays a significant role in the desorption process of hydrogenated $Mg_{90}Ni_{10}$. In the case of $Mg_{80}Ni_{10}Y_{10}$ no formation of the $Mg_2NiH_{0.3}$ phase was observed. Compared to $Mg_{90}Ni_{10}$ and $Mg_{80}Ni_{10}Y_{10}$, it was found that in the case of $Mg_{85}Cu_5Ni_5Y_5$ the dehydrogenation of the hydride phases and the transformation of $Mg_2Ni_{0.5}Cu_{0.5}$ take place simultaneously.

Materials and methods

$Mg_{80}Ni_{10}Y_{10}$ and $Mg_{85}Cu_5Ni_5Y_5$ were produced by induction-melting of a mixture of pure Mg (99.9% purity) metal, Ni (99.9% purity) powder, Cu (99.99% purity) powder and a Ni-Y alloy (Ni-25.4 wt.%; Y-75.5 wt.%) in a tantalum crucible at 1000°C under argon atmosphere. For production of the $Mg_{90}Ni_{10}$ master alloy, appropriate amounts of the raw

materials (Mg and Ni) were mixed together and melted in an induction furnace using a BN coated crucible under argon. During melt spinning of these alloys, continuous ribbons with 35 µm in thickness and 10 mm in width were obtained from a single roller melt-spinning device (PSI) which contains a copper wheel with a diameter of 200 mm and a constant surface velocity of 40 m/s as rapid cooling component. The melt spinning experiments were carried our under argon.

The thermal activation of the melt-spun ribbons was achieved during three cycles at 385°C and pressures between 2 and 30 bar H_2 (99.9998% purity) for 11 h.

In-situ synchrotron XRD studies of melt-spun, activated and hydrogenated $Mg_{90}Ni_{10}$, $Mg_{80}Ni_{10}Y_{10}$ and $Mg_{85}Cu_5Ni_5Y_5$ were performed at the Rossendorf Beamline (ROBL-CRG, BM 20) of the European Synchrotron Radiation Facility (ESRF) in Grenoble. The measurements were carried out in a special annealing chamber, using a hemispherical radiation window (Be-dome), which allows in-plane and out-of-plane measurements in horizontal and vertical directions. The hydrogenated ribbons were manually ground into fine powders by adding acetone. A small amount of the sample was put together with a thermocouple onto a Si single crystal sample holder as it shown in Fig. 1.

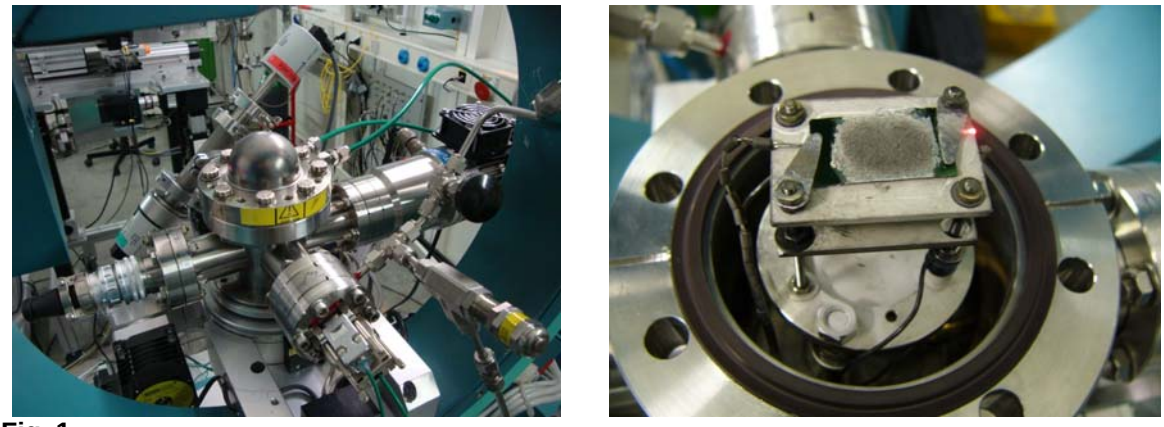

Fig. 1.
Experimental setup: (left) six-circle Goniometer at at the Rossendorf Beamline (ROBL-CRG, BM 20); (right) pulverized sample with a thermocouple on a Si single crystal sample holder.

The incident X-ray beam with an X-ray wavelength of 1.05 Å was used for the investigation in the scanning range of the diffraction angle between 17.5° and 28° (2Θ) in reflection geometry. The hydrogen desorption of the melt-spun alloys was studied in vacuum at 200°C. The heating to 200°C was carried out with a rate of 50 K/min.

The obtained powder diffraction data were analyzed based on the Rietveld method, using Topas 4.2 for the refinement of the crystal structures and for the calculation of phase abundances.

Results and discussion

Mg-Ni system: Fig. 2 shows the evolution of the diffraction pattern during the time-resolved SR-XRD studies of the hydrogen desorption obtained for $Mg_{90}Ni_{10}$.The X-ray diffraction pattern at t=0 min represents the X-ray diffraction pattern of hydrogenated $Mg_{90}Ni_{10}$ at ambient temperature which exhibits three hydride phases: MgH_2, Mg_2NiH_4 and $Mg_2NiH_{0.3}$. From the Fig. 2 it can be also seen that the vacuum thermal desorption of Mg-Ni alloy could be divided into three stages:

Stage 1 (first 5 Minutes): Dehydrogenation of Mg_2NiH_4 to $Mg_2NiH_{0.3}$

Stage 2 (25 Minutes): Dehydrogenation of MgH_2 in the presence of $Mg_2NiH_{0.3}$ to Mg

Stage 3 (after 30 Minutes): Dehydrogenation of $Mg_2NiH_{0.3}$ to Mg_2Ni

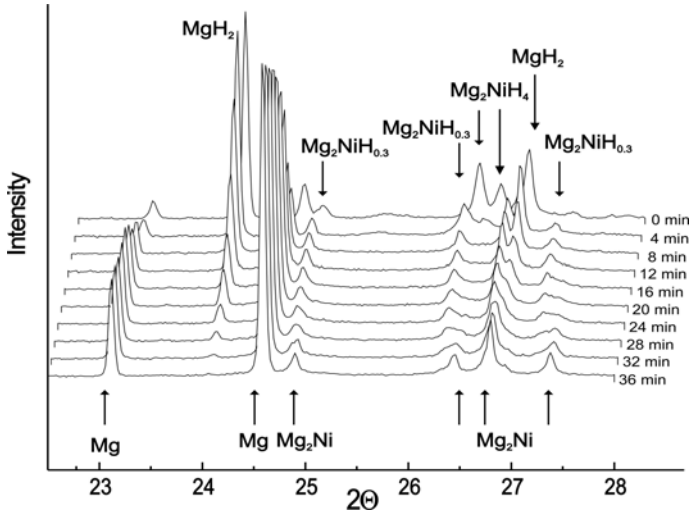

Fig. 2.
Evolution of the in situ SR-XRD pattern of the as-spun and hydrogenated $Mg_{90}Ni_{10}$ during its vacuum thermal decomposition at 200 °C (pressure: 10^{-2} mbar) from [10].

Fig. 3 summarizes the evolution of the phase fractions from the in-situ SR-XRD patterns of $Mg_{90}Ni_{10}$. The small increase of the amount of MgH_2 and HT-$MgNi_2H_4$ between t=0 (25°C) and 4 minutes (200°C) and the increase of $Mg_2NiH_{0.3}$ fraction between t=8 and 25 minutes are considered as inaccuracy in the Rietveld refinement (goodness-of-fit parameters for the refinements were with Rwp in the range of 10%).

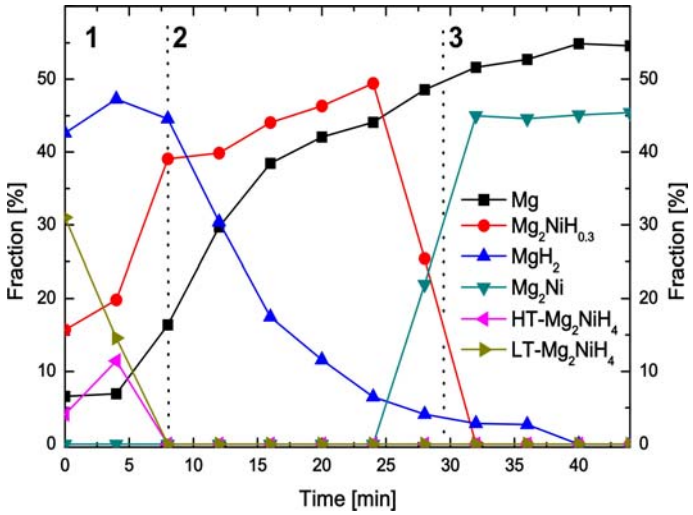

Fig. 3.
The evolution of the structural phase transformation from the in-situ SR-XRD patterns of $Mg_{90}Ni_{10}$ at 200°C in vacuum from [10].

Mg-Ni-Y system: The evolution of the in-situ SR-XRD patterns of hydrogenated $Mg_{80}Ni_{10}Y_{10}$ during its vacuum thermal decomposition are shown in Fig. 4. The scanning range was extended to 17-28° (2Θ) in order to observe the decomposition of YH_3.

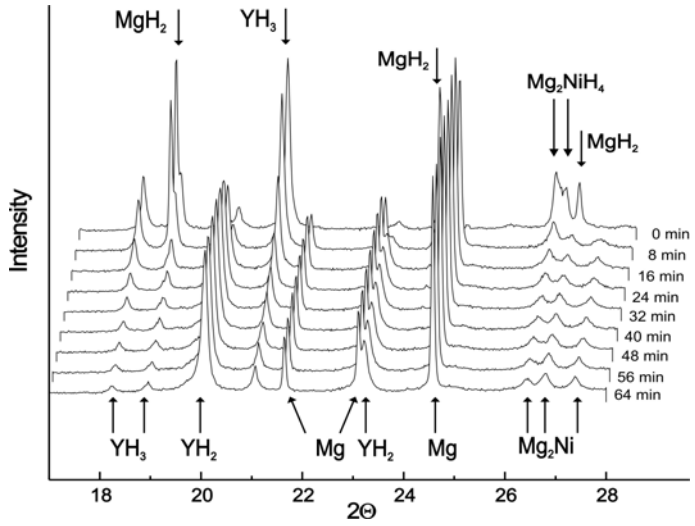

Fig. 4.
Evolution of the in situ SR-XRD pattern of the as-spun and hydrogenated $Mg_{80}Ni_{10}Y_{10}$ during its vacuum thermal decomposition at 200 °C (pressure: 10^{-2} mbar) from [10].

It can be noticed that hydrogen desorption of MgH_2 and Mg_2NiH_4 was almost completed within 24 minutes. From Fig. 4 it is also evident that the transformation of YH_3 into YH_2 is much slower than the dehydrogenation of MgH_2 and Mg_2NiH_4. It should be mentioned that even after 64 minutes at 200°C a residual amount of YH_3 is observed in the diffraction pattern. There exist four phases in the material after hydrogen desorption: metallic Mg, intermetallic Mg_2Ni, YH_2 and YH_3.

Surprisingly, in-situ SR-XRD investigations of the thermal decomposition of $Mg_{80}Ni_{10}Y_{10}$ revealed that no formation of $Mg_2NiH_{0.3}$ is observed in this case during the dehydrogenation. This finding can be explained by the presence of yttrium which is solved in Mg_2Ni which could lead to a microstructural refinement of Mg_2Ni and therefore to a faster kinetics of dehydrogenation. Hence, the time resolution of in-situ SR-XRD investigation of the thermal decomposition of $Mg_{80}Ni_{10}Y_{10}$ was probably not sufficient to explore this structural phase transformation in detail.

Mg-Cu-Ni-Y system: The evolution of the in situ SR-XRD patterns of as-spun and hydrogenated $Mg_{85}Cu_5Ni_5Y_5$ during vacuum thermal decomposition presented in Fig. 5. The patterns of hydrogenated Mg-Cu-Ni-Y (at t=0) exhibit five hydride phases: MgH_2, Mg_2NiH_4, $Mg_2NiH_{0.3}$, YH_2, YH_3 as well as $MgCu_2$. During the dehydrogenation of $Mg_{85}Cu_5Ni_5Y_5$ several processes can be identified: decomposition of the hydride phases according to Eqns. (1) to (4) and transformation of $MgCu_2$ and formation of $Mg_2Ni_{0.5}Cu_{0.5}$.

$$MgH_2 \longrightarrow Mg + H_2 \quad (1)$$

$$Mg_2NiH_4 \longrightarrow Mg_2Ni + 2\,H_2 \quad (2)$$

$$Mg_2NiH_{0.3} \longrightarrow Mg_2Ni + 0.15\,H_2 \quad (3)$$

$$2\,YH_3 \longrightarrow 2\,YH_2 + H_2 \quad (4)$$

However, in contrast to $Mg_{90}Ni_{10}$ and $Mg_{80}Ni_{10}Y_{10}$ these dehydrogenation reactions take place simultaneously. Dehydrogenated $Mg_{85}Cu_5Ni_5Y_5$ consist of five different phases: hcp-Mg, Mg_2Ni, Mg_2Cu, YH_2 and YH_3. It is also evident that the transformation of YH_3 into YH_2 is the slowest step of the reaction and even after 54 minutes at 200°C a residual amount of YH_3 can be observed in the XRD pattern.

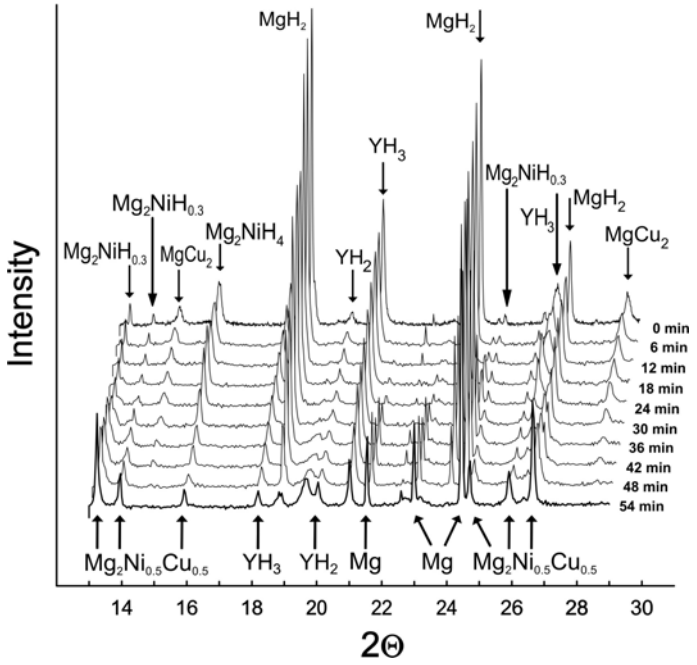

Fig. 5.
Evolution of the in situ SR-XRD pattern of the as-spun and hydrogenated $Mg_{85}Cu_5Ni_5Y_5$ during its vacuum thermal decomposition at 200 °C (pressure: 10^{-2} mbar) from [13].

It is well known that Cu and Mg_2Ni form Cu-substituted Mg_2Ni ($Mg_2Ni_{1-x}Cu_x$). These alloys exhibit a large homogeneity range for *x* values up to 0.85 [15]. In our investigation we observed the formation of the hexagonal $Mg_2Ni_{0.5}Cu_{0.5}$ phase. The cell parameters obtained from the X-ray patterns for this alloy (a = 5.22Å b = 13.51 Å) are in good agreement with literature data [15]. From the XRD results, the hydrogen release reaction between Mg_2NiH_4, MgH_2 and $MgCu_2$ may be described with the following equation:

$$0.75\ MgH_2 + 0.25\ MgCu_2 + 0.5\ Mg_2NiH_4 \longrightarrow Mg_2Ni_{0.5}Cu_{0.5} + 1.75\ H_2 \qquad (5)$$

Conclusions

Melt-spun $Mg_{90}Ni_{10}$, $Mg_{80}Ni_{10}Y_{10}$ and $Mg_{85}Cu_5Ni_5Y_5$ were activated and hydrogenated in the same way as described recently in [10, 11, 12]. The structural phase transformations during dehydrogenation of these materials has been examined at the Rossendorf Beamline (ROBL-CRG, BM 20) of the European Synchrotron Radiation Facility (ESRF) in Grenoble using in-situ synchrotron XRD. In the present study it was found that the alloys show different reactions during the dehydrogenation:

During the dehydrogenation of $Mg_{90}Ni_{10}$ two separate processes were identified: desorption of Mg_2NiH_4 to $Mg_2NiH_{0.3}$ and desorption of MgH_2 in the presence of $Mg_2NiH_{0.3}$. Thus, it is assumed that $Mg_2NiH_{0.3}$ might act as a catalyst transfer phase for the dehydrogenation of adjacent MgH_2.

In-situ SR-XRD investigations of the thermal decomposition of $Mg_{80}Ni_{10}Y_{10}$ showed no formation of $Mg_2NiH_{0.3}$ during dehydrogenation. The reason for this finding could be explained by yttrium which is solved in Mg_2Ni. Yttrium, having a larger atomic radius (1.8 Å) compared to nickel (1.25 Å), can partially substitute Ni in the Mg_2Ni lattice and, thereby, the lattice parameter of Mg_2Ni is increased [14]. This could lead to a fast and more direct transformation of Mg_2NiH4 into Mg_2Ni.

In the case of $Mg_{85}Cu_5Ni_5Y_5$ the SR-XRD results indicate that the dehydrogenation of the hydride phases, the transformation of $MgCu_2$ and formation of $Mg_2Ni_{0.5}Cu_{0.5}$ take place

at the same time. It must be also mentioned that no formation of Mg_2Cu was observed during the dehydrogenation of $Mg_{85}Cu_5Ni_5Y_5$.

The achieved results for the phase transformations play an important role for understanding reactions during desorption of Mg-based melt-spun alloys. However, further studies with better time resolution are required for more detailed investigations.

Acknowledgements

The authors would like to acknowledge financial support of the Boysen-Stiftung, the Fraunhofer Attract program and the European Synchrotron Radiation Facility. We are also grateful to R. Leuschner and M. Hesse for their practical support.

References

[1] B. Sakintuna, F. Lamari-Darkrim, M. Hirscher, Int J Hydrogen Energy 32 (2007) 1121.

[2] I.P. Jain, C. Lal, A. Jain, Int J Hydrogen Energy 35 (2010) 5133.

[3] A.W.C. van den Berg, C.O. Areań, Chem Commun 6 (2008) 668–681.

[4] M. Fichtner, Adv Eng Mater 7 (2005) 443.

[5] L. Zaluski, A. Zaluska, J.O. Strom-Olsen, J. Alloys Compds. 253-254 (1997) 70.

[6] K.-F. Aguey-Zinsou, J.R. Ares Fernandez, T. Klassen, R. Bormann, Int J Hydrogen Energy 32 (2007) 2400.

[7] C. Suryanarayana, Editor, Non-equilibrium processing of materials, Pergamon, Oxford (1999).

[8] M.Y. Song, S. Kwon, J.S. Bae, S.H. Hong, Int J Hydrogen Energy 33 (2008) 1711.

[9] T. Spassov, U. Lyubenova, U. Köster, M.D. Barò, Mater Sci Eng A 375–377 (2004) 794.

[10] S. Kalinichenka, L. Röntzsch, C. Baehtz, B. Kieback, J. Alloys Compds. 496 (2010) 608.

[11] S. Kalinichenka, L. Röntzsch, B. Kieback, Int J Hydrogen Energy 34 (2009) 7749.

[12] S. Kalinichenka, L. Röntzsch, Th. Riedl, Th. Gemming, Th. Weißgärber, B. Kieback, Int J Hydrogen Energy 36 (2011) 1592.

[13] S. Kalinichenka, L. Röntzsch, C. Baehtz, Th. Weißgärber, B. Kieback, J. Alloys Compds, in press, corrected proof, DOI: 10.1016/j.jallcom.2010.10.067.

[14] N. Cui, B. Luan, H.J. Zhao, H.K. Liu, S.X. Dou, J Alloys Compds 233 (1996) 236.

[15] P. Darnaudery, M. Pezat and B. Darriet, J Less-Common Metals 92 (1983) 199.

Reactive DC magnetron sputtering and X-ray investigations of (GeO_x-SiO_2) superlattices for Ge nanocrystal formation

N.M. Jeutter, M. Zschintzsch, J. von Borany, C. Baehtz, A. Mücklich

Institute of Ion Beam Physics and Materials Research,
Forschungszentrum Dresden-Rossendorf e.V., P.O. Box 51 01 19, 01314 Dresden, Germany

Introduction

Semiconductor nanoparticles (-clusters, -crystals: NC) attracted continuously increasing interest, caused by their outstanding properties (e.g. luminescence, charge storage). Numerous studies were performed [1-3], but achieving a high density (> 10^{12} cm^{-2}) of Si or Ge NC (< 5 nm size) regularly ordered in dielectric films remains still a challenge. In our studies we follow the approach of Zacharias et al. [4] and other groups to obtain size controlled Si NCs with the help of SiO/SiO_2 multilayer structures. We applied this method to GeO_x/SiO_2 multilayers in order to get size and density controlled Ge NC for photovoltaic applications. Depending on the NC size and the surrounding matrix, the bandgap energy of Ge NC can be tuned between 0.66 eV and ~ 2 eV which covers almost the complete spectrum of sunlight. Further benefits of Ge compared to Si are the larger light absorption coefficient and the significantly lower thermal budget to generate Ge NC (< 700°C). Here we present the fabrication of GeO_x/SiO_2 superlattices (SL) using dc reactive magnetron sputtering from elemental targets [5]. Main attention is directed towards tailoring the GeO_x composition in a wide range ($0 \le x \le 2$), to generate tiny Ge NC of < 5 nm size after subsequent annealing without destroying the SL and to separate the stacked Ge NC layers by very thin SiO_2 films which might allow charge transport via direct tunnelling.

Experimental

The deposition of the (GeOx/SiO2) SL was performed in the dual magnetron sputter chamber of the ROBL Beamline [6]. This equipment is especially dedicated for in-situ experiments and gives the opportunity to apply a precisely controlled Ar/O2 mixture. Afterwards, the SL were annealed in vacuum (< 5×10-4 Pa) up to TA = 850°C to initiate phase separation (GeOx → Ge + GeO2), Ge nucleation and NC growth. The SL properties and the NC formation were continuously monitored after deposition and during annealing by X-ray reflectivity (XRR) and grazing incidence X-ray diffraction (GiXRD) using synchrotron radiation of 1.08 Å (E = 11.5 keV).

Results and discussion

GeO_x/SiO_2 SL films (19 periods) were grown at two different substrate temperatures at T_D = 200°C (#SL-01) and T_D = 25°C (#SL-02). XRR scans (Fig. 1) reveal highly ordered SL with smooth interfaces ($\sigma \le 1$ nm) for both deposition temperatures.

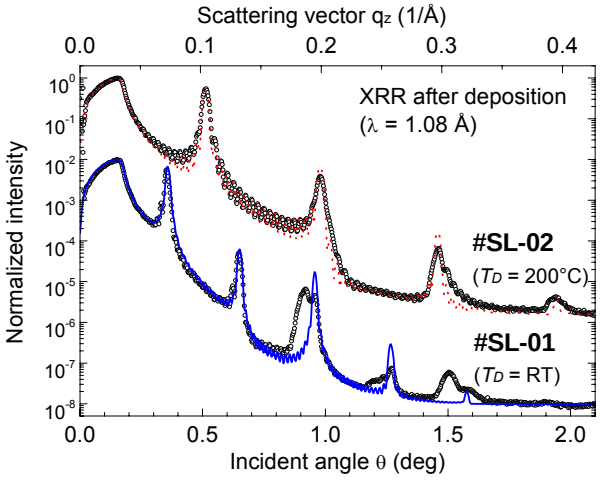

Fig. 1: XRR profiles of the as-deposited films. The symbols represent the measured data, the RC*RefSiMW* fits are included by lines. An offset (factor 100) is used for better visibility.

However for the sample #SL-02 (T_D = 25°C) the XRR pattern shows SL fringes with multiple Bragg peaks which confirms the co-existence of at least two (lateral or vertical) SL periods. The period thicknesses differ by 0.4 nm, which is of minor relevance. The behaviour is less pronounced for the sample #SL-01 (T_D = 200°C) and therefore suggesting better deposition conditions at slightly elevated substrate temperatures. The fitting results using *RefSim* [7] are summarized in tab. 1.

Parameter	#SL-01	#SL-02
T_D	200°C	RT
GeO_x stoichiometry	x = 0.25	x = 0.90
Multilayer thickness	(120 ± 2) nm	(187 ± 2) nm
Period thickness	6.3 nm	9.8 nm
GeO_x / SiO_2 thickness	2.8 / 3.5 nm	4.8 / 5.0 nm
Interface roughness	0.7 nm	1.0 nm

Table I: *RCRefSimW* [7] results of the XRR data for the as-deposited films. If not specified the thickness error amounts to ± 0.1 nm. For constant O_2 partial pressure (20 mPa) and magnetron power, T_D influences the GeO_x stoichiometry (proved by RBS) and the deposition rate: Details are described in ref. [5].

After deposition the samples were stepwise annealed at temperatures T_A ranging from 500°C to 810°C without breaking the vacuum conditions. The temperature-dependent XRR profiles for #SL-02 (T_D = 25°C) are shown in Fig. 2. Above 500°C, one obtains an ongoing degradation of the SL structure, starting with the loss of the 5th order SL peak. At T_A = 630°C, only the first two SL peaks are still visible. Finally at T_A = 690°C most of the Kissig fringes disappeared and only the first SL peak is left. This correlates with a remarkable change of interface roughness, which increases from 1.0 nm (as-deposited) to 3.4 nm. From recent investigations we conclude that this disappearance of the SL peaks is a strong indication for the formation of separated Ge NC into the former GeOx sublayers. The significant increase of interface rougnness is caused by multilayer bulging (not shown here) without generally destroying the multilayer structure.

Figure 3 shows the XRR data of #SL-01 (T_D = 200°C) collected after deposition and annealing at 545°C and 600°C. After annealing at T_A = 540°C the intensity of the SL Bragg reflections increases and even a 5th SL peak occurs at θ = 2.4° which indicates an improved periodicity. The simulation shows that the interface roughness decreases to σ = (0.5 ± 0.1) nm after annealing to T_A =600°C. The different behaviour compared to #SL-02 is explained by the higher Ge content in the GeO_x film (see tab. 1) leading after annealing to the formation of a nanocrystalline Ge film with smooth interfaces to the surrounding SiO_2 layers (instead of separated Ge NC). The stability of Ge/SiO_2 SL is given until annealing temperatures of at least T_A =750°C.

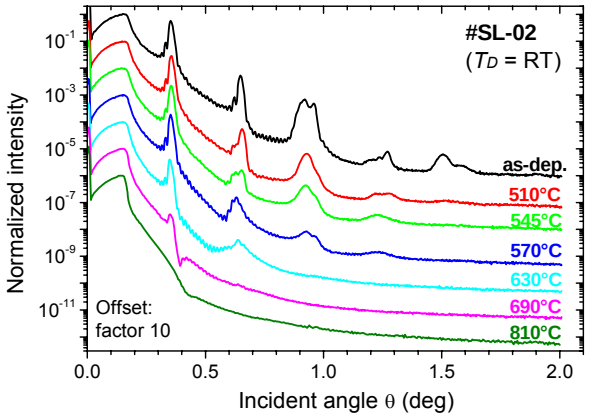

Fig. 2: XRR of #SL-02 (T_D = RT) measured after deposition and during post-annealing treatment up to 690°C.

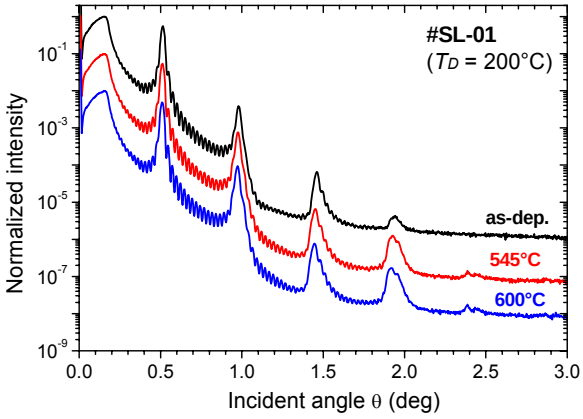

Fig. 3: XRR of #SL-01 (T_D = 200°C) measured after deposition and during the post-annealing treatment up to 600°C. Offset like in fig. 2.

GIXRD scans (incident angle $\alpha_i = 0.25°$) were performed *in-situ* directly after deposition and during each annealing step under high-vacuum conditions ($p < 5\times10^{-4}$ Pa). The diffraction pattern was treated with respect to background subtraction and Gaussian peak fitting using the *XOP* tool [8]. For the sample #SL-02 ($T_D = 25°C$) not any characteristic pattern of Ge NC could be observed after deposition. But the sample #SL-01 ($T_D = 200°C$) already showed a broad hump (FWHM ≈ 6°) around the Ge (111) position (Fig. 4a).

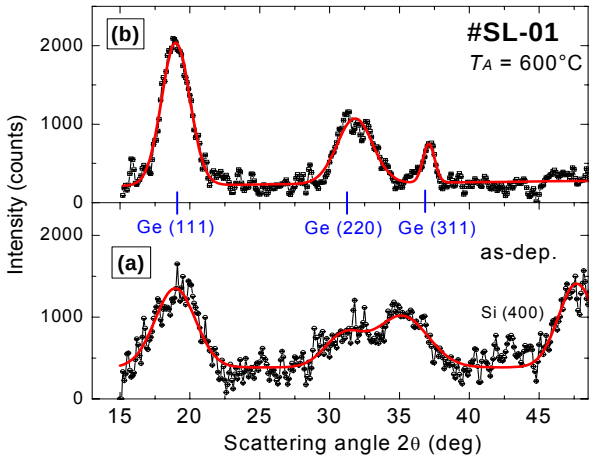

Fig. 4: GIXRD ($\alpha_i = 0.25°$) for #SL-01 (T_D=200°C). (a) As-deposited pattern with the glassy near-order peak of Ge. (b) XRD pattern obtained after annealing at 600°C. From (111) and (220) Ge reflections an average NC size of (2.6 ± 0.2) nm can be derived.

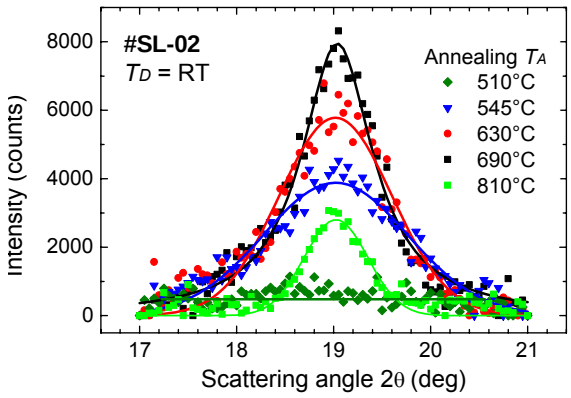

Fig. 5: #SL-02 ($T_D = 25°C$): Development of Ge(111) bragg peak intensity during annealing. The loss in intensity at $T_A = 810°C$ indicates a strong loss of Ge (60%), while the Ge NC are even bigger then at $T_A = 690°C$. The lines represent the fitting results.

Our HRTEM studies [5] do not reveal crystalline Ge after the deposition. Therefore most likely this signal originates from a "glass-like" near-ordering of the Ge atoms. Similar patterns have been reported by Zacharias *et al.* [1] and Fujii *et al.* [9]. A typical threshold temperature for Ge NC formation out of GeO_x or $SiGeO_x$ matrix is $T_A = 500°C$ [1, 10]. In agreement, a distinct Ge(111) peak was observed during the annealing at $T_A = 540°C$. At $T_A = 600°C$ a well pronounced diffraction pattern (Fig. 4b) is obtained. The grain size within the nanocrystalline film derived from Ge(111) and (200) reflections amounts to (2.6 ± 0.2) nm (see Fig. 6) which perfectly fits to the GeO_x sublayer thickness of the ML stack.

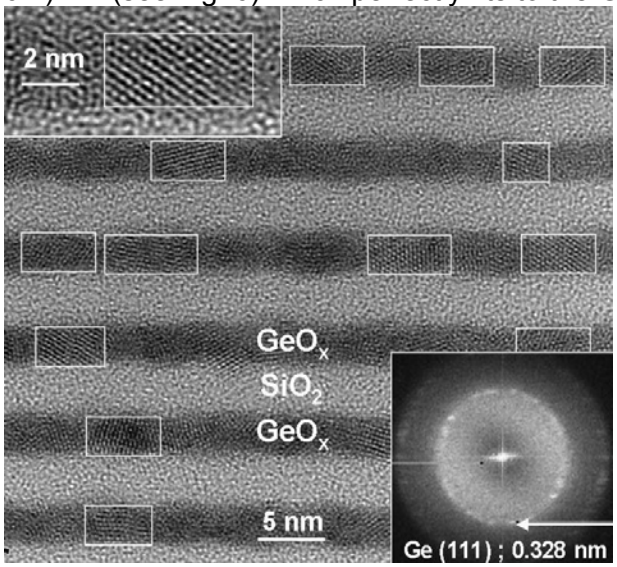

Fig. 6: High-resolution TEM image of #SL-01 after 600°C annealing showing disk-like Ge NC (size: 3 nm × 6 nm). The lower inset shows the powder-like orientation distribution of Ge(111) in the corresponding FFT image.

For sample #SL-02 crystallisation is starting also slightly above 500°C. After $T_A = 630°C$ annealing the NC size of 4.7 nm corresponds with the GeO_x sublayer thick-

ness (see Tab. I). Further annealing to T_A = 690°C leads to a growth of Ge NC up to 5.7 nm which now clearly exceeds the initial GeO_x sublayer thickness. Even more, after T_A = 810°C, NC growth to a size of > 8 nm and XRR indicates a complete dissolution of the SL (see Fig. 2). For this temperature, also a strong decrease of the integrated scattering intensity (Fig. 5) has been observed which is caused by a Ge loss (proved ex-situ by Rutherford Backscattering Spectrometry due to the formation of volatile GeO. The Ge loss can be significantly suppressed by the deposition of an additional SiO_2 cap layer.

Conclusions

The deposition of GeO_x/SiO_2 SL via dc reactive magnetron sputtering offers an easy way to fabricate Ge NC with high density after subsequent annealing by phase separation. Due to the larger sticking coefficient of oxygen at Si compared to Ge, the deposition of SiO_2 and GeO_x ($0.5 \le x \le 2$) can be alternatively performed with a constant oxygen partial pressure [5]. According to the GeO_x stoichiometry it is possible to generate nanocrystalline films or stacked layers of separated NC. As the SL interface roughness at T_D = 200°C is $\sigma \sim 0.5$ nm, the separating SiO_2 film thickness can be reduced to < 3 nm allowing direct charge tunnelling. The formation of Ge NC of 2 – 5 nm size has been shown by GiXRD after annealing at $T_A \approx 550$°C, which is a very convenient temperature for opto-electronic applications. The crystal size at moderate annealing temperatures, keeping the SL stable, can be tuned by the GeO_x layer thickness. During phase separation the formation of volatile GeO competes with the usually considered reaction path $GeO_x \rightarrow Ge + GeO_2$ in particular for GeO_x films with $x \ge 1$. Recent studies have shown that the magnetron sputtering multilayer approach can be used the fabricate SL with ultrathin SiO_2 separation layers ≤ 1 nm. Further effort is necessary to investigate different GeO_x compositions ($0.5 \le x \le 1.5$) leading to different shapes of the NCs to locate the optimum between carrier transport and strength of quantum confinement.

Acknowledgements

The authors thank Dr. Jörg Grenzer (both HZDR) for technical support at ROBL and corresponding scientific discussions.

References

[1] M. Zacharias, J. Bläsing, M. Löhmann, J. Christen, Thin Solid Films **278**, 32-36 (1996).

[2] S. Foss, T.G. Finstad, A. Dana, A. Aydinli, Thin Solid Films **515**, 6381-6384 (2007).

[3] M. Buljan, U.V. Desnica, G. Drazic, M. Ivanda, N. Radic, P. Dubcek, K. Salamon, S. Bernstorff, V. Holy, Nanotechnology **20**, 085612 (2009).

[4] M. Zacharias J. Heitmann, R. Scholz, U. Kahler, M. Schmidt, J. Blaesing, Appl. Phys. Lett. **80,** 661-663 (2002).

[5] M. Zschintzsch, N.M. Jeutter, J. von Borany, M. Krause, A. Muecklich, J. Appl. Phys. **107**, 034306 (2010).

[6] N. Schell, W. Matz, F. Eichhorn, F. Prokert, F. Berberich, J. Alloys & Compounds **328**,105-111 (2001).

[7] *RCRefSimW* Software by P.Zaumseil (see http://www.ihp-microelectronis.com/4.html)

[8] The XOP freeware is available at http://www.esrf.eu/computing/scientific/xop2.1

[9] M. Fujii, S. Hayashi, K. Yamamoto, Japanese J. Appl. Phys. **30**, 687 (1991).

[10] C.J. Sahle, C. Sternemann, H. Conrad, A. Herdt, O.M. Feroughi, M. Tolan, A. Hohl, R. Wagner, D. Luetzenkirchen-Hecht, R. Frahm, A. Sakko, Appl. Phys. Lett. **95,** 021910 (2009).

[11] M. Zschintzsch et al.; submitted for publication in Nanotechnology (2011).

2. Technical Documentation and Statistics

2.1. Technical status and developments

Overview and optical characteristics

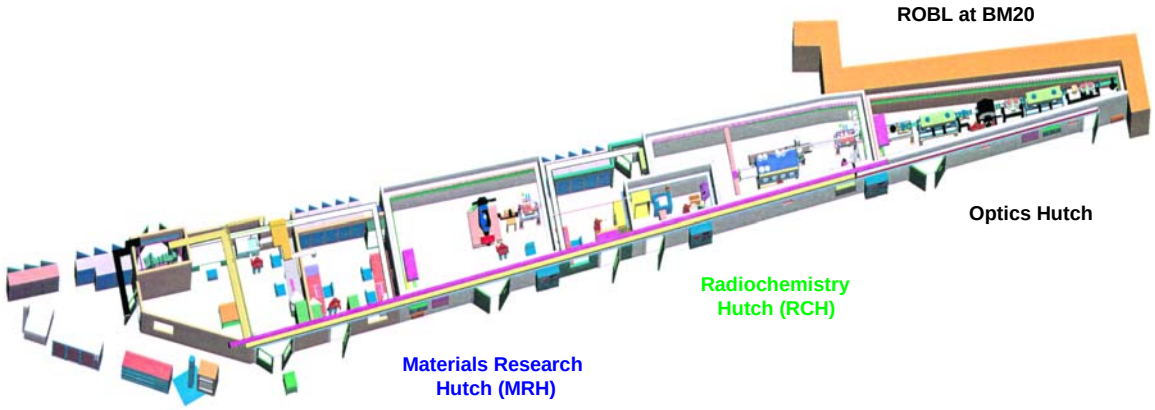

The optics with two mirrors and a double-crystal monochromator in fixed-exit mode provide both a high flux at high angular resolution (for diffraction) and a high flux over a wide energy range with high energy resolution (for EXAFS spectroscopy).

energy range	**5 – 35 keV**
with Si-mirrors	5 – 12 keV
energy resolution Si(111)	1.5 – 2.5x10^{-4}
energy resolution Si(311)	0.5 – 1.0x10^{-4}
integrated flux (calc.)	**6·10^{11} phot. / s** @ 20 keV/200 mA
standard beam size	20 × 3 mm^2 (w×h)
focussed beam size	≤ 0.5 x 0.5 mm^2

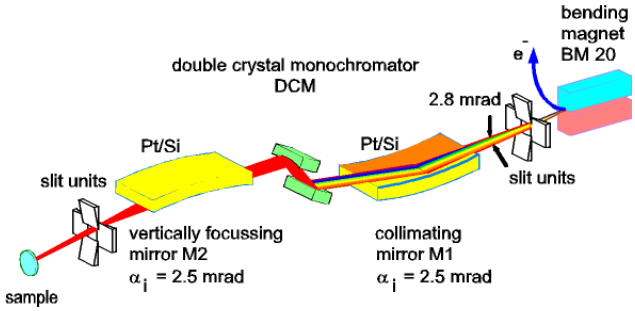

1a	2a	3b	4b	5b	6b	7b	8			1b	2b	3a	4a	5a	6a	7a	0
H																	He
Li	Be											B	C	N	O	F	Ne
Na	Mg											Al	Si	P	S	Cl	Ar
K	Ca	Sc	Ti	V	Cr	Mn	Fe	Co	Ni	Cu	Zn	Ga	Ge	As	Se	Br	Kr
Rb	Sr	Y	Zr	Nb	Mo	Tc	Ru	Rh	Pd	Ag	Cd	In	Sn	Sb	Te	I	Xe
Cs	Ba	La	Hf	Ta	W	Re	Os	Ir	Pt	Au	Hg	Tl	Pb	Bi	Po	At	Rn
Fr	Ra	Ac	Rf	Ha													

Lan	Ce	Pr	Nd	Pm	Sm	Eu	Gd	Tb	Dy	Ho	Er	Tm	Yb	Lu
Act	Th	Pa	U	Np	Pu	Am	Cm	Bk	Cf	Es	Fm	Md	No	Lr

The energy range allows to investigate the elements in yellow by K-edge EXAFS, and those in blue by L-edge EXAFS. Radionuclides presently permitted at the beamline are shown in red.

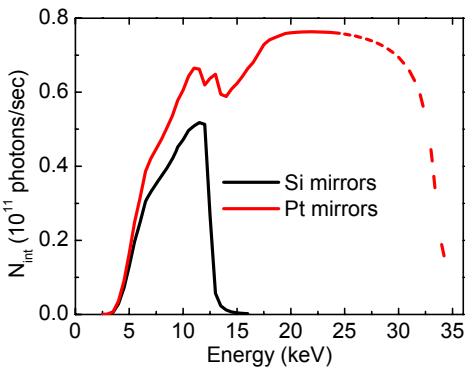

Energy range with different crystals and mirror materials

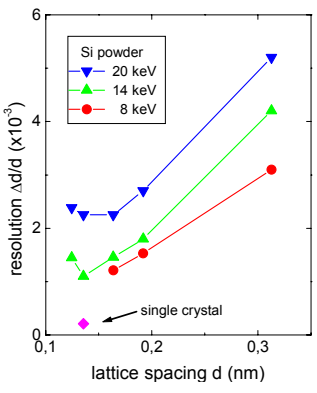

Experimental resolution determined with Si(111) and Si powder

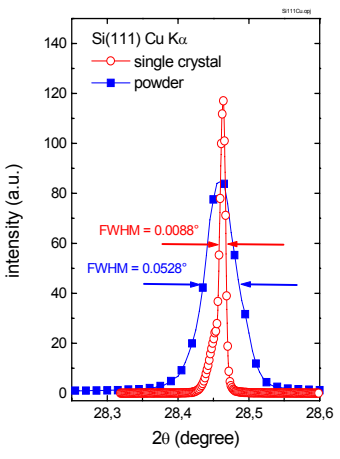

FWHM comparison

Technical characteristics of the Radiochemistry station

The Radiochemistry experimental station is a highly specialized *unique* **radiochemical laboratory** designed for **radioecological research** using x-ray absorption spectroscopy (XAS) in transmission and fluorescence mode. Solid and liquid samples with a total activity of **185 MBq** (5 mCi) and a surface dose rate of **15 µSv/h** can be investigated. A **multi-barrier safety concept** with separate ventilation, constant radiation monitoring and redundancy of all essential components was developed to satisfy legal requirements.

Tc-99	**Po-208**	**Po-209**	**Ra-226**	**Th-nat**	**Pa-231**
30,000	0.008	0.3	5	10^6	106
U-nat	**Np-237**	**Pu-238**	**Pu-239**	**Pu-240**	**Pu-241**
10^6	7000	0.3	80	22	0.049
Pu-242	**Am-241**	**Am-243**	**Cm-244**	**Cm-246**	**Cm-248**
124	1.4	25	0.062	17	1,156

List of permitted **radionuclides** and their maximum amount in mg (shown in blue). Additional radionuclides may be used if accepted by the ESRF safety group.

During the measurement, the **spectroscopic glove box** envelops the samples, which are mounted either on a remote-control 8-fold multistage holder or in a cryostat. The fluorescence and transmission detectors remain outside of the glove box.

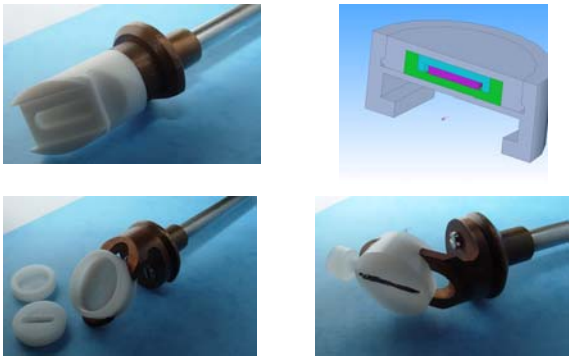

Sample holders fulfilling the necessary safety requirements exist in a wide variety to match different sample. Technical drawings and detailed information on filling procedures may be downloaded from our home page.

13 element LEGe detector with a high-rate digital multi-channel analysis spectrometer (XIA) and dedicated analysis program integrated into the XAS data collection software XATROS.

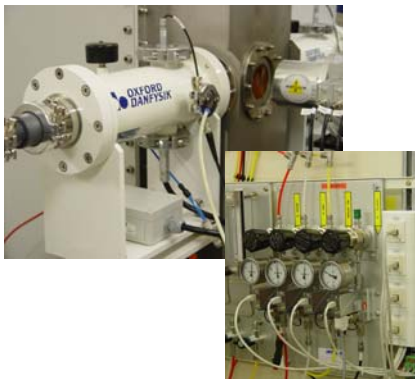

3-kV ionization chambers with remote-controlled gas mass-flow controllers.

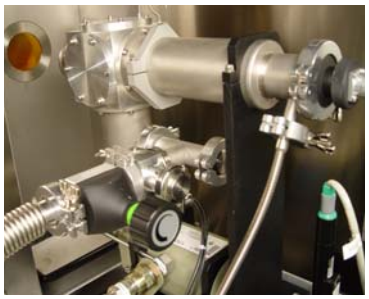

Closed-cycle He cryostat with large fluorescence window adapted to the 13-element detector and very low vibration levels cools samples down to 15 K.

Technical characteristics of the Materials Research station

The materials research hutch MRH with a heavy load six-circle diffractometer is designed for the various scattering and diffraction experiments, which can also be combined with spectroscopic measurements. The core competence of MRH is in-situ research, where the system under investigation was characterized during synthesis or processing while besides structural information also physical properties like electrical conductivity were determined. For this purposed MRH is equipped with different specialized sample environments and detector systems, which can also be completed by the use of the ESRF-detector pool on special request.

Detectors

- Scintillation detectors (BEDE EDRa) with motorized slits, analyzing crystal or Soller collimator are available.
- energy-dispersive PIN-Diode (AmpTec, energy resolution 200 eV, area 7 mm^2)
- One-dimensional linear position sensitive detector Meteor 1D, GE Inspection Technology GmbH, identical in construction with Mythen detector Dectris Ltd.
- Pilatus 100K pixel detector from Dectris Ltd.

Sample environment

- High temperature chamber of Bühler design up to 2.000 °C
- In-house developed heating chamber with a semispherical Be-dome for different diffraction geometries up to 1200°C, and under controlled atmospheres up to 800 mbar 30 sccm inert or reducing gases by the use of the Kapton dome. Optional in-situ conductivity measurement by 4 point probe setup is available.
- In-house developed heating-cooling chamber, dedicated for the temperature range of -100 to 200°C and vacuum or controlled atmosphere.

In-situ magnetron sputter deposition chamber with two magnetrons and an ion gun port allows temperature up to 700°C. The arrangement of the Be-windows enables in-plane and out-off-plane diffraction experiments as well as GISAXS. One RF power generator incl. impedance matchbox is now available onsite.

Fig. 1.: Sputter deposition chamber.

Fig. 2.: High temperature furnace.

New detectors at ROBL-MRH

MRH has got a strong focus on *in-situ* investigations mainly in thin film and nanostructure synthesis and processing and is facing new challenges in this research field. Therefore, new detector systems were installed in order to keep up with the requirements of a modern synchrotron radiation beamline.

A Meteor 1D Si strip detector from GE Inspection Technology GmbH (identical in construction with a Mythen from Detris Ltd.) is replacing the existing Braun PSD. It is also a 1D detector with similar dimension; The detector has an active area of 64 x 8 mm², a spatial resolution of 50 µm (pitch width, 1280 channels) and thus spectra over a certain angular range (up to 20° depending on the measuring circle) can be recorded simultaneously. Compared to Braun PSD the Meteor offers three striking advantages:

- The fast detector read-out of 0.3 ms is a key feature for *in-situ* measurements.
- The detector is working in the whole accessible at ROBL energy range (5-35 keV) with a high detection efficiency.
- The maximum count rate of this device is 2×10^5 phot/sec/pixel and therefore approx. three orders of magnitude higher as the Braun PSD.

The Meteor 1D can be used in combination or as replacement of the current detector setup. The detector head can be rotated from horizontal to vertical orientation of the detector window, without dismounting from its holder. Software engineering to integrate this detector in the instrument control software "spec" is conducted in cooperation of the HZDR with the ESRF software group and G. Swislow, Certified Scientific Software Ltd.

Fig. 1. Left, Pilatus 100K mounted on the detector bench. Right, Meteor 1D mounted dedicated holder.

As 2D Si pixel detector now a Pilatus 100k from Dectris Ltd. is available at the beamline. The pixel size is 172×172 µm²; the active area 83.5×33.5 mm². Due to the low weight of only 4 kg it is very flexible in operation. It can be used for diffraction experiments on the detector circle or alternatively for GISAXS experiments mounted on the detector bench behind the goniometer. The maximum count rate of 2×10^6 phot/sec/pixel is nowadays the maximum available, as well as 2.7 ms read-out time.

Further development in *in-situ* sample environments

The increasing demand in experiments under controlled atmospheres leads to the design of a new window system suitable for the existing furnaces. The new kapton foil dome allows the operation with chamber gas pressures up to 800 mbar absolute and substrate temperatures up to 900°C, which is due to obvious safety reasons not possible with the existing beryllium dome. The windows withstand a time limited overpressure of 2 bar and can be easily exchanged. However, the kapton foil chamber is limited for use in out-of-plane scattering geometry within an angular range of 0 to 50°. The dome is water cooled; the Kapton windows can be additionally cooled by an air blower. In addition to the existing four-channel gas mixing and supply unit, the absolute pressure in the furnace is monitored and integrated into a safety regulation circuit in the exhaust line. Now *in-situ* experiments with continuous gas flow and regulated pressure in the range up to 800 mbar and 30 sccm are possible. The new kapton dome can be combined with the different existing furnaces at ROBL.

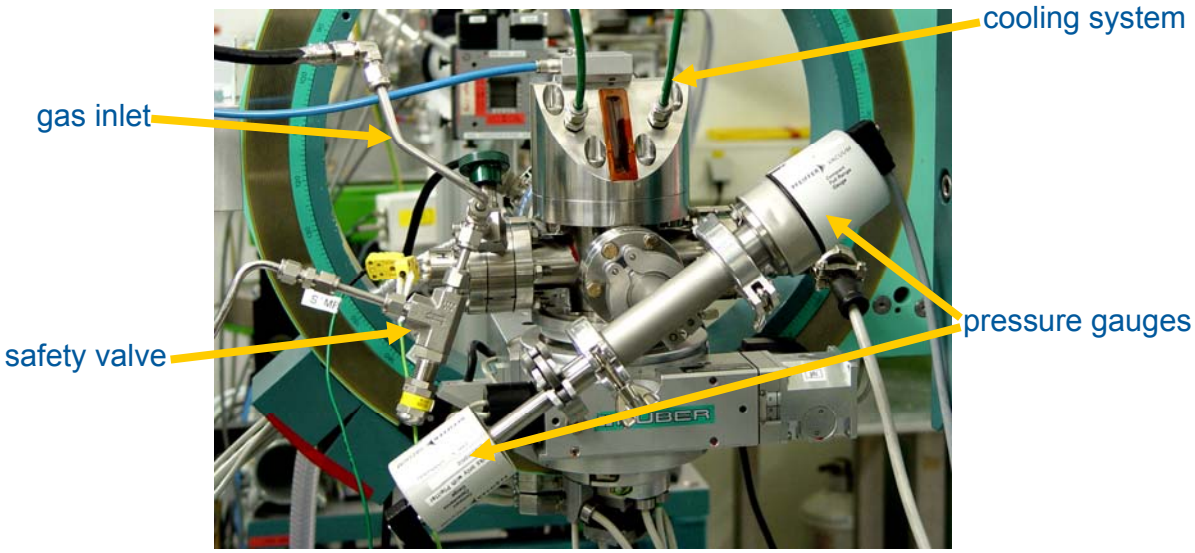

Fig. 2. Kapton dome mounted on the furnace in the goniometer.

The temperature region from -100 to 200°C for the utilization of technical devices is of unique importance. Therefore a new furnace operating in this temperature range has been developed. The sample holder is a massive copper part which is connected to an external liquid nitrogen Dewar, sample cooling is performed by heat transport. A heating cartridge integrated in the copper part is counteracting and allows temperature stabilization and heating up to 200°C. Additionally the electrical resistance can be measured by 4 point probe setup directly during the diffraction experiment. This furnace can be combined with the new Kapton dome and the Beryllium dome as well.

The magnetron sputtering chamber at MRH is one of the working horses at the beamline. To sputter non-conducting oxides or nitrides, a Cesar 133 RF Power generator and an impedance matching box from Advanced Energy Inc. is disposable and broadens the range of material classes under investigation. These devices can be controlled remotely from the instrument control hutch.

Mono-capillary versus CRL; new devices for X-ray focusing

Spatial resolved informations and thus an X-ray beam with a spot size of 10 to 100 µm in diameter is desired for several experiments. For this purpose two different focusing devices were tested at MRH. A parabolic monocapillary mounted 235 mm in front of the sample is already reported elsewhere (1). Using this device only one sided as a focusing mirror; spot sizes down to 45 µm diameter were achieved with an acceptable gain greater 100. Main disadvantages are the reduced free working space and based on the intrinsic imperfection of the inner surface and shape of the mono capillary the extreme sensibility to small beam movements or instabilities. Therefore in the order of several hours no stable µ-focus spot can be provided.

Another option is the use of Compound Refractive Lenses (CRL). 30 Be lenses with R=1.5mm are placed 11.5 m in front of the sample, hereby the free working space remains and the increase of divergence in the beam is moderate. The spot size of 80 µm diameter and gain greater 80 is lower than employing a capillary, test were performed at 8 and 11keV. This optical device is achromatic, which means, focus length depends on the energy or wave length respectively. Test measurements demonstrate that changes in focal length in an energy scan of 1 keV can be neglected due to the long focusing distance and the long focus depth. In opposite to the mono capillary the CRLs are absolutely unaffected by beam instabilities and rock solid, therefore they are the preferred device in user service.

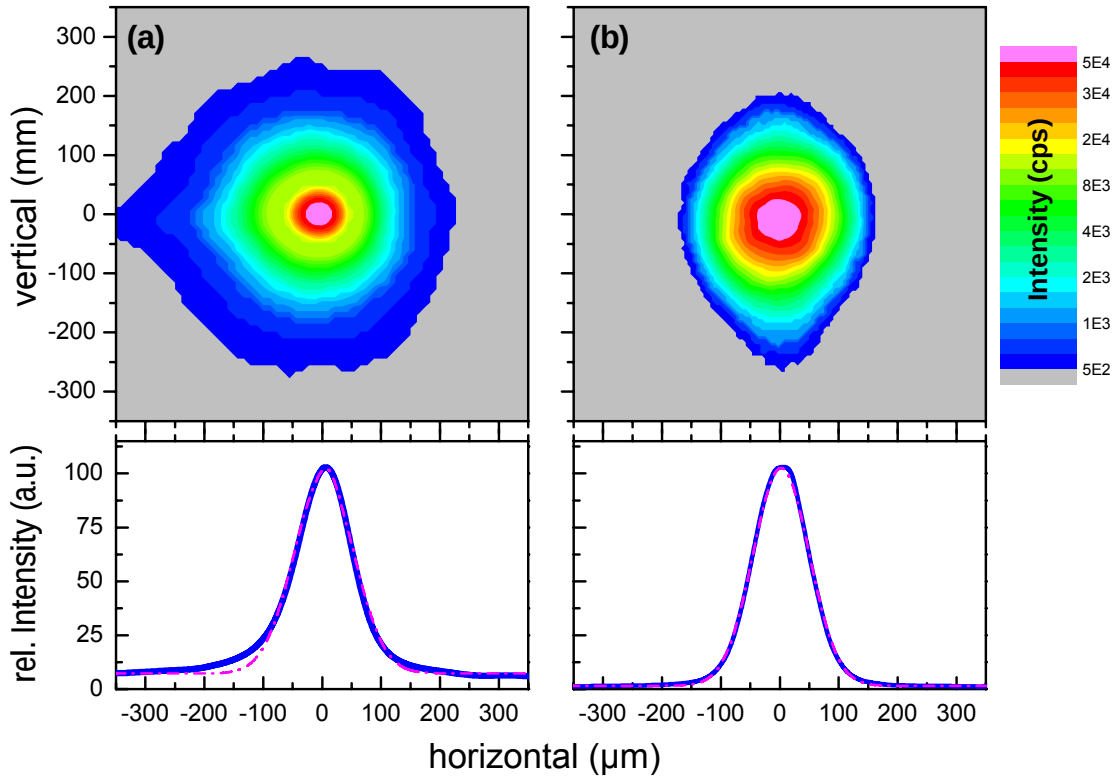

Fig. 3. Left, Spot of the mono-capillary and the corresponding FWHM. Right: CRL spot and corresponding FWHM. Both recorded with a FDI-2 camera from Photonics Ltd.

1) N. Schell et al, ROBL Biannual Report 2005-2006, (2007), 49-55.

Upgrade of Optics

The following list compiles the major goals of the upgrade as well as the optics selected to achieve these goals:

- Higher flux by horizontal focusing: Double toroid focusing mirror
- Higher flux by wider energy bandgap: double multilayer monochromator
- Better energy resolution and glitch management: Si(111)/Si(111)$_{90}$/Si(311) crystal sets permanently mounted
- Faster spectroscopy: Quick-XAS-suited monochromator
- Wider energy coverage: mirrors with Si, Rh and Pt surfaces
- Faster beamline adjustment: beam diagnostics after each optical element
- More stable beam: active beam position control
- Adaption to ESRF storage ring upgrade: optional LN_2 cooling

Key data:

- Time frame: 2010-2011, back to friendly user operation in May 2012
- Investment: 2 Mio EUR by FZD
- Supplier: FMB-Oxford

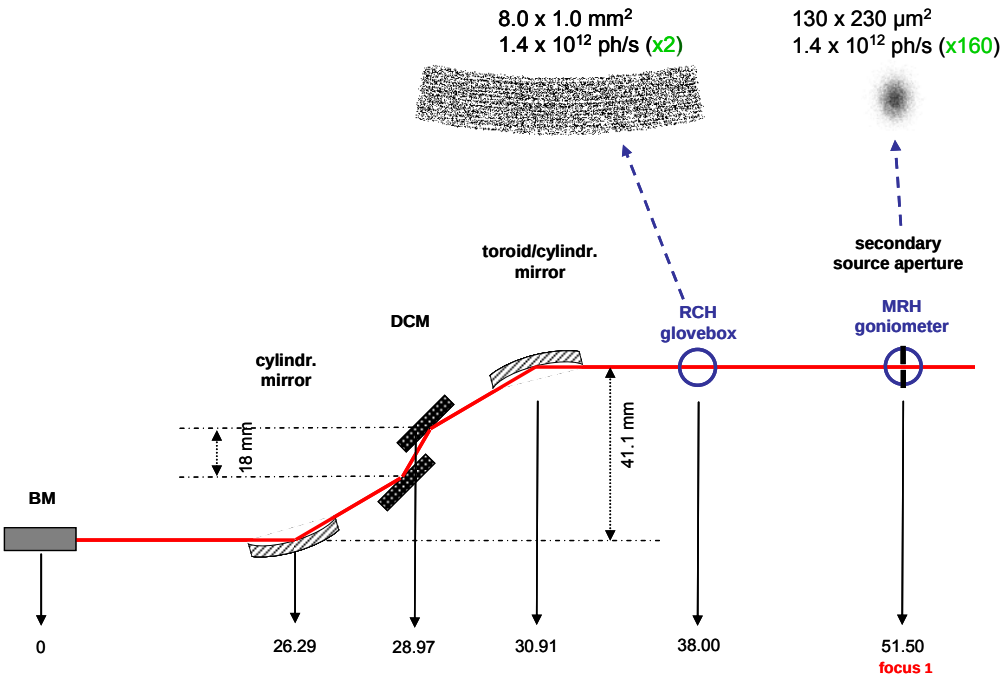

Fig. 1. Schematic design of new optics, and beam size and integrated flux at the two end stations as determined by ray tracing calculations. The toroid focusing mirror has a fixed focus at MRH, thereby increasing both total flux and flux density significantly. In contrast, the beam size in RCH remains large, with only a modest increase in flux and flux density, in order to reduce photon-induced beam damage to sensitive samples, while maintaining a very low detection limit (about 1 ppm for XANES, 25-100 ppm for EXAFS).

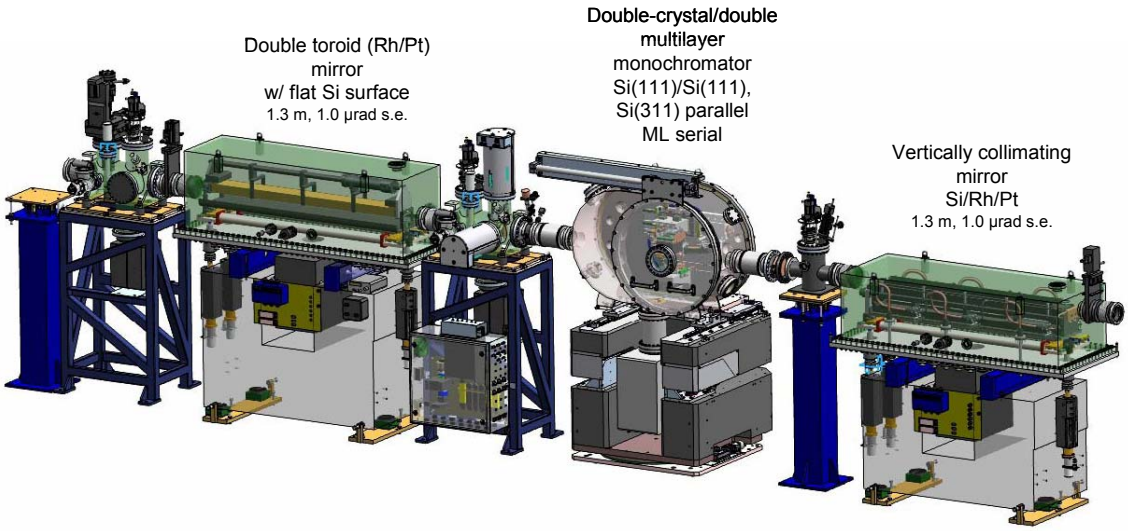

Fig. 2. Design drawing of new optical components.

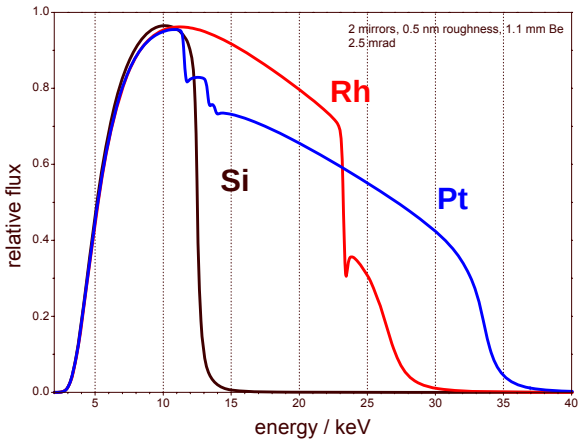

Fig. 3.

In addition to the previous Si and Pt reflecting mirror surfaces, a third Rh-coating will be added to increase flux at intermediate energy and to avoid the Pt absorption edges interfering with EXAFS of relevant elements like Ge, Se, Au, Hg, Pb and Po.

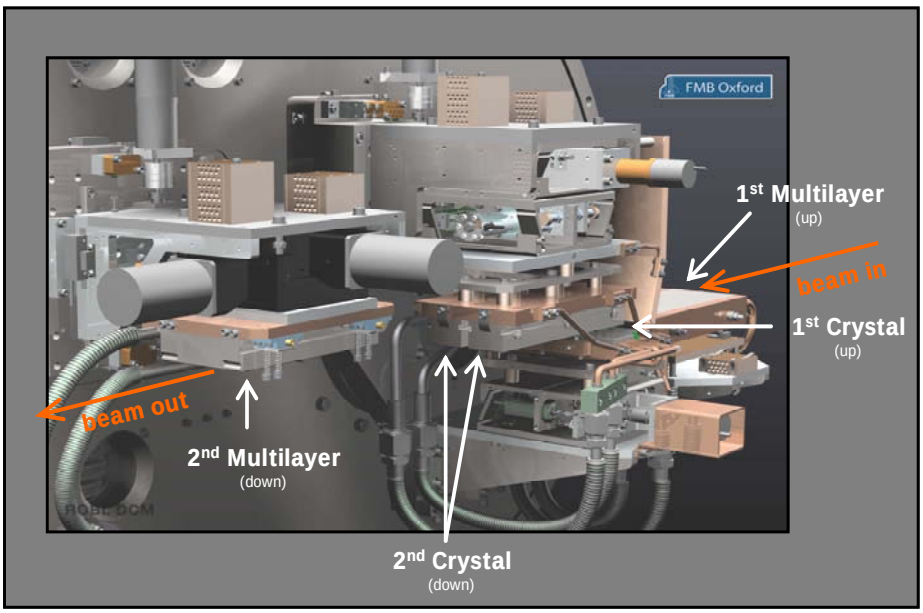

Fig. 4. Design drawing of the combined double crystal/double multilayer monochromator. The 1st multilayers are mounted together with the 1st and 2nd crystals on a common Bragg drive, while the 2nd multilayers are mounted on an independent stage.

2.2. Beamline personnel

Head of the beamline / responsible for RCH: Andreas Scheinost (-2462)
Responsible for MRH: Carsten Bähtz (-2367)

	Name (phone)	Position/Education/Research Interests
Support	Marion Glückert (-1967)	Office administration
	Joerg Exner (-2372)	Beamline Technician (Physics) *since 09/2010*
	Matthias Fengler (-1941)	Beamline Technician (Electronics) *since 11/2010*
	Marco Hesse	Beamline Technician *until 09/2010*
Radiochemistry	Dipanjan Banerjee (-2463)	Postdoc *since 11/2007* Ph.D. in Geology (1999), Univ. of Western Ontario, Canada ACTINET, Sorption and redox processes, XPS
	Harald Funke (-2339)	Beamline Scientist *until 04/2009* Ph.D. in Physics (1974), University of Moscow (Russia) wavelet analysis for EXAFS
	Christoph Hennig (-2005)	Beamline Scientist Ph.D. in Crystallography (1995), Universität Leipzig aqueous chemistry and electrochemistry of actinides
	Regina Kirsch (-2849)	Ph.D. student diploma in Chemistry (2007), Universität Leipzig redox reactions of Sb and Pu on iron minerals
	Andre Rossberg (-2847)	Beamline Scientist Ph.D. in Chemistry (2002), TU Dresden new methods for EXAFS analysis, aqueous actinide chemistry
	Andreas Scheinost (-2462)	Head of Beamline Ph.D. in Agricultural Engineering (1994), TU München radionuclide speciation in soils, interfacial redox processes
Materials Research	Carsten Baehtz (-2367)	Beamline Scientist, responsible for MRH Ph.D. in Materials Science (2000), TU Darmstadt in-situ XRD techniques, carbon nanotube growth mechanisms
	Artem Shalimov	Postdoc *since 09/2010* Ph.D. in Physics (2006), Institute of Physics PAS Warsaw hgh-resolution XRD, nanostructures and defects, magnetic nanoparticles and Preisach modeling
	Nicole Jeutter (-2872)	Postdoc *until 09/2010* Ph.D. in surface crystallography (2006), LMU München X-ray diffraction and small-angle scattering of semiconductors

Postal address Rossendorf Beamline
(ROBL-CRG, BM20)
ESRF / sector 21
BP 220
F-38043 Grenoble cedex France

Phone: +33 (476) 88 xxxx
Fax: +33 (476) 88 2505
E-mail: surname@esrf.fr

FZD personnel involved in the scientific and technical programme

Department of Research Technology

Frank Herbrand	Winfried Oehme	Jürgen Claussner
Nicole Kretzschmar	Jens Hauser	

Institute of Ion Beam Physics and Materials Research

Johannes von Borany	Joerg Grenzer	Natalia Shevchenko
Andrea Scholz	Rene Weidauer	

Institute of Radiochemistry

Gerd Bernhard	Satoru Tsushima	Christian Lucks
Stephan Weiss	Alix Guenther	Heidemarie Heim
Siriwan Dulnee	Anette Rumpel	Astrid Barkleit

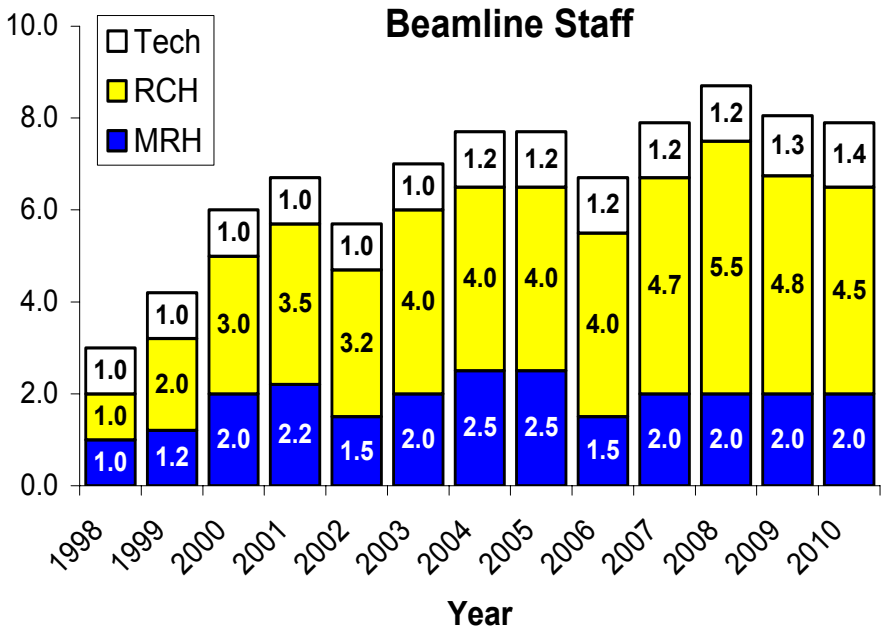

Fig. 2.2.1.
Evolution of beamline personnel since 1998.

2.3. Beamtime allocation and user groups

In the past two years, 97 experiments have been performed involving 226 users traveling to the ESRF (Table 2.3.1). A total of 1386 shifts have been delivered for experiments, i.e. 89 % of the available beam, and 11 % for commissioning and other technical shifts. Distribution of time between RCH and MRH was 50/50. For ESRF experiments, 33 % of the experimental shifts were provided, as foreseen in the contract between ESRF and FZD. 8 % of the inhouse shifts of RCH were provided for Radiochemistry experiments in the framework of ACTINET-I3 (see below).

Table 2.3.1. Use of beamtime at the Rossendorf Beamline.

	Year	FZD shifts	ESRF shifts	Actinet shifts	Technical shifts	Experiments FZD / ESRF / Actinet	Users FZD / ESRF / Act
RCH	**2009**	191	99	6	3	17 / 10 / 1 = 28	16 / 41 / 1 = 58
RCH	**2010**	221	120	27	6	15 / 10 / 2 = 27	17 / 25 / 4 = 46
MRH	**2009**	203	97	-	110	16 / 7 / - =23	37 / 23 / - = 60
MRH	**2010**	178	92	-	33	12 / 7 / - = 19	40 / 22 / - = 62
sum		**793**	**409**	**33**	**152**	**60/34/3 = 97**	**110/111/5 = 226**

Figure 2.3.1 shows the beamline overbooking by giving the ratio between requested and allocated beamtime of ESRF experiments. Until 2008, the overbooking factor was close to the long-term average of 2. In 2009 and 2010, overbooking was raising to more than 3.5. These numbers clearly demonstrate the attractiveness of ROBL for outside users.

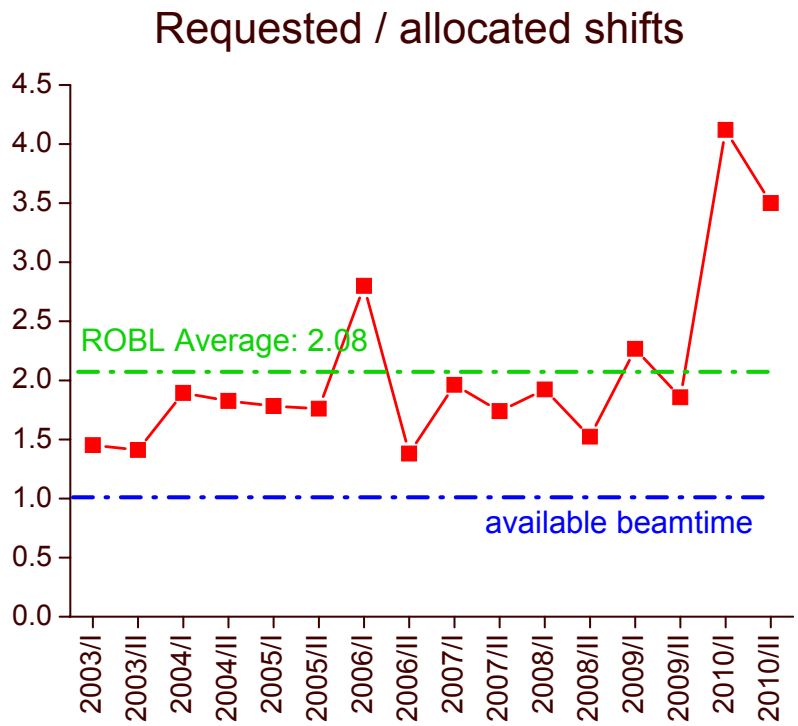

Fig. 2.3.1.
Beamtime request for ESRF experiments.

User Groups

Figure 2.3.2 shows the origin of user groups, excluding all FZD groups. The strongest demand for beamtime for both end stations is from Germany, followed by France with demand predominantly for RCH. Users from ten other European countries have performed experiments at ROBL. An experiment from Japan was performed in the framework of a collaborative agreement between the University of Tokyo and the FZD.

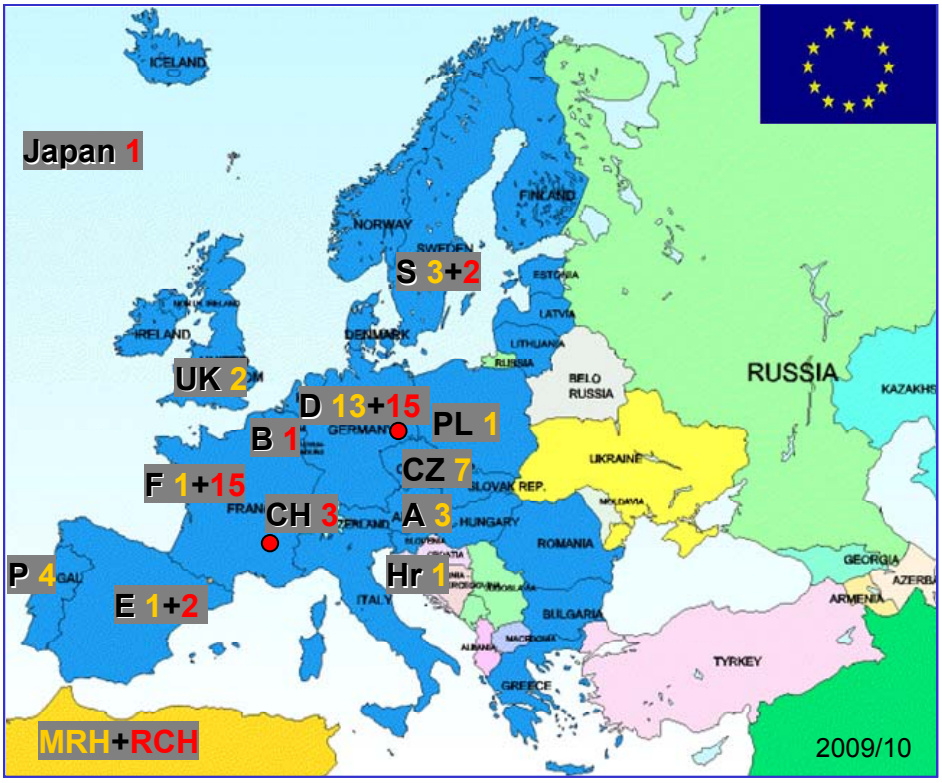

Fig. 2.3.2.
User groups for both inhouse and ESRF experiments according to nationality. RCH experiments are shown in red, MRH experiments in yellow. User groups of FZD are not counted.

Germany

- Forschungszentrum Jülich, Inst. für Bio & Nanosysteme, Inst. für Energie- & Klimaforschung
- Universität Siegen, Festkörperphysik
- Fraunhofer Institut IFAM Dresden
- Friedrich-Schiller-Universität Jena, Institute for Optics & Quantum Electronics
- Georg-August Universität Göttingen, Inst. für Röntgenphysik und Inst. für Materialphysik
- Helmholtz-Zentrum Berlin für Materialien und Energie
- Johannes Gutenberg Universität Mainz, Institut für Kernchemie
- Karlsruhe Institute of Technology, Inst. für Nukleare Entsorgung
- RWTH Aachen University, Institut für Anorganische Chemie
- TU Bergakademie Freiberg, Inst. of Geology, Inst. of Materials Science, Inst. of Physical Metallurgy
- TU Clausthal, Inst. für Metallurgie

Austria	- Johannes Kepler University Linz, Inst. of Semiconductor Physics
Belgium	– Katholieke Universiteit Leuven, Departement of Microbial and Molecular Systems
Croatia	- Rudjer Boskovic Institute Zagreb, Materials Physics
Czech Republic	– Institute of Chemical Technology-Praha, Dept. of Solid State Chemistry
	– Charles University, Praha, Dept. of Low Temperature Physics; Dept. of Condensed Matter Physic
	– National Museum Praha, Dept Mineralogy and Petrology
France	– CEA at Cadarache, Grenoble, Marcoule
	– Centre National de la Recherche Scientifique (CNRS) at Grenoble, Dijon and Saclay
	– Institut de Physique Nucléaire, Université Paris XI, Orsay, Lyon
	– Institut de Recherches Subatomiques (IRES), CNRS-IN2P3, Strasbourg
	– LGIT, Université Joseph Fourier (UJF), Grenoble
	– Université de Bourgogne Dijon, Institut de Chimie Moléculaire
Great Britain	– University of Cambridge, Centre for Advanced Photonics & Electronics
Japan	– University of Tokyo, Dept. Quantum Engineering & System Sciences
Poland	– Institute of Electronic Materials Technology (ITME), Warsaw
Japan	– Department of Nuclear Engineering & Management, The University of Tokyo
Portugal	– CENIMAT F.C.T./Universidade Nova de Lisboa, Monte da Caparica
Spain	– Amphos21- Barcelona
	– Universidad San Pablo-CEU, Departamento de Ciencias Químicas, Madrid
	– Universidad de Granada, Department of Microbiology
	– Universidad Politecnica de Catalunya Barcelona, Dept. de Ingenieria Quimica
	– Centre Tecnologic de Manresa, Laboratori de Gestió de Residus
Sweden	– Royal Institute of Technology , KTH Stockholm
	– Linköping University, Engineering Materials
Switzerland	– Paul-Scherrer-Institut, Villigen, Laboratory for Waste Management

ACTINET-I3 Integrated Infrastructure Initiative for Actinide Sciences

A follow-up on ACTINET – European Network for Actinide Science, where ROBL-RCH participated since March 2004, ACTINET-I3 has been established as Integrated Infrastructure Initiative within FP-7 and is in operation since October 2009, again including ROBL-RCH. The objective of ACTINET-I3 is to reinforce the networking of existing European infrastructures in actinide sciences, and to facilitate their efficient use by the European scientific community in order to keep a leading position in the field of nuclear energy. The three lines of action are:

(i) to establish a network of actinide facilities across the EU to integrate and structure better the way these actinide infrastructures operate and to foster their joint development in terms of capacity and performance;

(ii) to support and manage jointly a program of access to appropriate infrastructures for training and associated research projects making use of the proposed facilities;

(iii) to conduct on a limited scale a set of Joint Research Activities (JRA) involving consortium member organizations, with an objective to improve the performance of infrastructures by developing new relevant instrumentations and/or data of common interest. Further, these activities are complemented by a virtual infrastructure providing a limited support in theory and modeling, with a focus on the complementarities between theory and experiments.

The Rossendorf beamline contributes its radiochemistry end station to the ACTINET-I3 Pooled Facilities, providing beamtime for Joint Research Projects granted by ACTINET-I3. In return, ROBL receives annual funds for user support. In 2009/20010, 3 experiments have been performed for ACTINET (see list of experiments 2.5.1.), a number which will significantly increase in 2011, when ACTINET-I3 calls are in full swing. ROBL belongs to one of the most heavily used facilities of ACTINET (among them the ATALANTE facility of CEA, the ITU user labs and hot cells, the INE labs and beamline, the PSI beamline and micro-XAS, and the Theoretical User Lab), providing a fundamental contribution to actinide research.

Within ACTINET-I3, ROBL is also leading one of the four joint research activities, the creation and maintenance of an actinide reference x-ray absorption spectroscopy database (Fig. 2.3.3.). The purpose of this effort is to provide users with XAFS spectra of well characterized actinide compounds (solids, solutions, sorption complexes), thereby minimizing the need to repeatedly measure their own references. While similar efforts have been undertaken for non-radioactive samples, no database exists for actinides and other radionuclides to date, although an efficient use of scarce beamtime and sample materials is crucial, not to speak about costly and administratively challenging sample transports. As first step, the Web database will allow retrieval of reference spectra for comparison. A later upgrade will allow for pattern searching. Through establishing the database as a joint effort of all European actinide beamlines, including the ROBL beamline with 10 years of operation, access to the largest number of spectra possible is assured.

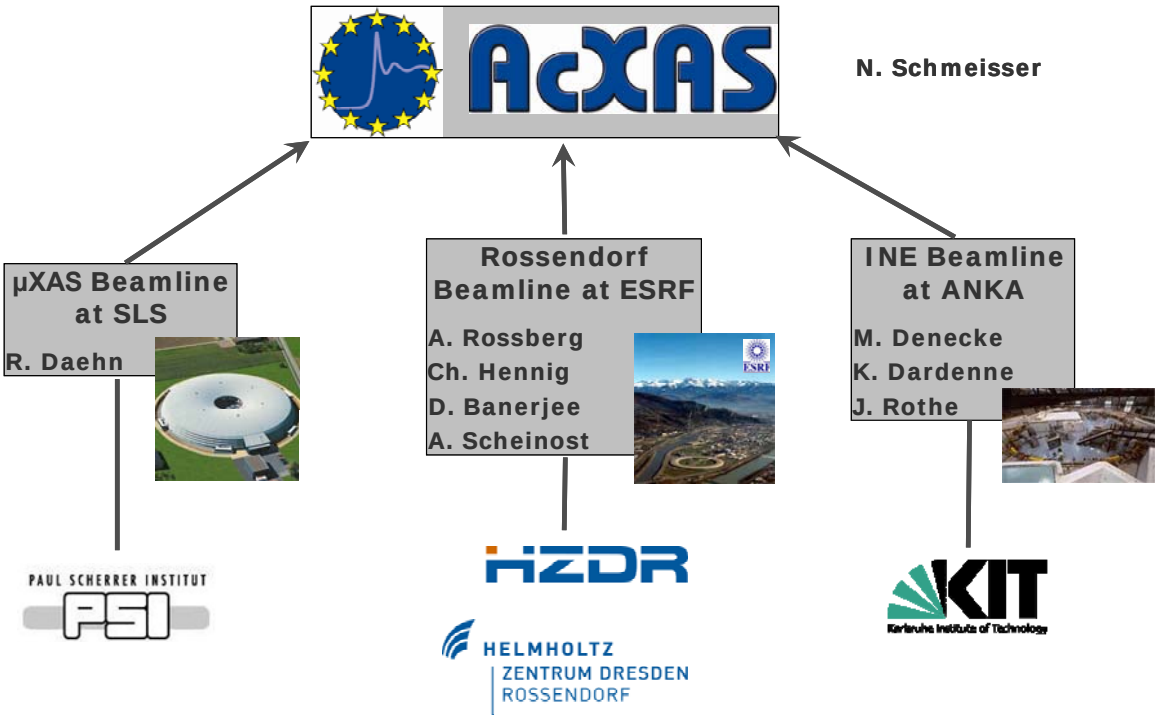

Fig. 2.3.3.
The ACTINET-I3 joint research activity AcXAS of the three European actinide XAS beamlines, coordinated and headed by ROBL.

2.4. Publications

This section lists all publications which are based on experiments at the Rossendorf Beamline, whether they have been performed using in-house or ESRF allocated shifts. In contrast to previous Biannual Reports, only peer-reviewed journal articles are listed. As a further selection criterion, only journals listed in the Journal Citation Report (ISI Web of Knowledge) were accepted.

Figure 2.4.1 gives an overview on the publication activities since the commissioning of the beamline. After a continuous increase from 1999 to 2002, publication activity decreased in 2003 and 2004, followed by a sharp rise in 2005. Since then, the total number varies between 25 and 38 publications per year, with RCH producing about 60% and MRH about 40% of the publications. Fig. 2.4.2 gives the impact factors (IF) of the journals, where the articles have been published. For RCH, the average IF has doubled from 2 to 4 in the last 10 years, MRH maintains its level around 2. Both end stations publish routinely in journals with good IF in their respective fields (Inorganic Chemistry, Environmental Science & Technology, Geochimica et Cosmochimica Acta for RCH, Applied Physics Letters for MRH). In 2010, a paper in Angewandte Chemie raised the bar even further. In conclusion, the number of publications as well as their quality has achieved a high level.

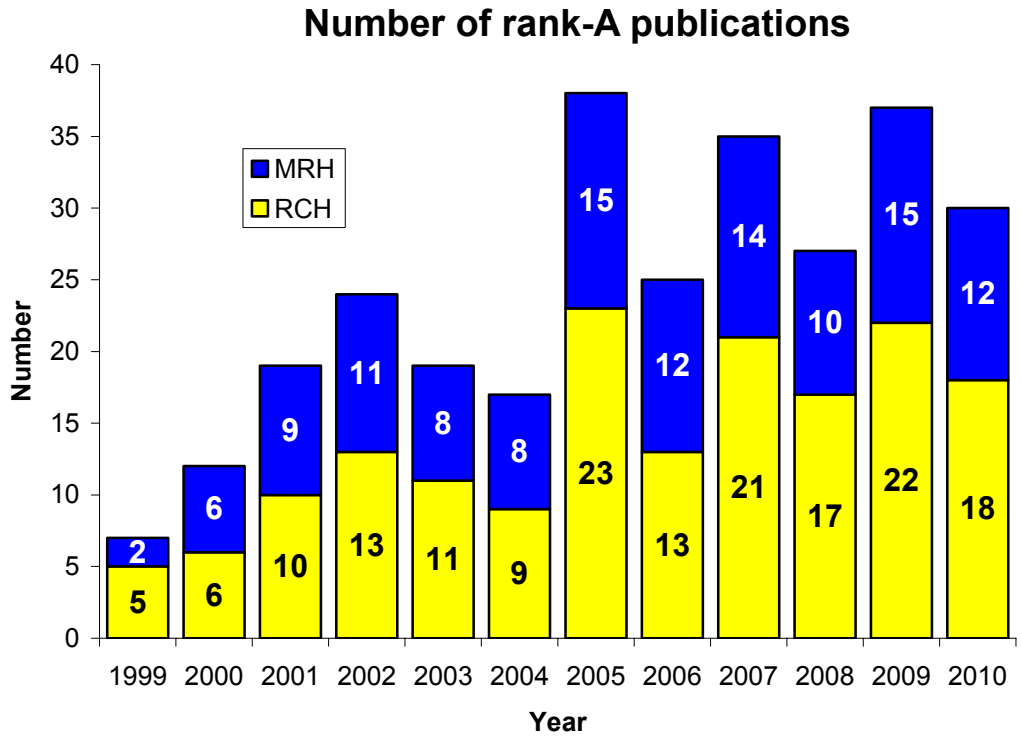

Fig. 2.4.1.
Number of publications per year, based on data collected in RCH and MRH by internal and external user groups. Note that only peer-reviewed articles in citation-indexed journals are listed.

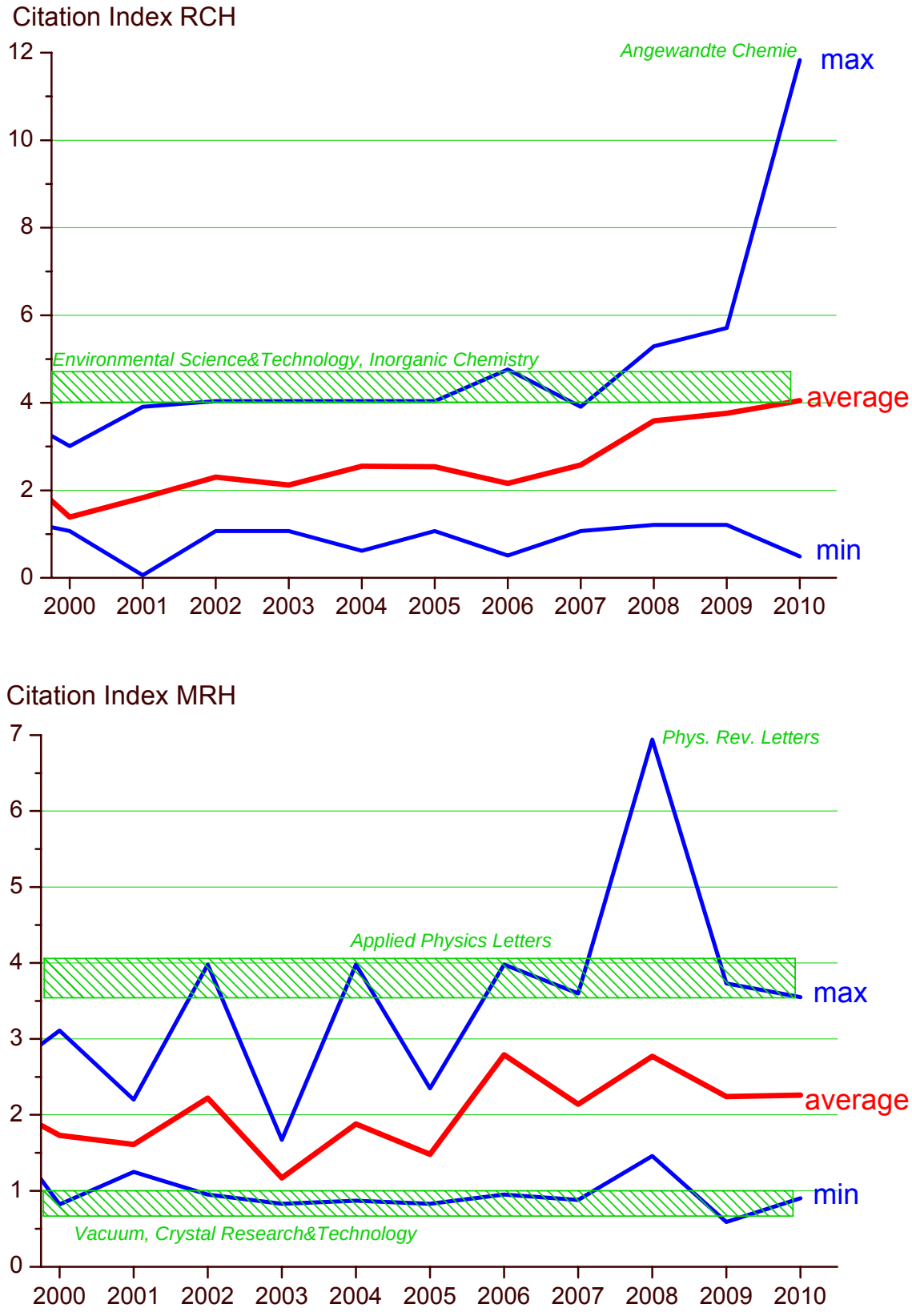

Fig. 2.4.2.
Citation indices of the articles listed in Fig. 2.4.1 and section 2.4.1. Top: RCH, bottom: MRH.

2.4.1. Publications in Radiochemistry

2009

Belin, R.C., Martin, P.M., Valenza, P.J., and Scheinost, A.C.
Experimental insight into the radiation resistance of zirconia-based americium ceramics
Inorg. Chem. **48** (2009) 5376-5381

Bonin, L., Guillaumont, D., Jeanson, A., Auwer, C.D., Grigoriev, M., Berthet, J.-C., C. Hennig, Scheinost, A., and Moisy, P.
Thermodynamics and structure of actinide(IV) complexes with nitrilotriacetic acid
Inorg. Chem. **48** (2009) 3943-3953

Breynaert, E., Kirschhock, C.E.A., and Maes, A.
EXAFS and DFT: Evidence for the $[Tc=O]^{2+}$ core
Dalton Transactions (2009) 9398-9401

Di Giandomenico, M.V., Le Naour, C., Simoni, E., Gulliaumont, D., Moisy, P., Hennig, C., Conradson, C., and Den Auwer, C.
Structure of early actinides(V) in acidic solutions
Radiochimica Acta **97** (2009) 347-353

Geissler, A., Merroun, M., Geipel, G., Reuther, H., and Selenska-Pobell, S.
Biogeochemical changes induced in uranium mining waste pile samples by uranyl nitrate treatments under anaerobic conditions
Geobiology **7** (2009) 282-294

Hattori, T., Saito, T., Ishida, K., Scheinost, A.C., Tsuneda, T., Nagasaki, S., and Tanaka, S.
The structure of monomeric and dimeric uranyl adsorption complexes on gibbsite: A combined DFT and EXAFS study
Geochim. Cosmochim. Acta **73** (2009) 5975-5988

Hennig, C., Ikeda-Ohno, A., Tsushima, S., and Scheinost, A.C.
The sulfate coordination of Np(IV), Np(V), and Np(VI) in aqueous solution
Inorg. Chem. **48** (2009) 5350-5360

Hiemstra, T., van Riemsdijk, W.H., Rossberg, A., and Ulrich, K.-U.
A surface structural model for ferrihydrite II: Adsorption of uranyl and carbonate
Geochim. Cosmochim. Acta **73** (2009) 4437-4451

Ikeda-Ohno, A., Hennig, C., Tsushima, S., Scheinost, A.C., Bernhard, G., and Yaita, T.
Speciation and structural study of U(IV) and -(VI) in perchloric and nitric acid solutions
Inorg. Chem. **48** (2009) 7201-7210

Ikeda-Ohno, A., Tsushima, S., Takao, K., Rossberg, A., Funke, H., Scheinost, A.C., Bernhard, G., Yaita, T., and Hennig, C.
Neptunium carbonato complexes in aqueous solution: An electrochemical, spectroscopic, and quantum chemical study
Inorg. Chem. **48** (2009) 11779–11787

Jeanson, A., Berthon, C., Coantic, S., Den Auwer, C., Floquet, N., Funke, H., Guillaneux, D., Hennig, C., Martinez, J., Moisy, P., Petit, S., Proux, O., Quemeneur, E., Solari, P.L., and Subra, G.
The role of aspartyl-rich pentapeptides in comparative complexation of actinide(IV) and iron(III). Part 1
New J. Chem. **33** (2009) 976-985

Livi, K.J.T., Senesi, G., Scheinost, A.C., and Sparks, D.L.
A microscopic examination of nanosized mixed Ni-Al hydroxide surface precipitates on pyrophyllite
Environmental Science & Technology **43** (2009) 1299–1304

Martin, P.M., Belin, R.C., Valenza, P.J., and Scheinost, A.C.
EXAFS study of the structural phase transition in the americium zirconate pyrochlore
J. Nucl. Mater. **385** (2009) 126–130

Missana, T., Alonso, U., Scheinost, A.C., Granizo, N., and García-Gutiérrez, M.
Selenite retention by nanocrystalline magnetite: Role of adsorption, reduction and dissolution/co-precipitation processes
Geochim. Cosmochim. Acta **73** (2009) 6205-6217

Nockemann, P., Thijs, B., Lunstroot, K., Parac-Vogt, T.N., Gorller-Walrand, C., Binnemans, K., Van Hecke, K., Van Meervelt, L., Nikitenko, S., Daniels, J., Hennig, C., and Van Deun, R.
Speciation of rare-earth metal complexes in ionic liquids: A multiple-technique approach
Chemistry-a European Journal **15** (2009) 1449-1461

Rossberg, A., Ulrich, K.-U., Weiss, S., Tsushima, S., Hiemstra, T., and Scheinost, A.C.
Identification of uranyl surface complexes on ferrihydrite: Advanced EXAFS data analysis and CD-MUSIC modeling
Environmental Science & Technology **43** (2009) 1400–1406

Seco, F., Hennig, C., Pablo, J.d., Rovira, M., Rojo, I., Mart, V., Gimnez, J., Duro, L., Griv, M., and Bruno, J.
Sorption of Th(IV) onto iron corrosion products: EXAFS study
Environmental Science & Technology **43** (2009) 2825–2830

Sornein, M.O., Mendes, M., Cannes, C., Le Naour, C., Nockemann, P., van Hecke, K., van Meervelt, L., Berthet, J.C., and Hennig, C.
Coordination environment of $[UO_2Br_4]^{2-}$ in ionic liquids and crystal structure of $[Bmim]_2[UO_2Br_4]$
Polyhedron **28** (2009) 1281-1286

Suess, E., Scheinost, A.C., Bostick, B.C., Merkel, B.J., Wallschlaeger, D., and Planer-Friedrich, B.
Discrimination of thioarsenites and thioarsenates by x-ray absorption spectroscopy
Anal. Chem. **81** (2009) 8318–8326

Takao, K., Takao, S., Scheinost, A.C., Bernhard, G., and Hennig, C.
Complex formation and molecular structure of neptunyl(VI) and -(V) acetates
Inorg. Chem. **48** (2009) 8803–8810

Takao, K., Tsushima, S., Takao, S., Scheinost, A.C., Bernhard, G., Ikeda, Y., and Hennig, C.
X-ray absorption fine structures of uranyl(V) complexes in a nonaqueous solution
Inorg. Chem. **48** (2009) 9602–9604

Takao, S., Takao, K., Kraus, W., Emmerling, F., Scheinost, A.C., Bernhard, G., and Hennig, C.
First hexanuclear U^{IV} and Th^{IV} formate complexes – Structure and stability range in aqueous solution
Eur. J. Inorg. Chem. **32** (2009) 4771-4775

2010

Breynaert, E., Scheinost, A.C., Dom, D., Rossberg, A., Vancluysen, J., Gobechiya, E., Kirschhock, C.E.A., and Maes, A.
Reduction of Se(IV) in Boom Clay: XAS solid phase speciation
Environmental Science & Technology **44** (2010) 6649-6655

Burkhart, E.-M., Akobi, D.M., Bischoff, S., Sitte, J., Kostka, J.E., Banerjee, D., Scheinost, A.C., and Küsel, K.
Impact of biostimulated redox processes on metal dynamics in an iron-rich creek soil of a former uranium mining area
Environmental Science & Technology **44** (2010) 177-183

Chakraborty, S., Boivin, F.F., Banerjee, D., Scheinost, A.C., Mullet, M., Ehrhardt, J.-J., Brendle, J., Vidal, L., and Charlet, L.
U(VI) Sorption and Reduction by Fe(II) Sorbed on Montmorillonite
Environmental Science & Technology **44** (2010) 3779–3785

Chave, T., Nikitenko, S.I., Scheinost, A.C., Berthon, C., Arab-Chapelet, B., and Moisy, P.
First Synthesis of Uranyl Aluminate Nanoparticles
Inorg. Chem. **49** (2010) 6381-6383

Gaillard, C., Chaumont, A., Billard, I., Hennig, C., Ouadi, A., Georg, S., and Wipff, G.
Competitive Complexation of Nitrates and Chlorides to Uranyl in a Room Temperature Ionic Liquid
Inorg. Chem. **49** (2010) 6484-6494

Galbis, E., Hernández-Cobos, J., Den Auwer, C., Le Naour, C., Guillaumont, D., Simoni, E., Pappalardo, R.R., and Marcos, E.S.
Solving the Hydration Structure of the Heaviest Actinide Aqua Ion Known: The Californium(III) Case
Angewandte Chemie-International Edition **49** (2010) 3811-3815

Hennig, C., Ikeda-Ohno, A., Emmerling, F., Kraus, W., and Bernhard, G.
Comparative investigation of the solution species $[U(CO3)_5]^{6-}$ and the crystal structure of $Na_6[U(CO3)_5]\ 12H_2O$
Dalton Transactions **39** (2010) 3744-3750

Hennig, C., Skanthakumar, S., and Soderholm, L.
Double photoexcitation of 2p and 4f electrons in curium
J. Electron. Spectrosc. Relat. Phenom. **180** (2010) 17-20

Jankowski, U., Merroun, M.L., Selenska-Pobell, S., and Fahmy, K.
S-Layer protein from Lysinibacillus sphaericus JG-A12 as matrix for Au-III sorption and Au-nanoparticle formation
Spectroscopy-an International Journal **24** (2010) 177-181

Jeanson, A., Ferrand, M., Funke, H., Hennig, C., Moisy, P., Solari, P.L., Vidaud, C., and Den Auwer, C.
The role of transferrin in actinide(IV) uptake: Comparison with iron(III)
Chemistry-a European Journal **16** (2010) 1378-1387

Mendes, M., Hamadi, S., Le Naour, C., Roques, J., Jeanson, A., Den Auwer, C., Moisy, P., Topin, S., Aupiais, J., Hennig, C., and Di Giandomenico, M.V.
Thermodynamical and Structural Study of Protactinium(V) Oxalate Complexes in Solution
Inorg. Chem. **49** (2010) 9962-9971

Planer-Friedrich, B., E., S., Scheinost, A.C., and Wallschlaeger, D.
Arsenic speciation in sulfidic waters: Reconciling contradictory spectroscopic and chromatographic evidence
Anal. Chem. **82** (2010) 10228–10235

Reitz, T., Merroun, M.L., Rossberg, A., and Selenska-Pobell, S.
Interactions of Sulfolobus acidocaldarius with uranium
Radiochimica Acta **98** (2010) 249-257

Rossberg, A. and Funke, H.
Determining the radial pair distribution function from X-ray absorption spectra by use of the Landweber iteration method
J Synch. Rad. **17** (2010) 280-288

Sitte, J., Akob, D.M., Kaufmann, C., Finster, K., Banerjee, D., Burkhardt, E.-M., Kostka, J.E., Scheinost, A.C., Büchel, G., and Küsel, K.
Microbial Links between Sulfate Reduction and Metal Retention in Uranium- and Heavy Metal-Contaminated Soil
Applied and Environmental Microbiology **76** (2010) 3143-3152

Takao, K., Kato, M., Takao, S., Nagasawa, A., Bernhard, G., Hennig, C., and Ikeda, Y.
Molecular Structure and Electrochemical Behavior of Uranyl(VI) Complex with Pentadentate Schiff Base Ligand: Prevention of Uranyl(V) Cation-Cation Interaction by Fully Chelating Equatorial Coordination Sites
Inorg. Chem. **49** (2010) 2349-2359

Takao, K., Takao, S., Scheinost, A.C., Bernhard, G., and Hennig, C.
In situ spectroelectrochemical investigation of Pt(II/IV) oxidation in aqueous solution using X-ray absorption spectroscopy
Inorg. Chim. Acta **363** (2010) 802-806

Vogel, M., Günther, A., Rossberg, A., Li, B., Bernhard, G., and Raff, J.
Biosorption of U(VI) by the green algae Chlorella vulgaris in dependence of pH value and cell activity
Sci. Total Environ. **409** (2010) 384-395

2.4.2. Publications in Materials Research

2009

Abrasonis, G., Kovacs, G.J., Mucklich, A., Zhou, S., Babonneau, D., Martinavicius, A., Berndt, M., Munnik, F., Vinnichenko, M., Heinig, K.H., Grenzer, J., Kolitsch, A., Schmidt, H., and Moeller, W.
Substrate effects on the morphology of carbon encapsulated nickel nanoparticles grown by surface diffusion assisted phase separation
Journal of Physical Chemistry C **113** (2009) 8645-8651

Bauer J., Pietsch U., Davydok A., Biermanns A., Grenzer J., Gottschalch V. and Wagner G.
X-ray investigations of the interface structure of free standing InAs nanowires grown on GaAs $[111]_B$
*Appl.Phys.A **96**, (2009),851-859*

Beckers, M., Hoehlund, C., Baehtz, C., Martins, R.M.S., Persson, P.O.A., Hultman, L., and Moeller, W.
The influence of subtrate temperature and Al mobility on the micro structural evolution of magnetron sputtered ternary Ti-Al_N thin films
Journal of Applied Physics **106** (2009) 064915

Cantelli, V., Von Borany, J., Jeutter, N.M., and Grenzer, J.
In situ grazing incidence scattering investigations during magnetron sputtering deposition of FePt/Ag thin films
Advanced Engineering Materials **11** (2009) 478

Kanjilal, A., Rebohle, L., Baddela, N.K., Zhou, S., Voelskow, M., Skorupa, W., and Helm, M.
Probing the impact of microstructure on the electroluminescence propoerties of Ge-nanocrystal enriched Er-doped SiO_2 layers
Phys. Rev. B **79** (2009) 161302 (R)

Martins, R.M.S., Schell, N., Gordo, P.R., Maneira, M.J.P., Silva, R.J.C., and Fernandes, F.M.B.
Development of sputtered Shape Memory Alloy (SMA) Ni-Ti films for actuation in ice cooled environments
Vacuum **83** (2009) 1299-1302

Martins, R.M.S., Schell, N., Mahesh, K.K., Pereira, L., Silva, R.J.C., and Fernandes, F.M.B.
Texture Development and Phase Transformation Behavior of Sputtered Ni-Ti Films
Journal of Materials Engineering and Performance **18** (2009) 543-547

Potzger, K., Shalimov, A., Zhou, S., Schmidt, H., Mucklich, A., Helm, M., Fassbender, J., Liberati, M., and Arenholz, E.
Amorphous clusters in Co implanted ZnO induced by boron pre-implantation
Journal of Physics D: Applied Physics **105** (2009) 123917

Potzger, K. and Zhou, S.
Non-DMS related ferromagnetism in transition metal doped zinc oxide
Phys. Stat. Sol. (b) **246** (2009) 1147

Rogozin, A., Vinnichenko, M., Shevchenko, N., Kreissig, U., Kolitsch, A., and Möller, W.
Real-time evolution of electrical properties and structure of indium oxide and indium tin oxide during crystallization
Scripta Materialia **60** (2009) 199

Shalimov, A., Potzger, K., Geiger, D., Lichte, H., Talut, G., Misiuk, A., Reuther, H., Stromberg, F., Zhou, S., Baehtz, C., and Fassbender, J.
Fe nanoparticles embedded in MgO crystals
Journal of Applied Physics **105** (2009) 064906-7

Talut, G., Grenzer, J., Reuther, H., Shalimov, A., Baehtz, C., Novikov, D., and Walz, B.
In situ observation of secondary phase formation in Fe implanted GaN annealed in low pressure N-2 atmosphere
Applied Physics Letters **95** (2009)

Zhou, S., Potzger, K., Xu, Q., Kuepper, K., Talut, G., Marko, D., Mucklich, A., Helm, M., Fassbender, J., Arenholz, E., and Schmidt, H.
Spinel ferrite nanocrystals embedded inside ZnO: magnetic, electronic and magneto-transport perperties
Phys. Rev. B **80** (2009) 094409

Zhou, S., Potzger, K., Xu, Q., Talut, G., Lorenz, M., Skorupa, W., Helm, M., Fassbender, J., Grundmann, M., and Schmidt, H.
Ferromagnetic transition metal implanted ZnO: a diluted magnetic semiconductor?
Vacuum **83** (2009) S13-S19

Zhou, S.Q., Shalimov, A., Potzger, K., Jeutter, N.M., Baehtz, C., Helm, M., Fassbender, J., and Schmidt, H.
Memory effect of Mn_5Ge_3 nanomagnets embedded inside a Mn-diluted Ge matrix
Applied Physics Letters **95** (2009) 192505

2010

Abrasonis, G., Oates, T.W.H., Kovacs, G.J., Grenzer, J., Persson, P.O.A., Heinig, K.H.H., Martinavicius, A., Jeutter, N., Baehtz, C., Tucker, M., Bilek, M.M.M., and Muller, W.
Nanoscale precipitation patterns in carbon-nickel nanocomposite thin films: Period and tilt control via ion energy and deposition angle
Journal of Applied Physics **108** (2010)

Beckers, M., Eriksson, F., Lauridsen, J., Baehtz, C., Jensen, J., and Hultman, L.
Formation of basal plane fiber-textured Ti2AlN films on amorphous substrates
Physica Status Solidi-Rapid Research Letters **4** (2010) 121-123

Hanisch, A., Biermanns, A., Grenzer, J., Facsko, S., and Pietsch, U.
Xe ion beam induced rippled structures on differently oriented single-crystalline Si surfaces
Journal of Physics D-Applied Physics **43** (2010) 5

Hoglund, C., Alling, B., Birch, J., Beckers, M., Persson, P.O.A., Baehtz, C., Czigany, Z., Jensen, J., and Hultman, L.
Effects of volume mismatch and electronic structure on the decomposition of ScAlN and TiAlN solid solutions
Physical Review B **81** (2010) 2241011-17

Kalinichenka, S., Rontzsch, L., Baehtz, C., and Kieback, B.
Hydrogen desorption kinetics of melt-spun and hydrogenated $Mg_{90}Ni_{10}$ and $Mg_{80}Ni_{10}Y_{10}$ using in situ synchrotron, X-ray diffraction and thermogravimetry
Journal of Alloys and Compounds **496** (2010) 608-613

Krausslich, J., Hofer, S., Zastrau, U., Jeutter, N., and Baehtz, C.
Temperature dependence of lattice parameters of langasite single crystals
Crystal Research and Technology **45** (2010) 490-492

Martins, R.M.S., Schell, N., Reuther, H., Pereira, L., Mahesh, K.K., Silva, R.J.C., and Fernandes, F.M.B.
Texture development, microstructure and phase transformation characteristics of sputtered Ni-Ti Shape Memory Alloy films grown on TiN < 111 >
Thin Solid Films **519** (2010) 122-128

Martins, R.M.S., Schell, N., von Borany, J., Mahesh, K.K., Silva, R.J.C., and Fernandes, F.M.B.
Structural evolution of magnetron sputtered shape memory alloy Ni-Ti films
Vacuum **84** (2010) 913-919

Shalimov, A., Zhou, S.Q., Roshchupkina, O., Jeutter, N., Baehtz, C., Talut, G., Reuther, H., and Potzger, K.
Multiple ferromagnetic secondary phases in Fe implanted yttria stabilized zirconia
Journal of Applied Physics **108** (2010)

Talut, G., Reuther, H., Grenzer, J., Mücklich, A., Shalimov, A., and Skorupa, W.
Spinodal decomposition and secondary phase formation in Fe-oversaturated GaN
Physical Review B **81** (2010) 155212

Vinnichenko, M., Gago, R., Cornelius, S., Shevchenko, N., Rogozin, A., Kolitsch, A., Munnik, F., and Moller, W.
Establishing the mechanism of thermally induced degradation of ZnO:Al electrical properties using synchrotron radiation
Applied Physics Letters **96** (2010) 3

Zschintzsch, M., Jeutter, N.M., Borany, J.v., Krause, M., and Muecklich, A.
Reactive DC magnetron sputtering of (GeO_x-SiO_2) superlattices for Ge nanocrystal formation
Journal of Applied Physics **107** (2010) 034306

2.5. Experiments

The following tables list all experiments which have been performed at the beamline, ordered by end-station (RCH, MRH) and by type of experiment (in-house, ESRF, Actinet). Experiments with more than 18 shifts usually have been performed during several experimental runs and are part of long-term research programs.

2.5.1. List of RCH Experiments

RCH 2009 in-house

Number	Title	Proposers	Institution	Experimenters	Shifts
20-01-656	EXAFS investigations of uranium species formed by monocellular and polycellular algae	A. Guenther A. Rossberg A. Scheinost	FZD	A. Rossberg	3
20-01-664	Structure of neptunium species in Solution	C. Hennig A. Ikeda	FZD	C. Hennig S. Takao	9
20-01-668	Abiotic antimony reduction by Fe(II) systems	A. Scheinost R. Kirsch L. Charlet	FZD UJF Grenoble	A. Scheinost R. Kirsch D. Banerjee	12
20-01-675	Investigation of the aqueous phase in the ternary sorption system uranium(VI), goethite, organic model compounds	A. Rossberg A. Scheinost	FZD	C. Hennig A. Rossberg H. Funke A. Scheinost C. Lucks	39
20-01-681	Development of a 2nd generation spectro-electrochemical cell for *in situ* electrolysis	C. Hennig K. Takao A. Scheinost	FZD	C. Hennig K. Takao	18
20-01-683	Structure determination of U(VI)-opalinus clay surface complexes in absence and presence of humic acid by EXAFS	C. Joseph	FZD	A. Rossberg C. Joseph	9
20-01-685	Binding forms of actinides and lanthanides with single constituents of biofluids	A. Barkleit	FZD	C. Hennig A. Rossberg H. Funke A. Scheinost D. Banerjee A. Barkleit	9
20-01-686	EXAFS investigation of austenitic alloys nitrided at low temperature	G. Abrasonis A. Martinavicius	FZD	A. Martinavicius G. Abrasonis	6
20-01-687	Neptunyl adsorption to calcite	F. Heberling	FZ Karlsruhe	F. Heberling C. Burmeister	3
20-01-688	Molecular scale studies on the speciation of U(VI) bound to cells and S-layer proteins of *Archaea*	T. Reitz M. Merroun S. Selenska-Pobell	FZD	A. Rossberg T. Reitz	18
20-01-689	EXAFS investigation of the effects of humic acid on uranyl adsorption on goethite	T. Saito A. Scheinost	Univ. Tokyo	T. Saito	12

Number	Title	Proposers	Institution	Experimenters	Shifts
20-01-690	Molecular structure of actinide hexacyanometalates	C. Den Auwer T. Dumas S. Dahou G. Dupouy M. Mendes	CEA IPN Orsay	C. Den Auwer G. Dupouy S. Dahou M. Sonzano Rodriguez	15
20-01-691	EXAFS-investigations on U(IV) precipitates	S. Weiss	FZD	C. Hennig I. Dreissig	8
20-01-692	Effect of metal-reducing bacteria on uranium mobilization	K. Kuesel	Univ. Jena	A. Rossberg	6
20-01-693	EXAFS and XANES investigation of plutonium sorption complexes on iron minerals	R. Kirsch	FZD	A. Scheinost A. Rossberg R. Kirsch D. Banerjee	9
20-01-694	EXAFS and Rietveld-MEM analysis of sorption structure of uranium onto zeolite	C. Hennig S. Takao K. Takao	FZD	C. Hennig A. Rossberg	9
20-01-695	EXAFS studies of the structure and bonding in solution of dioxouranium(VI)-nucleotide complexes	Z. Szabo A. Rossberg A. Scheinost	KTH FZD	A. Rossberg	6

RCH 2009 ESRF

Number	Title	Proposers	Institution	Experimenters	Shifts
CH - 2423	Free and silica-gel-bound tetraazamacrocycles as complexing agents of actinide cations: investigation of the solid-state coordination scheme	M. Meyer A. Scheinost	LIMSAG-Dijon FZD	C. Hennig M. Meyer S. Faure B. Batifol L. Neguyen D. Banerjee	9
CH - 2738	XAS investigation of $(U,Am)O_2$ and $(U,Pu)O_2$ solid solutions obtained by oxalic co-precipitation	P. Martin B. Arab-Chapelet S. Grandjean C. Robisson-Thomas H. Palancher	CEA	P. Martin E. Welcomme B. Arab-Chap. I. Jobelin V. Brethenoux S. Arpigny S. Picart C. Tamain	12
CH - 2739	Structure of uranyl-arsenate complexes sorbed on bentonite	E. Suess G. Bernhard A. Scheinost B. Merkel B. Planer-Friedrich W. Gezaheg.	TU Freiberg FZD	A. Scheinost E. Suess B. Merkel B. Planer-Friedrich W. Gezaheg.	12
CH - 2843	Structural XAS analyses of uranylarsenate and uranylthioarsenate sorption on FeOOH	W. Gezaheg. B. Planer-Friedrich E. Suess B. Merkel	TU Freiberg	W. Gezaheg.	6

Number	Title	Proposers	Institution	Experimenters	Shifts
CH - 2969	Investigation of the molecular structure of actinide solvent extraction compounds	C. Fillaux C. den Auwer	CEA Marcoule	X. Crozes C. Den Auwer T. Dumas G. Dupouy S. Dahou C. Fillaux	12
CH - 2972	EXAFS-investigations on U(IV) precipitates	S. Weiss	FZD	S. Weiss H. Zaenker	6
EC - 424	EXAFS study of the sorption of Np(V) on Opalinus Clay	S. Amayri T. Reich	Uni Mainz	T. Reich S. Amayri J. Drebert D. Froehlich	9
EC - 425	EXAFS study of neptunium binding mechanisms to cementitious materials	E. Wieland R. Daehn J. Tits	PSI	R. Daehn J. Tits D. Kunz J. Gaona	12
EC - 540	EXAFS study of neptunium(V) sorption on Opalinus Clay in the presence and absence of humic acid under aerobic and anaerobic conditions	S. Amayri T. Reich	Uni Mainz	T. Reich S. Amayri J. Drebert D. Froehlich	6
EC – 541	EXAFS investigations on the influence of carbonate complexation on the sorption of actinides (Am(III), U(VI)) on clay minerals	M. Marques Fernandes B. Baeyens R. Daehn	PSI	M. Marques Fernandes B. Baeyens R. Daehn V. Kalbermatt.	15

RCH 2009 ACTINET

Number	Title	Proposers	Institution	Experimenters	Shifts
20-01-676	Reduction of uranium(VI) by adsorbed Fe(II) on clays and by structural Fe(II) in smectites in O_2, CO_2 free atmosphere	S. Chakrabort. A. Scheinost	LGIT FZD	S. Chakrabort.	6

RCH 2010 in-house

Number	Title	Proposers	Institution	Experimenters	Shifts
20-01-675	Investigation of the aqueous phase in the ternary sorption system uranium(VI), Goethite, organic model compounds.	A. Rossberg D. Banerjee C. Hennig A. Ikeda C. Lucks A. Scheinost	FZD	A. Rossberg C. Lucks A. Scheinost	30
20-01-681	Development of a 2nd generation spectro-electrochemical cell for in situ electrolysis	C. Hennig K. Takao A. Scheinost	FZD	C. Hennig K. Takao A. Rossberg D. Banerjee	18
20-01-688	Molecular scale studies on the speciation of U(VI) bound to cells and S-layer proteins of *Archaea*	T. Reitz M. Merroun A. Rossberg S. Selenska	FZD Univ. Granada	V. Chapon M. Carrier M. Merroun A. Rossberg	15

Number	Title	Proposers	Institution	Experimenters	Shifts
20-01-690	Molecular structure of actinide hexacyanometalates	C. Den Auwer T. Dumas S. Dahou G. Dupouy M. Mendes	CEA IPN Orsay	C. Den Auwer S. Dahou C. Hennig A. Rossberg	24
20-01-695	EXAFS studies of the structure and bonding in solution of dioxouranium(VI)-nucleotide complexes	S. Szabo A. Rossberg A. Scheinost	KTH Sweden FZD	A. Rossberg C. Hennig D. Banerjee	6
20-01-696	Redox behavior of neptunium species in solution	C. Hennig K. Takao	FZD	C. Hennig K. Takao A. Rossberg	3
20-01-697	EXAFS / XANES investigations of K volume-doped $CoTiO_3$	S. Neumeier	FZ Juelich RWTH Aachen	C.J. Belle A. Scheinost D. Banerjee A. Rossberg	15
20-01-698	EXAFS investigation of Mg-Al layered double hydroxides containing Zr-IV, Hf-IV and Cd-II ions	H. Curtius	FZ Juelich	A. Scheinost D. Banerjee	6
20-01-699	Comparative investigation of the uranium complexation onto -Al_2O_3 by means of FT-IR and EXAFS spectroscopy	H. Foerstendorf K. Mueller	FZD	H. Foerstendorf K. Mueller A. Rossberg D. Banerjee C. Hennig A. Scheinost	9
20-01-701	Comparative investigation of uranium and thorium coordination in solution and solid state	C. Hennig K. Takao	FZD	C. Hennig D. Banerjee A. Rossberg A. Scheinost	38
20-01-702	EXAFS investigation on uranium complexes formed by fungi and reference samples	A. Guenther	FZD	A. Guenther A. Scheinost A. Rossberg	12
20-01-703	Structural investigation of complex of TcO_4^- and ReO_4^- with MIDOA by EXAFS spectroscopy	M. Saeki	FZD	M. Saeki D. Banerjee	6
20-01-704	EXAFS investigation of sorbed selenium oxyanions onto anatase	N. Jordan	FZD	N. Jordan A. Scheinost C. Hennig D. Banerjee	9
20-01-706	Selenium liquid phase speciation in Boom Clay conditions	E. Breynaert A Maes A. Scheinost	KU Leuven FZD	E. Breynaert D. Dom D. Banerjee C. Hennig A. Rossberg	12
20-01-708	Sorption and redox reactions of Sn^{II} and Sn^{IV} at the magnetite/water interface in presence and absence of organic ligands	S. Dulnee A. Scheinost	FZD	S. Dulnee A. Scheinost D. Banerjee	9

RCH 2010 ESRF

Number	Title	Proposers	Institution	Experimenters	Shifts
CH-2843	Structural XAS analyses of unanylarsenate and uranylthioarsenate sorption on FeOOH	W. Gezahegne B. Planer-Friedrich E. Suess B. Merkel	TU Freiberg	W. Gezahegne D. Banerjee C. Hennig	6
CH-2972	EXAFS-investigations on U(IV) precipitates	S. Weiss	FZD	C. Hennig A. Rossberg A. Scheinost	9
CH-2967	Study of americium and plutonium chemistry in mixed oxide nuclear fuel	R. Belin J.C. Dumas P. Martin C. Robisson-Thomas	CEA	R. Belin P. Martin S. Noyau E. Gavilan A. Scheinost A. Rossberg D. Banerjee	12
CH-3081	Structural XAS analyses of uranyl-arsenic species and their sorption onto FeOOH and montmorillonite	W. Gezahegne B. Merkel B. Planer-Friedrich	TU Freiberg Univ. Bayreuth	A. Scheinost E. Suess D. Banerjee C. Hennig	21
CH-3082	Study of thorium and uranium complexation with alpha-hydroxy carboxyliate ligands	M. Grive E. Colas L. Duro	Amphos ENVIROS	I. Rojo E. Colas M. Grive	12
CH-3083	EXAFS/XANES investigation of uranium plutonium mixed carbide	A. Handschuh S. Vaudez P. Martin G. Leturcq R. Belin F. Abraham	CEA ENSC Lille	S. Vaudez P.Martin A. Handschuh C. Hennig D. Banerjee A. Rossberg	12
CH-3205	Comparative investigation of the uranium complexation onto γAl_2O_3 by means of FT-IR and EXAFS spectroscopy	H. Foerstendorf	FZD	K. Mueller K. Gueckel A. Rossberg C. Hennig	9
CH-3206	Complexation between U(VI) and Re(VII) in a hydrophobic ionic liquid	C. Gaillard I. Billard	IPNL Lyon IReS Strasbourg	C. Gaillard I. Billard A. Ouadi	15
EC-616	EXAFS study of plutonium sorption on Opalinus Clay	S. Amayri T. Reich	Univ. Mainz	S. Amayri T. Reich J. Drebert U. Kaplan	9
EC-617	Determination of neptunium redox states on C-S-H and cement samples	J. Gaona R. Daehn E. Wieland J. Tits	PSI	R. Daehn J. Tits D. Kunz J. Gaona A. Rossberg D. Banerjee C. Hennig	15

RCH 2010 ACTINET

Number	Title	Proposers	Institution	Experimenters	Shifts
20-01-693	Spectroscopic investigation of redox reactions of plutonium with iron minerals	R. Kirsch	FZD ITU KIT	R. Kirsch A. Scheinost A. Rossberg C. Hennig D. Banerjee	15
20-01-705	XAS study of dense $U_{1-y}Am_yO_{2-x}$ (y=0.10; 0.15) obtained by conventional powder metallurgy	D. Prieur	CEA FZD	P. Coste E. Gavilan P. Martin D. Prieur	12

2.5.2. List of MRH Experiments

MRH 2009 in-house

Number	Title	Proposers	Institution	Experimenters	Shifts
20-02-670	Optical properties of planar and lithographic x-ray waveguides	T. Salditt	Univ. Goettingen	S. Krueger H. Neubauer M. Bartels	9
20-02-673	Influence of ion beam channeling for ripple formation at amorphous-crystalline interface after ion-bombardment	A. Biermanns	Univ. Siegen	A. Hanisch A. Biermanns	9
20-02-675	Thermal stability of nanostructures in the Ti-Al-Si-N and Cr-Al-Si-N nano-composites	D. Rafaja C. Baehtz	TU-Freiberg FZD	M. Motylenko C. Wuestefeld M. Dopita	9
20-02-676	GISAXS study of self organized metallic islands and nanowires on rippled substrates	G. Abrasonis T. Oats G. Kovacs	FZD	G. Abrasonis G. Kovacs	12
20-02-677	Self –assembled Fe and FePt nanoparticles in yttria-stabilized zirconia after iron-platinum implantation	A. Shalimov	FZD	A. Shalimov G. Kovacs	9
20-02-678	Structural investigation of Co-B ferromagnetic nanoparticles in ZnO single crystals	A. Shalimov	FZD	A. Shalimov G. Kovacs	9
20-02-679	In situ XRD and electrical resistivity study of the phase transformations in Ni--Ti shape memory alloys	F. Braz Fernandes R. Martins M. Karimbi Koosappa R. Silva Cordeiro J. von Borany	CENIMAT FZD	J. von Borany F. Braz Fernandes R. Silva Cordeiro M. Karimbi Koosappa	12
20-02-681	Phase separation patterns in lattice-mismatched ternary Sc-Al-N films	M. Beckers C. Hoglund L. Hultman	FZD IFM Linkoping	C. Hoglund M. Beckers J. Birch	18
20-02-682	In-situ investigation of the dewetting process of thin iron film in the CNT growth process	C. Baehtz S. Hofmann C. Wirth	FZD Univ. Cambridge	C. Baehtz C. Wirth B. Bayer	18

Number	Title	Proposers	Institution	Experimenters	Shifts
20-02-683	Anisotropic strain-distribution in ion-beam irradiated silicon	A. Biermanns U. Pietsch J. Grenzer A. Hanisch	Univ. Siegen	A. Hanisch A. Biermanns	15
20-02-684	Thermal stability and interface interactions in the TM-Al-N (TM = Ti, Cr) thin film nanocomposites	T. Rafaja C. Bähtz	TU Freiberg FZD	C. Wuestefeld M. Motylenko M. Dopita	18
20-02-685	GISAXS study of the self-organized multilayers of carbon encapsulated transition metal nanoparticles	G. Abrasonis T. Oates G. Kovacs M. Krause	FZD Univ. Linkoping	A. Martinavicius G. Abrasonis G. Kovacs T. Oates	12
20-02-686	Structural diagnostic of metal-doped transparent oxides and germanium employed at photovoltaic, magneto-optical and magnetic applications	A. Shalimov	FZD	A. Shalimov M. Liedke I. Li	9
20-02-687	Structural investigations of SiO_2/Cr/NiFe/FeMn/Cr multilayers representing unusual exchange bias properties	A. Shalimov	FZD	A. Shalimov M. Liedke I. Li	9
20-02-689	Rietveld-MEM Analysis of sorption structure of uranium onto zeolite	C. Hennig S. Takao K. Takao	FZD	C. Hennig C. Baehtz	20
20-02-690	Phase separation patterns in cubic $Sc_{1-x}Al_xN$ films	M. Beckers C. Hoglund C. Baehtz	FZD Univ. Linkoping	C. Hoglund M. Beckers	15

MRH 2009 ESRF

Number	Title	Proposers	Institution	Experimenters	Shifts
HS - 3849	Nucleation conditions for diamond nanocrystals in amorphous silica matrix	M. Buljan V. Holy	IRB Univ. Prague	V. Holy J. Grenzer M. Buljan V. Vales	18
HS - 3850	HRXRD characterization of MOCVD-grown GaN layers on 4H, 6H 001 SiC substrates with AlGaN/GaN heterostructures as a buffer layer	J. Gaca M. Wojcik K. Mazur	ITME Warsaw	J. Gaca M. Wojcik K. Mazur	12
MA - 645	Temperature dependence of lattice parameters of langasite single crystals ($La_3Ga_5SiO_{14}$)	J. Kraeusslich O. Wehrhan U. Zastrau	Univ. Jena	J. Kraeusslich U. Zastrau S. Hoefer	9
MA – 896	In-situ time-resolved diffraction of phase formation during annealing of amorphous and hydrogenated Mg-Ni-Y alloys	L. Roentzsch	IFAM	L. Roentzsch S. Kalinichenka	12
Si - 1797	Influence of codoping on nanocrystal formation in GaFeN	R. Lechner V. Holy A. Bonnani G. Bauer	JKU-Linz Univ. Prague	R. Lechner A. Navarro Quezada M. Meduna M. Rovezzi	12
SI – 1980	In-situ investigation of the ordering of Ge quantum dots during the growth of Ge+SiO_2 multilayers	M. Buljan V. Holy N. Radic	Univ. Prague	V. Holy J. Grenzer M. Buljan N. Radic	17

Number	Title	Proposers	Institution	Experimenters	Shifts
SI – 1981	In-situ x-ray diffraction investigation of growth of ferromagnetic clusters in (Ga,Mn)N epitaxial layers	R. Lechner G. Bauer A. Bonanni V. Holy	JKU Univ. Prague	R. Lechner A. Navarro Quezada M. Rovezzi	17

MRH 2010 in-house

Number	Title	Proposers	Institution	Experimenters	Shifts
20-02-688	In-situ investigation of the behavior of Fe catalyst during the CNT formation	C. Baehtz B. Bayer S. Hofmann C. Wirth	FZD CAM Cambridge	C. Wirth B. Bayer R. Weatherup C. Baehtz S. Hofmann	18
20-02-691	Determination of point defect concentrations in nano-crystalline platinum	H. Schmidt W. Gruber S. Chakravarty	TU Clausthal	S. Chacravarty H. Schmidt W. Gruber	15
20-02-692	Microstructure and interface interactions in Cr/ta-C multilayer thin films	D. Rafaja C. Baehtz U. Ratayski	TU Freiberg FZD	U.Ratayski T. Schucknecht C. Schimpf	15
20-02-693	Simultaneous XRD and electrical resistivity measurements of the phase transitions in Co-Ni-Ga ferromagnetic shape memory alloy system	C. Craciunescu F.M. Braz Fernandes K. Mahesch J. von Borany	CENIMAT FZD	F. Braz Fernandes M. Karimbi Koosappa C. Craciunescu	12
20-02-694	In-situ synchrotron X-ray diffraction studies of the crystallization and hydrogen sorption properties of rapidly quenched Mg-Ni-Y-(Cu) alloys	L. Roentzsch S. Kalinichenka	Frauen-hofer Institut	L. Roentzsch S. Kalinichenka	18
20-02-695	Temperature dependent crystallisation and ordering of Germanium nanocrystals in SiO2 matrix	M. Zschintzsch J. von Borany N. Jeutter	FZD	J. von Borany M. Zschintsch	15
20-02-696	Grain growth induced by focused ion beam irradiation in thin magnetic films	J. Grenzer	FZD	J. Grenzer O. Roshchupkina	17
20-02-697	Hydrogen loading of thin films	A. Pundt	Univ. Göttingen	M. Vlcek S. Wagner H. Uchida M. Vlach F. Lukac	20
20-02-698	GISAXS study of the secondary phase morphology in transparent conductive oxide thin films	G. Abrasonis M. Vinnichenko K. Ellmer	FZD Helmholtz-Berlin	G. Abrasonis M. Vinnichenko S. Brunken	9
20-02-699	In-situ X-ray scattering investigations of phase transformation and interface properties of LaLuO3 / metal gate films	J. von Borany J. Schubert	FZD FZ-Jülich	J. von Borany J. Schubert	9
20-02-700	Grain growth induced by focused ion beam irradiation in thin magnetic films	O. Roshchupkina J. Grenzer	FZD	A. Shalimov J. Grenzer O. Roshchupkina	21

20-02-706	In situ diffraction study of the electrochemical insertion-deinsertion of lithium in a high potential layered oxide	JF. Colin C. Bourbon L. Daniel JF. Martin L. Simonin	CEA	L. Simonin JF. Martin JF. Colin M. Rey C. Barchasz T Gutel E. Radvanyi A. Boulieau	9

MRH 2010 ESRF

Number	Title	Proposers	Institution	Experimenters	Shifts
CH-3085	Unknown crystal structures of selected uranyl sulfates: solution from high resolution powder data combined with EXAFS spectroscopy	J. Plasil M. Husak	Nat. Museum Prague I.C.T. Prague	J. Plasil M. Husak J. Rohlicek	12
CH-3207	Investigation of electrochemical lithium insertion-deinsertion reactions in promising cathode materials for lithium batteries using in situ synchrotron diffraction techniques	A. Kuhn F. Garcia-Alvarado E. Gonzalo J.C. Perez Flores	CEU	A. Kuhn J.C. Perez Flores E. Gonzalo	12
HS-4246	Effect of Mg-codoping on the formation of Fe-rich phases in (Ga,Fe)N	A. Navarro Quezada G. Bauer A. Bonanni T. Devillers M. Rovezz	JKU Linz	T. Devillers A. Navarro Quezada E. Wintersberger	17
MA-895	Combined in-situ XRD and Electrical Resistivity Study of the Phase Transformations in Ni-Ti Shape Memory Alloys	F.M. Braz Fernandes	FCT Lisbon	F.M. Braz Fernandes R.J. Silva Cordeiro M. Karimbi Koosappa	12
MA-1019	Concurrent Effect of Meltspinning and Severe Plastic Deformation on Shape Memory Alloy Ribbons by Simultaneous XRD and Electrical Resistivity Measurements	F.M. Braz Fernandes C. Craciunescu K. Mahesh J. von Borany	FCT Lisbon FZD	F.M. Braz Fernandes M. Karimbi Koosappa C. Craciunescu	9
MA-1148	Microstructure design of electrodeposited GMR multilayers via annealing	D. Rafaja T. Schucknecht C. Baehtz	TU-Freiberg FZD	T. Schucknecht C. Schimpf U. Ratayski	12
SI-2151	Growth of Ge quantum dot lattices in alumina matrix	M. Buljan V. Holy N. Radic	IRB	L. Horak N. Radic M. Buljan J. Grenzer	18

3. Experimental Reports

3.1. Experimental Reports Radiochemistry

The following section compiles the experimental reports for experiments conducted in 2009 and 2010. A few reports are lacking, either because a difficult sample preparation failed (e.g. CH-2843), or because of detector (EC-540) or monochromator problems (20-01-706). These experiments have been repeated in early 2011, and experimental reports will be presented in the Biannual Report 2011/2012.

ROBL-CRG	**Experiment title:** EXAFS investigations of uranium species formed by monocellular and polycellular algae	**Experiment number:** 20 - 01 - 656
Beamline: BM 20	**Date of experiment:** 09/02/09 – 10/02/09	**Date of report:** 08/01/10
Shifts: 3	**Local contact(s):** André Roßberg	*Received at ROBL:*

Names and affiliations of applicants (* indicates experimentalists):
A. Günther[1], M. Vogel*[1] A. Roßberg*[2], A. C. Scheinost*[2], C. Hennig*[2], H. Funke*[2]
[1]Forschungszentrum Dresden-Rossendorf e.V., Institute of Radiochemistry, P.O. Box 510119, 01314 Dresden, Germany
[2]ESRF-ROBL/CRG, Avenue des Matryrs, B.P. 220, 38043 Grenoble Cedex, France

Report:

Experimental

The aim of this study was to determine the structural parameters of the formed uranyl complex species in active monocellular *Chlorella vulgaris* cells at pH 4.4 with $UO_2(NO_3)_2$ concentrations between 0.1 mM and 1.0 mM. The freshly grown active algal cells were re-suspended in uranium containing mineral medium and incubated for 48 h. After separation of the washed algal biomass by centrifugation, the fresh samples were put into polyethylene sample holders surrounded with Capton tape and shock frozen in liquid nitrogen. The U L_{III}-edge spectra were measured in transmission mode at 15 K using a closed-cycle He-cryostat. The EXAFS spectra were analyzed using the program suite EXAFSPAK /1/. The theoretical scattering phases and amplitudes were calculated by using X-ray structural data of meta-autunite, uranyl-triacetate and uranyl-AMP with the scattering code FEFF8.2 /2/.

Results

Figure 1 shows the raw U L_{III}-edge k^3-weighted EXAFS spectra and their corresponding Fourier transforms (FT) of uranium containing active algal cells (samples A-C) measured at 15 K after shock freezing of the samples. The spectra of algal cells incubated with 0.1 mM, 0.5 mM and 1 mM uranium at pH 4.4 are well reproduced by taking backscattering of oxygen, carbon and phosphate atoms into account. In all cases the common linear trans-dioxo structure of two axial oxygen atoms U-O_{ax} at a distance of 1.77-1.78 Å and two equatorial oxygen shells with distances U-O_{eq1} of 2.34-2.35 Å and U-O_{eq2} of 2.49-2.50 Å were obtained. In the uranyl-algae complexes uranium is coordinated via a six-fold coordination sphere with 4 short U-O distances and two long ones. The longer oxygen distance of U-O_{eq2} indicates a bidentate binding of uranium by carboxylic groups. This estimation is supported by the determination of a U-C contribution at 2.89-2.91 Å.

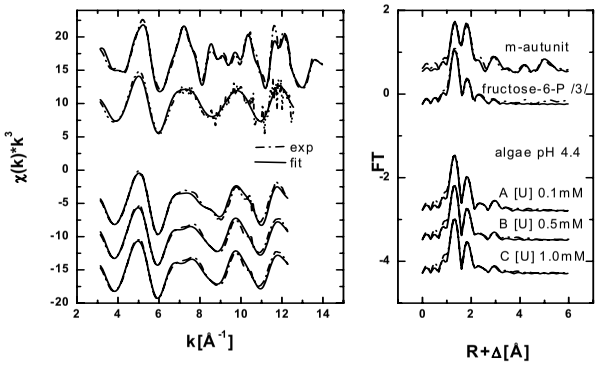

Fig. 1.
Raw U L_{III}-edge k^3-weighted EXAFS spectra (left) and corresponding Fourier transform (right) of different algal samples and reference samples
[Algae] = 0.76g $_{dry\ mass}$ / L
[U(VI)] = 0.1-1.0 mM

Additionally, phosphate groups might be involved in the interaction with uranium by active algae cells. The short bond length of the equatorial oxygen shell U-O_{eq1} suggests binding of the uranyl ion via organic phosphate groups in a mondentate fashion (see Fig. 1 fructose-6-P /3/). The contribution of phosphate to the EXAFS spectrum is displayed in the FT peak at R+Δ ~3 Å with radial distances of 3.60 Å – 3.61 Å and coordination numbers of 3 for sample A and 2 for the samples B and C. Therefore, we conclude that at lower uranium concentrations (0.1 mM) and at pH 4.4 U(VI) is coordinated preferentially by organic phosphate groups with a contribution of carboxylic groups. With increasing U(VI) concentrations at pH 4.4 the contribution of carboxylic groups to the U(VI) coordination by active algae seems to become more important. Above ~4 Å the FT obtained for the inorganic uranyl phosphate meta-autunite differs strongly from the FT obtained for the uranyl-algae complexes (see Fig. 1 meta-autunite). Therefore the interaction of inorganic phosphate seems to be of minor importance for the uranium coordination under the given experimental conditions.

References

/1/ George, G. N., Pickering, I. J.: EXAFSPAK A Suite of Computer Programs for Analysis of X-Ray Absorption Spectra. Stanford Synchrotron Radiation Laboratory, Stanford, CA. USA. (1995)

/2/ Ankudinov et al.: Real-space multiple scattering calculation and interpretation of x-ray absorption near-edge structure, Phys. Rev. B 58 (1998), 7565-7576

/3/ Koban et al.: Uranium(VI) complexes with sugar phosphates in aqueous solution. Radiochim. Acta 92 (2004), 903–908.

ROBL-CRG	**Experiment title:** Structure of Neptunium Species in Solution	**Experiment number:** 20-01-664
Beamline: BM 20	**Date of experiment:** from: 31.03.09 to: 03.04.09	**Date of report:** 6.2.2009
Shifts: 9	**Local contact(s):** Christoph Hennig	*Received at ROBL:*
Names and affiliations of applicants (* indicates experimentalists): Atsushi Ikeda-Ohno*, Christoph Hennig*, A.C. Scheinost*		

The solution samples investigated in this proposal were prepared by dissolving $NpO_2(ClO_4)_2{\cdot}nH_2O$ into aqueous solutions, to give a Np concentration of 0.04 M. The oxidation state of Np in the samples was electrochemically adjusted. Np L_{III}-edge (17.625 keV) EXAFS measurements were carried out in transmission mode using a Si(111) double-crystal monochromator, and two Pt-coated mirrors for rejection of higher harmonics.

Figure 1 shows the k^3-weighted Np L_{III}-edge EXAFS spectra for Np(IV), -(V), and -(VI) in 1.0 M $HClO_4$ (left), and their corresponding Fourier transforms (right). Perchlorate is known to be a noncomplexing ligand to actinide ions in aqueous solution, and hardly coordinates to the primary coordination sphere of actinide ions. Accordingly, the chemical species formed in aqueous $HClO_4$ solution are considered to be pure hydrate species. The EXAFS spectrum of Np(IV) is composed of a single oscillation pattern, giving a peak at 1.9 Å in the Fourier transform. The structural parameters determined by shell fitting are a Np-O distance ($R_{Np\text{-}O}$) of 2.40 Å with a coordination number (CN) of 10.4, corresponding to water molecules of the primary coordination sphere. The EXAFS spectra for the two higher oxidation states, V and VI, exhibit more intricate oscillation patterns and the corresponding Fourier transforms show several significant backscattering peaks. The most prominent peak at around 1.4 Å arises from the single scattering of the double-bond axial oxygen atoms (O_{ax}), indicative of the neptunyl unit (NpO_2^{n+}). The following two peaks at around 1.9 Å arise from oxygen atoms of the water molecules in the neptunyl equatorial plane ($O_{eq}(H_2O)$), while the small but sufficiently distinguishable peak at 2.9 Å is due to the multiple scattering of O_{ax}, respectively. The shell fitting results reveal that the neptunyl(V) ion is coordinated in its equatorial plane by 5.2 water molecules with O atoms at a distance of 2.49 Å, whereas the neptunyl(VI) ion is coordinated by 5.3 water molecules with a shorter interatomic distance of 2.42 Å. Our EXAFS data show therefore a structural rearrangement of Np hydrate species with oxidation state as illustrated in Figure 2: both Np(V) and (VI) ions exist predominately as pentaaquo neptunyl complexes, $[NpO_2(H_2O)_5]^{n+}$ with n = 1 for Np(V) and 2 for Np(VI), whereas the Np(IV) ion forms a spherically coordinated decaaquo complex, $[Np(H_2O)_{10}]^{4+}$. It is this drastic change in complex structure between Np(IV) and Np(V), which makes the transition between these two redox states almost irreversible (DE ~0.9 V), while the transition between Np(V) and Np(VI) requires no structural change, hence is quasi-reversible (DE = ~0.2 V). These results support our initial hypothesis that there is a strong relationship between the electrochemical behaviour of Np and its complex structure.

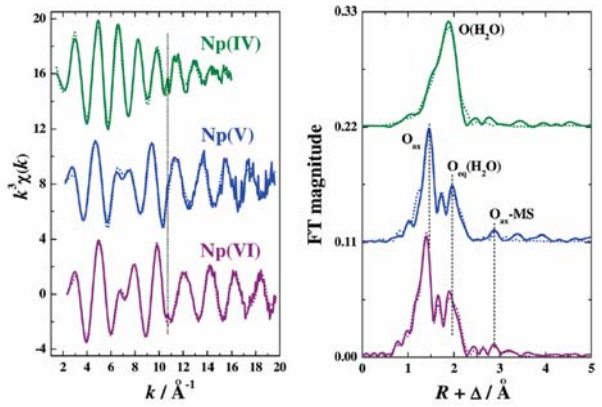

Fig. 1: k^3-weighted Np-L_{III} edge EXAFS spectra. Solid lines represent experimental data and dotted lines represent theoretical fit. The line colours reflect the actual colour of sample solutions.

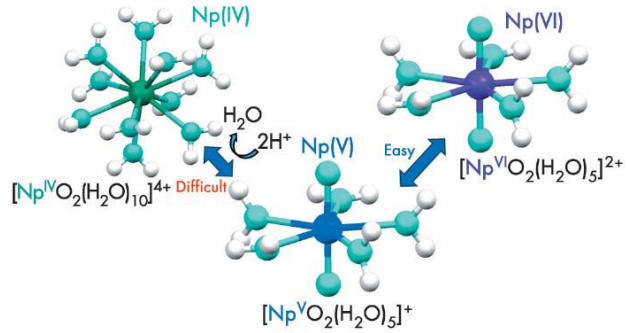

Fig. 2: Structural rearrangement of Np hydrate species through the redox reaction.

Ikeda-Ohno, A., Hennig, C., Rossberg, A., Funke, H., Scheinost, A.C., Bernhard, G., Yaita T. Electrochemical and complexation behavior of neptunium in aqueous perchlorate and nitrate solutions, *Inorg. Chem.* **47** (2008) 8294-8305.

ROBL-CRG	**Experiment title:** Abiotic antimony reduction by Fe(II) systems	**Experiment number:** 20-01-668
Beamline: BM 20	**Date of experiment:** from: Mar 12 to: Mar 16, 2009	**Date of report:** Apr 17 2011
Shifts: 12	**Local contact(s):** A.C. Scheinost	*Received at ROBL:* Apr 17 2011

Names and affiliations of applicants (* indicates experimentalists):
A. C. Scheinost*[1], R. Kirsch*[1,2],
[1]Institute of Radiochemistry, FZD, Dresden, Germany
[2]Laboratoire de Géophysique interne et Tectonophysique, Université Joseph Fourier, Grenoble, France

EXAFS and XPS investigation of Sb(V) reduction on mackinawite

Reduction of Sb(V) at the surface of nanoparticulate mackinawite was studied using X-ray photoelectron spectroscopy (XPS) and extended X-ray absorption fine structure (EXAFS) spectroscopy. Two series of experiments, at pH 5 and pH 8 respectively, were conducted where four different Sb concentrations (0.1, 0.3, 0.6, 0.8 mM) were reacted with aqueous suspension of mackinawite under CO_2-free, anoxic conditions. XPS results demonstrate high surface loading and complete reduction of Sb(V) to Sb(III) at pH 5, whereas at pH 8 lower surface loading coupled with incomplete reduction of Sb(V) is observed. Presence of Fe(III)-O and S^0 as oxidation products were identified at the surface of reacted samples at both pH. Sb K-edge EXAFS results indicate that Sb(III) is coordinated by three sulfur atoms at pH 5. At pH 8, however, only a small part of Sb(V) is reduced to Sb(III) which is most likely bound to S atoms, while the remaining Sb(V) atoms are in edge sharing and bidentate corner sharing linkages with $Fe(O,OH)_6$ octahedra which are formed as a reaction product.

Table 1. Fitting parameters for EXAFS spectra.

Sample	Shell	C.N.	Distance (Å)	σ^2
0.3 mM Sb, pH 5	Sb-S	2.97	2.48	0.0039
	Sb-Sb	0.60	3.81	0.0078
0.1 mM Sb, pH 8	Sb-O	3.7	1.98	0.0043
	Sb-S	1.0	2.44	0.0037
	Sb-Fe	1.0	3.12	0.0038[c]
	Sb-Fe	2.0	3.55	0.0038[c]
0.8 mM Sb, pH 8	Sb-O	4.8	1.97	0.0033[c]
	Sb-S	0.2	2.46	0.0033[c]
	Sb-Fe	1.0	3.09	0.0058[c]
	Sb-Fe	2.3	3.55	0.0058[c]

c: correlated, S_0^2 :1.1, fit mode: k^3+k^2

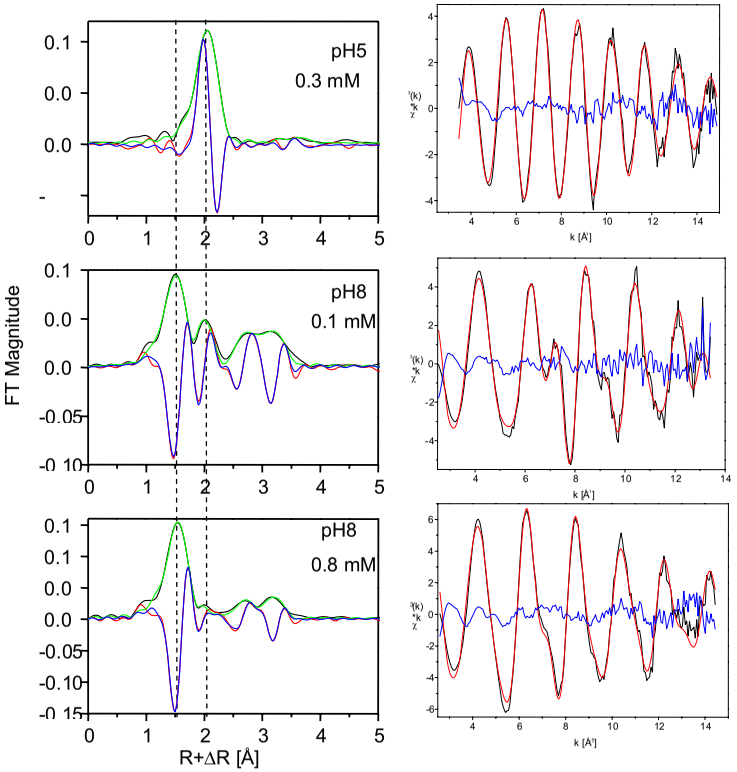

Fig. 1. Fitted Sb K-edge EXAFS spectra and the corresponding Fourier transforms.

The figure below gives a reaction scheme highlighting the more chalcophile nature of Sb(III) versus the more oxyphile nature of Sb(V).

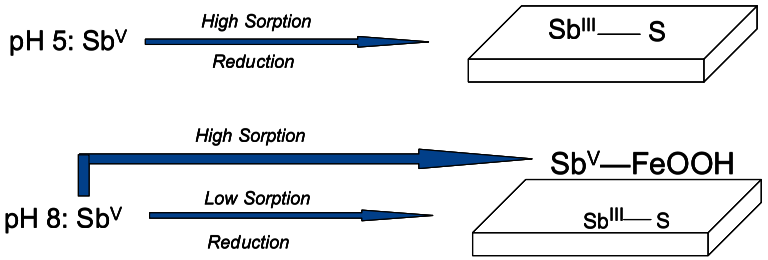

Kirsch R., Banerjee D., Charlet L., and Scheinost A. C. (2011) EXAFS and XPS investigation of Sb(V) reduction on mackinawite. *Environmental Science & Technology*, submitted.

ROBL-CRG	**Experiment title:** Investigation of the aqueous phase in the ternary sorption system uranium(VI), Goethite, organic model compounds.	**Experiment number**: 20 - 01 - 675
Beamline: BM 20	**Date of experiment**: from: 29/04 14/06 04/09 28/10 12/03 02/07 24/08 11/11 to: 02/05/09 16/06/09 08/09/09 01/11/09 14/03/10 06/07/10 28/08/10 14/11/10	**Date of report**: 01/04/11
Shifts: 78	**Local contact(s)**: André Roßberg	*Received at ROBL:*
Names and affiliations of applicants (* indicates experimentalists): A. Roßberg*, C. Lucks* Helmholtz-Zentrum Dresden-Rossendorf e.V., Institute of Radiochemistry, P.O. Box 510119, 01314 Dresden, Germany		

Experimental

The aim of this study was to investigate the structural influence of small organic (hyroxy)carboxylic acids on the sorption of U(VI) at the hematite/water interface. The system was divided in three subsystems which were investigated: solution phase of U(VI)/Fe(III) complexes with several (hyroxy)carboxylic acids, U(VI)-hematite sorption complexes, and U(VI) sorption complexes in the presence of hematite and (hyroxy)carboxylic acids as ternary systems. Due to the partly incomplete/and unreliable results in the literature for the aqueous U(VI) complexes with acetic(ac)-, succinic-, and tartaric acid the molecular structures of all present complexes were determined including their pH speciation by using EXAFS, FT-IR and UV-Vis. For malic- , malonic-, lactic-, and citric acid the structures of the most prominent (highest spectral activity in EXAFS, UV-Vis) complexes were determined. The structures of the sorption complexes in the binary system U(VI)-hematite were determined whereas the structures of the sorption complexes in the more complex ternary systems are still under investigation. The state of the art data analysis was done by partly self-developed methods and programs which cover explorative factor analysis (FA)[1], Monte-Carlo modeling (MC) of EXAFS spectra[2] and Landweber iteration[3] for solving ill posed problems.

Results

While several of the results were already shown at conferences and in annual reports of our institute we present here as an interesting methodological example the $Fe_3(OH)_2ac_6^+$ complex[4] which might be present in the aqueous phase of the ternary sorption system. The spectrum of the complex was isolated from the spectral mixtures of the EXAFS pH- series by FA. The starting structure for the MC was taken from a crystal structure.

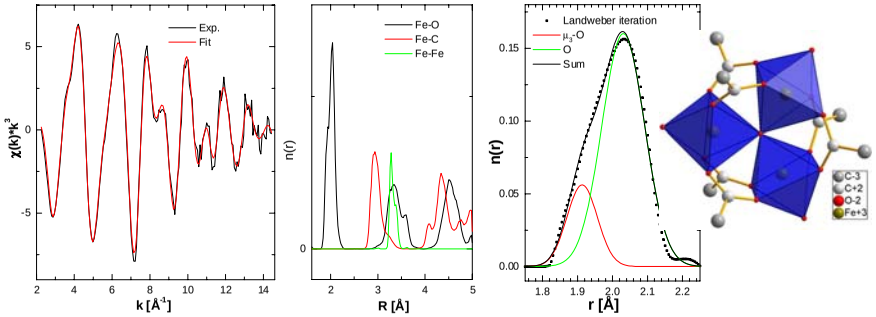

Fig. 1: Left – FA isolated EXAFS (black) with MC reproduction (red) and corresponding Fe-O, Fe-C, and Fe-Fe RPDF. Right – U-O RPDF of the first shell determined by Landweber iteration. Inset – structure of the $Fe_3(\mu_3\text{-}O)ac_6^+$ complex.

The FA extracted spectrum is shown in Fig. 1 together with the MC result. The MC calculated radial pair distribution function RPDF accounts for all spectral features in the EXAFS as can be seen by the good reproduction (Fig. 1). The Landweber iteration enables a more detailed analysis of the first O shell of this complex. The resulting Fe-O RPDF shows clearly the asymmetry at the left side which is expected due to the presence of a central μ_3-O atom. While this central O is up to now only reported for the solid structure, the developed methods enabled for the first time the investigation and the EXAFS spectroscopic proof of this special atomic arrangement for the aqueous medium. Due to this result the proposed stochiometry $(Fe_3(OH)_2ac_6^+)^4$ of this complex is $Fe_3(\mu_3\text{-}O)ac_6^+$.

REFERENCES

[1] E. R. Malinowski, *Factor Analysis in Chemistry*, 2 ed. (John Wiley & Sons, New York, 1991); A. Rossberg, T. Reich, and G. Bernhard, *Analytical and Bioanalytical Chemistry* **376** (5), 631 (2003).
[2] M. Winterer, *Journal of Applied Physics* **88** (10), 5635 (2000); A. Rossberg and A. C. Scheinost, *Analytical and Bioanalytical Chemistry* **383(1)**, 56 (2005).
[3] A. Rossberg and H. Funke, *Journal of Synchrotron Radiation* **17**, 280 (2010).
[4] L. Ciavatta, G. Nunziata, and L. G. Sillen, *Acta Chemica Scandinavica* **23** (5), 1637 (1969).

ROBL-CRG	**Experiment title:** Reduction of uranium(VI) by adsorbed Fe(II) on clays and by structural Fe(II) in smectites in O_2, CO_2 free atmosphere	**Experiment number**: 20-01-676
Beamline: BM 20	**Date of experiment**: from: 12.06.09 to: 14.06.09	**Date of report**: 15.2.11
Shifts: 6	**Local contact(s)**: Dipanjan Banerjee	*Received at ROBL:* 15.2. 11
Names and affiliations of applicants (* indicates experimentalists): Sudipta Chakraborty LGIT-OSUG, University of Grenoble-I, Grenoble, France		

Report:

Introduction

Uranium is an important element because of its presence in soils and sediments as a result of mining activities and for predicting the fate of spent fuel in nuclear waste repositories. The reduction of U(VI) to U(IV) greatly decreases uranium mobility through precipitation of sparingly soluble U(IV) minerals and therefore has been extensively studied using biotic and abiotic processes. Montmorillonite is a constituent clay mineral of various soils, sediments in reducing environments, and the major component of bentonite, which is a candidate material for the backfill of radioactive waste repositories. However, almost no studies have evaluated the reactivity of Fe(II) in heterogeneous sorption-reduction of U(VI) mediated by a montmorillonite surface. The aim of this study is to (1) investigate the influence of pH on the reduction capacity of surface-bound Fe(II) in U(VI) reduction and (2) identify reduced uranium product using wet chemistry, X-ray absorption spectroscopy (XAS), X-ray photoelectron spectroscopy (XPS), and transmission electron microscopy (TEM).

Experimental

X-ray absorption near-edge structure (XANES) and extended X-ray absorption finestructure (EXAFS) spectra were collected at the Rossendorf Beamline at the European Synchrotron Radiation Facility (ESRF, Grenoble, France). The energy of the X-ray beam was tuned by a doubled crystal monochromator operating in pseudo channel-cut mode using a Si(111) crystal pair. Two platinum-coated Si mirrors before and after the monochromator were used to collimate the beam into the monochromator and to reject higher harmonics. Uranium LIII-edge spectra were collected in fluorescence mode using a 13-element high purity germanium detector (Canberra) together with a digital signal processing unit (XIA). Spectra were collected at 15 K using a closed cycle He cryostat with a large fluorescence exit window and a low vibration level (CryoVac). The energy was calibrated using the maximum of the first derivative of the yttrium K-edge (17038 eV).

Results

The normalized XANES spectrum of the Fe-free reference sample (MONT + U(VI) at pH 5.9) in Figure 1A shows the characteristic features of the uranyl ($U^{VI}O_2^{2+}$) structure, including a white line peak centered at 17179 eV and a shoulder centered at approximately 17190 eV. The feature at 17190 eV has previously been shown to result from multiple scattering resonances of the linear uranyl ion structure, specifically due to the short U-O_{ax} bonds (1). The XANES spectrum of U1 at pH 6.1 is very similar to the U(VI) reference, implying that the dominating phase of uranium in these samples is in +VI oxidation state. With increasing pH, the shoulder at 17190 eV starts to diminish (U2 at pH 7.5) and disappears completely in U3 (pH 8.5). The latter spectrum is similar to the reference U(IV) (UO_2) spectrum but different from the spectrum of U_3O_8, suggesting a reduction of uranium from +VI to the +IV state. On the basis of visual observation, one can conclude that the reduction increases with pH. This observation is consistent with the XANES quantitative estimation obtained from linear combination fit (LCF) with U(VI) and U(IV) references. However, none of the spectra of partially reduced samples (U1-U3) are similar to that of the reference mixed valence spectra of U_3O_8(s).

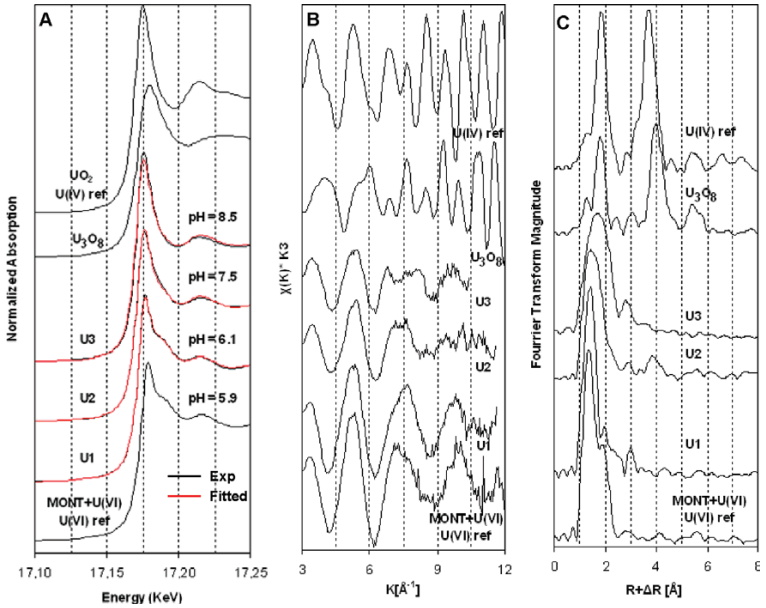

Fig 1. U L_{III}-edge XAS spectra of U(VI) sorbed on MONT in the presence of Fe(II) compared to the U(VI) and U(IV) references. (A) fitted XANES; (B) EXAFS, and (C) Fourier transform of EXAFS.

The corresponding U L_{III}-edge background-subtracted, k^3-weighted EXAFS spectra are shown in Figure 1B. A qualitative comparison of the Fourier-transformed EXAFS data of the samples with U(VI) and U(IV) references (Figure 1C) indicates that the average local chemical environments of uranium in U1-U3 are not similar to that of UO_2 or U_3O_8. Most notably, the strong FT peaks between 3.5 and 4.0 Å (uncorrected for phase shift), which are due to U-U interactions are completely absent in the samples, suggesting that the uranium phase formed after reduction is not a solid. Fitting of the EXAFS part of the spectra (results not presented) was only successful in obtaining U-O distances of 1.78, 2.26, and 2.47 Å. The distance of 1.78 Å is in line with the axial oxygen of U(VI). The other two distances are the equatorial shell of U(VI) and the first coordination sphere of U(IV). However, the possibility of a split equatorial shell of U(VI) due to inner sphere sorption cannot be ruled out (*2*). In addition, multiple scattering (MS) from the axial oxygens in the first shell overshadowed any weak backscattering signal from the clay surface (Si or Al).

Reference

Allen, P. G.; Shuh, D. K.; Bucher, J. J.; Edelstein, N. M.; Palmer, C. E. A.; Silva, R. J.; Nguyen, S. N.; Marquez, L. N.; Hudson, E. A. *Radiochim. Acta* **1996**, *75*, 47–53.

Catalano, J. G.; Brown, G. E. *Geochim. Cosmochim. Acta* **2005**, *69*, 2995–3005.

	Experiment title:	Experiment number:
	Develpoment of a 2nd generation spectro-electrochemical cell for in-situ electrolysis	20-01-681
Beamline: BM 20	**Date of experiment:** From 31/01/2010 to 01/02/2010 03/02/2010 to 06/02/2010 30/06/2010 to 02/072010 11/03/2009 to 12/03/2009 09/06/2009 to 12/06/2009 30/09/2009 to 02/10/2009	**Date of report:** 17.2.2011
Shifts: 18	**Local contact(s):** Christoph Hennig	*Received at ESRF:*

Names and affiliations of applicants (* indicates experimentalists):

Christoph Hennig*, Koichiro Takao*, Shinobu Tako*, Atsushi Ikeda-Ohno*

Helmholz-Zentrum Dresden-Rossendorf, Institute of Radiochemistry, Bautzner Landstrasse 400, 01314 Dresden Germany

Report:

To clarify the coordination of the limiting U(IV) carbonate complex, we investigated a crystal structure by X-ray diffraction, followed by a comparative investigation of the $[U(CO_3)_n]^{4-2n}$ complex in solid and solution state by U L_3–edge EXAFS spectroscopy [1]. EXAFS is an appropriate method to test if the solution species is preserved in a crystal structure [2] or undergoes a ligand rearrangement [3] during crystallization. Because most of the authors mentioned difficulties to prevent the reoxidation of U(IV), we applied a new electrolysis route to obtain a pure U(IV) carbonate solution.

EXPERIMENTAL. Single crystals were obtained from 0.05 M U(IV) solution in 1 M $NaHCO_3$ after several weeks without evaporation of the solution (sample **A**).The U(IV) solution sample was prepared by bulk electrolysis of 0.05 M U(VI) carbonate in the 1.0 M $NaHCO_3$ solution at a constant potential of –1.45 V, using a 4.9 cm^2 Hg pool electrode, a Pt wire counter electrode, and a Ag/AgCl reference electrode (sample **B**).

RESULTS. The solid compound $Na_6[U(CO_3)_5]\cdot 12H_2O$ crystallizes in the triclinic space group $P\bar{1}$ with two $[U(CO_3)_5]^{6-}$ anions in the unit cell. The U(IV) atom is coordinated by five carbonate ligands resulting in a coordination number of 10. The carbonate ligands coordinate exclusively in bidentate mode as shown in Fig. 1.

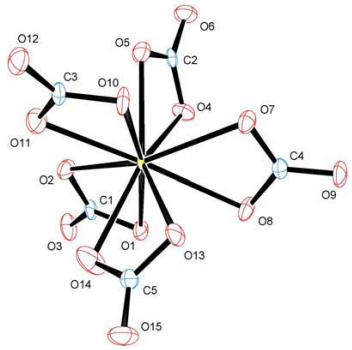

Fig. 1: $[U(CO_3)_5]^{6-}$·anionic complex obtained from single crystal diffraction.

Figure 2 compares the crystalline $Na_6[U(CO_3)_5]\cdot 12H_2O$ with the solution of 0.05 M U(IV) in 1 M $NaHCO_3$. The carbonate coordination shows a linear arrangement of uranium, the carbon atoms C and the distal oxygen O_{dist}. The bidentate-chelating coordination mode of the carbonate group is related with specific multiple scattering effects. The collinear arrangement of two ligand atoms C and O_{dist} with the absorbing atom results in strong multiple-scattering processes which usually increase the scattering power of a more distant atom like O_{dist} about several magnitudes.

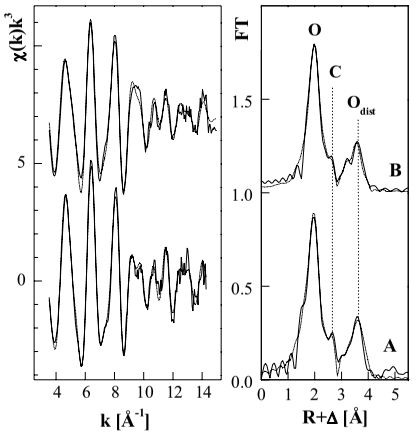

Fig. 2: U L_3-edge k^3-weighted EXAFS data and the Fourier transforms (FT) of $Na_6[U(CO_3)_5]\cdot 12H_2O$ (**A**) and the solution of 0.05 M U(IV) in 1 M $NaHCO_3$ (**B**). Experimental data – solid line, fit results – dotted line.

The data fit of the solution sample reveal within the typical error limits 5 bidentate coordinated carbonate ligands with distances similar to the ones observed in the solid state. This result corroborate the existence of the $[U(CO_3)_5]^{6-}$ anionic species in solution with the same coordination mode as the solid U(IV) carbonate complex.

REFERENCES

[1] C. Hennig et al. *Dalton Transactions* (2010) **39** 3774.
[2] C. Hennig et al. *Inorg. Chem.* (2008) **47**, 1634.
[3] C. Hennig et al. *Inorg. Chem.* (2008) **47**, 2987.

ROBL-CRG	**Experiment title:** Structure determination of U(VI)-opalinus clay surface complexes in absence and presence of humic acid by EXAFS	**Experiment number:** 20-01-683
Beamline: BM 20	**Date of experiment:** from: 06.04.2009 to: 10.04.2009	**Date of report:** 15.01.2010
Shifts: 8	**Local contact(s):** Dr. André Rossberg	*Received at ROBL:*

Names and affiliations of applicants (* indicates experimentalists):
C. Joseph*[1], A. Rossberg*[2], D. Banerjee*[2], A. Scheinost*[2]
[1]Forschungszentrum Dresden-Rossendorf e. V., Institute of Radiochemistry, P.O. Box 51 01 19, 01314 Dresden / Germany
[2]ESRF-ROBL/CRG, Avenue des Matryrs, B.P. 220, 38043 Grenoble Cedex / France

Report:

The U(VI) sorption ($[U]_0 = 1x10^{-4}$ M) onto opalinus clay (OPA), a natural clay from Mont Terri, Switzerland, was studied in the absence and presence of humic acid (HA) ($[HA]_0 = 10$ mg/L). OPA has a very complex composition. Beside clay minerals, also calcite, quartz and pyrite are contained. Because of its heterogeneity it is not known which mineral acts as main adsorbent. Thus, U(VI) surface species onto OPA were studied using EXAFS spectroscopy. During the experiments the influence of pH value, CO_2 presence, HA presence and background electrolyte (0.1 M $NaClO_4$, pH 3.2, 6.8, 7.4, 8.4; OPA pore water, pH 7.6, I = 0.39 M [1]) on the U(VI) sorption were investigated. The samples were measured as wet pastes. The U L_{III}-edge EXAFS spectra ($E_0 = 17185$ eV) were measured in fluorescence mode at room temperature. The EXAFS spectra were analyzed using the suite of programs EXAFSPAK [2]. The theoretical scattering phases and amplitudes were calculated using the scattering code FEFF8.2 [3].

At pH 3.2-6.8 and at 7.4-8.4 two types of EXAFS spectra were measured. For pH 3.2, beside two axial oxygen atoms, O_{ax}, of the uranyl unit (R = 1.764 ± 0.004 Å) and five equatorial oxygen atoms, O_{eq}, (R = 2.31 ± 0.01 Å) also a Si/Al shell (R = 2.751 ± 0.009 Å) was fitted. These results point out the U(VI) sorption onto the clay fraction of OPA. But in comparison with literature data for kaolinite [4] the U-Si/Al distance is very short. The U(VI) complexation with HA could also be excluded, because of the too short U-O_{eq} distance compared with values published for uranyl humate complexes [5]. Speciation calculations showed, that independent of CO_2 and HA presence and background electrolyte, always $Ca_2UO_2(CO_3)_3(aq)$ is the dominating species in solution between pH 7 and 9 due to dissolution of the calcite fraction of the clay. Therefore, for pH values 7.4-8.4 the structural data of swartzite were used to fit the spectra. The obtained EXAFS spectra are still under investigation. However, due to their similarity it can be assumed, that there is no significant influence of background electrolyte, CO_2 and HA presence on the formed U(VI) surface complexes.

[1] Pearson, F.J. (1998) Opalinus Clay experimental water: A1 type, Version 980318, *PSI Internal Report TM-44-98-07*, Paul Scherrer Institut, Villigen PSI, Switzerland.

[2] George, G.N., Pickering, I.J. (1995) EXAFSPAK: A Suite of Computer Programs for Analysis of X-Ray Absorption Spectra. Stanford Synchrotron Radiation Laboratory, Stanford, CA. USA.

[3] Ankudinov, A.L., Ravel, B., Rehr, J.J., Conradson, S.D. (1998) Real-space multiple-scattering calculation and interpretation of x-ray absorption near-edge structure, *Physical Review B 58*, 7565.

[4] Křepelová, A., Reich, T., Sachs, S., Drebert, J., Bernhard, G. (2008) Structural characterization of U(VI) surface complexes on kaolinite in the presence of humic acid using EXAFS spectroscopy, *Journal of Colloid and Interface Science 319*, 40.

[5] Schmeide, K., Sachs, S., Bubner, M., Reich, T., Heise, K.H., Bernhard, G. (2003) Interaction of uranium(VI) with various modified and unmodified natural and synthetic humic substances studied by EXAFS and FTIR spectroscopy, *Inorganica Chimica Acta 351*, 133.

ROBL-CRG	**Experiment title: Binding forms of actinides (U(VI)) and lanthanides (Eu(III)) with single constituents of biofluids (saliva, urine)**	**Experiment number**: 20-01-685
Beamline: BM 20	**Date of experiment**: from: 11/02/09 to: 14/02/09	**Date of report**: 13/08/09
Shifts: 9	**Local contact(s)**: C. Hennig	*Received at ROBL:*
Names and affiliations of applicants (* indicates experimentalists): A. Barkleit*, A. Heller, C. Hennig*, D. Banerjee*, A. Rossberg, A. Scheinost, G. Bernhard		

Report: Synchrotron-based EXAFS is a powerful technique to obtain structural information on radionuclide bioligand species. Within this proposal we explore structural parameter of U(VI) and Eu(III) species with the protein α-amylase (Amy). This enzyme is to be found in biofluids like saliva and pancreatic fluid and is responsible for starch degradation.

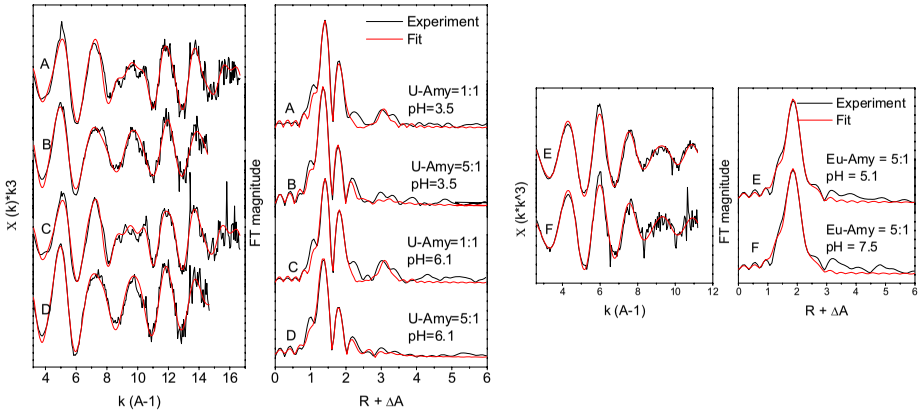

Fig. 1. U L_{III} edge (left) and Eu L_{III} (right) k^3-weighted EXAFS spectra and the corresponding Fourier transforms and the theoretical fits (red lines).

Experimental. U L_{III} and Eu L_{III} edge EXAFS measurements were carried out with wet pastes of α-amylase after contact with concentrated UO_2^{2+} or Eu^{3+} solutions, adjusted to a fixed pH (see Table 1). These samples were measured at 15 K (U(VI)) and room temperature (Eu(III)) either in transmission or in fluorescence mode.

Results. A selection of the measured EXAFS oscillations and corresponding Fourier transforms are presented in Fig. 1. The extracted structural parameters are summarized in Table 1.

Table 1. Summary of the determined structural parameters.

Sample	Shell	N	R [Å]	σ^2 [Å^2]	ΔE_0 (eV)
A:	U=O	2*	1.79	0.00124	5.4
1.8 µmol UO_2^{2+},	U-O_{eq}	3.1(2)	2.28(1)	0.00276	
100 mg Amy, pH = 3.6	U-C	/3.1	3.47(1)	0.00153	
B:	U=O	2*	1.78	0.00164	4.8
9.0 µmol UO_2^{2+},	U-O_{eq1}	2.8(8)	2.30(2)	0.004078	
100 mg Amy, pH = 3.6	U-O_{eq2}	1.9(4)	2.48(2)	0.004148	
	U-C	/1.0	2.84(2)	0.002f	
C:	U=O	2*	1.79	0.0015	5.1
1.8 µmol UO_2^{2+},	U-O_{eq}	3.4(3)	2.28(1)	0.00244	
100 mg Amy, pH = 6.1	U-C	/3.4	3.48(1)	0.00202	
D:	U=O	2*	1.79	0.00208	5.2
9.0 µmol UO_2^{2+},	U-O_{eq1}	3.1(6)	2.33(1)	0.005056	
100 mg Amy, pH = 6.1	U-O_{eq2}	1.1(6)	2.52(2)	0.001257	
	U-C	/0.6	2.93(2)	0.00603	
E:	Eu-O	10.3(4)	2.41(1)	0.00984	-11.5
13 µmol Eu^{3+},	Eu-C1	2.7(6)	2.96(1)	0.00177	
500 mg Amy, pH = 5.1	Eu-C2	4*	3.42(1)	0.00945	
F:	Eu-O	10.8(7)	2.39(1)	0.0103	-13.2
13 µmol Eu^{3+},	Eu-C1	4.8(1,6)	2.95(1)	0.00614	
500 mg Amy, pH = 7.5	Eu-C2	2*	3.41(3)	0.0049	

** fixed parameter, / linked parameter.*

The uranyl amylase samples with similar composition and only different pH are very similar among each other. The coordination sphere in the uranyl equatorial plane seems to be independent from the pH but only dependent from the uranyl to protein ratio. The short U-Oeq distances, connected with a quite small coordination number for the samples with lower uranyl concentration (A and C) can be interpreted as a four-fold coordination with carbonyl groups. The splitted equatorial shell for the samples with higher uranyl concentration (B and D) can be interpreted as a mixed coordination with monodentate carbonyl groups (shorter U-O_{eq1} distances) and bidentate carboxyl groups (longer U-O_{eq2} distances).

The EXAFS spectra of Eu(III) amylase samples are also quite similar among each other at different pH. It seems to be a mixed coordination with carbonyl and carboxyl groups and some remaining water molecules.

Acknowledgement. This work is supported by the DFG (no. BE 2234/10-1).

	Experiment title: EXAFS investigation of austenitic alloys nitrided at low temperature	**Experiment number:** 20-01-686
Beamline: BM20	**Date of experiment:** from: 02/09/2009 to:4/09/2009	**Date of report:** 18/05/2010
Shifts: 6	**Local contact(s):** Andreas Scheinost	*Received at ESRF:*

Names and affiliations of applicants (* indicates experimentalists):

Gintautas Abrasonis* and Andrius Martinavičius*

Institute of Ion Beam Physics and Materials Research, P .O. Box 510119, Forschungszentrum Dresden-Rossendorf, 01314 Dresden, Germany

Report:

Chemical environment of the principal constituents (Fe, Ni, Cr) of the austenitic stainless steel (ASS) AISI 316L in the S phase has been investigated by means of x-ray absorption near edge structure (XANES) and extended x-ray absorption fine structure (EXAFS). The S phase has been produced by plasma nitriding at 400°C for 30h. This results in the nitrided layer thickness of ~20 µm and nitrogen near-surface atomic ratio of ~27 at.%. In order to get some insights into the chemical environment of Fe, Ni, Cr, the XANES and EXAFS spectra of virgin ASS and ASS plasma nitrided at 550°C for 30h have been recorded. The former serves as a reference for Fe, Ni, Cr in fcc metallic state. Nitriding at 550°C induces the precipitation of CrN which serves as a reference for Cr in CrN state.

Figure 1 summarizes the XANES and EXAFS data on chromium. The XANES and k^3 weighted Fourier transform of the EXAFS spectrum (FT|$\chi(k)k^3$|) of the virgin ASS sample are characteristic for the *fcc* structure. There are four strong amplitude peaks in FT|$\chi(k)k^3$| between 1.5 and 6 Å whose distance R are ~2.2, 3.2, 4.2 and 5 Å, respectively. The peaks correspond to metallic neighbors in different coordination shells. The shape of the K-edges for all elements is similar (not shown) which suggests that the chemical environments and geometry are the same for Ni, Fe and Cr. Cr XANES of the ASS nitrided at 550°C has a well-defined edge feature (~5 eV), main peak (~18.8 eV), and a second peak (~32 eV) which almost identical to CrN XANES reported in the literature. The edge is shifted by 0.44 eV as compared to non-nitrided sample indicating that Cr is in the oxidation state similar to Cr^{3+}. This corresponds to the formation of the CrN. FT|$\chi(k)k^3$| shows additional coordination shell closer than any Me-Me which corresponds to N atoms. For the sample nitrided at 400°C, the Cr XANES is very similar to that of the sample nitrided at 550°C. Also the edge shift is close to that of the CrN reference sample. The peaks above the absorption edge are less intense while their positions are slightly shifted to the higher energies. The latter is attributed to slightly smaller lattice parameter, while the smoother shape can be attributed to a lower order of crystallinity. FT|$\chi(k)k^3$| shows very similar coordination shell structure as that of CrN. The results point out that the Cr in the S phase is in the state similar to that of CrN. Similar analysis of other elements (not shown here) shows that Fe in the S phase is in the environment close to Fe_4N while Ni is in metallic disordered environment.

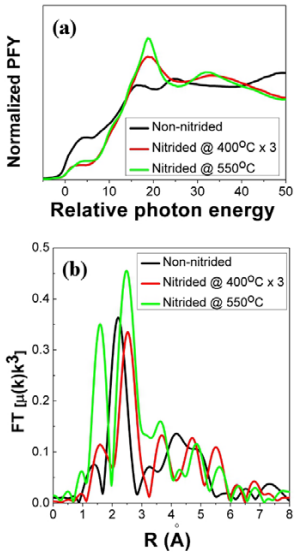

Figure 1. Chemical environment of Cr in metallic (non-nitrided), CrN (nitrided at 550°C) and S phase (nitrided at 400°C) states: XANES partial fluorescence yield (PFY) (a) and Fourier Transform (FT) of EXAFS oscillations (b).

The results above strongly indicate that the interstitial nitrogen incorporation into ASS at 400°C results in the local decomposition of otherwise homogeneous solid solution of Fe-Ni-Cr, each principal element showing different local environment. This points out that the diffusion of the matrix atoms takes place even at the temperatures as low as 400°C. The fact that no different phases are observed by x-ray diffraction points out that such zones must be small and coherent with the matrix. Such composite structure explains the mechanical properties as well as ferromagnetism of the S phase reported in the literature. These findings show that reactive interstitial diffusion can be used to induce the local decomposition which shows a unique set of properties. These results make a part of the PhD thesis of A. Martinavičius (under preparation at the moment). The preparation of a publication is planned in the nearest future.

	Experiment title: Neptunyl adsorption to calcite	Experiment number: 20-01-687
Beamline: RoBL	**Date of experiment:** from: 05.02.2009 to: 06.02.2009	**Date of report:** 13.10.2009
Shifts: 2	**Local contact(s):** Andreas C. Scheinost	*Received at ESRF:*

Names and affiliations of applicants (* indicates experimentalists):

*Frank Heberling
Institut für Nukleare Entsorgung
Karlsruher Institut für Technologie (Forschungszentrum Karlsruhe)
Hermann von Helmholtz Platz 1
76344 Eggenstein Leopoldshafen

Report:

Neptunyl, $Np(V)O_2^+$, along with the other actinyl ions $U(VI)O_2^{2+}$ and $Pu(V,VI)O_2^{(+,2+)}$, is considered to be highly mobile in the geosphere, but may be retained by interactions with mineral surfaces (inner- or outer-sphere adsorption, ion-exchange, coprecipitation/structural incorporation). Detailed information about the exact mechanisms including the structure and stoichiometry of the adsorption complexes is crucial to predict the retention behavior in diverse geochemical environments. Here, we investigated the structure of the neptunyl adsorption complex at the calcite-water interface at pH 8.2 in equilibrium with air by means of low temperature (15 K) EXAFS spectroscopy at the Np-L3 edge. The coordination environment of neptunyl consists of two axial oxygen atoms at 1.87(±0.01)Å, and an equatorial oxygen shell of six atoms at 2.51(±0.01) Å. Two carbon backscatterers at 2.94(±0.02) Å indicate that there are two bidentate carbonate ions in the coordination sphere, while two oxygen backscatterers at 3.50(±0.04) Å can be related to two monodentately bound carbonate groups. This structural environment, together with two calcium backscatterers at 3.95(±0.03) Å, is conclusively interpreted as neptunyl adsorbing at the calcite (104) face as an bidentate inner-sphere biscarbonato complex. Formation of this sorption complex at the calcite surface constitutes an important retention mechanism for neptunyl. No spectroscopic evidence for slow sequestration reactions like structural incorporation by subsequent dissolution and reprecipitation and was found within the 3 month reaction period.

Adsorption samples were prepared as described before [1]. As calcite we used Merck calcium carbonate suprapur with a BET surface of 1.3 m^2/g. Suspensions were in equilibrium with calcite and air. The initial neptunyl concentration was 40 µM, solution pH was 8.2. Two samples (Np-O1 and Np-O2) were allowed to react for three month, and two samples (Np-Y1 and Np-Y2) for 48 hours. After the reaction time suspensions were allowed to sediment and the supernatant was removed. The reacted calcite powder was filled as a wet paste into the SH01B-cryoholder, designed by the ROBL staff for low temperature EXAFS measurements of low activity radioactive samples. After sealing the sample holders the samples were frozen in liquid nitrogen in order to stop the reaction. During the transport to the ESRF in Grenoble samples were cooled in dry ice. EXAFS measurements at the Np L3-edge (17610 eV) were performed at the Rossendorf beamline (ROBL) at the ESRF in fluorescence mode at low temperature (15 K) in a Helium cryostat in a glovebox. Parallel measurement of a zirkonium foil (Zr K-edge: 17998 eV) in transmission mode enabled energy calibration of the spectra. We measured 15 spectra of sample Np-O2 and 16 spectra of sample Np-Y1. As we found no significant difference between the young (Np-Y1) and the old sample (Np-O2) we decided to analyze the structure from the spectrum with the better signal to noise ratio, which was the one measured from the old sample, Np-O2. The extracted EXAFS signal was used in a k-range from 2.0 $Å^{-1}$ to 10.2 $Å^{-1}$. Using a larger k-range caused the noise in the spectrum to contribut significantly to the R-space spectrum. Hanning windows are used in the Fourier Transformations. The axial oxygen path was used to correct for phase shift. R-range was 1.0 Å to 5.0 Å, fitting was performed in R-space, and k-weights for fitting were 1, 2, and 3. Bond-valence calculations are used to check the plausibility of the of the obtained coordination environment of the central neptunium atom.

Results and Discussion

The goal of measuring EXAFS spectra of samples after different reaction times (48 h and three months) was to see if we can find spectroscopic evidence for recrystallization processes that lead to neptunyl incorporation into the calcite surface layers under calcite equilibrium conditions over extended reaction times. Indication for such processes was found in experiments on adsorption kinetics and in desorption experiments. However, no significant difference in the EXAFS spectra of samples Np-Y1 and Np-O2 could be observed.

Due to the better quality of the spectrum from sample Np-O2 we decided to use this spectrum for detailed analyses of the adsorption complex structure. The k^3-weighted extracted EXAFS signal together with the model spectrum of sample Np-O2 is shown in Figure 1. Figure 2 displays magnitude and imaginary part of the corresponding Fourier transform spectra in R-space. A structural model giving a good fit between measured and modelled spectrum and saturating the bond-valence of the neptunium atom could be achieved using 5 different electron backscattering paths. Structural parameters obtained from the EXAFS data analyses are listed in table 1.

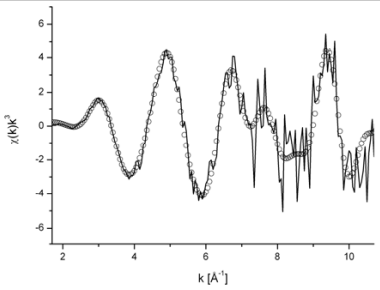

Figure 1: k^3-weighted extracted EXAFS data (line) and model spectrum (circles) of sample Np-O2.

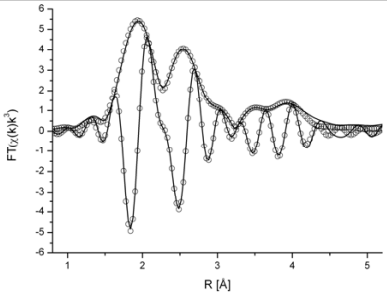

Figure 2: Fourier transform amplitude and imaginary part of the k^3-weighted EXAFS data (line) and model spectrum (circles). Spectra are corrected for phase shift.

Table 1: Coordination numbers, N, distances, R (Å), and Debye-Waller factors, σ^2 (Å^2), resulting from EXAFS data analyses.

Backscatterer	N	R (Å)	σ^2 (Å^2)
O (O-ax)	2.0(±0.1)	1.87(±0.01)	0.001(±0.001)
O (O-eq)	6.1(±0.5)	2.51(±0.01)	0.009(±0.003)
C (C-bi)	2.7(±1.2)	2.94(±0.02)	0.001(±0.003)
O (O-surf)	2.0(±0.8)	3.50(±0.04)	0.001(±0.006)
Ca	1.8(±1.0)	3.95(±0.03)	0.003(±0.004)

Uncertainties, in brackets, are twice the standard deviation calculated by the Artemis software. The amplitude reduction factor was fixed at $S_0^2 = 0.8$, relative shift in ionization energy $\Delta E_0 = 8(1)$ eV, and the goodness of fit parameter for all three k-weights together, r = 0.007. Number of independent points, NI = 20, 16 parameters were used to fit the data.

It is however not trivial to find a structural explanation for the measured model parameters. The 2.0(±0.1) oxygen backscatterers at 1.87(±0.01) Å can surely be related to the axial oxygen atoms (O-ax) of the linear neptunyl molecule. 6.1(±0.5) oxygen backscatterers at 2.51(±0.01) Å are addressed to the equatorial oxygen shell (O-eq). This coordination environment is in good agreement with bond-valence calculations. Using bond-valence parameters R0 = 2.035 and b = 0.422, the bond valence sum (BV) for the central neptunium atom is: BV = 4.94.

The sorption site that results in the best agreement with measured bond distances and the coordination numbers can be found at step edges on the calcite (104) face. This leads us to the conclusion that the most probable sorption site for neptunyl at the calcite (104) face is at step edges, where neptunyl forms a bidentate inner sphere sorption complex with two monodentate coordinating carbonate groups from the calcite surface. On the solution side of the neptunyl ion two bidentate bound carbonate ions can be found. A ball-and-stick representation of this most likely sorption complex is shown in Figure 3.

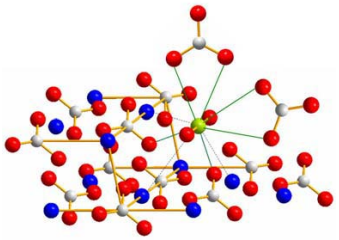

Figure 3: Structure of the most likely neptunyl-calcite adsorption complex according to the results of the EXAFS data analyses, bond-valence calculations, and geometrical considerations: neptunyl sorbs at step edges on the calcite (104) face as a bidentate inner-sphere bicarbonato complex. Indicated with green lines are the bonds to the six equatorial oxygen atoms. Dashed lines indicate the nearest calcium neighbours. (Np – green, Ca –blue, O – red, C – grey)

References

1. Heberling, F., Brendebach, B., Bosbach, D., Neptunium(V) adsorption to calcite, *J. Contam. Hydrol.* 102, pp. 246-252, **2008**

ROBL-CRG	**Experiment title:** Molecular scale studies on the speciation of U(VI) bound to cells and S-layer proteins of Archaea.	**Experiment number**: 20-01-688
Beamline: BM 20	**Date of experiment**: from: 06.02.2009 to: 09.02.2009	**Date of report**: 30.09.2009
Shifts: 9	**Local contact(s)**: Dr. A. Rossberg	*Received at ROBL:*

Names and affiliations of applicants (* indicates experimentalists):
T. Reitz*[1], M.L. Merroun[2], A. Rossberg[1], S. Selenska-Pobell[1]
[1] Institute of Radiochemistry, FZD e.V., P.O. Box 510119, 01324 Dresden, Germany
[2] Departamento de Microbiología, Universidad de Granada, Avenida Fuentenueva s/n, 18071, Granada, Spain
Tel.: +34 958 242858

Report:

INTRODUCTION. Microorganisms are known to play an important role in the migration behavior of uranium in the environment [1]. In contrast to the well studied interactions of bacteria with uranium, little is known about the processes implicated in the complexation of this radionuclide by representatives of the second microbial domain of life, the "*Archaea*".

EXPERIMENTAL. *S. acidocaldarius* was cultivated at pH 2.5 and 70 °C in a mineral salt medium [2] supplemented with 0.1% tryptone and 0.005% yeast extract. Cells grown to the late exponential phase were harvested by centrifugation and washed twice with 0.1M $NaClO_4$. Four parallel cell suspensions were prepared with pH 1.5, 3, 4.5 and 6. They were shaken at room temperature in 10 ml uranium solution (0.5 mM $UO_2(NO_3)_2 \cdot 6\ H_2O$, pH 1.5, 3, 4.5 or 0.05 mM $UO_2(NO_3)_2 \cdot 6\ H_2O$ at pH 6). The sample preparation and the set-up of the X-ray absorption spectroscopic measurements were performed as described earlier [3].

RESULTS. Quantitative fit results of the EXAFS data indicated that at all acidic conditions studied the adsorbed U(VI) has the common linear trans-dioxo structure: two axial oxygen atoms at about 1.77-1.78 Å, and an equatorial shell of 4 to 6 oxygen atoms at 2.25-2.35 Å. The U-O_{eq1} bond distance is within the range of previously reported values for phosphate bound to uranyl [4,5]. The FT spectra of the U-treated microbial samples contain a FT peak at about R+Δ ~ 2.3 Å, interpreted as a contribution from oxygen neighbors (O_{eq2}). The fourth FT peak, which appears at R+Δ ~ 3 Å (radial distance R = 3.57-3.62 Å) is a result of the back-scattering from phosphorus atoms. This distance is typical for a monodentate coordination of U(VI) by phosphate [4,5]. The phosphate groups implicated in the coordination of U could have organic origin since the EXAFS spectrum shows high similarity to those resulting from the uranium complexes with organic phosphate groups, e.g. fructose phosphates as shown in Figure 1. At pH 4.5 a high Debye-Waller factor of the U-O_{eq1} shell was calculated. That suggests the existence of more than one oxygen atoms bond in the equatorial plane. The shell may be split into a shorter U-O_{eq1} distance, from the back-scattering contribution of phosphate oxygen(s) in a monodentate binding mode, and a longer bond distance most likely from oxygen(s) of carboxyl groups in a bidentate binding mode.

The U(VI) EXAFS spectrum of the cells treated at pH 6 differs significantly from that obtained after the U treatment at pH 4.5. This spectrum has a high similarity with those arising from inorganic uranyl phosphate mineral phases, like meta-autunite [4]. The structural parameters of these uranium complexes are also in favour of that finding, e.g. the coordination number of the U-P shell is nearly four and the radial distance of the U-O_{eq1} shell is about (2.25 ± 0.02) Å.

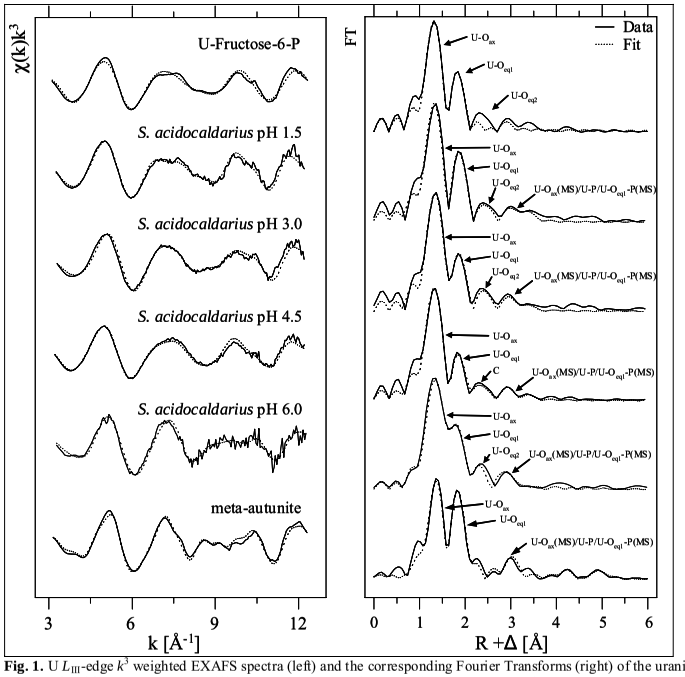

Fig. 1. U L_{III}-edge k^3 weighted EXAFS spectra (left) and the corresponding Fourier Transforms (right) of the uranium complexes formed by *S. acidocaldarius* DSM 639 at different pH values and of the model compounds UO_2-fructose(6)phosphate [6] and meta-autunite [4].

Table 1. Structural parameters of the uranium complexes formed by the cells of *S. acidocaldarius* DSM 639.

Sample	Shell	N[a]	R [Å][b]	σ^2 [Å^2] [c]	ΔE (eV)
UO_2-fructose(6)P[6]	U-O_{ax}	2.0[d]	1.78	0.0015	0.1
	U-O_{eq1}	4.8(5)	2.30	0.0200	
	U-O_{eq2}	1.3(2)	2.88	0.0040[d]	
pH 1.5	U-O_{ax}	2.0[d]	1.77(1)	0.0022(2)	-12.0
	U-O_{eq1}	3.9(3)	2.35(1)	0.0066(7)	
	U-O_{eq2}	1.2(2)	2.87(1)	0.0038[d]	
	U-P	4.6(5)	3.62(1)	0.0080[d]	
	U-O_{eq1}-P (MS)	9.2[e]	3.74[f]	0.0080[d]	
pH 3.0	U-O_{ax}	2.0[d]	1.78(1)	0.0023(2)	-13.4
	U-O_{eq1}	4.1(4)	2.30(1)	0.0047(5)	
	U-O_{eq2}	1.2(2)	2.86(1)	0.0038[d]	
	U-P	3.3(6)	3.59(2)	0.0080[d]	
	U-O_{eq1}-P (MS)	6.6[e]	3.70[f]	0.0080[d]	
pH 4.5	U-O_{ax}	2.0[d]	1.78(1)	0.0025(2)	-11.3(4)
	U-O_{eq1}	6.2(8)	2.33(1)	0.017(2)	
	U-C	1.4(3)	2.90(1)	0.0038[d]	
	U-P	2.2(5)	3.61(2)	0.0080[d]	
	U-O_{eq1}-P (MS)	4.4[e]	3.72[f]	0.0080[d]	
pH 6	U-O_{ax}	2.0[d]	1.77(1)	0.0031(2)	-16.4(9)
	U-O_{eq1}	4.7(5)	2.25(1)	0.0058(7)	
	U-O_{eq2}	1.2(3)	2.85(1)	0.0038[d]	
	U-P	4.9(7)	3.57(2)	0.0080[d]	
	U-O_{eq1}-P (MS)	9.8[e]	3.67[f]	0.0080[d]	
meta-autunite[4]	U-O_{ax}	2.2(1)	1.76	0.0045	-11.0
	U-O_{eq1}	3.9(2)	2.29	0.0026	
	U-P	2.3(3)	3.60	0.008[d]	

Standard deviations as estimated by EXAFSPAK are given in brackets
[a] Errors in coordination numbers are ± 25%
[b] Errors in distance are ± 0.02 Å
[c] Debye-Waller factor
[d] Parameter fixed for calculation
[e] Coordination number (N) linked twice to the N of the U-P path.
[f] Radial distance (R) linked to R of the U-P path, according to the model of m-autunite.

In summary, EXAFS analysis of the uranium complexes formed by the cells of *Sulfolous acidocaldarius* demonstrated that oranic and inorganic phosphate groups as well as carboxylic groups are involved in the uranium complexation at acidic conditions.

REFERENCES

[1] Pedersen *et al.* (2005) J. Nucl. Radiochem. Sci. 6, 11-15.
[2] Brock *et al.* (1972) Arch. Microbiol. 84, 54-68.
[3] Reitz *et al.* (2008) Uranium, Mining and Hydrogeology, p. 703-710, Springer-Verlag, Berlin.
[4] Hennig *et al.* (2001) Radiochim. Acta 89, 625-631.
[5] Merroun *et al.* (2003) Radiochim. Acta 91, 583-591.
[6] Koban *et al.* (2004) Radiochim. Acta 92, 903-908.

ROBL-CRG	**Experiment title:** Molecular scale studies on the speciation of U(VI) bound to cells and S-layer proteins of Archaea.	**Experiment number**: 20-01-688
Beamline: BM 20	**Date of experiment**: from: 06.11.2009 to: 09.11.2009	**Date of report**: 07.06.2010
Shifts: 9	**Local contact(s)**: Dr. A. Rossberg	*Received at ROBL:*

Names and affiliations of applicants (* indicates experimentalists):

T. Reitz*[1], M.L. Merroun[2], A. Rossberg[1], S. Selenska-Pobell[1]

[1] Institute of Radiochemistry, FZD e.V. P.O. Box 51 01 19, 01324 Dresden, Germany

[2] Departamento de Microbiología, Universidad de Granada, Avenida Fuentenueva s/n, 18071, Granada, Spain

Report:

INTRODUCTION. Highly ordered and self-assembling proteinaceous surface layers (S-layers) are widespread structures of procaryotic cell envelopes [1, 2]. In many archaea, as in the case of the acidophilic creanarchaeon *Sulfolobus acidocaldarius*, studied in this work, they represent the only cell wall component. Up to date nothing is known about the possible role of archaeal S-layers for the protection of the cells against toxic metals and radionuclides. In this study the interactions of the S-layer of *S. acidocaldarius* with U(VI) was investigated to differentiate its role in the complexation of this radionuclide.

EXPERIMENTAL. *S. acidocaldarius* was cultivated at pH 2.5 and 70 °C in a mineral salt medium [3] supplemented with 0.1% tryptone and 0.005% yeast extract. Cells were harvested at the end of the logarithmic growth phase and cell lysis was performed with 0.15% SDS according to Michel *et al.* (1980) [4]. For the complete removal of the cytoplasmic membrane the suspension was treated with 2% SDS and stirred overnight. After centrifugation, the lower dark part of the resulting pellet was discarded, whereas the upper white part was resuspended in HEPES buffer (pH 7) containing 2 mM EDTA and 2% SDS and incubated once again for 30 min at 60 °C. Subsequently the suspension was centrifuged again and the upper part of the resulting pellet, containing the isolated S-layer polymers, was resuspended in distilled water. SDS was removed by five wash steps with distilled water. Uranium was added to the S-layer polymers in form of uranyl nitrate (0.5 mM and 0.05mM $UO_2(NO_3)_2 \cdot 6\ H_2O$ at pH 4.5 and pH 6, respectively) and shaken at room temperature for 48 h. The sample preparation and the set-up of the X-ray absorption spectroscopic measurements were performed analogously to the XAS studies conducted with whole cells of the strain [5, 6].

RESULTS. As shown in Figure 1 the absorption edge in the XANES spectra of both samples is located at ~17166 eV and therewith corresponds well to the edge position of the U(VI) reference solution. In addition, a peak located at 17188 eV, arising from the multiple scattering contribution of the two axial oxygen atoms of U(VI) [7], was observed in the NEXAFS region of both spectra. These findings clearly demonstrate that uranium is present in both samples as U(VI).

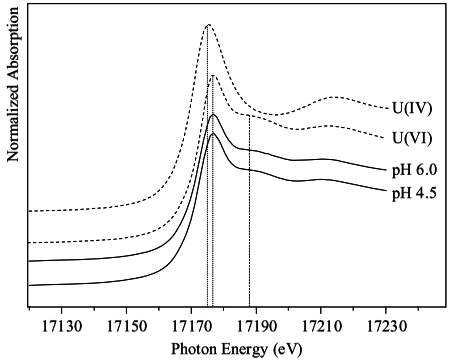

Fig. 1. Uranium L_{III}-edge XANES spectra recorded from the uranium complexes formed at the S-layer protein of *S. acidocaldarius* DSM 639 at pH 4.5 and pH 6 together with those of two reference solutions, one of U(VI) and another one of U(IV). For comparison, the position of the white line of U(IV) and U(VI). Moreover, the position of the XANES peak, which represents the multiple scattering path of the axial oxygen atoms of U(VI) (~17188 eV), is marked by a dashed line.

The isolated U L_{III}-edge k^3-weighted EXAFS spectra and their corresponding Fourier Transforms (FT) are shown in Figure 2. Quantitative fitting of the spectra was performed by using the theoretical phase and amplitude functions calculated with the FEFF8.2 code from a structural model of uranyl triacetate. The best calculated fits for both samples are also shown in Figure 2 and the corresponding structural parameters are summarized in Table 1.

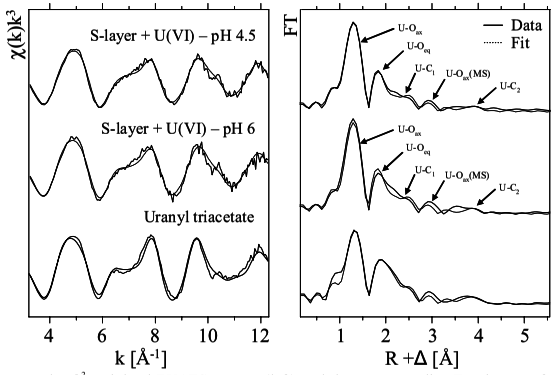

Fig. 2. Uranium L_{III}-edge k^3 weighted EXAFS spectra (left) and the corresponding Fourier transforms (right), along with the best shell fit, of the uranium complexes formed by *S. acidocaldarius* DSM 639 at pH 4.5 and pH 6 and that of the model compound uranyl triacetate.

Table 6. Structural parameters of the uranium complexes formed at the S-layer proteins of *S. acidocaldarius* at pH 4.5 and 6, as well as those of the model compound uranyl triacetate.

Sample	Shell	N[a]	R (Å)[b]	σ^2 (Å^2)[c]	ΔE_0 (eV)
pH 4.5	U-O_{ax}	2.0[d]	1.77(1)	0.0026(1)	2.8(4)
	U-O_{ax} (MS)	2.0[d]	3.54[e]	0.0052[e]	
	U-O_{eq}	4.3(4)	2.42(1)	0.013(1)	
	U-C_1	2.5(2)	2.90(1)	0.0038[d]	
	U-C_2	2.5[f]	4.35(1)	0.0038[d]	
	U-C_1-C_2 (MS)	5.0[f]	4.35[g]	0.009(1)	
	U-C_1-C_2-C_1 (MS)	2.5[f]	4.35[g]	0.009[h]	
pH 6	U-O_{ax}	2.0[d]	1.77(1)	0.0024(1)	2.3(5)
	U-O_{ax} (MS)	2.0[d]	3.54[e]	0.0048[e]	
	U-O_{eq}	5.0(5)	2.43(1)	0.013(1)	
	U-C_1	3.0(3)	2.89(1)	0.0038[d]	
	U-C_2	3.0[f]	4.37(3)	0.0038[d]	
	U-C_1-C_2 (MS)	6.0[f]	4.37[g]	0.012(3)	
	U-C_1-C_2-C_1 (MS)	3.0[f]	4.37[g]	0.012[h]	
Uranyl triacetate	U-O_{ax}	2.0[d]	1.78(1)	0.0023(1)	4.7(4)
	U-O_{ax} (MS)	2.0[d]	3.56[e]	0.0046[e]	
	U-O_{eq}	4.8(3)	2.47(1)	0.0065(6)	
	U-C_1	3.1(3)	2.89(1)	0.0038[d]	
	U-C_2	3.1[f]	4.38(1)	0.0038[d]	
	U-C_1-C_2 (MS)	6.2[f]	4.38[g]	0.008(1)	
	U-C_1-C_2-C_1 (MS)	3.1[f]	4.38[g]	0.008[h]	

Standard deviations as estimated by EXAFSPAK are given in parenthesis
[a] Errors in coordination numbers are ± 25%
[b] Errors in distance are ± 0.02 Å
[c] Debye-Waller factor
[d] Parameter fixed for calculation
[e] Radial distance (R) and Debye-Waller factor (σ^2) linked twice to R and σ^2 of the of the U-O_{ax} path.
[f] Coordination number (N) linked to the N of U-C_1 path.
[g] R linked to R of U-C_2 path.
[h] Debye-Waller factor linked to that of the U-C_1-C_2 (MS) path.

The EXAFS spectra recorded from both samples strongly resemble to each other, which confirms the formation of highly similar uranium complexes at both investigated pH values. In addition, the EXAFS spectra is well in line with that of uranyl triacetate indicating that similar U(VI) complexes were formed at the archaeal S-layer. The most prominent peak of both FT's located at R + Δ ~1.3 Å is assigned to the single backscattering mode (U-O_{ax}) of the two axial oxygen atoms of U(VI). The multiple scattering path (U-O_{ax}-U-O_{ax}) of this axial oxygen shell is also quite important for the fitting of uranyl EXAFS spectra and have an intensity maximum in the FT at R + Δ ~2.9 Å. The second peak of both FT's is attributed to the scattering contribution of the oxygen atoms in the equatorial plane. Fitting results of both investigated samples revealed four to five equatorial oxygen atoms at a radial distance of 2.42 to 2.43 Å. However, the high Debye-Waller factor of 0.013 Å^2 calculated for the U-O_{eq} shell of both samples, indicates that this shell includes equatorial oxygen atoms at different radial distances. In addition, a shell containing two to three carbon atoms (U-C_1) was fitted at a radial distance of 2.89 to 2.90 Å. This distance is typical for the U-C backscattering of U(VI) complexed by the two oxygen atoms of a carboxylate group in a bidentate binding mode. A corresponding complexation modus was already suggested by the EXAFS studies of the uranium complexes formed by whole cells of *S. acidocaldarius* at identical conditions [6]. However, these EXAFS spectra, obtained from whole cells, were rather complex and dominated by a monodentate complexation of U(VI) by organic phosphate groups. Hence, a proper determination of the structural parameters of the U(VI) complexes formed at carboxylate groups was difficult. Comparable complexes, possessing a bidentate coordination of uranium by carbon atoms had also been found at bacterial cells and their S-layer proteins [8]. With respect to the EXAFS parameters obtained for the U-O_{eq} shell, we assume that the uranyl ion is predominantly complexed by two carboxylate groups. In addition, the uranyl unit exhibit one or two fully hydrated equatorial oxygen atoms. By using this complexation model the high Debye-Waller can be explained by the different radial distances of the equatorial oxygen atoms which are bound to the uranium in a bidentate binding mode - characteristic distance: 2.45-2.51 Å [9] - and that of the equatorial oxygen atoms which exists in their hydrated form - characteristic distance: 2.41-2.42 Å [10, 11]. A second shell of carbon atoms (U-C_2) resulting from the C-atom bearing the carboxylic group was detected at radial distances of (4.35 ± 0.02) Å and (4.37 ± 0.03) Å in the sample incubated at pH 4.5 and pH 6, respectively.

The XAS studies demonstrate that U(VI) forms inner sphere complexes at carboxylate groups of the S-layer proteins in a bidentate binding mode. According to the structural parameters, 1:2 and/or 1:3 uranyl carbonate complexes were formed.

REFERENCES

[1] Sleytr and Beveridge (1999) Trends Microbiol. 7, 253-260.
[2] König *et al.* (2007) *Archaea* - Molecular and Cellular Biology, p. 315-353, ASM Press, Herndon.
[3] Brock *et al.* (1972) Arch. Microbiol. 84, 54-68.
[4] Michel *et al.* (1980) Electron microscopy at molecular dimensions, p. 27-35, Springer-Verlag, Berlin.
[5] Reitz *et al.* (2010) Radiochim. Acta 98, 249-257.
[6] Reitz *et al.* (2010) Geobiol. submitted
[7] Hudson *et al.* (1996) Phys. Rev. B, 54,156-165.
[8] Merroun *et al.* (2005) Appl. Environ. Microbiol. 71, 5532-5543.
[9] Denecke *et al.* (1997) J. Phys. IV France 7, 637-638.
[10] Thompson *et al.* (1997) Am. Miner. 82, 483-496.
[11] Vallet *et al.* (2001) Inorg. Chem. 40, 3516-3525.

ROBL-CRG	**Experiment title:** Molecular scale studies on the speciation of U(VI) bound to cells and S-layers of Archaea	**Experiment number**: 20-01-688
Beamline: BM 20	**Date of experiment**: from: 24/06 to: 29/06/10	**Date of report**: 20/04/11
Shifts: 15	**Local contact(s)**: André Roßberg	*Received at ROBL:*

Names and affiliations of applicants (* indicates experimentalists):
M.L. Merroun[1], A. Roßberg*, C. Lucks*
[1]Departamento de Microbiología, Universidad de Granada, Granada, Spain
*Helmholtz-Zentrum Dresden-Rossendorf e.V., Institute of Radiochemistry, P.O. Box 510119, 01314 Dresden, Germany

Experimental

This study aimed to characterize at molecular scale the local coordination of U(VI) associated with the marine bacterium, *Idiomarina loihiensis* MAH1, in seawater using X-ray absorption spectroscopy. The strain MAH1 was isolated from the Alboran Sea in the west side of the Mediterranean Sea, and their cells were able in the absence of U(VI) to precipitate minerals including phosphates (e.g. struvite, $NH_4MgPO_4.\ 6H_2O$) and carbonates (Ca–Mg kutnahorite, $CaMg(CO_3)_2$) in sea water (González-Muñoz et al. 2008).

The speciation of U(VI), at environmentally relevant concentrations ranging between 10^{-6} and 10^{-4} M, associated with the cells of the strain MAH1 was studied in sea water system, the natural habitat of this bacterium using TRLFS spectroscopy and transmission electron microscope (TEM). TRLFS analysis indicated that the cells of the studied bacterium precipitate U(VI) as U calcium carbonate mineral phases with fluorescence properties similar to those of liebigite $Ca_2(UO_2)(CO_3)_3.11(H_2O)$. In addition, a second mineral phase, uranyl phosphates (meta-autunite), could be implicated in the biomineralization of this radionuclide. High Resolution Transmission Electron Microscope (HRTEM) analysis indicated that the mineral phases precipitated were localized on the cell wall. However, these techniques were not able to determine the structural parameters of the U(VI) species precipitated by the marine bacterium.

The results of this study will help to understand the role of microbial process on the transport and mobility of radionuclides in the Alboran Sea as it is the only connection between the Mediterranean Sea and the Atlantic Ocean, and where the transportation of radioactive wastes and the traffic of nuclear submarines are very intense.

Results

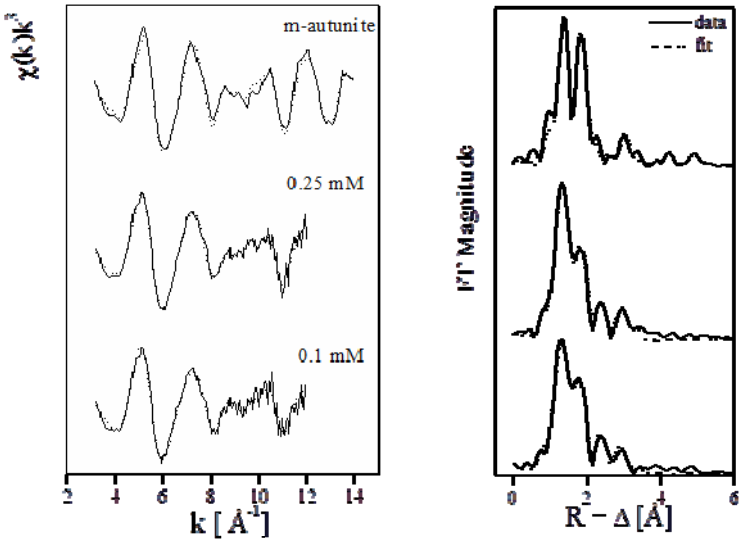

Fig1. Uranium L_{III}-edge k3–weighted EXAFS spectra (left) and the corresponding Fourier transforms (FT) (right) of the uranium complexes formed by the cells of the strain MAH1 at U(VI) concentration of 0.1 and 0.25 mM and reference compound (m-autunite.

A visual comparison of the XANES fingerprints for the reference samples U(VI) and U(IV) indicated the presence of U(VI) in the two samples studied in this work (data not shown). The presence of U(VI) in the XANES spectra is evidenced by the display of a characteristic shoulder at 17.188 eV, which is consistent with U(VI) oxidation state.

The uranium L_{III}-edge EXAFS spectra and their corresponding Fourier transforms (FT) for the uranium species formed by the cells of the strain MAH1 in seawater at U(VI) concentrations of 0.1 and 0.25 mM are presented in Fig. 1. The FT represents a pseudo-radial distribution function of the uranium near-neighbor environment. The EXAFS spectra of the U-treated bacterial cell samples are similar to m-autunite spectrum with regard to the U-Oeq, U-P and U-U distances. These findings suggest the precipitation of an inorganic m-autunite-like uranyl phosphate phase by the bacterial cells in seawater.

REFERENCES

1. Gonzaléz-Muñoz et al. (2008) Chemosphere 72 (3), 465-472.

ROBL-CRG	**Experiment title:** EXAFS investigation of the effects of humic acid on uranyl adsorption on goethite	**Experiment number:** 20-01-689
Beamline: BM 20	**Date of experiment:** from: 25.07.2009 to: 28.07.2009	**Date of report:** 01.06.2010
Shifts: 12	**Local contact(s):** A. Scheinost	*Received at ROBL:*

Names and affiliations of applicants (* indicates experimentalists):

T. Saito* and S. Nagasaki

Department of Nuclear Engineering and Management, School of Engineering, The University of TOkyo
7-3-1 Hongo, Bunkyo-ku, Tokyo 113-8656, JAPAN

Report:

Humic substance (HS) is a group of organic nanocolloids found in diverse environments. HS affects the buffering and barring capacity of the environments against the inputs of toxic metal ions such as heavy metals and radionuclides[1]. Although the effects of HS on metal adsorption are now recognized, our understanding on the underlying mechanisms is far from satisfactory. Depending on solution conditions, the type of a adsorbing metal and the magnitude of HS loading on a surface, the adsorption of metal is enhanced, diminished or virtually unaffected, which have never been explained clearly. This is partly due to the lack of the molecular-scale information on a metal/HS/mineral ternary system. In this study uranyl (UO_2^{2+}) adsorption on goethite was studied by EXAFS spectroscopy both in the absence and presence of humic acid (HA) in order to extract the structural information on dominant species.

Sorption of UO_2^{2+} on synthesized goethite particles with and without purified Aldrich HA (PAHA) was studied by both macroscopic batch adsorption experiments and molecular-level EXAFS measurements. All samples were prepared in Ar or N_2 atmosphere to exclude CO_2. The adsorption experiments were performed with 1 g/L goethite suspension as a function of pH, salt concentration and PAHA concentrations. The total concentrations of UO_2^{2+} and PAHA were 50 μM and 50 mg/L, respectively. The salt concentration was adjusted with 1 M $NaClO_4$ to 0.1 or 0.01 M. The U L_{III} EXAFS measurements were performed with 5 g/L goethite suspension at pH 4 and 0.1 M $NaClO_4$, where the UO_2^{2+} sorption was enhanced in the presence of PAHA. As reference UO_2^{2+}/HA and UO_2^{2+}/goethite binary samples were measured as well. For the UO_2^{2+}/gothite binary and the UO_2^{2+}/PAHA/ goethite ternary samples, the total UO_2^{2+} concentration was 200 μM UO_2^{2+}, which resulted in similar surface loading of UO_2^{2+} on goethite. The concentration of PAHA in the latter samples was varied from 20 to 500 mg/L. The UO_2^{2+}/PAHA binary sample was prepared with 500 mg/L PAHA and 400μM UO_2^{2+}. The obtained EXAFS spectra were analyzed by the iterative target transformation factor analysis $(ITTFA)^2$ to determine the number of different UO_2^{2+} species and their structural characteristics as a function of the HA loading.

The adsorption of UO_2^{2+} on goethite was increased by PAHA at pH < 5.5 and diminished at pH > 6. The former can be explained by the formation of ternary complexes among UO_2^{2+}, PAHA and goethite and the latter by the binding of UO_2^{2+} to PAHA in aqueous phase. From the EXAFS radial distribution function (RDF) of UO_2^{2+} adsorbed on goehite without PAHA in Figure 1, there were distinct contribtions both at 3 and 3.5 Å (without phase-shift correction), suggesting the formation of both edge-sharing and corner-sharing bidentate coordination of UO_2^{2+} to iron octahedra[3]. The comparison of EXAFS RDF of the binary and ternary samples at pH 4 (Figure 2) showed a systematic variation in the elemental arrangements around adsorbed UO_2^{2+} ions. The ITTFA analysis further revealed that the variation is a mixture of HA- and goethite-like contributions (Figure 2 (a)) and that the latter dominated even at relatively high PAHA loading (Figure 2 (b)). This strongly suggests that the formation of the PAHA/UO_2^{2+}/goethite Type-A ternary complex is responsible for the observed enhancement of UO_2^{2+} adsorption in the presence of PAHA.

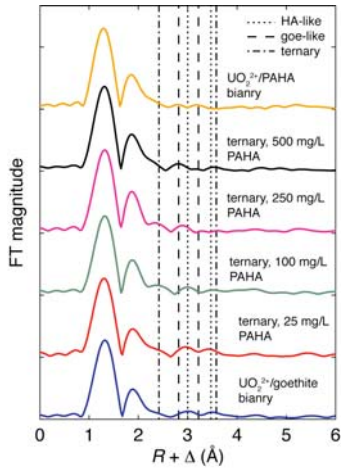

Figure 1. EXAFS radial distribution function (RDF) of UO_2^{2+} adsorbed on goethite in the presence of PAHA (the UO_2^{2+}/PAHA/goethite ternary samples). For comparison, the RDF of the UO_2^{2+}/ goethite and UO_2^{2+}/PAHA binary samples are included.

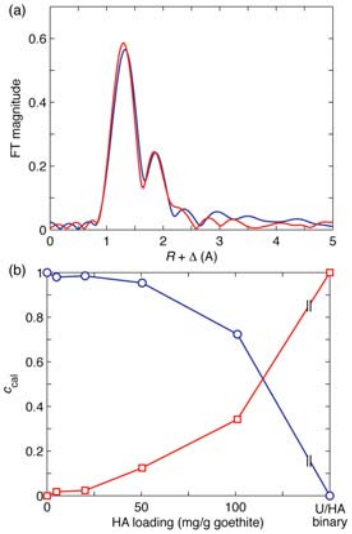

Figure 2. Extracted goethite- and HA-like RDF (a) and their contributions (a) from the ternary EXAFS spectra by ITTFA.

Literature cited

1. Saito, T., et al., *Environ. Sci. Technol.* **2005**, *39*, 4886-4893.
2. Rossberg, A., et al., *Anal. Bioanal. Chem.* **2003**, *376*, 631-638.
3. Sherman, D. M., et al., *Geochim. Cosmochim. Acta* **2008**, *72*, 298-310.

	Experiment title: Molecular structure of actinide hexcyanometalates	**Experiment number**: 20-01-690
Beamline: BM29	**Date of experiment**: from: 02/10/2009 to: 05/10/2009	**Date of report**: 06/07/2010
Shifts: 9	**Local contact(s)**: C. Hennig	*Received at ESRF:*

Names and affiliations of applicants (* indicates experimentalists):
Christophe DEN AUWER*[a] DEN/DRCP/SCPS
G. Dupouy* DEN/DRCP/SCPS
T. Dumas* DEN/DRCP/SCPS

a CEA Marcoule
30207 Bagnols sur Cèze, France

Report:

Among the *quasi* infinity of synthetic molecular edifices, the hexacyanometallate family is well known in transition metal chemistry to foster remarkable electronic delocalization along the metal-cyano-metal bond. Furthermore, this delocalization may be tuned up or down in order to design systems that exhibit a large variety of physical properties.

From a structural point of view, the $KLn^{III}/Fe^{II}(CN)_6.xH_2O$ (Ln = lanthanide element) family can be separated in three series. The first one with Ln = La to Nd presents the general formula $KLnFe^{II}(CN)_6.4H_2O$ [1]. These compounds crystallize in the hexagonal $P6_3/m$ space group. The second series has a unique representative, $KSmFe^{II}(CN)_6.3H_2O$, which crystallizes in a monoclinic group ($P2_1/m$) [2]. For these two series, the nine-coordinated lanthanide cation is bound to six $\{Fe(CN)_6\}$ motifs and to three water molecules in a distorted trigonal tricapped prism. Finally the third series involves Ln = Eu to Lu. They all occur in the orthorhombic space group: $KLnFe^{II}(CN)_6.3.5H_2O$ crystallizes in the Cmcm space group [3] while $KLnFe^{II}(CN)_6.3H_2O$ crystallizes in the Pnma space group [4]. The difference between the two space groups is the lanthanide coordination number: in the Cmcm group the lanthanide cation is nine-coordinated like for the La-Nd series; in the Pnma group the lanthanide cation is eight-coordinated to six nitrogen atoms and only two water molecules.

A few years ago we have started describing the molecular and electronic structures of the materials formed by the $\{Fe(CN)_6\}$ building blocks and actinide(IV) (An = Th, U, Np). We have compared these new materials to their homologues of the lanthanide series, our major interest originated in fundamental understanding of actinide *versus* lanthanide chemistry. In this report we present briefly the first investigation of americium and californium hexacyanoferrates, two actinide cations from the middle of the actinide series. Americium is considered as the first element of the series with stronger lanthanide character (Americium is often considered as a turning point in actinide chemical properties) and californium is the heaviest element available in the laboratory for weighable chemistry. Both elements are also very good representatives of the +III actinide chemistry with no other stable oxidation state achievable in our experimental conditions.

Figure 1 shows the experimental XANES spectrum at the Cf and Am L_3 edge of $\mathbf{Am^{III}/Fe^{II}}$ and $\mathbf{Cf^{III}/Fe^{II}}$ respectively. The absorption edges have all been rescaled with respect to the edge ramp for comparison. As expected, the Am and Cf L_3 edges are very similar since both cations are at the same oxidation state in similar environments. In addition, in order to fully characterize the actinide coordination sphere, the EXAFS spectra of $\mathbf{Am^{III}/Fe^{II}}$ and $\mathbf{Cf^{III}/Fe^{II}}$ at the actinide L_{III} edge have also been recorded and adjusted [5].

In the following discussion we detail the comparison between $\mathbf{Am^{III}/Fe^{II}}$ with the neodymium equivalent on the one hand, and $\mathbf{Cf^{III}/Fe^{II}}$ with the gadolinium equivalent on the other hand.

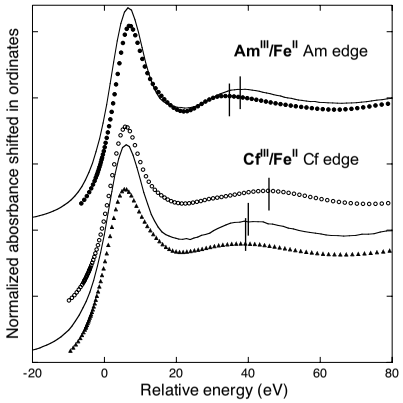

Experimental XANES spectra at the Am L_3 edge of $\mathbf{Am^{III}/Fe^{II}}$ and at the Cf L_3 edge of $\mathbf{Cf^{III}/Fe^{II}}$ (straight line). Comparison with the simulated spectra (Feff84) of $KNdFe^{II}(CN)_6.4H_2O$[7d] (black dots), $KGdFe^{II}(CN)_6.3H_2O$[10b] (black triangles) and $KGdFe^{II}(CN)_6.3.5H_2O$[9b] (white dots). Spectra have all been shifted in energy with respect to absorption ramp.

In $KNd^{III}Fe^{II}(CN)_6.4H_2O$, the neodymium cation is nine coordinated to six nitrogen atoms (d(NdN) = 2.52 Å) and three water molecules (d(NdO) = 2.68 Å). A direct comparison between the distances obtained by EXAFS for $\mathbf{Am^{III}/Fe^{II}}$ (not shown, see [5] for details) and the above ones suggests that the americium and neodymium environments are analogous. Therefore, by analogy, $\mathbf{Am^{III}/Fe^{II}}$ must contains nine-coordinated $\{AmN_6(H_2O)_3\}$ units. Consequently, as shown in Figure 1 by comparing the experimental and simulated (from $KNdFe^{II}(CN)_6.3H_2O$) XANES spectra, the americium polyhedron may be attributed to a tri-capped trigonal prism in which the americium is bonded to six nitrogen atoms in apical sites and to three water molecules in the equatorial plane. Simulations have been performed here by replacement of the lanthanide atomic number in the input file by the corresponding actinide number (*i.e.* Nd replaced by Am), everything else being kept equal to the crystal structure.

Comparison between the californium ionic radius and the gadolinium one suggests that $\mathbf{Cf^{III}/Fe^{II}}$ may crystallize as $KGdFe^{II}(CN)_6.3.5H_2O$ or as $KGdFe^{II}(CN)_6.3H_2O$ do. As described in the introduction, gadolinium adducts may occur in two different forms: $KGdFe^{II}(CN)_6.3.5H_2O$ crystallizes in an orthorhombic space group (Cmcm) with a coordination number of nine, while $KGdFe^{II}(CN)_6.3H_2O$ crystallizes in a orthorhombic space group (Pnma) with a coordination number of eight. Figure 1 compares the experimental XANES spectra of $\mathbf{Cf^{III}/Fe^{II}}$ at the Cf L_3 edge to two simulations carried out from the gadolinium analogues : $KGdFe^{II}(CN)_6.3H_2O$ and $KGdFe^{II}(CN)_6.3.5H_2O$. Although the direct comparison must be taken with care, it appears clearly that in the case of $\mathbf{Cf^{III}/Fe^{II}}$, the position of the first oscillation (vertical mark in Figure 1) is in better agreement with that of simulated $KCf(Gd)Fe^{II}(CN)_6.3H_2O$ than with that of simulated $KCf(Gd)Fe^{II}(CN)_6.3.5H_2O$. In conclusion, all the above results strongly suggest that $\mathbf{Cf^{III}/Fe^{II}}$ may be written as $KCf^{III}Fe^{II}(CN)_6.nH_2O$ as in $KGdFe^{II}(CN)_6.3H_2O$. This has been also confirmed by the EXAFS data analysis (not shown, see [5] for details).

The striking point of this study is the decrease of coordination number by one unit going from neodymium (americium) to gadolinium (californium), from trigonal tricapped prism for the first ones to trigonal bicapped prism for the second ones. This example is to be related to the latest studies on the aquo or hydrate adducts for the lanthanide and the actinide series at oxidation state +III [6].

1. a) G. W. Beall, D. F. Mullica, W. O. Milligan, *Acta Cryst*, **B34**, 1446 (1978); b) D. F. Mullica, W. O. Milligan, J. D. Oliver, *Inorg. Nucl. Chem. Lett.*, **15**, 1 (1979); c) D. F. Mullica, E.L. Sappenfield, H.O. Perkins, *Journal of Solid State Chemistry*, **73,** 65 (1988) ; d) W.O. Milligan, D. F. Mullica, H. O. Perkins, *Inorg. Chim. Acta.*, **60**, 35 (1982); e) D. F. Mullica, E. L. Sappenfield, *Powder Diffraction*, **4**, 101, (1989).
2. D. F. Mullica, E. L. Sappenfield, H. O. Perkins, *J. Solid State Chem.*, **78**, 301 (1989).
3. a) F. Goubard, A. Tabuteau, *J. Solid State Chem.*, **167**, 34 (2002); b) F. Goubard, A. Tabuteau, *Struct. Chem.*, **14**, 257 (2003); c) D. F. Mullica, E. L. Sappenfield, T. A. Cunningham, *J. Solid State Chem*, **91**, 98 (1991).
4. a) X. L. Xu, F. Hulliger, *Eur. J. Solid State Inorg. Chem.*, **27**, 443 (1990); b) D. F. Mullica, J. L. Ward, E. L. Sappenfield, *Acta Cryst*, **C52**, 2952 (1996).
5. G. Dupouy, I. Bonhoure, S. D. Conradson, T. Dumas, C. Hennig, C. Le Naour, P. Moisy, S. Petit, A. Scheinost, E. Simoni, C. Den Auwer, New J. Chem., submitted.
6. a) I. Persson, P. D'Angelo, S. De Panfilis, M. Sandstrom, and L. Eriksson, *Chem. Eur. J.*, **14**, 3056 (2008) ; b) C. Apostolidis, B. Schimmelpfennig, N. Magnani, P. Lindqvist-Reis, O. Walter, R. Sykora, A. Morgenstern, E. Colineau, R. Caciuffo, R. Klenze, R. G. Haire, J. Rebizant, F. Bruchertseifer, T. Fanghänel, *Angew. Chem. Int. Ed.*, **49**, 1 (2010).

	Experiment title: Molecular structure of actinide hexcyanometalates	**Experiment number**: 20-01-690
Beamline: BM29	**Date of experiment**: from: 10/03/2010 to: 12/03/2010	**Date of report**: 10/03/2011
Shifts: 9	**Local contact(s)**: C. Hennig	*Received at ESRF:*

Names and affiliations of applicants (* indicates experimentalists):
Christophe DEN AUWER*[a] DEN/DRCP/SCPS
S. Dahou* DEN/DRCP/SCPS
T. Dumas* DEN/DRCP/SCPS

a CEA Marcoule
30207 Bagnols sur Cèze, France

Report:

In aqueous solution, synthesis with actinide elements at oxidation state +IV is always hampered by competition with hydrolysis. Clearly, the hydrolytic form of actinides and in particular actinide(IV) in medium acidic media is a key question in order to assess the reaction, incorporation or transportation mechanisms from the aqueous medium to the system of interest. A tremendous amount of data has been produced about the hydrolytic forms of actinides from strong acidic to natural water pH. It is far beyond the scope of this project to address all these forms. However we would like to report in this experiment on the behavior of neptunium(IV) in buffered HEPES (4-(2-hydroxyethyl)-1-piperazineethanesulfonic acid) solutions. The scheme bellow shows the formula of HEPES. From literature data, it is believed that in water, the acidic proton is positioned either on the sulfonate group or on the amine function.

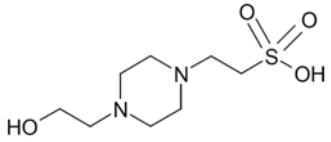

In this experiment, we have combined pHmetric measurements with *in situ* spectrophotometry and *post mortem* EXAFS studies to better understand the behavior of the neptunium(IV) aqueous ion in HEPES buffered acidic solution. The solution of Np(IV) in HCl has been obtained by reduction of Np(V) with NH_3OHCl. EXAFS measurements have been carried out *post mortem*. An aliquot of the above solution has been diluted in HEPES solution (14 µl of [Np] = 0.216 M in HCl at about 1M in 286 µl of HEPES solution at 0.25 M) and adjusted at designated pH with ammonia (called **Np-HEPES** in the text). The final Np concentration was 0.010 M. A spectrophotometric control of the solution has been carried out before and after sample measurement at the synchrotron, ensuring that no change of neptunium oxidation state has occurred during this time. EXAFS measurements were performed 4 hours after sample preparation. This short delay between sample preparation and measurement could only be achieved by a very good coordination between the RCTs of CEA Marcoule and ESRF. Note that we have observed a slow oxidation of Np(IV) into Np(V) with time higher than 10 hours (and strongly depending on the pH of the solution).

Figure 1 shows the UV-PIR spectrophotometric spectra of the **Np-HEPES** solution at various pH. Two sets of absorption bands are characteristic of Np(IV) in HCl (bottom curve) : one intense band at 960 nm, another intense band at 723 nm with three shoulders at 695, 713 and 740 nm. The spectrum at pH = 1 is very similar to that of the aqueous form. From pH 2.5 and above, there is a Red shift of all the bands and a dramatic decrease of intensity. For instance, the band at 960 nm is shifted to 980 nm with significant broadening. However no precipitate of suspension is visible in the solution. At pH = 4.5, a very similar spectrum is observed with no significant change.

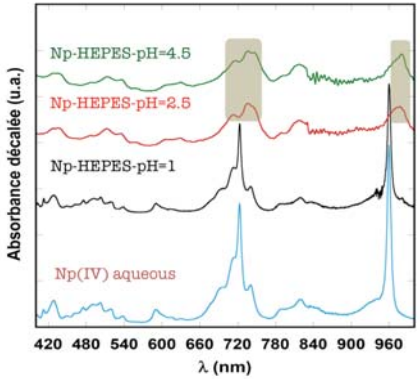

Figure 1 : Spectrophotometric measurements of **Np-HEPES** solutions at pH = 1.0, 2.5 and 4.5.

EXAFS measurements of two **Np-HEPES** solutions at pH = 2.5 and 4.5 show significant changes with respect to aqueous Np(IV) and the appearance of a long range contribution that may be attributed to Np-Np interactions. Figure 2 shows the Fourier transform of the EXAFS spectra together with best fit metrical parameters.

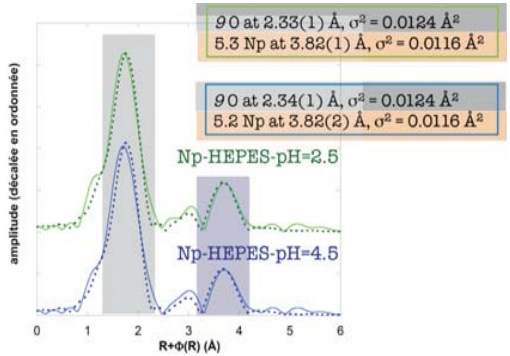

Fig. 2 : FT of the EXAFS spectra of **Np-HEPES** solutions at pH = 2.5 and 4.5.

As suggested by the spectrophotometric measurements, no difference occurs between the two pH values. Comparison of the fitted metrical parameters with the crystal structure of $[Np_2(OH)_{10}NH_4]_n$ finds some similarities (on the average 9 O at 2.33 Å and 3 Np at 3.87 Å around each Np [1]). The exact mechanisms of formation and stabilization of the **Np-HEPES** clusters in solution is still not known as well as the molecular weight of the edifice.

In addition, slow oxidation of Np(IV) into Np(V) has been observed but not quantified. This oxidation occurs typically over few hours and increases with pH. A XANES and EXAFS measurement of the post mortem solution of **Np-HEPES** at pH = 4 and after 30 days clearly shows the presence of $\{NpO_2^+\}$ in the aqueous form (*2* Oyle at 1.82(1) Å, σ^2 = 0.0005 Å^2 and *5* Oeq at 2.50(1) Å, σ^2 = 0.0069 Å^2). This result suggests the reversible state of these clusters in solution. In the future we shall perform complementary pH metric data with *in situ* spectrophotometric measurements in order to rationalize the speciation (and stoechiometry) of these species.

1 A. Cousson et al. *Journal of the less common metals* (1986), 121, 405

	Experiment title: Molecular structure of actinide hexcyanometalates	**Experiment number**: 20-01-690
Beamline: BM20	**Date of experiment**: from: 17/04/2010 to: 20/04/2010	**Date of report**: 10/03/2011
Shifts: 9	**Local contact(s)**: C. Hennig	*Received at ESRF:*

Names and affiliations of applicants (* indicates experimentalists):

Christophe DEN AUWER*[a] DEN/DRCP/SCPS

C. Fillaux* DEN/DRCP/SCPS

T. Dumas* DEN/DRCP/SCPS

a CEA Marcoule

30207 Bagnols sur Cèze, France

Report:

Among the *quasi* infinity of synthetic molecular edifices, the hexacyanometallate family is well known in transition metal chemistry to behave with remarkable electronic properties. It is also an interesting example of building block chemistry with structurally defined subfamilies. From structure control, electronic delocalization may be tuned up or down in order to design systems that exhibit a large variety of physical properties. This project aims to fully describe the building block chemistry of the actinide cyanometallates and thiocyanometallates and to assess the electronic properties of the actinide-cyano bond using a combination of X-ray spectroscopic and theoretical chemical tools. For the f elements, the lanthanide hexacyanometallate derivatives have been reported extensively, whereas the actinide family is much less present in the literature.

Since the beginning of this project, five series of synthesis have been performed. They have been performed in mid acidic aqueous solution at room temperature, except for the third series in DMF. In most cases, powders have been obtained. Table 1 summarizes the complexes obtained in this task.

Table 1 : list of samples obtained at CEA Marcoule and IPN Orsay. Sample name is designated by the formal oxidation state of the precursors.

Sample name	Final oxidation states	remarks
Series 1		
U^{VI}/Fe^{II}	U^{VI}/Fe^{II}	
U^{VI}/Fe^{III}	$U^{VI}/Fe^{II} + U^{VI}/Fe^{III}$	mixing
Np^{V}/Fe^{III}	Np^{V}/Fe^{III}	
Np^{V}/Fe^{II}	Np^{IV}/Fe^{II}	
Pu^{VI}/Fe^{III}	Pu^{VI}/Fe^{III}	Evolves to Pu^{IV}/Fe^{II} with time
Pu^{VI}/Fe^{II}	Pu^{IV}/Fe^{II}	
Series 2		
Th^{IV}/Fe^{II}	Th^{IV}/Fe^{II}	
U^{IV}/Fe^{II}	U^{IV}/Fe^{II}	
Pu^{IV}/Fe^{II}	Pu^{IV}/Fe^{II}	
Series 3		
Th^{IV}/Fe^{III}/DMF	Th^{IV}/Fe^{III}/DMF	
U^{VI}/Fe^{III}/DMF	U^{VI}/Fe^{III}/DMF	
Np^{IV}/Fe^{III}/DMF	Np^{IV}/Fe^{III}+Fe^{II}/DMF	mixing
Pu^{IV}/Fe^{III}/DMF	Pu^{IV}/Fe^{III}/DMF	
Series 4		
Am^{III}/Fe^{III}	Am^{III}/Fe^{III}	Becomes Am^{III}/Fe^{II} with time
Am^{III}/Fe^{II}	Am^{III}/Fe^{II}	
Cf^{III}/Fe^{II}	Cf^{III}/Fe^{II}	
Series 5		
Lu^{III}/SCN	Lu^{III}/SCN	

We have already reported on the results of series 4 (report of the 06/07/2010) with the Am and Cf adducts. We would like to report here on series 3. For EXAFS data analysis, an original parameterized fitting procedure based on the two edge fit has been implemented and tested on model compound **Lu^{III}/Fe^{III}/DMF** ($[Lu^{III}(DMF)_4(H_2O)_3(Fe^{III}(CN)_6)].H_2O$) described by Mullica.[1] The model compound **Lu^{III}/Fe^{III}/DMF** ($[Lu^{III}(DMF)_4(H_2O)_3(Fe^{III}(CN)_6)].H_2O$) has been selected to test the parameterized fitting procedure. In this complex, the lutetium atom is eight-coordinated to four DMF groups, three water molecules and only one ferricyanide motif. It contains one "Fe-C-N-Lu" link, therefore of very weak intensity. In order to test our fitting procedure, both iron K edge and Lu L_{III} edge of **Lu^{III}/Fe^{III}/DMF** have been adjusted using a parameterization of the metrical parameters at both edges. In the crystal structure of **Lu^{III}/Fe^{III}/DMF**, the Fe-C-N angle is equal to 177 ° and can be considered nearly linear while the Lu-N-C angle (noted θ) is equal to 164°. Similarly, the Th(IV) adduct $(H_5O_2)[Th(IV)(DMF)_5(H_2O)]_2[Fe(III)(CN)_6]_3$ as well as Np(IV) and Pu(IV) adducts (but not crystallized) have been prepared. As confirmed by XANES measurements (at both actinide and Fe edges) they show (except for the Np adduct, as detailed in Table 1) an interesting stability of the An^{IV}/Fe^{III} form instead of An^{IV}/Fe^{II} form in the absence of DMF. Figure 1 exemplifies the two edge fitting methodology from the **Lu^{III}/Fe^{III}/DMF** model compound.

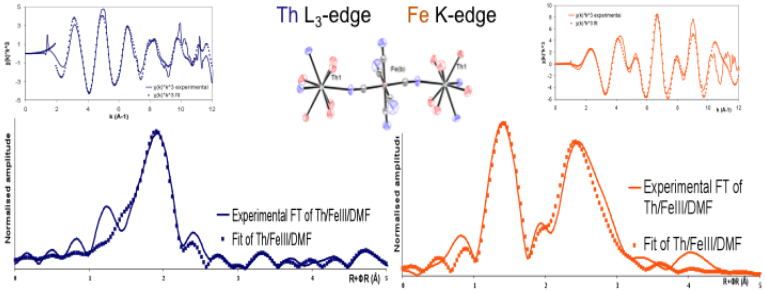

Fig. 1 : two edge fitting procedure of $(H_5O_2)[Th(IV)(DMF)_5(H_2O)]_2[Fe(III)(CN)_6]_3$. The Fe K edge was recorded at the SSRL synchrotron.

The best fit metrical parameters of **Th^{IV}/Fe^{III}/DMF** are in very good agreement with the crystallographic data. EXAFS data : Th-N = 2.59 Å (σ^2=0.006 Å), C-N = 1.17 Å (σ^2=0.010 Å), Fe-C = 1.92 Å (σ^2=0.009 Å) ; XRD data : Th-N = 2.578 Å, C-N = 1.149 Å, Fe-C = 1.923 Å. We are currently working on the adjustment of the **Pu^{IV}/Fe^{III}/DMF** adduct. One of the objectives is to understand the role of the DMF in the structure in preventing the formation of the ferrocyanide adduct.

In parallel, we have started the investigation of the actinide thiocyanide adducts. Crystallographic parameters have already been obtained from lanthanide (Nd and Lu) and thorium $[NBu_3]_3[Th(NCS)_4(NO_3)_3]$ adducts. A first attempt in the synthesis of the Am(III) thiocyanate equivalent has failed and will be the object of the next beam time period.

1 D. F. Mullica, J. M. Farmer, B. P. Cunningham, J. A. Kautz, *J. Coord. Chem.*, **49**, 239 (2000).

	Experiment title: **EXAFS investigation of U(IV) precipitates**	**Experiment number:** 20-01-691
Beamline: BM 20	**Date of experiment:** from: 2.5.2009 to: 4.5.2009	**Date of report:** 19.04.2011
Shifts: 8	**Local contact(s):** Christoph Hennig	*Received at ESRF:*

Names and affiliations of applicants (* indicates experimentalists):

Stephan Weiss*, Christoph Hennig*

Helmholtz-Zentrum Dresden-Rossendorf, Institute of Radiochemistry, Bautzner Landstrasse 400, 01314 Dresden Germany

Report:

Mobility and migration of actinides in the environment is an important issue to predict appropriate construction aspects of nuclear waste repositories. Because uranium(IV) has a very low solubility at pH ~7, it is considered as immobile under the redox conditions of a nuclear waste repository. The same is valid for uranium mining areas. However, the U(IV) precipitate may occur as nano-sized colloids which are very mobile in the environment. Nuclear waste and uranium mining with open shafts and tunnels contain under oxic conditions uranium predominantly in oxidation state VI. The reduction process of such U(VI) to U(IV) may result in U(IV) colloids as observed in the laboratory especially in low pH. Similar colloids appear with Th(IV) and Pu(IV). Such colloids are meta-stable and may migrate out of the retaining barriers. Anoxic water with a certain amount of carbonate and silicate is usually present in geological formations used for uranium waste disposal. We found meta-stable colloids of U(IV) and Th(IV) at near-neutral pH, especially in presence of silicate. The structure of these colloids is recently under discussion. It is known that tetravalent oxyhydroxy colloids undergo over time ordering processes and form sequences of AnO_2 structures. The question raises, if such ordered domains occur also in An(IV) silica colloids. Subsequently we compare the EXAFS spectrum of ThO_2 with the spectrum of a Th/Si colloid sample.

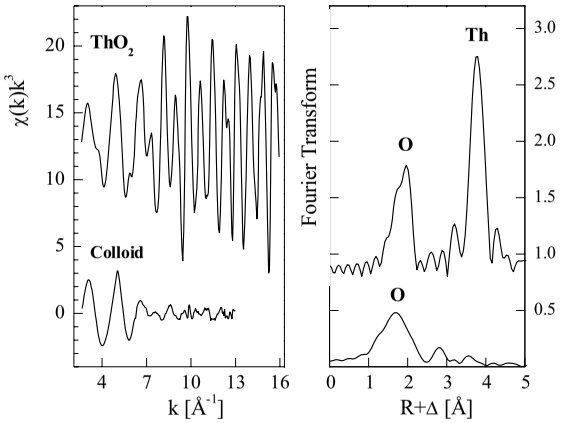

Figure 1. Th L_3 edge EXAFS (left) and the corresponding Fourier Transformation (left) of ThO_2 and a Th/Si colloid sample.

ThO_2 crystallizes in the space group Fm-3m. Each Th atom is directly coordinated by 8 oxygen atoms and is sourrounded in the next coordination sphere by 12 Th atoms. The EXAFS spectrum of ThO_2 in Fig. 1 shows 8 identical Th-O distances at 2.42 Å and 12 Th-Th distances of 3.96 Å. The spectrum of the colloid sample shows clear differences. The first peak, corresponding with the oxygen shell is broadened, indicating a variety of oxo and hydroxo bonds in the coordination sphere of thorium. A peak representing the Th-Th interaction is completely missing, indicating that the structure is either completely changed, e.g. by replacing Th-O-Th bonds by Th-O-Si bonds, or at least highly disordered. There is also no structural similarity with the crystalline $ThSiO_4$ polymorphs. Thus, so far we could not identify any ordered domains in such colloids.

	Experiment title: Effect of metal-reducing bacteria on uranium mobilization	**Experiment number:** 20-01-692
Beamline: **BM20**	Date of experiment: from: 13. May 2009 to: 15. May 2009	**Date of report:** 11. Jan. 2010
Shifts: **6**	**Local contact(s):** Andreas C. Scheinost, Dipanjan Banerjee	*Received at ESRF:*
Names and affiliations of applicants (* indicates experimentalists): Kirsten Küsel Institute of Ecology, Friedrich Schiller University Jena, Dornburger Straße 159, D-07743 Jena, Germany		

Report:

The results of this experiment have been published or will be published in the following two papers:

1) Impact of Biostimulated Redox Processes on Metal Dynamics in an Iron-Rich Creek Soil of a Former Uranium Mining Area

Eva-Maria Burkhardt[1], Denise M. Akob[1,2], Sebastian Bischoff[1], Jana Sitte[1], Joel E. Kostka[2], Dipanjan Banerjee[3,4], Andreas C. Scheinost[3,4], Kirsten Küsel[1]

[1] Institute of Ecology, Friedrich Schiller University Jena, Dornburger Straße 159, D-07743 Jena, Germany,
[2] Department of Oceanography, Florida State University, 255 Atomic Way, Tallahassee, FL 32306 USA,
[3] Institute of Radiochemistry, Forschungszentrum Dresden-Rossendorf, D-01314 Dresden, Germany, The
[4] Rossendorf Beamline at ESRF, F-38043 Grenoble, France

Abstract

Understanding the dynamics of metals and radionuclides in soil environments is necessary for evaluating risks to pristine sites. An iron-rich creek soil of a former uranium-mining district (Ronneburg, Germany) showed high porewater concentrations of heavy metals and radionuclides. Thus, this study aims to i) evaluate metal dynamics during terminal electron accepting processes (TEAPs) and ii) characterize active microbial populations in biostimulated soil microcosms using a stable isotope probing (SIP) approach. In biostimulated soil slurries, concentrations of soluble Co, Ni, Zn, As, and unexpectedly U increased during Fe(III)-reduction. This suggests that there was a release of sorbed metals and As during reductive dissolution of Fe(III)-oxides. Subsequent sulfate-reduction was concurrent with a decrease of U, Co, Ni, and Zn concentrations. The relative contribution of U(IV) in the solid phase changed from 18.5 to 88.7% after incubation. The active Fe(III)-reducing population was dominated by *δ-Proteobacteria* (*Geobacter*) in ^{13}C-ethanol amended microcosms. A more diverse community was present in ^{13}C-lactate amended microcosms including taxa related to *Acidobacteria*, *Firmicutes*, *δ-Proteobacteria*, and *β-Proteobacteria*. Our results suggested that biostimulated Fe(III)-reducing communities facilitated the release of metals including U to groundwater which is in contrast to other studies.

Zitation: Burkhardt, E.-M., D. M. Akob, S. Bischoff, J. Sitte, J. E. Kostka, D. Banerjee, A. C. Scheinost, and K. Küsel. 2010. Impact of biostimulated redox processes on metal dynamics in an iron-rich creek soil of a former uranium mining area. Environ. Sci. Technol. 44:177-183.

2) Sulfate-Reducing Activity Linked to Metal Retention in Contaminated Soil Located at a Former Uranium-Mining District (Ronneburg, Germany)

Jana Sitte[1], Denise M. Akob[1,2], Christian Kaufmann[1], Kai Finster[3], Dipanjan Banerjee[4], Eva-Maria Burkhardt[1], Joel E. Kostka[2], Andreas C. Scheinost[4], Georg Büchel[5] and Kirsten Küsel[1]

[1] Institute of Ecology, Friedrich Schiller University Jena, D-07743 Jena, Germany

[2] Department of Oceanography, Florida State University, Tallahassee, FL 32306, USA

[3] Department of Microbial Ecology, Institute for Biological Sciences, DK-8000 Aarhus C, Denmark

[4] Institute of Radiochemistry, Forschungszentrum Dresden-Rossendorf, D-01314 Dresden, Germany, The Rossendorf Beamline at ESRF, F-38043 Grenoble, France

[5] Institute of Earth Science, Friedrich Schiller University, D-07749 Jena, Germany

Abstract

Sulfate-reducing prokaryotes (SRP) can affect metal mobility either directly by reductive transformation of metal ions, e.g., uranium, into their insoluble forms or indirectly by formation of metal sulfides. This study evaluated *in situ* and biostimulated activity of SRP in groundwater influenced soils from a creek bank contaminated with heavy metals and radionuclides within the former uranium-mining district, Ronneburg (Germany). *In situ* activity of SRP, measured by the $^{35}S\text{-}SO_4^{2-}$-radiotracer method, was restricted to reduced soil horizons with rates ≤142 ± 20 nmol cm^{-3} day^{-1}. Although concentrations of heavy metals were enriched in the solid phase of the reduced horizons, porewater concentrations were low. XANES measurements demonstrated that ~80% of uranium was present as reduced uranium, but appeared to occur as a sorbed complex. Soil-based *dsrAB* clone libraries were dominated by sequences most closely affiliated to members of the *Desulfobacterales*, but also *Desulfovibrionales*, *Syntrophobacteraceae* and *Clostridiales*. ^{13}C-acetate and ^{13}C-lactate biostimulated soil microcosms were dominated by sulfate and Fe(III) reduction, which was associated with enrichment of similar SRP found using the *dsrAB* marker in soil and with sequences related to *Geobacter*. Concentrations of soluble nickel, cobalt, and occasionally zinc declined ≤100% during anoxic soil incubations. In contrast to other studies, soluble uranium increased in carbon-amended treatments reaching ≤1407 nM in solution. Our results suggest that (i) contaminated reduced soil with on-going sulfate reduction resulted in *in situ* metal attenuation and (ii) the fate of uranium mobility is not predictable and may lead to downstream contamination of adjacent ecosystems.

Submitted to Applied and Environmental Microbiology on 08.01.2010

	Experiment title: EXAFS and XANES investigation of plutonium sorption complexes on iron minerals	**Experiment number:** 20-01-693
Beamline: BM20	**Date of experiment:** from: 22/07/2009 to: 25/07/2009 07/07/2010 to: 12/07/2010	**Date of report:** 3rd February 2011
Shifts: 9+15	**Local contact(s):** Andreas C. Scheinost	*Received at ESRF:*

Names and affiliations of applicants (* indicates experimentalists):

Regina Kirsch*[1,2], Andreas C. Scheinost*[,2]

[1]Institute of Radiochemistry, Helmholtz-Zentrum Dresden Rossendorf, Dresden, Germany

[2]Institut des Science de la Terre, Université Joseph Fourier and CNRS, Grenoble, France

Report:

Due to their redox reactivity, surface sorption characteristics, and ubiquity as corrosion products or natural sediment constituents, iron(II)-bearing minerals control to a large extent the environmental fate of actinides. In this experiment, Pu-L_{III}-edge XANES and EXAFS spectra were collected of a total of 22 samples, consisting of ^{242}Pu(III) or ^{242}Pu(V) reacted under anoxic conditions for 40 days or 6 months with magnetite, mackinawite, siderite, hematite, maghemite, or goethite. In the presence of the iron(III)-minerals hematite, goethite and maghemite, Pu(V) was largely reduced to Pu(IV) (30 % Pu(V), 70% Pu(IV) after 6 months reaction with hematite at pH8, 80% Pu(IV) after 6 months reaction with maghemite, pH6). In magnetite suspensions, reduction of Pu(V) to Pu(III) and formation of a Pu(III)-magnetite surface sorption complex was observed (see below for details). At the two pH value (pH 6 and pH8) tested for mackinawite suspensions and for a reaction period of 6 months, both aqueous Pu(V) and Pu(III) transformed into PuO_2. Small differences between EXAFS spectra as a function of initial Pu oxidation state and reaction pH are apparent and currently being interpreted. PuO_2-Pu(III) mixtures result from addition of Pu(V) or Pu(III) to siderite suspensions (e.g. 67% PuO_2, 33 % Pu(III) after reaction of initially Pu(V) with siderite for 40 d). So far, it is not clear to what extent the oxidation state composition of the reaction product depends on reaction time and initial Pu oxidation state and in how far other parameters such as variations in reaction pH and associated variations in Fe(II) concentrations and redox potential are crucial.

These results highlight the necessity to consider under anoxic conditions Pu(III) species in addition to PuO_2 for risk assessment. Our results also demonstrate the necessity to combine thermodynamic calculations and spectroscopic data.

Results highlight:

The three Pu-magnetite spectra in Figure 1, obtained by reaction of Pu(III) or Pu(V) with magnetite at pH6 or pH8 for 40 days, are characterized by very similar edge and peak positions, irrespective of the initial Pu oxidation state and the reaction pH and strongly resemble the $(Pu^{III})_{aq}$ spectrum in position and shape. Using an Iterative Target Test (ITT) (1) on the XANES and EXAFS regions of the spectra, Pu(III) contents higher than 90 % were found for all three. Also shell fitting of the first peak in the Fourier Transform yields Pu-O distances of 2.48 Å to 2.49 Å, characteristic of aqueous Pu(III) complexes. Under the given experimental conditions, the oxidation state of Pu after reaction with magnetite appears therefore to be independent of the initial oxidation state (III or V) suggesting that thermodynamic equilibrium has been attained. To elucidate the structure of the Pu(III) species on magnetite, shell fitting was extended to the FT peaks beyond the oxygen coordination sphere. A second shell could be fitted with backscattering from three to five Fe atoms at a distance of 3.54 Å, suggesting either a sorption complex or formation of a solid phase. The sorption complex hypothesis was tested using FEFF-Monte Carlo (MC) modeling (2) on the k^3-weighted EXAFS spectrum of the Pu(V)-Magnetite-pH8 sample. One geometrically specific position in relation to magnetite, situated on a (111) surface with octahedral termination, was identified (Fig. 1d). In the corresponding surface complex, one Pu atom is linked via three oxygen atoms to three edge-sharing FeO_6-octahedra. The contribution of Pu-Pu backscattering to the experimental spectrum could be ruled out, thereby excluding formation of a dimeric surface complex or PuIII(hydr)oxide clusters. The radial Pu-atom distances found in the "raw" structure of the sorption complex were refined by reverse Monte Carlo (RMC) simulation. The resulting $\chi(k) \times k^3$ spectrum and the experimental spectrum (Fig. 1b) are in excellent agreement. The refinement yields the Pu-O and Pu-Fe radial pair distribution functions (RPDF) (Fig. 1c), wherein the first Pu-O peak corresponds to 9 oxygen atoms at 2.49 Å and the first Pu-Fe peak to three iron atoms at 3.54 Å. Due to the tridentate nature of the complex, it is likely to be very stable and play an important role in controlling Pu-magnetite reactions and Pu mobility under anoxic conditions. Details on sample preparation and analysis methods can be found in (3).

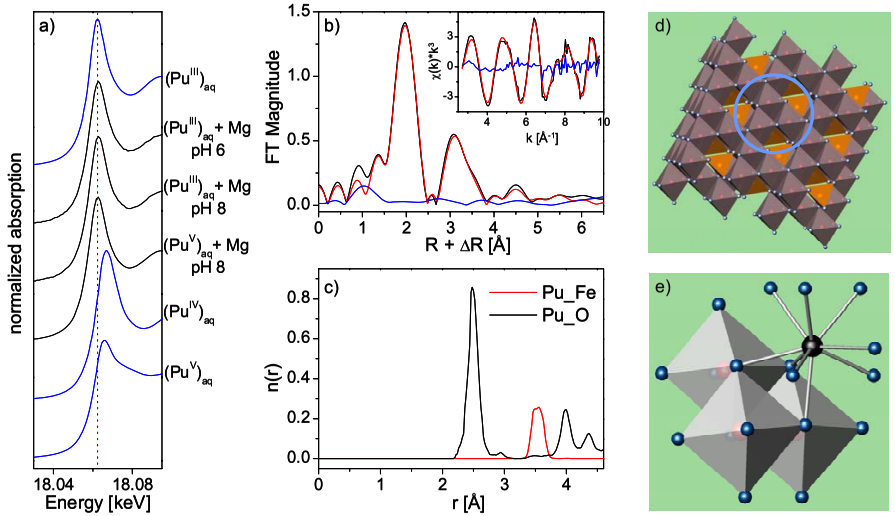

Figure 1. a) Experimetal Pu-L_{III} XANES spectra of Pu reacted with magnetite (black) and $(Pu^{III})_{aq}$, $(Pu^{IV})_{aq}$ and $(Pu^{V})_{aq}$ for reference (blue); b) experimental Pu-L_{III} EXAFS spectrum of Pu^{V}+Mg, pH8 sample and final spectrum resulting from radial refinement by MC simulation, FT and chi-spectrum (inset) (black - experimental, red - MC simulation, blue - residual); c) Pu-O and Pu-Fe radial pair distribution functions resulting from radial refinement. d) octahedrally terminated (111) face of magnetite with position of Pu(III) sorption circled e) sorption complex structure of Pu(III) on edge-sharing FeO_6-octahedra (Pu – black, O – blue, Fe – red).

References:

(1) Rossberg, A. et al. *Anal Bioanal Chem* **2003,** *376* (5), 631-638.

(2) Rossberg, A. and Scheinost, A. C. *Anal Bioanal Chem* **2005,** *383* (1), 56-66.

(3) Kirsch, R. et al., in prep. for Environ. Sci. Technol.

ROBL-CRG	**Experiment title:** EXAFS studies of the structure and bonding in solution of dioxouranium(VI)-nucleotide complexes	**Experiment number**: 20 - 01 - 695
Beamline: BM 20	**Date of experiment**: from: 01/11 29/01 to: 03/11/09 31/01/09	**Date of report**: 01/04/11
Shifts: 12	**Local contact(s)**: André Roßberg	*Received at ROBL:*

Names and affiliations of applicants (* indicates experimentalists):
A. Roßberg*, Z. Szabo
Helmholtz-Zentrum Dresden-Rossendorf e.V., Institute of Radiochemistry, P.O. Box 510119, 01314 Dresden, Germany

Experimental

The aim of this investigation was to prove the existence of the hexameric U(VI)-adenosine-monophosphate (AMP) complex proposed by NMR studies [1]. Eight aqueous samples were prepared in the pH range pH 9.63 to pH 11.36. According NMR at pH 9.63 49% and at pH 11.36 only 10% of the hexameric species is present. The other acting complex is a trimeric species which has nearly 90% at pH 11.36. Fig. 1 shows the proposed structure of the hexamer and the structure of the trimer [1]. The structure of the trimer was determined by XRD and NMR [1]. The UL_{III} EXAFS spectra of the pure complexes were isolated from the spectral mixtures by factor analysis [2].

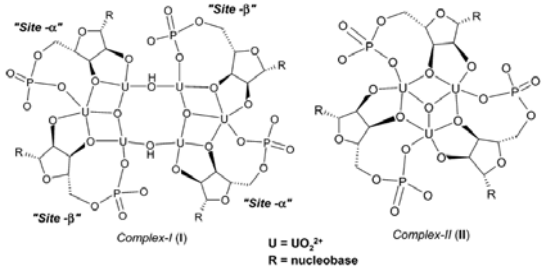

Fig. 1: Proposed hexameric (left) and trimeric U-AMP complex [1].

Results

Figure 2 contains the best shell fit for the hexamer and the trimer. The fit includes the axial oxygen atoms with the corresponding multiple scattering path, the equatorial(eq) oxygen atoms and the U-U interaction. In case of the hexamer the O_{eq} shell is splitting in two shells (2.30 Å, 2.49 Å) while the trimer shows only one major O_{eq} shell at 2.35 Å. Also the U-U distances are different. In case of the hexamer the U-U distance is 3.83 Å while for the trimer the U-U distance is 0.04 Å longer.

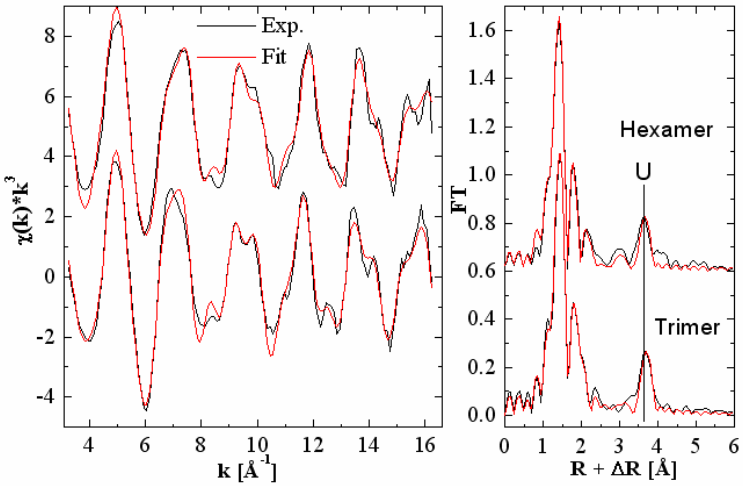

Fig. 2: EXAFS spectra of the hexamer and the trimer (left) with corresponding Fourier transform (FT) (right).

According the proposed hexameric structure (Fig. 1) at least three different U-U distances should be present, hence we expect a highly distorted or several U shell/s. At the moment we investigate this system also by UV-VIS and IR spectroscopy in order to understand the structural features of the hexamer represented by the EXAFS spectrum.

REFERENCES

1 Z. Szabo, I. Furo, and I. Csoregh, *Journal of the American Chemical Society* 127 (43), 15236 (2005).
2 A. Rossberg, T. Reich, and G. Bernhard, *Analytical and Bioanalytical Chemistry* 376 (5), 631 (2003).

	Experiment title: Redox behavior of neptunium species in solution	Experiment number: 20-01-696
Beamline: BM 20	**Date of experiment:** From 01/02/2010 to 02/02/2010	**Date of report:** 17.2.2011
Shifts: 3	**Local contact(s):** Christoph Hennig	*Received at ESRF:*

Names and affiliations of applicants (* indicates experimentalists):

Christoph Hennig*, Koichiro Takao*, Shinobu Tako*, Andreas C. Scheinost*

Helmholz-Zentrum Dresden-Rossendorf, Institute of Radiochemistry, Bautzner Landstrasse 400, 01314 Dresden Germany

Report:

Stability and coordination of Np(VI) and Np(V) acetate complexes in aqueous solution was studied by using UV-Vis-NIR and EXAFS spectroscopy [1]. In the Np(VI) acetate system, the formation of $Np^{VI}O_2(AcO)^+$, $Np^{VI}O_2(AcO)_2(aq)$, and $Np^{VI}O_2(AcO)_3^-$ were detected (Fig. 1). Both methods resulted in the comparable stability constants ($\log K_1 = 2.98 \pm 0.01$, $\log \beta_2 = 4.60 \pm 0.01$, $\log \beta_3 = 6.34 \pm 0.01$ from UV-Vis-NIR; $\log K_1 = 2.87 \pm 0.03$, $\log \beta_2 = 4.20 \pm 0.06$, $\log \beta_3 = 6.00 \pm 0.01$ from XAFS at $I = 0.30$ M $(H,NH_4)ClO_4$).

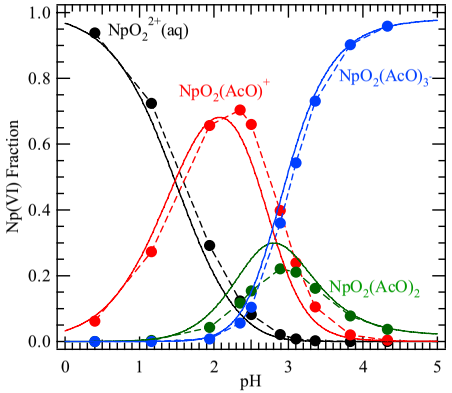

Figure 1. Species distribution of Np(VI) acetates derived from UV-Vis-NIR (solid lines) and XAFS (solid circles with dashed lines) spectroscopy at 0.015 M Np(VI) and 1 M AcOH in $I = 0.3$ M.

The extracted EXAFS spectra of $Np^{VI}O_2^{2+}(aq)$, $Np^{VI}O_2(AcO)^+$, and $Np^{VI}O_2(AcO)_3^-$ (Fig. 2) provided the structural data consistent with their stoichiometry, being well-explained by a bidentate coordination of acetate ($Np–O_{ax}$: 1.76-1.77 Å, $Np–O_{eq}$: 2.43-2.47 Å, $Np–C_c$: 2.87 Å, $Np–C_t$: 4.38 Å).

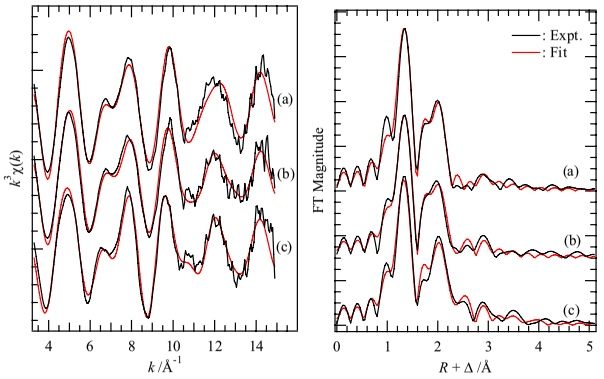

Figure 2. k^3-weighted Np L_{III}-edge EXAFS spectra (left) and their Fourier transforms (right) of individual Np(VI) species: $Np^{VI}O_2^{2+}(aq)$ (a), $Np^{VI}O_2(AcO)^+$ (b), $Np^{VI}O_2(AcO)_3^-$ (c).

Also, Np(V) forms complexes with acetate in 3 steps. The stability constants of $Np^{V}O_2(AcO)(aq)$, $Np^{V}O_2(AcO)_2^-$, and $Np^{V}O_2(AcO)_3^{2-}$ were determined by UV-Vis-NIR titration to $\log K_1 = 1.93 \pm 0.01$, $\log \beta_2 = 3.11 \pm 0.01$, $\log \beta_3 = 3.56 \pm 0.01$ at $I = 0.30$ M $(H,NH_4)ClO_4$. The present result is corroborated by the structural information from EXAFS ($Np–O_{ax}$: 1.83-1.85 Å, $Np–O_{eq}$: 2.51 Å, $Np–C_c$: 2.90-2.93 Å) and electrochemical behavior of the Np(V/VI) redox couple in the presence of AcOH as a function of pH.

Reference

[1] Takao, K., Takao, S., Scheinost, A.C., Bernhard, G., Hennig, C. Complex formation and molecular structure of neptunyl(VI) and –(V) acetates Inorg. Chem. **48** (2009) 8803-8810.

ROBL-CRG	**Experiment title:** EXAFS / XANES investigations of K volume-doped $CoTiO_3$	**Experiment number:** 20-01-697
Beamline: BM 20	**Date of experiment:** from: 20.01.2010 to: 21.01.2010; 02.03.2010 to: 05.03.2010	**Date of report:** 28.02.2010
Shifts: 6+9	**Local contact(s):** Dr. Andreas Scheinost	*Received at ROBL:*
Names and affiliations of applicants (* indicates experimentalists): Prof. Dr. Ulrich Simon, RWTH Aachen University, Germany Dr. Stefan Neumeier, IEK-6, FZ Jülich, Germany Dipl.-Chem. Clemens J. Belle*, RWTH Aachen University, Germany		

Scientific Background

The climate relevant exhaust gases of automobiles powered by fossil fuels are of topical public interest. One way to reduce these emissions is the usage of fuels based on regenerative sources. Such fuels will contain an increasing amount of ethanol, e.g. up to 10 % in Germany and 85 % in USA. For the purpose of engine management and exhaust after-treatment, specific in-situ gas sensors are required, which operate under these harsh conditions at elevated temperature. Fot that reason chemiresistors [1] appear to be tailor-made as in-situ ethanol-sensors. By the application of high-throughput impedance spectroscopy (HTIS) [2] K-doped $CoTiO_3$ was identified as the most promising material due to response behaviour and reproducibility [3]. Polycrystalline $CoTiO_3$ samples with different K amounts were prepared via a polyol-mediated synthesis and calcinated. Further detailed investigations of the influence of K-doping on the atomic structure will ultimatively enhance the comprehension of the complex interactions between the active sensing surface and the ambient gas atmosphere.

Experiments

The coordination chemistry and lattice structure of 2 at% K-doped $CoTiO_3$ is of particular interest with respect to the specific position of the potassium ions in the volume-doped material. Therefore, Ti-K edge and Co-K edge XANES and EXAFS spectroscopy was employed to investigate the electronic and molecular structure of Ti and Co in pristine and K-doped CoTiO3 samples (K ≤ 15 at%). The samples were measured as BN pellets in transmission mode at 15 K using a closed-cycle He cryostat. Data reduction and shell fitting was performed with WinXAS, using theoretical phase-shift and amplitude function calculated by FEFF8.2. The XANES and EXAFS spectra were also analyzed chemometrically using the ITFA software [4].

Results

Both Co-XANES and Ti-XANES showed no change with K-doping (Fig. 1), hence there is no detectable influence of K-doping on the electronic structure of these two elements. The same is true for the series of Co-EXAFS spectra, suggesting no change of the local structure around Co within the detection limit of the method. In contrast, the ITFA analysis showed four statistically significant components in the Ti-EXAFS spectra. The 2 at% K containing sample 3 is clearly discriminated from all other samples by factor 4 (Fig. 2, right). This factor is characterized by FT peaks in the 1 to 2.5 Å range (distance uncorrected for phase shift). The shell fit results in Table 1 showing significant structural changes of sample 3 versus the undoped sample 1, a shortening of the Ti-Co distance at 2.90 Å, and an extension of the Ti-Co distance at 3.44 Å.

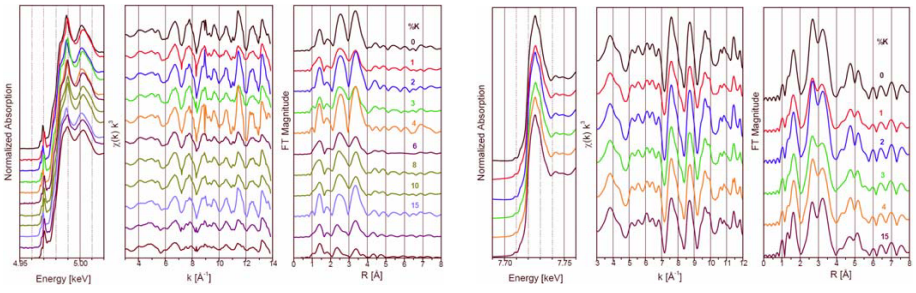

Fig. 1: Ti (left) and Co (right) K-edge XANES and EXAFS spectra as well as Fourier transform of volume-doped $CoTiO_3$ samples with different amounts of K dopant (0-15 %) at room temperature and ambient conditions.

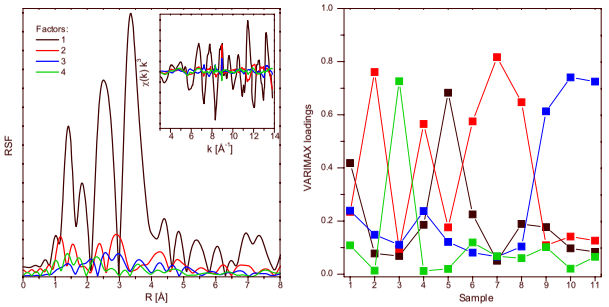

Fig. 2. Ti-K EXAFS factor analysis. Left: Factors 1 to 4 in R-space and in k-space (insert). Right: Varimax loadings of factors 1 to 4.

Table 1. Ti-K EXAFS shell fit results in comparison to the $CoTiO_3$ structure.

	$CoTiO_3$ XRD	AK-1 EXAFS	AK-1 EXAFS	AK-3 EXAFS	AK-3 EXAFS
	R / Å	R / Å	σ^2 / Å^2	R / Å	σ^2 / Å^2
3 O	1.87	1.87	0.0010	1.86	0.0010
3 O	2.09	2.08	0.0029	2.06	0.0031
1 Co	2.92	2.90	0.0010	2.87	0.0010
3 Ti	2.98	3.01	0.0017	3.00	0.0012
3 Co	3.39	3.44	0.0077	3.51	0.0071
6 Co	3.74	3.74	0.0018	3.73	0.0010

Literature

[1] M. E. Franke, T. J. Koplin, U. Simon, *Small* **2006**, *2(1)*, 110-118.
[2] M. Siemons, T. J. Koplin, U. Simon, *Appl. Surf. Sci.* **2007**, 254(3), 669-676.
[3] M. Siemons, U. Simon, *Sens. Actuat. B* **2007**, *126(2)*, 595-603.
[4] A. Rossberg; T. Reich, G. Bernhard, *Anal. Bioanal. Chem.* **2003**, *376,* 631-638.

ROBL-CRG	**Experiment title:** EXAFS investigations of Mg-Al layered double hydroxides containing Zr-IV, Hf-IV and Cd-II ions	**Experiment number:** 20-01-698
Beamline: BM 20	**Date of experiment:** from:20.01.2010 to: 21.01.2010	**Date of report:** 30.06.2010
Shifts: 6	**Local contact(s):** Dr. Andreas Scheinost	*Received at ROBL:*

Names and affiliations of applicants (* indicates experimentalists):

Hilde Curtius*, G. Kaiser, A. Neumann, D. Bosbach
Forschungszentrum Jülich, Institut für Energieforschung IEF-6,
Gebäude 05.3

D-52425 Jülich
Germany

The aim of the experiments was to give detail informations about the structural incorporation of different ions in the structure of Mg-Al layered double hydroxides. EXAFS investigations with Mg-Al layered double hydroxides containing Zr-IV, Hf-IV and Cd-II ions were performed. The samples were synthesised via the coprecipitation method and the following stoichiometries were obtained:

$[Mg_3Al_{0.93}Zr_{0.099}(OH)_8]Cl_{0.94}(CO_3)_{0.03}\ 2.71 \cdot H_2O$

$[Mg_3Al_{0,9191}Hf_{0.096}(OH)_8]\ Cl_{1,028}\ 2{,}27\ H_2O$

$[Mg_{2,91}Cd_{0,09}Al_1(OH)_8]Cl_{0,98}(CO_3)_{0,01}\ 1{,}91\ H_2O$

Prior to the EXAFS investigations results from XRD investigations showed that the LDHs were the only crystalline phases detected.

Layered double hydroxides of trivalent Al and either divalent Mg or 3d-metals are characterized by six-fold oxygen coordination of the metal, a nearest metal-metal distance in the range of 3.05 to 3.10 Å. The fit results are summarized in table 1.

In the **Zr-doped LDH** the Zirconium is in eight-fold oxygen coordination as supported by the coordination number of 7.6 and the distance of 2.14 Å. The DW of 0.0073 $Å^2$ shows a substantial structural disorder typical for eight-fold coordination. The second shell FT peak at about 3.25 Å is fitted by two Zr atoms at a distance of 3.57 Å. The observed k-wave amplitude distribution shows only one maximum at about 8.1 $Å^{-1}$, evidence that only heavier atoms like Zr can be present in this shell. In conclusion, first shell coordination, as well as distance and atomic nature of the second shell contradict incorporation of Zr into the crystal lattice of the MgAl-LDH.

As for the Zr-doped LDH the first-shell coordination number and distance suggest an 8-fold oxygen coordination for the **Hf-doped LDH** as well. A detailed wavelet analysis of the second shell shows backscattering from two different types of atoms. The best fit was achieved by using two shells with Al and Hf. The Hf-Hf distance of 3.37 Å is similar to that in orthorhombic hafnia (HfO_2, 3.39 Å). The longer Hf-Al/Mg distance of 3.63 Å could point towards a (monodentate?) sorption complex at LDH edge sites.

For the **Cd-doped LDH** the coordination shell is split into two shells. The first peak is fit by about 5 oxygen atoms at a distance of 2.26 Å, the distance in line with a 6-fold oxygen coordination of Cd(II). The second peak is fit by about one chlorine atom at a distance of 2.62 Å, the distance in line with a 6-fold chlorine coordination (e.g. 2.64 Å in $CdCl_2$). The Cd-O shell and the Cd-Mg/Al shell would rather point to a sorption complex than to a isomorphic substituation in LDH.

Table 1: EXAFS fit results

Phase	Edge	Fit	coord				Metal				ΔE_0	χ_{res}	S_0^2
			E	CN	R	σ^2	E	CN	R	σ^2			
Zr-doped LDH	Zr	A	O	7.6	2.14	0.0073	Zr	1.9	3.57	0.0088	-0.3	11.9	0.9
Hf-doped LDH	Hf	A	O	7.7	2.12	0.0078	Hf	2.7	3.37	0.0074	11.8	6.2	0.9
							Mg/Al	1.4	3.63	0.0014			
		B	O1	7.7	2.12	0.0078	Mg/Al	2.3	3.57	0.0041	11.8	8.9	0.9
		C	O2	7.7	2.12	0.0078	Hf	4.9	3.42	0.0117	11.7	8.8	0.9
Cd-doped LDH	Cd	A	O	4.9	2.26	0.0087	Mg/Al	1.0	3.17	0.0016	8.4	8.1	0.9
			Cl	0.9	2.62	0.0070	Cd	2.0	3.86	0.0131			

Especially the EXAFS results for the Zr-doped LDH are contrary to results of recent XRD investigations. Different Zr-doped LDHs (molar exchange of Al by Zr in the range between 4 and 20 %) were synthesied and analysed. The expected increase in the a lattice parameter was observed clearly while increasing the Zr amount. More detail work is in progress.

Experiment title: Comparative investigation of the uranium complexation onto γ-Al_2O_3 by means of FT-IR and EXAFS spectroscopy		Experiment number: 20-01-699
Beamline: BM20	**Date of experiment:** from: Jan 23 2010 to: Jan 26 2010	**Date of report:** 8/31/2010
Shifts: 9	**Local contact(s):** André Rossberg (rossberg@esrf.fr)	*Received at ESRF:*

Names and affiliations of applicants (* indicates experimentalists):

Katharina Mueller, Harald Foerstendorf, André Rossberg

Forschungszentrum Dresden-Rossendorf, Institute of Radiochemistry, P.O. Box 51 01 19, D-01314 Dresden, Germany

Report:

For a better understanding of the sorption mechanisms of uranium(VI) on solid alumina oxide phases, structural information on a molecular level of the surface complexes is needed. In our recent comprehensive studies, a dependence between the formation of different surface complexes and the contact time was found between the actinyl ions and the solid phase using in situ infrared spectroscopy. From the spectra, an outer-sphere coordination followed by surface precipitation or polymerization was deduced.

However, because of overlapping vibrational bands in the IR spectra obtained, generated as well by aqueous species and surface precipitate, further information of the molecular structures is required. In particular, a confirmation of the vibrational spectroscopic findings of surface precipitation and polymerization at higher U(VI) loading rates of the solid phase was a main goal of the EXAFS experiments.

Therefore, a series of batch samples of sorbed U(VI) onto alumina was prepared showing different degree of U(VI) loading. These samples were expected to reflect the different stages of the sorption processes in analogy to the IR spectra.

RESULTS

Five out of six samples provided EXAFS spectra of a sufficiently high quality for factor analysis (FA). Figure 1 shows the EXAFS spectra obtained and the corresponding FT's. The amount of U(VI) sorbed onto

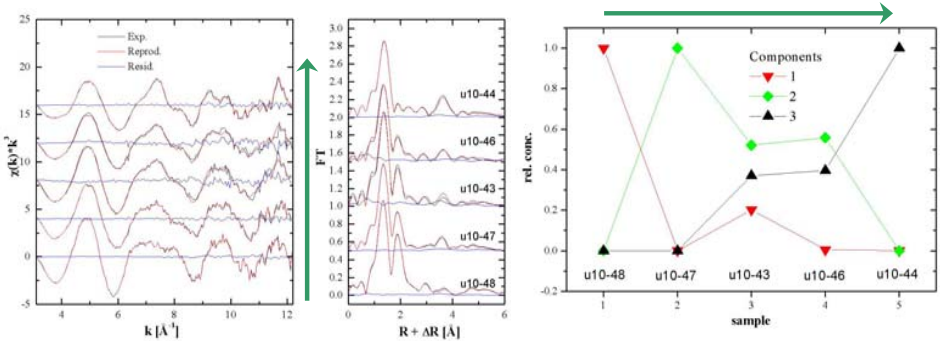

Fig. 1: EXAFS spectra (left panel) and the corresponding Fourier transforms (middle panel) of the batch samples of U(VI) on γ-Al_2O_3. The reproduced spectra after factor analysis (FA) and the residuals are also given. Composition of the three components obtained by FA in the samples (right panel). The arrows indicate the increasing U(VI) loading of the samples.

the solid phase was determined by ICP-MS and the spectra are listed with increasing U(VI) loading indicated by the arrow. In addition, the respective spectra reproduced by FA and the residuals are also given in the figure.

The main result of FA was the extraction of three components. The fractions of each component in the different samples change with the degree of U(VI) loading (Fig.1, right panel). Each component found by FA is tentatively assigned to different surface species upon comparison of the spectra with reference data.

Component 1 is obviously dominant at low U(VI) loading rates and most probably represents a sorption complex as it already suggested from IR spectra recorded during the first minutes after induced sorption. A detailed analysis and further experiments have to be carried for a comprehensive identification of this species.

Component 2 propably represents a sorption complex showing distinct U–U distances. This can be interpreted as a sorbed trimeric U(VI) species or another polymeric species formed under the prevailing conditions, that is an increased U(VI) loading.

Component 3 represents a surface precipitate, that is schoepite.

These findings confirm our previous results from IR spectroscopy of the proceeding sorption process. From these spectra, we assigned a characteristic spectral feature to the formation of a surface precipitate.

Future experiments will provide a more detailed insight into the early steps of U(VI) sorption on γ-Al_2O_3. In particular, additional structural information of the sorption complex (component 1) as well of the intermediate component 2 is still required. But also the impact of atmospheric carbonate on the sorption complexation has to be investigated. This will lead to a comprehensive description of the molecular processes occurring at the solid-liquid interface.

	Experiment title: **Redox behavior of neptunium species in solution**	**Experiment number:** 20-01-701
Beamline: BM 20	**Date of experiment:** From 05-03-10 to 09-03-10 23-04-10 to 25-04-10 28-08-10 to 31-08-10 22-09-10 to 25-09-10 27-11-10 to 28-11-10	**Date of report:** 17.2.2011
Shifts: 29	**Local contact(s):** Christoph Hennig	*Received at ESRF:*

Names and affiliations of applicants (* indicates experimentalists):

Christoph Hennig*, Koichiro Takao*, Shinobu Tako*, Andreas C. Scheinost*

Helmholz-Zentrum Dresden-Rossendorf, Institute of Radiochemistry, Bautzner Landstrasse 400, 01314 Dresden Germany

Report:

Tetravalent actinides show strong tendencies towards hydrolysis which promotes polynucleation and colloid formation of the hydroxides or oxides. We studied the complexation of U^{IV} and Th^{IV} with formate ($HCOO^-$) under moderately acidic condition.

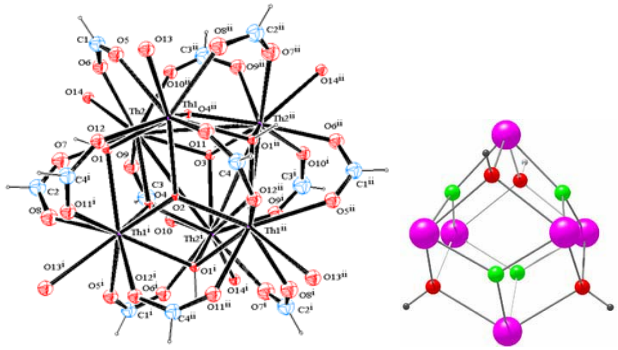

Fig 1. Structure of the complex

Left: ORTEP picture purple: Th; blue: C; red: O

Right: core structure (right, Purple, Th; green, μ_3-O; red; μ_3-OH; black, hydrogen) of **2**. Symmetry code i: x+1, y+1, z-1, and ii: x, y+1, z+1.

EXPERIMENTAL. Compound **1**: $[U_6(\mu_3\text{-}O)_4(\mu_3\text{-}OH)_4(HCOO)_{12}(H_2O)_6](N_2H_5)_2(ClO_4)_2\text{-}(H_2O)_{12}$, deposited from an aqueous solution containing 0.5 M U^{IV} with excess HCOOH at pH 2.5 through slow evaporation of the solvent. Compound **2**: $[Th_6(\mu_3\text{-}O)_4(\mu_3\text{-}OH)_4(HCOO)_{12}(H_2O)_6]Na_3(ClO_4)_{3.5}(H_2O)_{5.5}(H_3O)_{0.5}$ was obtained from an aqueous solution containing 0.05 M Th^{IV} and 1.0 M HCOOH at pH 1.0 during slow reduction of the solution volume by concentration. Crystal data were collected with a Bruker AXS SMART diffractometer at room temperature by using Mo-K_α radiation (λ = 0.71073 Å) monochromatized by a graphite crystal. X-ray absorption spectra of L_{III} edges of U^{IV} and Th^{IV} were recorded at ROBL.

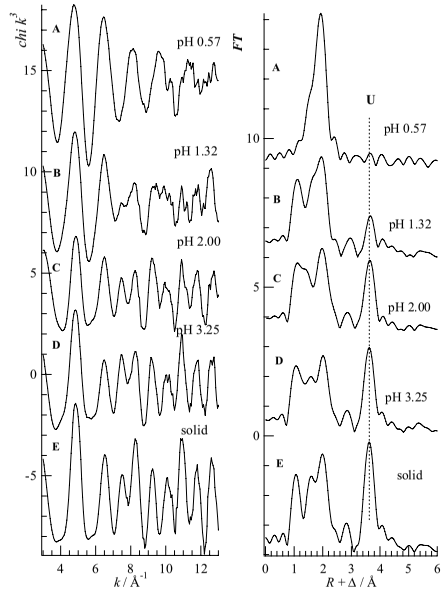

Fig. 2. k^3-weighted U L_{III}-edge EXAFS spectra (left) and their FTs (right) of aqueous solutions of U^{IV}-HCOOH, and of solid sample **1**. Phase shifts are not corrected on the FTs.

RESULTS. Fig. 1 shows the structure of **2** and its $[Th_6(\mu_3\text{-}O)_4(\mu_3\text{-}OH)_4]$ core. The crystal structure analyses of **1** and **2** reveal $[M_6(\mu_3\text{-}O)_4(\mu_3\text{-}OH)_4(HCOO)_{12}(H_2O)_6]$ cores. Each metal atom is surrounded by 4 O atoms from μ-$HCOO^-$, 4 O atoms from μ_3-oxygen, and 1 O atom of the terminal water molecule. Neighboring metal atoms are bridged by μ-$HCOO^-$ through a *syn-syn* coordination. Distortion of $\{\mu_3\text{-}O(H)\}_8$ hexahedra arises from the presence of two kinds of μ_3-oxygen atoms, i.e., μ_3-O^{2-} and μ_3-OH^-. In order to clarify the occurrence and stability range of the $[M_6\{\mu_3\text{-}O(H)\}_8]$ complexes in aqueous solution, EXAFS measurements were performed. Fig. 2 shows k^3-weighted EXAFS spectra and Fourier transforms of U^{IV} with 1.0 M HCOOH at different pH. With increasing pH, U···U interaction at $R + \Delta = 3.8$ Å becomes more significant indicating the presence of the complex in solution. The EXAFS spectrum at pH 3.25 shows strong similarity with that of the crystalline sample **1**. It can be concluded that $[U_6\{\mu_3\text{-}O(H)\}_8(HCOO)_{12}(H_2O)_6]$ is also formed as solution species. In contrast, $[Th_6\{\mu_3\text{-}O(H)\}_8(HCOO)_{12}(H_2O)_6]$ in the solution is always minor component under pH 1.0-3.5. This is probably related to the lower hydrolysis capacity of Th^{IV}.

REFERENCE

Takao, S., Takao, K., Kraus, W., Emmerling, F., Scheinost, A.C., Bernhard, G., Hennig, C. First hexanuclear U^{IV} and Th^{IV} formate complexes – structure and stability range in solution Eur. J. Inorg. Chem. (2009) 4771-4775.

ROBL-CRG	**Experiment title:** EXAFS investigations on uranium complexes formed by fungi and reference samples	**Experiment number:** 20 - 01 - 702
Beamline: BM 20	**Date of experiment:** 23/06/10 – 24/06/10 02/12/10 – 05/12/10	**Date of report:** 31/01/11
Shifts: 12	**Local contact(s):** André Roßberg	*Received at ROBL:*

Names and affiliations of applicants (* indicates experimentalists):
A. Günther[1], A. Roßberg*[2], C. Hennig*[2], A. Scheinost*[2]
[1]Helmholtz-Zentrum Dresden-Rossendorf e.V., Institute of Radiochemistry, P.O. Box 510119, 01314 Dresden, Germany
[2]ESRF-ROBL/CRG, Avenue des Matryrs, B.P. 220, 38043 Grenoble Cedex, France

Report:

Experimental

The aim of this study was to determine the structural parameters of the formed uranyl complex species in fungal cells of the *Schizophyllum commune*. The fungal cells were cultivated in an organic liquid full medium. The biomass was harvested and washed with mineral medium. For sorption experiments, the fungal biomass was resuspended (300 mg dry weight / L) in uranium containing mineral medium in a concentration range from $2 \cdot 10^{-6}$ M to $4 \cdot 10^{-4}$ M at pH 4 and 6 at room temperature. After 24 hours the cells were separated from the medium by filtration and washed with 0.1 M $NaClO_4$. Then, the fresh fungal biomass was put into polyethylene sample holders surrounded with Capton tape and shock frozen in liquid nitrogen. The U L_{III}-edge spectra were measured in fluorescence mode at 15 K using a closed-cycle He-cryostat. The EXAFS spectra were analyzed using the program suite EXAFSPAK /1/. The theoretical scattering phases and amplitudes were calculated by using X-ray structural data of meta-autunite and uranyl-triacetate with the scattering code FEFF8.2 /2/.

Results

Figure 1 shows the raw U L_{III}-edge k^3-weighted EXAFS spectra and their corresponding Fourier transforms (FT) of uranium containing fungal cells incubated with $8 \cdot 10^{-5}$ M uranium containing mineral medium at pH 4 and 6 and measured at 15 K after shock freezing of the samples. In all spectra the contribution of two axial oxygen atoms U-O_{ax} at a distance of 1.77-1.78 Å and one oxygen shell with very short distances between uranium and equatorial oxygen atoms of 2.28-2.30 Å were obtained.

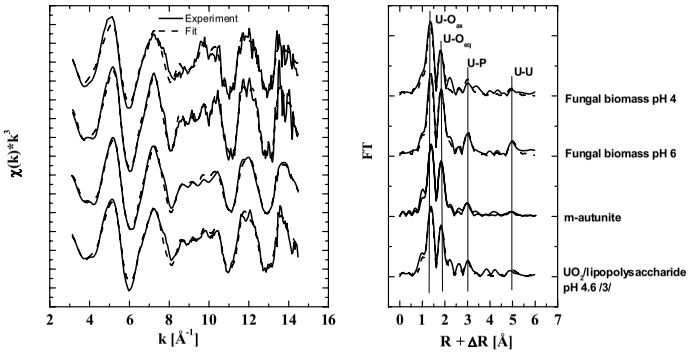

Fig. 1. Raw U L_{III}-edge k^3-weighted EXAFS spectra (left) and corresponding Fourier transforms (right) of uranium containing fungal cells and selected reference samples

Additionally, uranium-phosphorus interactions with a radial distance of 3.59 Å were found and support the TRLFS results, that uranium is mainly bound to phosphate groups on/in the fungal cells. U-U interactions are visible with a radial distance of 5.23-5.24 Å. The number of the coordinated oxygen atoms ($N_{U\text{-}Oeq}$) and phosphorus atoms ($N_{U\text{-}P}$) are different. They are higher in uranyl fungal species formed at pH 6 ($N_{U\text{-}Oeq}$=$N_{U\text{-}P}$=3.8) than those observed at pH 4 ($N_{U\text{-}Oeq}$=$N_{U\text{-}P}$ =2.7). All the spectra including the determined structural parameters could be described with the spectra of the m-autunit first of all, particulary the spectra of uranyl fungal species formed at pH 6. Also the EXAFS spectra of uranyl coordinated by lipopolysaccharide /3/, an organic uranyl phosphate, is very similar to the spectra of uranyl fungal species formed at pH 6 but differs from the spectrum in case of pH 4. So we assume, that at pH 4 and low uranium initial concentration a part of uranium is coordinated in a different way than observed for the other samples. This would support the TRLFS results again.

References

/1/ George, G. N., Pickering, I. J.: EXAFSPAK A Suite of Computer Programs for Analysis of X-Ray Absorption Spectra. Stanford Synchrotron Radiation Laboratory, Stanford, CA. USA. (1995)

/2/ Ankudinov et al.: Real-space multiple scattering calculation and interpretation of x-ray absorption near-edge structure, Phys. Rev. B 58 (1998), 7565-7576

/3/ A. Barkleit, project 20-01-661

ROBL-CRG	**Experiment title:** Structural investigation of complex of TcO_4^- and ReO_4^- with MIDOA by EXAFS spectroscopy	**Experiment number:** 20-01-703
Beamline: BM 20	**Date of experiment:** from: 16/9/2010 to: 18/9/2010	**Date of report:**
Shifts: 3	**Local contact(s):** Dipanjan Banerjee	*Received at ROBL:*
Names and affiliations of applicants (* indicates experimentalists): Morihisa Saeki*[1,2] and Harald Foerstendorf[1] ([1]Forschungszentrum Dresden-Rossendorf, [2]Japan Atomic Energy Agency)		

Report:

Introduction Recently, a new extractant, 2,2'-(methylimino) bis(N,N-dioctyl-acetamide) (MIDOA; Fig. 1) was synthesized by researchers of Japan Atomic Energy Agency [1]. The MIDOA extractant has high extraction ability for oxyanions, such as MO_4^- (M=Tc and Re), in liquid-liquid extraction, although the mechanism remains unresolved. To understand the mechanisms of liquid-liquid extraction by MIDOA, the structure of the MO_4^-–MIDOA complex was investigated. We observed infrared spectra of the complex by ATR FT-IR spectroscopy and analyzed them based on calculated structures and frequencies by density functional theory (DFT). As a result, the conformation shown in Fig. 2 was suggested as the most stable structure of MO_4^-–MIDOA, assuming that oxidation state of MO_4^- is kept constant during the extraction process. However, this assumption has not been assured. In this work we tried to get information about the oxidation state in the extraction and geometrical parameters of the MO_4^-–MIDOA complex by extended X-ray absorption fine structure (EXAFS) spectroscopy, in order to confirm the structure determined by IR spectroscopy and DFT calculation.

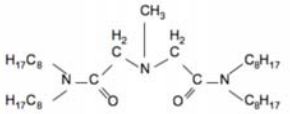

Figure 1: Structural formula of MIDOA

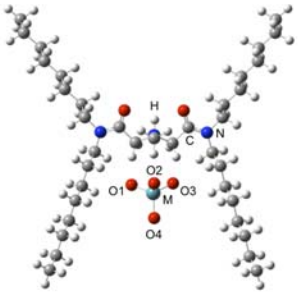

Figure 2: Suggested structure of the MO_4^-–MIDOA complex

Table 1: Geometrical parameters of MO_4^-–MIDOA at B3LYP/cc-pVDZ

Bond length (Å)	Tc	Re
M–O1	1.723	1.737
M–O2	1.735	1.748
M–O3	1.725	1.739
M–O4	1.704	1.721

Experimental The EXAFS samples, dodecane (DD) solution of the MO_4^-–MIDOA complex, were prepared by liquid-liquid extraction. At first, the DD solution of 100mM MIDOA (organic phase) was mixed with aqueous solution of 200mM HCl and 5–10mM KMO_4 (M=Tc and Re) (aqueous phase). The solution composed of organic and aqueous phases was shaken for 3 hours at room temperature. After 10-min centrifugation, the organic phase was separated and used as the sample. The EXAFS measurements were performed by using absorption edges of 21.05 keV for Tc(K) and of 10.53 keV for Re(LIII). The spectra were energy calibrated using Mo-K edge (20 004 eV).

Results The EXAFS measurement was performed for the DD solutions of the 5-mM MO_4^-– MIDOA complex (M-1), 10-mM MO_4^-–MIDOA complex (M-2) and the 200-mM HCl solutions of 5-mM MO_4^- (M-3), where M indicates ^{99}Tc and Re. Fig. 3 shows the Fourier transform magnitude (FTM) of the Tc and Re samples. Both FTM spectra of Tc and Re are dominated by the Tc–O and Re–O coordination shell. Two small peaks at 2.1 and 2.7 Å in Tc are 3-legged and 4-legged multiple scattering contributions from the Tc-O shell, respectively The coordination number (CN), radial distance (R) and Debye-Waller factor (σ^2), which were obtained by analysis of Fig. 3, are listed in Table 2. The uncertainty of these values is ±0.5 for CN, ±0.005Å for R and ±0.0005Å^2 for σ^2. Table 2 suggests that the CN values of all samples are 4 (within its uncertainty limit). It agrees with the fact that the Tc and Re metals are dissolved in the HCl solution as TcO_4^- and ReO_4^-, and indicates that their oxidation states are kept constant in the organic phase. The radial distance slightly increases from the Tc samples (1.72–1.73Å) to the Re samples (1.73–1.74Å). In both Tc and Re samples the radial distance hardly change by formation of the complex between MO_4^- and MIDOA. The calculated geometrical parameters of the MO_4^-–MIDOA complex are shown in Table 1, which suggest that the average bond length of M–O is 1.722Å and 1.736Å for Tc and Re, respectively. The calculated bond lengths are in good agreement with the R values by EXAFS. From Table 1 standard deviation of M–O is calculated to be 0.0129Å and 0.0112Å for Tc and Re, respectively. This results is also consistent with small Debye-Waller factors in Table 1, which are 0.0009–0.0014Å^2 for Tc and 0.0025–0.0031Å^2 for Re. Thus, we confirmed that the MO_4^-–MIDOA complex has the structure shown in Fig. 2.

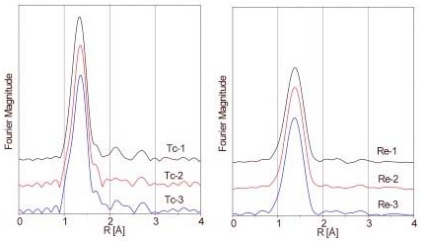

Figure 3: The FTM spectra of the Tc and Re complex

Table 2: Tc-K and Re-LIII edges EXAFS shell fit results.

Samples	CN	R	σ^2
Tc-1	4.0	1.72	0.0014
Tc-2	3.5	1.72	0.0009
Tc-3	3.8	1.73	0.0013
Re-1	4.2	1.74	0.0031
Re-2	4.0	1.74	0.0025
Re-3	4.4	1.73	0.0034

Acknowledgements We are grateful to Dr. D. Banerjee and Dr. A. C. Scheinost for their experimental support.

Reference

[1] Y. Sasaki, Y. Kitatsuji and T. Kimura, Chemistry Letter, Vol.36, 2007, p1394-1395.

ROBL-CRG

Experiment title:	Experiment number:
EXAFS investigation of sorbed selenium oxyanions onto anatase	20-01-704

Beamline:	Date of experiment:	Date of report:
BM 20	from: 24.11.2010 to: 27.11.2010 (9 shifts)	31.1.2011
Shifts:	**Local contact(s):**	*Received at ESRF:*
9	Andreas Scheinost	

Names and affiliations of applicants (* indicates experimentalists):

Norbert Jordan*

Helmholtz Forschungszentrum Dresden-Rossendorf, Institute of Radiochemistry, Bautzner Landstrasse 400, 01314 Dresden / Germany

Report:

For the first time, the mechanism leading to the retention of selenium(VI) and selenium(IV) onto pure anatase (a polymorph titanium dioxide TiO_2 with a tetragonal structure), as well as the nature of the sorbed species were elucidated by using XAS spectroscopy. Defined amounts of 0.1 M Se(VI) and Se(IV) stock solution (0.1 M NaCl, pH 4) were added to suspensions of TiO_2. To avoid an activation of anatase photocatalytic properties (Sanuki et al., 1999), all bottles were covered by aluminum foil. The starting suspensions consisted of 5 x 10^{-5} M Se, in NaCl 0.1 M as background electrolyte. The pH-dependence sorption of selenium(VI) and selenium(IV) onto anatase was studied from pH 3.5 to 5.0 and from pH 3.5 to 8.0, respectively. To check whether the Se(IV) surface loading or the ionic strength had an influence on the nature of the sorbed surface complexes (at constant pH), additional samples with a lower initial concentration of 10^{-5} M Se and a lower ionic strength (NaCl 0.01 M) were also prepared. After 3 days of stirring to reach sorption equilibrium, the samples were ultracentrifuged during 1 h at 285000 g and the slurries loaded as a wet paste in a sample holder, which was then sealed with Kapton tape. Great care was taken to exclude O_2 during sample transport and storage by keeping them in liquid N_2. At the beamline, they were rapidly (2 min) transferred to the closed-cycle He cryostat, where they were kept at 15 K for the XAS measurements. XANES and EXAFS spectra of Se reacted anatase were recorded on the Se K edge (E_0 = 12 658 keV) in fluorescence mode at the Rossendorf Beamline at ESRF (Grenoble, France). Corrections of energy and fluorescence deadtime as well as averaging of scans (4 to 12 depending on Se loading) were performed with SixPack, while data reduction steps and shell fitting were performed with WinXAS 3.1. The theoretical scattering phases and amplitudes were calculated using the scattering code FEFF8.2.

Fig. 1 shows the results of EXAFS measurements conducted on samples of selenium(VI) and selenium(IV) adsorbed onto anatase at pH 3.5, i.e. the Fourier transform magnitude corresponding to radial structure functions (RSF). Concerning Se(IV), there is clear evidence of two shells in the RSF: a Se–O shell (fit with ~3 O_2 at 1.69 Å) and a Se–Ti shell (fit with ~2 Ti at 3.38 Å). The best assignment of the bonding environment for selenite onto anatase is a bidentate binuclear surface complex. Neither the pH nor the selenium surface loading had an influence on the geometry of the sorbed surface species (data not shown).

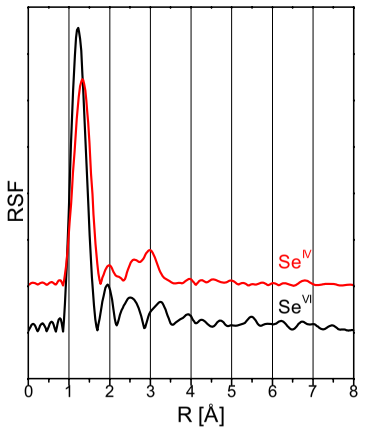

Fig. 1. Fourier transforms of Se(VI) (black) and Se(IV) (red) sorbed onto anatase at pH 3.5.

In the selenium(VI) reacted anatase sample (Fig. 1), the data could be fitted with approximately four O atoms at a distance of ~1.64 Å. The lack of second shell Se-Ti distance evidences that the sorption of selenate onto anatase proceeds via the formation of outer-sphere complexes.
Our findings are in good agreement with previous studies of selenium oxyanions adsorption on other minerals. Indeed, selenium(IV) has consistently been observed to form bidentate binuclear bridging complexes onto goethite (Hayes et al., 1987; Manceau and Charlet, 1994; Missana et al., 2009; Peak and Sparks, 2002; Su and Suarez, 2000), HFO (Manceau and Charlet, 1994), hematite (Catalano et al., 2006), Hydrous Aluminum Oxide (Peak, 2006) and γ-Al_2O_3 (Elzinga et al., 2009). Concerning selenium(VI), Elzinga et al. (2009) also evidenced by EXAFS the formation of non-protonated outer-sphere surface complexes during selenium(VI) sorption onto hydrated γ-Al_2O_3 surface (pH range 4-7.6).This study will also help to constrain the stoichiometries used during the surface complexation modeling of these two binary systems.

Acknowledgements We are grateful to Dr. C. Hennig, Dr. D. Banerjee and Dr. A. Rossberg for their experimental support.

References:

Catalano, J. G., Zhang, Z., Fenter, P., and Bedzyk, M. J., 2006. Inner-sphere adsorption geometry of Se(IV) at the hematite (100)-water interface. *J. Colloid Interface Sci.* **297**, 665-671.

Elzinga, E. J., Tang, Y. Z., McDonald, J., DeSisto, S., and Reeder, R. J., 2009. Macroscopic and spectroscopic characterization of selenate, selenite, and chromate adsorption at the solid-water interface of γ-Al_2O_3. *J. Colloid Interface Sci.* **340**, 153-159.

Hayes, K. F., Roe, A. L., Brown, G. E., Hodgson, K. O., Leckie, J. O., and Parks, G. A., 1987. In situ X-ray absorption study of surface complexes: Selenium oxyanions on α-FeOOH. *Science* **238**, 783-786.

Manceau, A. and Charlet, L., 1994. The mechanism of selenate adsorption on goethite and hydrous ferric-oxide. *J. Colloid Interface Sci.* **168**, 87-93.

Missana, T., Alonso, U., Scheinost, A. C., Granizo, N., and Garcia-Gutierrez, M., 2009. Selenite retention by nanocrystalline magnetite: Role of adsorption, reduction and dissolution/co-precipitation processes. *Geochim. Cosmochim. Acta* **73**, 6205-6217.

Peak, D., 2006. Adsorption mechanisms of selenium oxyanions at the aluminum oxide/water interface. *J. Colloid Interface Sci.* **303**, 337-345.

Peak, D. and Sparks, D. L., 2002. Mechanisms of selenate adsorption on iron oxides and hydroxides. *Environ. Sci. Technol.* **36**, 1460-1466.

Sanuki, S., Kojima, T., Arai, K., Nagaoka, S., and Majima, H., 1999. Photocatalytic reduction of selenate and selenite solutions using TiO_2 powders. *Metall. Mater. Trans. B-Proc. Metall. Mater. Proc. Sci.* **30**, 15-20.

Su, C. M. and Suarez, D. L., 2000. Selenate and selenite sorption on iron oxides: An infrared and electrophoretic study. *Soil Sci. Soc. Am. J.* **64**, 101-111.

	Experiment title: XAS study of dense $U_{1-y}Am_yO_{2-x}$ (y=0.10 ; 0.15; 0.20) obtained by conventional powder metallurgy	**Experiment number**: 20-01-705
Beamline: BM20	**Date of experiment**: from: 03/09/10 to: 07/09/10	**Date of report**: 05/01/11
Shifts: 12	**Local contact(s)**: SCHEINOST Andreas	*Received at ESRF:*

Names and affiliations of applicants (* indicates experimentalists):

D. PRIEUR [1*], P. M. MARTIN[2*], A. JANKOWIAK [1], , E. GAVILAN [1*], C. LEORIER [1], N. HERLET [1]

[1] CEA Marcoule - DEN/DTEC/SDTC/LEMA – 30207 Bagnols-sur-Cèze
[2] CEA Cadarache – DEN/DEC/SESC – 13108 Saint Paul Lez Durance

Report:

Partitioning and Transmutation of MA is the key issue for reducing nuclear waste radiotoxicity. $U_{1-y}Am_yO_{2-x}$ blankets are promising fuels for the transmutation of Minor Actinides (MA) in Fast Neutron Reactors.The $U_{1-y}Am_yO_{2-x}$ fabrication is challenging due to the high oxygen potential of the AmO_{2-x}. These oxides exhibit a significantly higher equilibrium oxygen potential in comparison to other actinide oxides such as UO_2 [1]. An accurate control of the sintering atmosphere is necessary to achieve the targeted O/M value. As a consequence, a thermodynamical modelling is currently developed to determine optimum sintering conditions for given O/M ratios and MA content. Due to the lack of experimental data in the U-Am-O system [2] to refine the modelling, an experimental determination of the O/M ratio is mandatory as also its eventual consequences on the homogeneity of the solid solution. The present work focuses on the XAS characterization of $U_{1-y}Am_yO_{2-x}$.

For this experiment, $U_{1-y}Am_yO_{2-x}$ (y=0.10; 0.15; 0.20) compounds were fabricated using conventional powder metallurgy process [3]. To study Am and U chemistry as a function of oxygen potenitial, samples were sintered in in various moisture-added Ar containing 5% of H_2 atmospheres. For each sample, fluorescence and transmission signals were collected at the uranium L_{II}, uranium L_{III} and the americium L_{III} edges. Energy calibrations were achieved using Y, Mo and Zr foil located after the second ionization chamber. All measurements were performed at 20K using the closed-cycle a helium cryostat. At both uranium L_{III} and americium L_{III} edges, EXAFS spectra were collected up to 18 $Å^{-1}$ but only up to 13.2 $Å^{-1}$ for uranium L_{II} edge. This limitation is due to the presence of a small amount of neptunium resulting from the ^{241}Am decay.

In a first part, we investigated the effect of the oxygen potential studying three $U_{0.85}Am_{0.15}O_{2\pm x}$ samples sintered in different atmospheres. The Am L_{III} edge XANES spectra of both $U_{0.85}Am_{0.15}O_{2\pm x}$ compounds and references ($Am^{+IV}O_2$ and mixed (U^{+IV},Am^{+III}) oxalate) are presented in Figure 1. It shows that the XANES spectra remain identical to the signal collected for the Am^{+III} reference compound. Thus, the oxidation state of americium is Am^{+III} whatever the sintering atmosphere. As already osberved in [4], Am^{+IV} is easily reduced in Am^{+III}. The U L_{III} edge XANES spectra, presented in Figure 2, point out the difference of the white line position for each spectrum. This shift is due to the decreasing of the U^{4+}/U^{5+} ratio while the oxygen potential increases. It indicates that, during the sintering, a total reduction of Am^{+IV} to Am^{+III} and a partial oxidation of U^{+IV} to U^{+V} are occuring. The oxidation of U^{+IV} to U^{+V} is enhanced as the oxygen potential increasing. The O/M ratios were calculated for each compounds using the determined oxidation state of U and Am. The results show that the O/M increase with the oxygen potential; which is in agreement with the expected results. These additional experimental data are currently used to refine the thermodynamical modelling

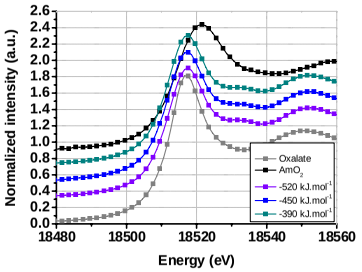

Figure 1: Am L_{III} edge XANES spectra

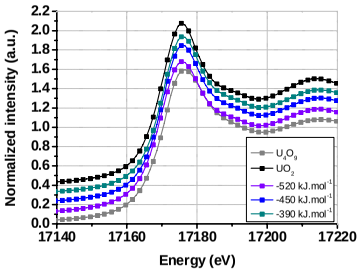

Figure 2: U L_{III} edge XANES spectra

In a second part, the effect of the Am was investigated studying $U_{1-y}Am_yO_{2-x}$ compounds with different Am contents (y=0.10; 0.15; 0.20). These materials were sintered in the same sintering conditions, i.e. reducing conditions. The collected Am L_{III} edge and U L_{III} edge XANES, presented in Figure 3, indicates that the Am oxidation state remains unchanged at +III while there is a U^{+IV}/U^{+V} mixted valence depending on Am content.

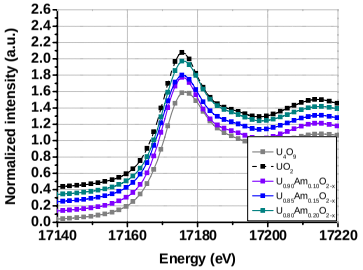

Figure 3: U L_{III} edge XANES spectra

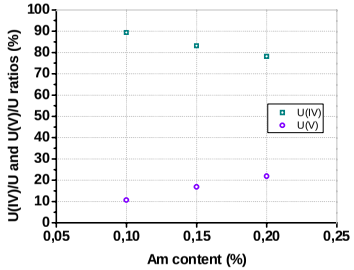

Figure 4: U^{+IV}/U and U^{+V}/U ratios as a function of Am content

The Figure 4 presents both U^{+IV}/U and U^{+V}/U ratios as a function of the Am content. According to linear fit, the U(V) molar fraction y' can be expressed by the equation (1).

$$y' = \alpha y(1-y) \quad (1)$$

Therefore, the solid solution can be described by $U^{4+}_{(1-\alpha y)(1-y)}U^{5+}_{\alpha y(1-y)}Am^{3+}_{y}O_{2-x}$ .for these sintering conditions.

The EXAFS analyses are still in progress.

[1] T. M. Besmann et T. B. Lindemer, "Chemical thermodynamic representations of <PuO_{2-x}> and <$U_{1-z}Pu_zO_w$>", Journal of Nuclear Materials, vol. 130, 489-504 (1985)

[2] W. Bartscher et C. Sari, "A thermodynamic study of the uranium-americium oxide $U_{0.5}Am_{0.5}O_{2\pm x}$", Journal of Nuclear Materials, vol. 118, 220-223 (1983)

[3] D. Prieur et al., "Fabrication and characterization of minor actinides bearing fuels obtained by conventional powder metallurgy process", Powder Technology (2010)

[4] P.M. Martin et al., "XAS investigation of (U,Am)O_2 and (U,Pu)O_2 solid solutions obtained by oxalic co-precipitation", ESRF, experimental report form CH-2738, (2009)

ROBL-CRG	**Experiment title:** Sorption and redox reaction of Sn^{II} and Sn^{IV} at the magnetite/water interface in presence and absence of organic ligands	**Experiment number:** 20-01-708
Beamline: BM 20	**Date of experiment:** from: 07-11-2010 to: 11-11-2010	**Date of report:** 19-03-2011
Shifts: 9	**Local contact(s):** Dr. Andreas Scheinost	*Received at ROBL:*
Names and affiliations of applicants (* indicates experimentalists): Siriwan Dulnee (Inst. of Radiochemistry, HZDR)		

Report:

Tin is a widespread contaminant in the environment due to its use in antifouling paints, PVC plastics and pesticides. Furthermore, the fission product ^{126}Sn is of substantial concern for nuclear waste disposal because of a rather long half-life (10^5 years). In contrast to its significance, the geochemistry of tin is not well understood, especially at neutral pH and low ionic strength. For tin concentrations lower than 10^{-7} M, Sn^{II} is assumed to be soluble, whereas Sn^0 and Sn^{IV} precipitates at favorable pH and Eh conditions. Hydrolysis products of Sn are controversially discussed, pointing to a large variety of possible hydrolysis species including polynuclear species similar e.g. to the early actinides. Currently, there exist only few data on the sorption of Sn^{II} and Sn^{IV} to relevant minerals in soils and sediments, showing both strong pH dependence and pH-independence of sorption – corresponding to the uncertainty of tin aqueous species. Finally, the redox equilibria between Sn^{II} and Sn^{IV} are under debate, hence the currently predicted prevalence of Sn^{IV} even under reducing conditions may be questioned. Therefore, significant research gaps exists in terms of tin aqueous speciation, sorption and redox, making predictions about the environmental behaviour and fate of tin, including ecotoxicity, rather uncertain. This is particularly true for anoxic conditions, which are of relevance for marine sediments (antifouling paints) as well as radwaste repositories (^{126}Sn).

As part of a wider investigation to be completed in the next two years, we have studied the local structure and oxidation state in the Sn(II)/magnetite/water system under varying pH, and under cryostatic conditions to maintain O_2-free conditions (see Figure). The XANES edge position, the oxygen coordination number of 6 and the Sn-O distance of 2.05 Å are all in line with Sn(IV), hence complete oxidation of Sn(II) took place within 24 h reaction time. Beyond the coordination sphere, two Sn-Fe paths could be fitted, indicative of edge-sharing and corner-sharing linkages between Sn(IV) ocathedra and Fe octahedra, suggesting inner-sphere complexation at the magnetite surface. With decreasing pH, the Sn-Fe distances become shorter and coordination numbers increase.

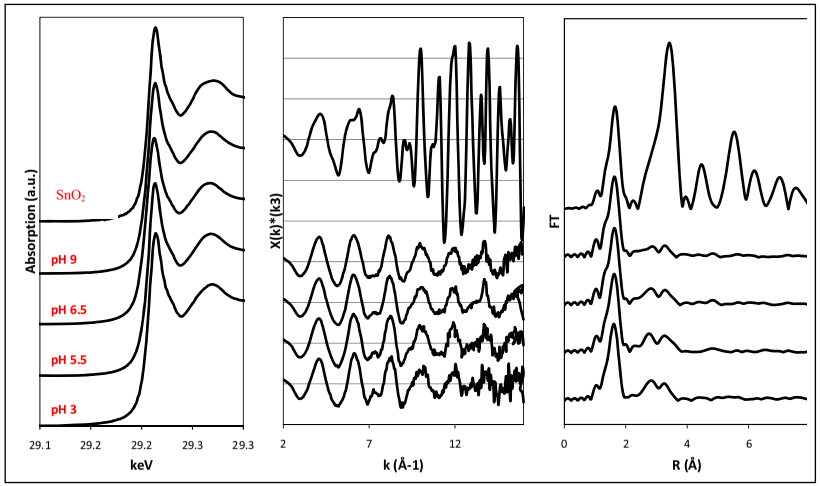

Figure 1. Sn K-edge XANES (left), EXAFS (middle), and Fourier transform (right) spectra of pH series of Sn-sorbed magnetite.

Table 1. EXAFS curve fit results of SnO_2 and Sn-sobed magnetite

Sample		Residual	Path	CN	Distance R	σ^2	E^0 shift	Area under XAFS paths
SnO_2		5.661	Sn - O	6	2.05	0.0026	10.1	49
			Sn - Sn	2.3	3.19	0.0022	10.1	40
			Sn - Sn	8.4	3.72	0.0022	10.1	100
Sn-sorbed magnetite	pH 3	8.102	Sn - O	6.1	2.05	0.0041	9.9	100
			Sn - Fe	1.2	3.14	0.0037	9.9	21
			Sn - Fe	3.4	3.58	0.0076	9.9	24
	pH 5.5	8.981	Sn - O	6.1	2.05	0.0040	9.7	100
			Sn - Fe	0.9	3.15	0.0012	9.7	26
			Sn - Fe	1.7	3.60	0.0025	9.7	26
	pH 6.5	9.040	Sn - O	5.9	2.05	0.0040	9.8	100
			Sn - Fe	0.9	3.16	0.0016	9.8	24
			Sn - Fe	1.6	3.60	0.0033	9.8	22
	pH 9	8.511	Sn - O	6.1	2.05	0.0038	9.9	100
			Sn - Fe	0.6	3.17	0.0018	9.9	15
			Sn - Fe	1.2	3.62	0.0038	9.9	14

ESRF	**Experiment title:** Free and silica-gel-bound tetraazamacrocycles as complexing agents of actinide cations: investigation of the solid-state coordination scheme.	**Experiment number**: CH-2423
Beamline: BM 20	**Date of experiment**: from: 14/02/2009 to: 17/02/2009	**Date of report**: October 12, 2009
Shifts: 9	**Local contact(s)**: Dr. Andreas SCHEINOST (scheinost@esrf.fr)	*Received at ROBL:*

Names and affiliations of applicants (* indicates experimentalists):

*Dr. Michel MEYER
Institut de Chimie Moléculaire de l'Université de Bourgogne
(ICMUB - UMR 5260 du CNRS)
9, avenue A. Savary
21078 DIJON Cedex

*Dr. Andreas SCHEINOST
Rossendorf Beamline at ESRF (ROBL - BM 20)

Report: Speciation of actinides in the presence of organic ligands is a topic that is extremely significant to the safe disposal of nuclear wastes resulting from the use of fission technologies, to assess the contamination risks in case of accidental release of radionuclides in the environment, to design new separation processes and remediation technologies, or to predict the behavior of radionuclides in biological systems. Most importantly, the migration and bioavailability of actinides in the biosphere are highly dependent upon the presence of both artificial and natural chelators. Currently, the systematic studies on complex formation of actinides with organic ligands are far beyond those of inorganic ligands. This is clearly reflected by the Nuclear Energy Agency (NEA) monograph series entitled *Chemical Thermodynamics*. Only one among the eleven volumes of this series reports data for actinide complexes with organic ligands, albeit in a limited number (only data for EDTA, oxalic, citric, and isosaccharinic acids are compiled). The same is valid for the overviews about studies on X-ray absorption spectroscopy of the actinides. The goal of our ongoing **chelation studies of uranium(VI) and plutonium(IV)** is to collect reliable **structural** and **thermodynamic solution data** (i.e. binding constants) by combining XAFS, potentiometric, and spectrophotometric measurements performed under strictly controlled experimental conditions with technologically and/or environmentally relevant ligands. Among them, two classes of compounds were targeted in this experiment, namely **polyaminocarboxylic acids** on the one hand and **siderochelates** like hydroxamic acids on the other.

1. Polyaminocarboxylic acids

Although known for more than 50 years and in spite of their technological, environmental and medicinal significance (the storage tanks on the US Hanford site are reputed to contain ca. 80 t of EDTA among the 350 000 m^3 of wastes, while DTPA is currently the only FDA-approved *in-vivo* decorporating agent for plutonium), solution equilibrium studies of ligands such as EDTA, CDTA, or DTPA with respect to 5f-elements are extremely scarce and most often unreliable as pointed out by the IUPAC and NEA-sponsored reviews. In that context, the applicants unraveled the complexation thermodynamics of Pu^{4+} with $EDTA^{4-}$, $CDTA^{4-}$, and $DTPA^{5-}$ in nitric media by means of potentiometry and visible spectrophotometry.[1] The purpose of this experiment was to complete these speciation studies of Pu^{4+} by XAFS measurements in order to gain insight into the structure of the various solution species. Hence, 9 samples of predefined pH were analyzed at room temperature. Moreover, these studies performed at the 0.05 M concentration level should also enable to validate the pH-dependent Pu speciation and thus ascertain the accuracy of the equilibrium constants measured at the millimolar concentration range.

2. Natural and biomimetic siderochelates

Until recently, siderophores have been perceived mainly as selective iron chelators that are excreted by most bacteria to solubilize ferric hydroxide and supply them with iron(III) as an essential nutrient. Indeed, ferric siderophore complexes are recognized by specific membrane proteins and transported inside the bacterial cell. However, such ligands may engage in a diverse chemistry with a variety of important metal ions, including actinides. It turns out that a more complex paradigm is required to describe their participation in bio- and geochemical processes. The general aim of our studies in that area is to investigate in-depth the complex formation of actinides with natural or synthetic siderophores.

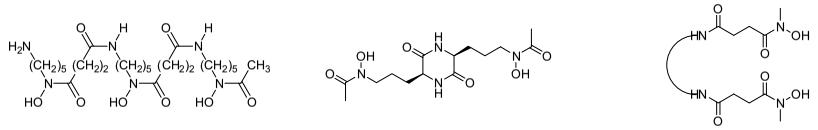

Figure 1. Chemical structure of desferrioxamine B (left), rhodotorulic acid (middle), and of the dihydroxamic analog studied herein (right, the curved line represents a propyl chain).

In the present experiment, we focused our attention on the UO_2^{2+} complexes formed in aqueous solution with two linear hydroxamic acids, the ubiquitous siderophore desferrioxamine B and a dihydroxamic analog of rhodotorulic acid (Figure 1). Preliminary equilibrium studies pointed towards the formation of various protonated species of $[UO_2(LH_x)]^{x+}$ general formula. Based on the stability constants, distribution diagrams were computed that enabled to define pH ranges where each species predominates. Accordingly, 3 room-temperature U L_{III}-edge spectra were collected for each ligand at such predefined pH values (Figure 2) in order to confirm the speciation of U(VI) and to assess the geometrical features related to the coordination sphere of uranium. Numerical modeling of the experimental spectra is under progress.

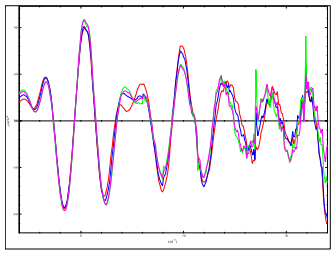

Figure 2. Overlay of the U L_{III}-edge EXAFS spectra of uranium(VI)-desferrioxamine B solutions recorded at three different pH values with that corresponding to an acidic $UO_2(NO_3)_2$ solution (red).

1 M. Meyer, R. Burgat, S. Faure, B. Batifol, J.-C. Hubinois, H. Chollet, R. Guilard, *C. R. Chimie* **2007**, *10*, 929-947.

ESRF	**Experiment title:** XAS investigation of (U,Am)O2 and (U,Pu)O2 solid solutions obtained by oxalic co-precipitation	**Experiment number:** CH- 2738
Beamline: BM20	**Date of experiment:** from: 15 may 2009 to: 19 may 2009	**Date of report:**
Shifts: 12	**Local contact(s):** Andreas Scheinost	*Received at ESRF:*

Names and affiliations of applicants (* indicates experimentalists):

P. M. Martin*[,1], B. Arab-Chapelet*[,2], S. Grandjean[2], S. Arpigny[2], E. Welcomme*[,2]

[1] CEA, DEN, DEC, 13108 St Paul Lez Durance, France.

[2] CEA, DEN, DRCP, BP 17171 F-30207 Bagnols-sur-Cèze Cedex, France

Report:

Innovative fuel cycles are currently studied within the framework of the fourth generation (GEN-IV) nuclear reactors development. The two main objectives of these fuel cycles are an efficient use of energetic resources by recycling together the major and valuable actinides such as uranium and plutonium, and a drastic decrease of the radiotoxicity of the ultimate wastes by partitioning and transmutating the minor ones such as americium, curium or neptunium. Indeed, the challenge is to be able to incorporate a large amount (up to ~20 at.%) of highly radioactive minor actinide into the mixed (U,Pu) nuclear fuel. Moreover, only a fluorite type solid solution, as in case of pure $(U,Pu)O_2$, has to be obtained for the final product.

Rather than a mechanical mixing of pulverulent compounds, as in the actual MOX manufacturing process, innovative synthesis methods based on co-precipitation are currently developed [1]. In particular, the oxalic co-precipitation of U(IV) and Pu(III) followed by the thermal conversion of the co-precipitate into oxide, was recently optimized in the CEA Atalante facility at Marcoule. Characterization on mixed U(IV)-An/Ln(III) oxalate structures [2] indicated that a solid solution with the generic formula $M_{2+x}U^{IV}_{2-x}An^{III}_{x}(C_2O_4)_5.nH_2O$ (M = monocharged cation) can be expected. The originality of this mixed oxalate is based on a mixed crystallographic site which can accept either a tetravalent actinide or a trivalent one. Monovalent cations equilibrate the charge in the structure depending on the molar ratio of An(III) to An(IV). Thermal conversion of the co-precipitates should lead to an ideal $(U,An)O_2$ fluorite-type solid solution. As demonstrated in a previous study [3], it must be noted that EXAFS appears to be the lone technique that could outline a discrepancy in cation local environments.

For this experiment we focused on one concentration: 10%. The following systems were characterized: $(U_{0.9}Pu_{0.1})$, $(U_{0.9}Am_{0.1})$, $(U_{0.9}Gd_{0.1})$ and $(U_{0.9}Ce_{0.1})$ and for each systems mixed oxalate and mixed oxide samples were analysed. XAS spectra for both cations were collected at 30K using He-cryostat. Energy calibrations were accomplished using Y foil (17 038 eV) or Mo foil (20 000 eV) positioned after the second ionization chamber. EXAFS curve fitting was performed in k^3 for R values in the range 1.5–4.4 Å for both edges. Phases and amplitudes for the interatomic scattering paths were calculated with the code FEFF8.40.

The XANES collected on mixed oxalates are compared with reference compounds in Figure 1. Conclusions are clear concerning oxidations states: for all samples uranium cation is +IV while americium and plutonium cations are +III. Thus, as in the case of U(IV)-Ln(III) mixed oxalate the trivalent state for americium and plutonium is now demonstrated.

Results of EXAFS fit performed on $(U_{0.9},Pu_{0.1})$ and $(U_{0.9},Am_{0.1})$ samples are summarized in Tables 1 and 2. The crystallographic structure of U(IV)-An/Ln(III) oxalates indicates that each cation is surrounded by 5 oxalate ligands (C_2O_4).

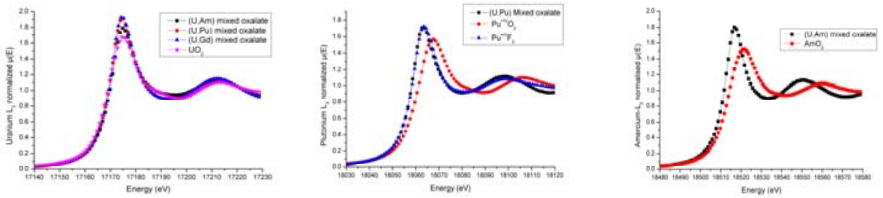

(a) Uranium L_3 *(b) Plutonium L_3* *(c) Americium L_3*

Figure 1: XANES spectra collected on mixed oxalate samples

	N	DW(Å^2)	R (Å)
U-O	10.7(5)	0.006	2.46(1)
U-C	9.2(5)	0.004	3.28(1)
U-O	10(1)	0.004	4.56(2)

(a) Uranium L_3

	N	DW(Å^2)	R (Å)
Pu-O	10.5(5)	0.007	2.53(1)
Pu-C	10.0(5)	0.004	3.32(1)
Pu-O	10.5(5)	0.004	4.60(2)

(b) Plutonium L_2

Table 1: Fit results on $(U_{0.9},Pu_{0.1})$ mixed oxalate sample

	N	DW(Å^2)	R (Å)
U-O	9.4(5)	0.006	2.45(1)
U-C	9.9(5)	0.007	3.28(1)
U-O	10(1)	0.016	4.50(2)

(a) Uranium L_3

	N	DW(Å^2)	R (Å)
Am-O	10.4(5)	0.007	2.50(1)
Am-C	9.0(5)	0.007	3.32(1)
Am-O	10(1)	0.004	4.54(2)

(b) Americium L_3

Table 2: Fit results on $(U_{0.9},Am_{0.1})$ mixed oxalate sample

As observed in Tables 1 and 2, coordination numbers for the three shells corresponding to the C_2O_4 ligands are equal to ~10 for each cation. These results confirm the presence of 5 oxalate ions around U(IV), Pu(III) and Am(III) cations in the mixed $(U_{0.9}Pu_{0.1})$ and $(U_{0.9}Am_{0.1})$ oxalates. For a same compound, the only significant differences observed between the two actinides are distances which are systematically shorter around uranium than around Pu or Am. These differences can be explained by the difference of ionic radii between U+IV and trivalent Pu and Am, but values are unknown for such cations coordinated with 10 atoms. To check this assumption, we can compared mean distances calculated from XRD cell parameters using atoms positions determined for U-Ln(III) [2] with which measured with EXAFS.

	U(Pu)-O	U(Pu)-C	U(Pu)-O
XRD (Å)	2.48	3.29	4.53
EXAFS (Å)	2.47 (2)	3.29 (2)	4.56 (4)

(a) $(U_{0.9},Pu_{0.1})$ mixed oxalate

	U(Am)-O	U(Am)-C	U(Am)-O
XRD (Å)	2.46	3.29	4.52
EXAFS (Å)	2.46 (2)	3.29 (2)	4.50 (4)

(b) $(U_{0.9},Am_{0.1})$ mixed oxalate

Table 3: Mean distances calculated from XRD results and measured by EXAFS

As shown in Table 3, a very good agreement can be observed between XRD and EXAFS. Thus, **by combining conventional XRD and XAS characterizations we have demonstrated that results obtained on U(IV)-Ln(III) (synthesis of an ideal solid solution) can be extended to $(U^{+IV}_{0.9}Pu^{+III}_{0.1})$ and $(U^{+IV}_{0.9}Am^{+III}_{0.1})$ systems.**

Concerning $(U_{0.9}Pu_{0.1})O_2$ and $(U_{0.9}Am_{0.1})O_2$ samples, due to experimental difficulties during the calcination step both mixed oxide samples are hyperstoichiometric with a massive oxidation of uranium IV to VI. As in the case of plutonium sample, the validity of the process was already shown with previous experiment [4], the demonstration remains to be performed with $(U,Am)O_2$. Moreover, unexpectedly the conditions was not sufficient to oxidize Am^{+III} ions to Am^{+IV} even with a large amount oxygen content in the furnace atmosphere. Thus, new experiments are needed to explore $(U,Am)O_2$ system in function of calcination conditions and americium concentration and a new proposal on this subject will be deposited at the ESRF.

References

[1] S. Grandjean *et al* J. Nucl. Mat. 385(2009)204-207.
[2] B. Arab-Chapelet *et al,* J. Solid State Chem. 178(2005)3046-3054.
[3] P. Martin *et al*, J. Alloys and Compounds, 444-445(2007)410-414.
[4] P. Martin *et al*, ESRF exp. report MA233 (2007) and ACTINIDES 2009 conference, Abstract 12A5.

ESRF	**Experiment title:** Structure of uranyl-arsenate complexes sorbed on bentonite	**Experiment number:** CH-2739
Beamline: BM 20	**Date of experiment:** from: 10/12/2008 to: 12/12/2008; 10/04/2009 to: 14/04/2009	**Date of report:** 01/09/2009
Shifts: 18	**Local contact(s):** Dr. Andreas Scheinost	*Received at ESRF:*

Names and affiliations of applicants (* indicates experimentalists):

E. Suess*[1,3], G. Bernhard[2], WA. Gezahegne*[1], BJ. Merkel[1], B. Planer-Friedrich*[3], AC. Scheinost*[2,4]

[1]Institute for Geology, TU Bergakademie Freiberg, 09599 Freiberg, Germany
[2]Institute for Radiochemistry, Research Center Dresden, 01314 Dresden, Germany
[3]Environmental Geochemistry, University of Bayreuth, 95447 Bayreuth, Germany
[4]ESRF-ROBL/CRG, 38043 Grenoble Cedex, France

Report:

Background. The occurrence of solid uranyl-arsenate phases such as Troegerite, $UO_2(H_2AsO_4)_2 \cdot H_2O$ and $UO_2(HAsO_4) \cdot 4H_2O$ in nature and as products of laboratory synthesis[1] indicate interactions between uranium (VI) and arsenate (V) and thus the existence of dissolved uranyl-arsenate species. Yet, little is known about the environmental relevance, stability conditions and structural characteristics of aqueous uranyl-arsenate species. Although solid uranyl-arsenate phases are known to be less soluble in natural waters, Rutsch et al.[2] were able to identify and report the existence of three aqueous uranyl-arsenate species in the pH range 1 to 3. Based on analogies to their uranyl-phosphate counterparts, they have been assigned as $UO_2(HAsO_4)_{(aq)}$, $UO_2H_2AsO_4^+{}_{(aq)}$, $UO_2(H_2AsO_4)_{2(aq)}$. Since effective strategies for rehabilitation of uranium and arsenic contaminated waters depend on the understanding of the speciation in such waters, the formation of aqueous uranyl-arsenate complexes has to be recognized as a potential factor controlling arsenic and uranium mobility and sorption behaviour. Recent TRLFS studies[3] have shown that a fourth uranyl arsenate species ($UO_2AsO_4^-$) was identified for the first time in the pH range between 7 and 8.5. With EXAFS, it was aimed to reaffirm the existence of the aquoeus uranyl-arsenate species. Although TRLFS is suitable for species identification, this technique provides no structural information of these complexes, neccassary to asses the behaviour of uranyl-arsenates in natural systems and for U and As remediation processes. Thus the task of the proposed XAS studies was to characterize the structure of aqueous uranyl-arsenate complexes existing at different pH-values from pH 2 to 8.

Experimental. Uranyl-arsenate solutions were prepared with uranyl to arsenate ratios of 1 to 10 using uranyl concentration levels of 0.01 mM, 0.05 mM and 1 mM at pH values of 2, 4, 5, and 7.5. Filtered solutions (0.2 µm cellulose acetate filters) were pipetted into PE sample holders, covered with kapton® tape and enclosed in a heat-sealed PE body as second confinement against radionuclide release. To gurantee stability of the aqueous complexes, samples were immediately flash-frozen and stored in liquid N_2 prior their analyses with XAS. Furthermore a uranyl-arsenate precipitate was prepared from a solution containing equimolar uranyl and arsenate concentations of 5 mM at pH 3.3. X-ray absorption spectroscopy spectra were recorded at the uranium L_{III}-edge (17185 eV) at the ESRF beamline BM-20 (Rossendorf Beamline - ROBL). Both transmission and fluorescence modes were used for sample measurements using argon-filled ionization chambers resp. a 13-element Ge-detector (Canberra) with a sample orientation of 45° and a detector orientation of 90° to the incident beam. To guarantee sample stability, avoid photo-induced redox-processes, and improve complex detectability, samples were measured at 15 K with a closed-cycle He-cryostat[4]. The EXAFS spectra were averaged, deadtime corrected and processed according to standard procedures[5] using the suit of programs EXAFSPAK[6]. Theoretical scattering phases and amplitudes are calculated using the scattering code FEFF 8.4.

Results. To find a concentration level of uranium where EXAFS measurements could be preformed without the formation of uranyl-arsenate precipitates, a wide range of uranyl concentration levels from 0.01 mM up to 1 mM were tested. The pre-experiments to check the essential concentrations necessary to obtain acceptable EXAFS spectra at low uranyl concentations have shown that extremely long measuring times for the samples were required as well as concentrations above 0.01 mM. Consequently, only part of the proposed samples, i.e. only the liquid samples with the established minimum concentration could be measured in the allocated beamtime span, setting aside the solid samples.
Only one sample with concentration levels of 0.05 mM uranyl and 0.5 mM arsenate at pH 2 showed aqueous uranyl-arsenate species in dissolved state (Tab. 1). This was indicated by the comparison of the determined U-As bond distance of the sample with that of known uranyl-arsenate minerals. The U-As bond distance of 3.3 Å of the sample indicated a bidentate coordination which is significantly different from the U-As bond distance of 3.7 Å characteristic for the monodentate coordination in uranyl-arsenate minerals, e.g. troegerite and the uranyl-arsenate precipitate from the present study (Tab. 1). At higher pH and concentration levels, the measured samples showed U-As bond distances of around 3.7 Å indicating the formation of precipitates. However, in the present study we present for the first time the identification and structural characterization of an aqueous uranyl-arsenate species existing at pH 2 using XAS.

Table 1. Structural parameters of aqueous uranyl-arsenate complexes and precipitate from XAS analyses at the uranium L_{III} –edge.

Samples	Shell	R[Å] [a]	N	σ^2 [Å^2]	ΔE0 [eV]
0.05 mM uranyl + 0.5 mM arsenate pH = 2	U-Oax	1.78	2 [b]	0.00351	0.8
	U-Oeq	2.39	4 [b]	0.00533	0.8
	U-As	3.39	2 [b]	0.00288	0.8
uranyl-arsenate precipitate	U-Oax	1.77	2 [b]	0.00139	-2.3
	U-Oeq	2.27	4 [b]	0.00418	-2.0
	U-As	3.68	2.75	0.00220	-2.0
	U-U1	5.37	2.53	0.00192	-2.0

[a] R ± 0.02 Å, [b] fixed, σ^2 Debye-Waller factor.

References.

(1) Barten, H.; Cordfunke, EHP; *Thermochim. Acta*, **1980**, *40*, 367
(2) Rutsch, M.; Geipel, G.; Brendler, V.; Bernhard, G.; et al. *Radiochim. Acta* **1999**, 86, 135.
(3) Charlet, L.; Scheinost, AC.; Tournassat, C.; et al., *Geochim. Cosmochim. Acta* **2007**, 71, 5731.
(4) Gezahegne, W; Geipel, G; Planer-Friedrich, et al. A TRLFS and EXAFS Investigation of Uranyl Arsenate Complexes in Acidic and Alkaline Aqueous Media; (in preparation for ES&T)
(5) Konigsberger, DC. *In:* Absorption. Principles, Application, Techniques of EXAFS, SEXAFS and XANES. 1st ed., John Wiley and Sons, Inc; New York, 1988
(6) George, GN.; Pickering, IJ. *In:* EXAFSPAK – A suite of computer Programs for Analysis of X-ray Absorption Spectra, SSRL; 1995

ESRF	**Experiment title:** Study of americium and plutonium chemistry in MOX fuel oxide	**Experiment number:** CH 2967
Beamline: BM20	**Date of experiment:** from: 06/02/2010 to: 10/02/2010	**Date of report:** 08/2010
Shifts: 9	**Local contact(s):** Andreas Scheinost	*Received at ESRF:*

Names and affiliations of applicants (* indicates experimentalists):

P. Martin*, R. Belin*, A.C. Robisson, J.C. Dumas

CEA, DEN, DEC, 13108 St Paul-lez-Durance, France

Report:

Innovative Mixed OXide (MOX) (U,Pu)O_{2-x} fuels for sodium fast neutron reactors (SFR's) systems are currently studied within the framework of the fourth generation (GEN-IV) nuclear reactor systems. GEN-IV's main purpose is to use energetic resources more efficiently by recycling valuable actinides such as uranium and plutonium. SFRs will also be able to burn long-lived minor actinides (MA) such as Am, Np and Cm recovered from used fuel leading to a drastic decrease in their potential radiotoxicity and the heat load for the final disposal. Among MA, americium is of main concern. Two options are considered: (a) homogeneously adding americium to the fuel in small amount (homogeneous mode) or (b) introducing it in higher concentration into fertile blankets (heterogeneous mode) [1]. Regarding the first option, MOX fuel incorporating up to 6% AmO_2 is a promising candidate [2].

Because they significantly affect the sintering properties as well as irradiation performances, the oxygen potential and the oxygen to metal (O/M) ratio are important factors to be considered when designing oxide fuels. Therefore, a thorough knowledge of the correlation between oxygen potential and O/M ratio is essential. To determine this relationship, an experimental determination of U, Pu and Am oxidation states as a function O/M in MOX fuel is needed.

The aim of this experiment was to follow the chemistry of uranium, plutonium and americium, and in particular their oxidation states, in (U, Pu, Am)O_{2-x} samples sintered under different oxygen potentials.

To this purpose, MOX samples with the following composition $(U_{0.750}Pu_{0.246}Am_{0.004})O_{2-x}$, were manufactured at the LEFCA facility at CEA Cadarache (France) using the COCA process (CObroyé CAdarache). This involved direct co-milling of the oxides and leads to a homogeneous plutonium distribution [3]. Three sets of samples were manufactured and sintered at 1750°C for 4 hours. Moisty conditions are given in table 1 as well as calculated oxygen potential (μO_2).

Sintering conditions	μO_2 (kJ.mol^{-1})
Ar 95% + H_2 5% + 200 ppm H_2O	-446
Ar 95% + H_2 5% + 90 ppm H_2O	-467
Ar 95% + H_2 5%	-506

Table 1 : sintering condition (O_2 impurity is taken equal to 20 ppm).

XANES spectra collected for U, Pu and Am cations are compared with reference compounds in Figure 1. As expected the oxidation state of uranium cations remains equal to +IV for the 3 compositions. Americium-L_{II} XANES also shows no variation up to the highest oxygen potential of -446 kJ.mol^{-1}, *i.e.* is always trivalent. A different behaviour is observed for plutonium with a slight shift of both white line maxima and first inflexion point of Pu-L_{III} XANES to a lower energy as a function of μO_2. Thus, a reduction of Pu^{+IV} to Pu^{+III} is clearly evidenced.

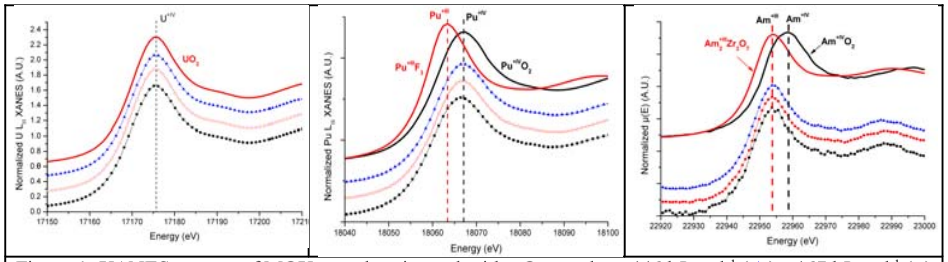

Figure 1: XANES spectra of MOX samples sintered with μO_2 equal to -446 kJ.mol^{-1} (▲), -467 kJ.mol^{-1} (○) and -506 kJ.mol^{-1} (■) compared with reference compounds (full lines).

By fitting XANES spectra collected on MOX samples with a linear combination of reference compounds relative concentrations of the Pu^{+III} and Pu^{+IV} could be determined. For Pu^{+IV} we used spectrum collected on PuO_2 and for Pu^{+III} we tested the fit using the spectra collected on PuF_3 or (U^{+IV},Pu^{+III}) mixed oxalate [4]. In both cases, we obtained the same values. Based on these results, the O/M ratio for the three sintering conditions have been calculated. Results are given in Table 2.

μO_2 (kJ.mol^{-1})	Pu cation repartition (%)		O/M
	Pu^{+IV}	Pu^{+III}	
-506	0.80	0.20	1.973
-467	0.88	0.12	1.984
-446	0.92	0.08	1.989

Table 2: Plutonium cations percentage and calculated O/M ratio.

Local environment around uranium and plutonium are compared in Figure 2. It reflects the XANES evolution: The lack of modification as a function of O/M observed around U ions is in agreement with the fixed U^{+IV} valency observed in XANES spectra. Whereas, slight modifications are present around Pu cations especially the intensity loss of coordination shells which indicates an increase disorder. This last observation is consistent with the Pu^{+III} occurrence in the fluorine structure.

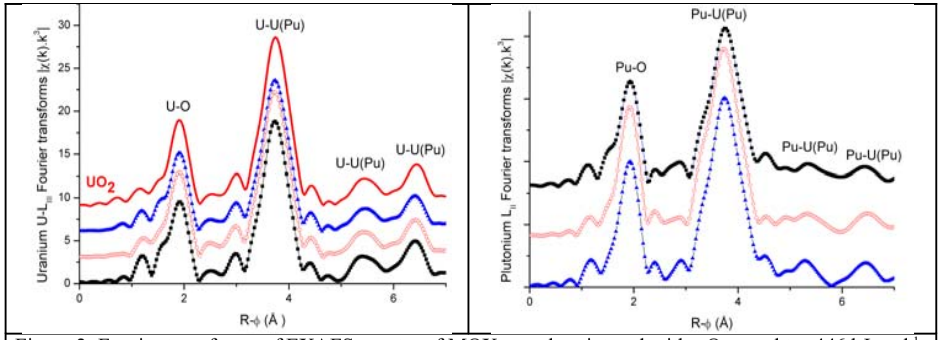

Figure 2: Fourier transforms of EXAFS spectra of MOX samples sintered with μO_2 equal to -446 kJ.mol^{-1} (▲), -467 kJ.mol^{-1} (○) and -506 kJ.mol^{-1} (■) compared with reference compounds (full lines).

Our results show that for substoichiometric $(U_{0.750}Pu_{0.246}Am_{0.004})O_{2-x}$ samples, americium reduction occurs more readily than plutonium reduction. Americium cations are fully reduced to Am^{+II} before any reduction of plutonium cations is observed. Moreover, uranium cations remain tetravalent. To our knowledge, it is the first time that experimental information on such a topic is reported. Thermochemical calculations to validate the model suggested by these results are in progress. The next step will be the study of MOX samples doped with a higher concentration of americium (~5%).

References

[1] "Actinide and fission product portioning and transmutation" – Status and assessment report, NEA, OECD, 1999.

[2] T. Wakabayashi *et al.*, Nucl. Technol. 118, (1997) 14.

[3] Y. Guerin *et al.*, in: ANS Internationl Topical Meeting on LWR Fuel Performance, Park City, UT, USA, ANS, La Grange Park, IL, 2000, p. 706.

[4] P. Martin *et al.*, ESRF experimental Report CH-2738 (2009).

ESRF	**Experiment title:** Investigation of the molecular structure of actinide solvent extraction compounds	**Experiment number:** CH-2969
Beamline: BM 20	**Date of experiment:** from: 4/12/2009 to: 8/12/2009	**Date of report:** 1/07/2010
Shifts:	**Local contact(s):** C. Hennig	*Received at ROBL:*

Names and affiliations of applicants (* indicates experimentalists):

Clara Fillaux*, Christophe Den Auwer*, Gaëlle Dupouy*, Thomas Dumas*, Samir Dahou*, Xavier Crozes*

CEA Marcoule, DEN/DRCP/SCPS, 30207 Bagnols-sur-Cèze, France

Report:

XAS measurements have been carried out on U(VI), Pu(IV), Np(IV)and Th(IV), in presence of nitric acid and tributylphosphate (TBP) solution. The data were acquired at the An L_3 edges, for each complex (17166 eV for U, 16300 eV for Th, 17610 eV for Np, 18057 eV for Pu).

Data fitting were carried out in R space, phases and amplitudes were calculated by Feff8 code on the basis of structures obtained from quantum chemical calculations on $UO_2(NO_3)_2(TBP)_2$, $Th(NO_3)_4(TBP)_2$, $Np(NO_3)_4(TBP)_2$ and $Pu(NO_3)_4(TBP)_2$ systems.
Three calculations were performed for the U(VI) complex: i) with two nitrates in bidentate coordination, ii) with one nitrate in bidentate coordination and one nitrate in monodentate coordination, iii) with two nitrates in monodentate coordination. Three calculations were also performed for the Pu(IV) complex: I) with four nitrates in bidentate coordination, ii) with three nitrates in bidentate coordination and one nitrate in monodentate coordination, iii) with two nitrates in bidentate coordination and two nitrates in monodentate coordination.

Figure 1 presents the Fourier transform of the EXAFS L_3 edge of U(VI) and Pu(IV) complexes. Fits performed with one or two monodentate nitrates did not reproduce the experimental spectra, for both U(VI) and Pu(IV) complexes.

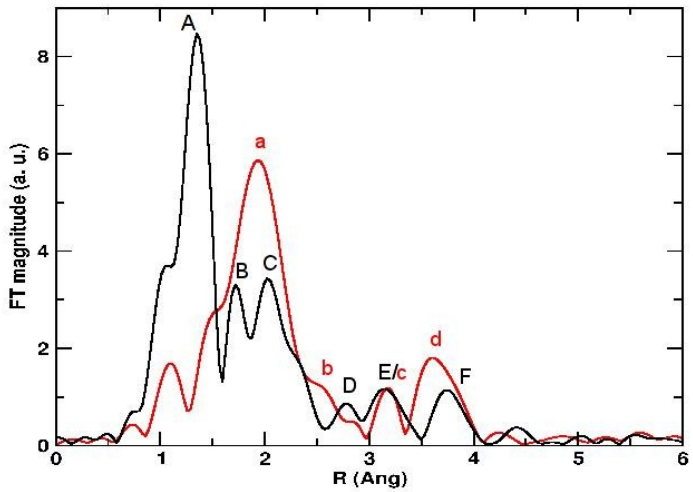

Figure 1: Fourier transform (not phase-shift corrected) of the L_3 edge EXAFS spectra of U(VI) complex (black curve) and Pu(IV) complex (red curve).

For $UO_2(NO_3)_2(TBP)_2$ the best fit is obtained with two nitrates in bidentate coordination. It gives two oxygen atoms at 1.76 Å (σ^2 =0.0022), two oxygen atoms of the phosphate group at 2.41 Å (σ^2 =0.0050), four oxygen atoms of the two bidentate nitrate ligands at 2.54 Å (σ^2 =0.0048), two corresponding nitrogen atoms at 2.99 Å (σ^2 =0.0056) and two phosphorus atoms at 3.62 Å (σ^2 =0.0095). In the FT spectrum, peak A is attributed to single scattering of oxygen atoms of the uranyl group, peak B is assigned to single scattering involving the oxygen atoms of the uranyl group and the oxygen atoms of the TBP group, peak C mainly contained single scattering signal due to the oxygen atoms of the nitrate group, peak D is assigned to single scattering of the nitrogen atoms and multiple scattering of the oxygen atoms of the uranyl group, peak E corresponds to single and multiple scattering of the phosphorus atom and peak F is assigned to single and multiple scattering signal due to the further oxygen atoms of the nitrate groups.

As for $UO_2(NO_3)_2(TBP)_2$ the best fit for $Pu(NO_3)_4(TBP)_2$ is obtained with all nitrates in bidentate coordination. The EXAFS fit leads to a first shell with two oxygen atoms of the phosphate group at 2.33 Å (σ^2 =0.0032), eight oxygen atoms corresponding to the four bidentate nitrate ligands at 2.46 Å (σ^2 =0.0065), four nitrogen atoms at 2.91 Å (σ^2 =0.0055) and two phosphorus atoms at 3.73 Å (σ^2 =0.0038). In figure 1, peak a is assigned to single scattering of both oxygen atoms of the TBP group and oxygen atoms of the nitrate group. Peak b is assigned to single scattering of nitrogen atoms and peaks c and d are attributed to single and multiple scattering signals of phosphorus atoms and further oxygen atoms of the nitrate ligands, respectively.

Structural parameters given by the fitting procedure are consistent with distances obtained by DFT calculations. Data analysis for Th(IV) and Np(IV) complexes are currently under progress in order to compare the coordination sphere of U(VI), Th(IV), Np(IV) and Pu(IV) in presence of nitric acid and TBP solution.

ESRF	**Experiment title:** EXAFS investigation of U(IV) precipitates	**Experiment number:** CH-2972
Beamline: BM 20	**Date of experiment:** from: 5.10.2009 to: 7.10.2009 (6 shifts); from: 27.2.2010 to: 29.2.2010 (6 shifts); from: 14.3.2010 to: 15.3.2010 (3 shifts)	**Date of report:** 18.3.2010
Shifts: 15	**Local contact(s):** Christoph Hennig	*Received at ESRF:* *18.3.2010*

Names and affiliations of applicants (* indicates experimentalists):

Stephan Weiss*, Harald Zänker*, Isabell Dreißig*, Christoph Hennig*

Forschungszentrum Dresden-Rossendorf, Institute of Radiochemistry, Bautzner Landstrasse 400, 01314 Dresden / Germany

Report:

Defined amounts of 0.02 M U(IV) stock solution (1 M $NaHCO_3$, pH 8.6) were added to freshly prepared and equilibrated solutions of silicic acid (pH ~7). Two samples with equal uranium concentration and different silicic acid content were prepared. The starting suspensions consisted of 1 x 10^{-3} M U and 1 x 10^{-3} M Si (sample **B**) and of 1 x 10^{-3} M U and 3 x 10^{-3} M Si (sample **C**). The colloids were precipitated from the suspensions through decreasing the pH to 4 by adding $HClO_4$. The decreased pH results in a loss of the repulsive forces between the particles due to neutralization of the surface charge. The precipitates were centrifuged and stored in wet state in air-tight double-sealed cuvettes. The molar Si/U ratio after centrifugation was 0.83 for sample **B** and 1.68 for sample **C**. The samples were measured at room temperature.

Furthermore, a sample of amorphous U(IV) oxyhydroxide was used as a reference sample (sample **A**). It was prepared by electrolysis of 0.05 M U(VI) in an aqueous solution of 0.1 M $HClO_4$ at -0.3 V (*vs.* Ag/AgCl) according to a procedure described previously (Ikeda et al., 2009). This sample was measured as a colloidal suspension in aqueous solution (pH <2) at room temperature. Coffinite served as a second reference sample (sample **D**). The sample was prepared by hydrothermal synthesis according to the procedure described by Fuchs and Hoekstra (1959) and measured as a dry powder at 15 K.

U(IV) forms stable colloidal suspensions at low pH values and in the absence of complexing media. The chemical composition of these colloids, which depends on preparation method, pH, temperature and alteration, can be described as amorphous U(IV) oxyhydroxide. The observation that silicic acid stabilizes such colloid suspensions at neutral pH values raises the question how the structure and surface of such colloids might be modified by the silicate. U L_3 edge EXAFS spectroscopy was applied to gain information on the next-neighbor arrangement of uranium. In the reference sample of U(IV) oxyhydroxide, uranium is coordinated by oxygen atoms from bound aquo ions, oxo and hydroxo groups. This leads to a variety of U-O scattering contributions approximated in the shell fit by a total of ~6 oxygen atoms with U-O distances of 2.34 and 2.52 Å. The next strong peak indicates an U-U distance of 3.85 Å. Whereas crystalline UO_2 has 12 uranium next neighbors, there is only an average value of 5.1 uranium next neighbors in the U(IV) oxyhydroxide of sample **A**. The reduced coordination number is a result of a strong structural disorder.

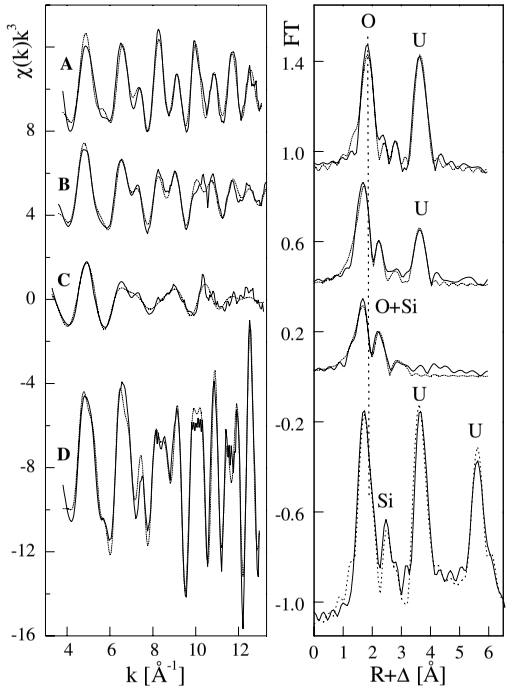

Fig. 1. Uranium L_3 edge EXAFS (left) and their corresponding Fourier transform (right) of $UO_n(OH)_{4-2n}{\cdot}mH_2O$ colloid (sample **A**), colloid samples with initial molar Si:U ratios of 0.83 (sample **B**) and 1.68 (sample **C**), and synthetic coffinite (sample **D**); the spectrum of sample **D** was collected at 15 K, the measurement of the other samples was performed at room temperature.

In the presence of silica there is a clear change in the first coordination sphere. The next neighbors around uranium of the silica containing samples **B** and **C** could be fitted with two contributions of oxygen at U-O distances of ~2.23 to 2.83 Å. It is obvious that the majority of the oxygen atoms is located at a distance of ~2.23 Å in the silica containing samples. This distance is significantly shorter than the main U-O distance of 2.34 Å observed in the U(IV) oxyhydroxide and indicates clear structural differences. It should be mentioned that carbonate does not play a major role because the U-O distance in U(IV) carbonate, $[U(CO_3)_5]^{6-}$, is 2.45 Å, i.e. it is significantly longer. The next longer distance can be fit with a U-O distance of 2.83 Å, but this value is too long to be physically reasonable for an oxygen coordination. The scattering contribution of this shell is assumed to be influenced by a superposition with a contribution from silicon. A short U-Si distance of 3.1 Å is for instance known from coffinite (sample **D**), $USiO_4$, where the shortest U-Si distance results from a SiO_4 polyhedron coordinated in a bidentate, edge-sharing fashion. However, there is no indication of an individual Si backscattering peak in the EXAFS Fourier transform. Furthermore, there is a significant weakening of the U-U backscattering signal with increasing silica content.

An interaction of both ions obviously results in the formation of a polymeric structure. Once silica enters the structure, the characteristic U-O-U bonds of U(IV) oxyhydroxide are replaced by U-O-Si bonds. That there exists chemical affinity between uranium(IV) and silicate can be deduced from the existence of the mineral coffinite. However, the structure of the uranium/silica polymers is much more disordered than that of crystalline coffinite.

ESRF	**Experiment title:** **Structural XAS analysis of uranyl-arsenic species and their sorption onto FeOOH and Montmorillonite**	**Experiment number**: CH-3081
Beamline: BM 20	**Date of experiment**: from: 14/04/2010 to: 17/04/2010; 01/09/2010 03/09/2010; 14/11/2010 16/11/2010	**Date of report**: 19. 04. 2011
Shifts:	**Local contact(s)**: Christoph Hennig	*Received at ESRF:*

Names and affiliations of applicants (* indicates experimentalists):

Wondemagegnehu A. Gezahegne*

Institute for Geology, Technische Universität Bergakademie Freiberg,

Gustav-Zeunerstrasse 12, 09599 Freiberg

Report:

The mobility of uranium(VI) in the environment is controlled by its soluble aqueous complexes and its precitiptates occurring as minerals. About one-third amongst the approx. 200 known uranium minerals is represented by uranyl-phosphate and uranyl-arsenate minerals. While the existence and behavior of dissolved uranyl phosphate complexes had been subject of research by several authors, the investigation of aqueous uranyl arsenate complexes is rare. There is no report to date that investigates aqueous uranyl arsenate complexes structurally. Consequently, more detailed knowledge on uranyl arsenate complexes is still needed.

The determination of structural parameters in aqueous solution with EXAFS spectroscopy is limited by uranium concentrations of ~ $5 \cdot 10^{-5}$ M. There is a strong tendency of uranyl-arsenates to precipitate at concentrations above ~ $5 \cdot 10^{-6}$ M, especially at pH values beyond 2. Such precipitates occur at room temperature within one to two minutes after mixing of the starting solutions. Because the detection limit of EXAFS can not easily be lowered, the samples must be prepared at or beyond the detection limit for uranium. Since the oversaturation leads to spontaneous precipitation we explored ways to conserve the solution species. We found that shock-freezing of the solution in liquid nitrogen immediately after mixing of the starting solutions is an appropriate approach.

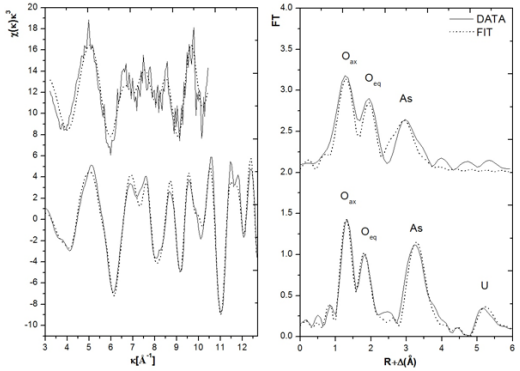

Figure 1. U L_{III}-edge k^3-weighted EXAFS spectra (left) and the corresponding Fourier transforms (right) of a shock frozen liquid sample at 15 K with uranium to arsenic concentrations of 0.05mM to 0.5mM at pH 2 (a), and solid uranyl-arsenate precipitate $H[(UO_2)(AsO_4)]\cdot 4H_2O$ at pH 3 (b)

The k^3-weighted EXAFS spectra of the solid precipitate $H[(UO_2)(AsO_4)]\cdot 4H_2O$ is shown in Figure 1 together with the frozen liquid sample. The EXAFS of $H[(UO_2)(AsO_4)]\cdot 4H_2O$ exhibits the characteristic short U-O_{eq} bond length of 2.28 Å. The monodentate bound arsenate shows a U-As distance of 3.69 Å and the next uranium atoms in a U-U distance of 5.38 Å. The coordination of the shock-frozen solution species differ clearly from the precipitate. The only structurally unchanged feature is the trans-dioxo cation of 2 axial oxygen atoms at a U-O_{ax} distance of 1.78 Å. The second peak in the EXAFS spectrum, which corresponds to the equatorial oxygen atoms, shows U-O_{eq} bond length of 2.39 Å with a coordination number of 4.8 – 5.1. In the liquid samples, the calculated U-As bond distance of 3.39 Å is shorter than that observed in solid $H[(UO_2)(AsO_4)]\cdot 4H_2O$. This short bond length indicates most likely a bidentate coordination between the central uranium atom and the arsenate ligand, instead of the monodentate one in the precipitate. Higher shells were not observed, indicating that the aquoeous species is a monomer.

ESRF	**Experiment title:** Study of Thorium and Uranium complexation with alpha-hydroxy carboxylate ligands	**Experiment number:** CH-3082
Beamline: BM20	**Date of experiment:** from: 13/July/2010 to: 17/July/2010	**Date of report:** January 2011
Shifts: 10	**Local contact(s):** Andreas Scheinost	*Received at ESRF:*

Names and affiliations of applicants (* indicates experimentalists):

*Mireia Grivé (Amphos21) ,
*Elisenda Colàs (Amphos21),
Lara Duro (Amphos21),
*Isabel Rojo (Centre Tecnològic de Manresa).

Report:

Introduction

Complexation of actinides by α-hydroxy carboxylate ligands (such as gluconate, $C_6H_{11}O_7^-$ and isosaccharinate, $C_6H_{11}O_6^-$) is of main interest on the context of radioactive waste disposal (Hummel et al., 2005). Nevertheless, there is a lack of information on the coordination number of these ligands with radionuclides, especially at high pH values. The general objective of this work is the spectroscopic study of Th(IV) complexes with gluconate and isosaccharinate ligands formed under alkaline environments.

The specific objectives of the work are:

-to gain information on the Th coordination chemistry with organic ligands, in terms of bond lengths and coordination numbers.

-to identify differences (if existing) among the coordination of thorium to gluconate and isosaccharinate.

-to investigate the possible change of coordination modes between Th and gluconate with pH.

-to study the role of calcium in the formation of mixed calcium-thorium-gluconate complexes.

Experimental

Several samples were prepared for their analysis:

1) Solid thorium oxohydroxide, aqueous thorium carbonate and aqueous thorium citrate samples, for comparison purposes.

2) Aqueous thorium gluconate samples at pH 12.0 and 7.6.

3) Aqueous thorium isosaccharinate samples at pH=12.0.

4) Aqueous thorium gluconate samples at pH=12.0 in the presence of calcium.

Aqueous samples were prepared from the oversaturation direction, mixing the appropriate amounts of ligand and thorium at 25ºC in $NaClO_4$ (I=0.5M) solutions. The final pH was adjusted with NaOH. Samples were prepared under nitrogen atmosphere to avoid carbonate contamination.

Before the analysis, the samples were filtered with ≈20 nm or ≈1.2 nm filters to avoid the presence of solid thorium particles or colloids. Final thorium concentrations in the aqueous samples were ≈ $1 \cdot 10^{-3}$ mol/dm^3; ligand aqueous concentrations in solution varied between 0.01 and 0.5 mol/dm^3.

The EXAFS spectra were collected in the fluorescence mode (except the solid thorium oxohydroxide, which was collected in the transmission mode) at room temperature.

Results

Preliminary data analysis was performed using the WinXAS (Ressler, 1998) software. Theoretical scattering amplitudes for each absorber and backscattered pair were calculated with the FEFF 8.20 code (Rehr and Albers, 2000). A single value of the shift in threshold energy, ΔE_0, was allowed to vary for all coordination shells of a given sample. Principal component (PC) analysis was done with the PC application in Sixpack (Webb, 2005).

The analysis of solid thorium oxohydroxide indicates the coordination of ~8 oxygens at 2.43 Å, which is in agreement with the theoretical structure of thorianite (Whitfield et al., 1966). Th-Th interactions are not observed in the spectra due to the amorphous nature of the sample.

Aqueous thorium carbonate spectra was fitted (Figure 1.A) using thorium pentacarbonato aqueous complex ($Th(CO_3)_5^{6-}$) as a model (Altmaier et al., 2006). According to the results, ~9 oxygens appear to be coordinated to Thorium at 2.47 Å. The fit also suggests the presence of ~4.5 carbon atoms at 2.47 Å and ~4.5 oxygen atoms (O_{dist}) at 4.52 Å.

In the case of thorium gluconate and thorium isosaccharinate samples, the EXAFS spectra were fitted using the reference crystal structures of Mn(III) citrate (Matzapetakis et al., 2000) and Na(I) isosaccharinate (Bontchev and Moore, 2004).

In the aqueous thorium gluconate sample at pH=12 (Figure 1.B), aside from the Th-O shell at 2.42 Å (with a coordination number around 10), the next most intense feature corresponds to a Th-C interaction at 4.27 Å. For the aqueous thorium isosaccharinate sample at the same pH (Figure 1.C), the Th-C contribution appears at 4.19 Å. No Th-Th interactions are observed in thorium-gluconate or thorium-isosaccharinate samples.

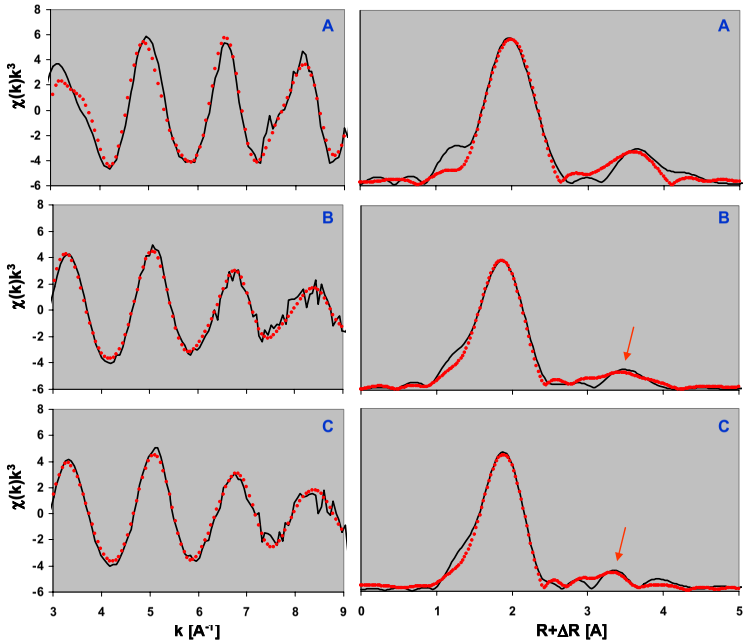

Figure 1: Thorium LIII edge k3-weighted EXAFS spectra (left) and their corresponding Fourier Transforms (right) for a) Thorium carbonate aqueous sample at pH=9.4; b) Thorium gluconate aqueous sample at pH=12; c) Thorium isosaccharinate aqueous sample at pH=12. Solid black line represents experimental data; red dots are the preliminary fit results. Red arrow indicates Th-C contribution for the organic ligands (see text).

Principal component analysis indicates that no important differences are observed between the Th-gluconate spectra at pH=7.6 or pH=12, and that similar aqueous complexes are being formed at both pH values. Likewise, no significant differences are observed in the spectra for thorium gluconate samples in the absence and presence of calcium. This may either indicate that the concentration of calcium in the samples is not high enough to allow the formation of a mixed calcium-thorium-gluconate complexes, or that Th-Ca path length is R>4 Å. At such distances the large signal-to-noise ratio of the experimental data prevents a detailed analysis of the spectra.

Further work is still on going in order to both improve the fitting results and compare them with the data gathered from independent solubility experiments.

References

- Altmaier, M. et al. Radiochim. Acta 2006, 94, 495–500
- Bontchev, R. P. and Moore, R. C. Carbohydrate Research, 2004, 339, 801–805
- Hummel, W. et al. Chemical Thermodynamics 9: Chemical thermodynamics of compounds and complexes of U, Np, Pu, Am, Tc, Se, Ni and Zr with selected organic ligands. NEA OECD, 2005.
- Matzapetakis, M. et al.. Inorg. Chem. 2000, 39, 4044-4051.
- Rehr, J. J. and Albers, R. C. Rev. Mod. Phys. 2000, 72, 621–654.
- Ressler, T. J. Synchrotron Radiat. 1998, 5, 118–122.
- Webb, S.M. Physica Scripta, 2005, T115, 1011-1014.
- Whitfield, H. J.; Roman, D.; Palmer, A. R. J. Inorg. Nucl. Chem. 1966, 28, 2817–2825.

ESRF	**Experiment title:** EXAFS/XANES investigation of uranium plutonium mixed carbides	**Experiment number:** CH-3083
Beamline: BM20	**Date of experiment:** from: 21/04/10 to 23/04/10 and 25/04/10 to 27/04/10	**Date of report:** 04/2011
Shifts: 12	**Local contact(s):** Andreas Scheinost	*Received at ESRF:*

Names and affiliations of applicants (* indicates experimentalists):

Alan HANDSCHUH [1*], Philippe MARTIN[1*], Stéphane VAUDEZ[1*], Gilles LETURCQ[2*], Renaud BELIN[1], Francis ABRAHAM[3]

[1] CEA Cadarache - DEN/DEC, Saint Paul Lez Durance, 13108, France.

[2] CEA Marcoule - DEN/DRCP, Bagnols Sur Ceze, 30207, France.

[3] Laboratoire de Cristallo- & Physicochimie du Solide U.S.T.L.-E.N.S.C.L., B.P. 108 F-59652, Villeneuve d'Ascq CEDEX, France

Since the 1960s', uranium plutonium mixed carbides have been studied as potential nuclear fuels for fast breeder reactors [1-2]. To date, only India has successfully used them in liquid-metal-cooled fast breeder reactors (LMFBRs) at large scale. Currently, in the Generation IV framework, mixed carbides (U,Pu)C1+x (a mixture of (U,Pu)C and (U,Pu)2C3) are being considered as promising fuels for both Gas Fast Reactor (GFR) and Sodium Fast Reactor (SFR). Compared to standard Mixed Oxide fuel (U,Pu)O2, mixed carbide should improve reactor performance due to higher thermal conductivity and metal atoms density [3], a better chemical compatibility with stainless steel [4], and a satisfactory in-pile performance at high burnup. Mixed actinide carbides are typically synthesized by carbothermic reduction of a mixture of uranium and plutonium dioxides under vacuum or under argon. A clear understanding of the elementary mechanisms involved into the carbothermic reduction is of main interest to optimize the manufacturing process of industrial fuels. Moreover, the influence of the initial nature of actinides oxides ($(U,Pu)O_2$ obtained by oxalic co-precipitation or mixture of UO_2 and PuO_2 oxides) is also to be studied.

Experimental results

XAFS characterizations at U L_3 and Pu $L_{2,3}$ edges were performed using He cryostat on the following samples

- UC_2, Pu_2C_3
- a biphasic compound PuC + Pu_2C_3,
- a mixed sesquicarbide $U_{1.80}Pu_{0.20}C_3$ obtained from a co-grinded oxides mixture,
- a biphasic compound $U_{0.90}Pu_{0.10}C$ + $U_{1.80}Pu_{0.20}C_3$ obtained from a co-grinded oxides mixture,
- 3 partially reduced PuO_2 + C samples (carbothermic reduction cycle interrupted at 3 different steps).

XANES results obtained at plutonium L_3 edge are summarized in Fig 1 and edge positions are compared in Fig 2. The carbide compounds ($(U,Pu)_2C_3$, (U,Pu)C, and PuO_2 reduced for 2 and 4 hours), the edge positions are ranging between Pu^{+3} and PuN position. These results suggest that plutonium cations have an electronic configuration very closed to Pu^{+3} instead of the expected metallic state.

Furthermore, as demonstrated with EXAFS results given in Fig 3, after 1 hour of thermal treatment the reduction process in the PuO_2+C mixture is very limited. No Pu-C bond is necessary for reproducing experimental data and all parameters (N, σ and R) are similar to those obtained on PuO_2.

After 4 hours of thermal treatment, characterizations performed in our laboratory has demonstrated that even a single Pu_2C_3 is observed by XRD a significant amount of oxygen is remaining in the sample (3 Wt%). EXAFS data obtained allowed us to eliminate the assumption of a solid solution $Pu_2(C,O)_3$. As shown in Fig 4, EXAFS fit demonstrate the presence of an oxygen atom shell around plutonium with a distance (R=2.34(1) Å) equal to the Pu-O distance observed in the PuO_2 structure. The Debye-Waller value measured for this Pu-O distance is equal to 0.008 $Å^2$, twice the value observed for crystalline PuO_2. This 'glassy' PuO_2 is thus in equilibrium with the Pu_2C_3 phase observed using XRD.

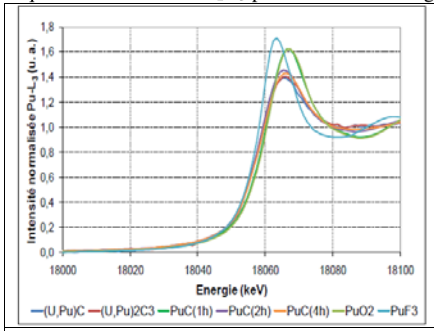

Fig 1: Pu L_3 XANES spectra

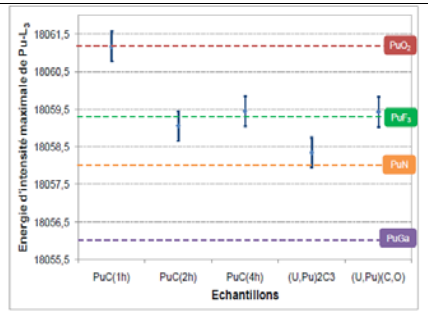

Fig 2: Pu L_3 XANES hite line maxima positions compared to reference compounds

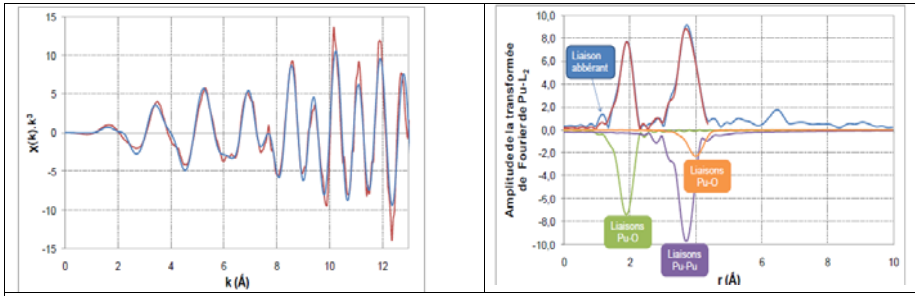

Fig 3: experimental data (-) and fit (-) obtained on PuO2+ C sample reduced during 1 hour

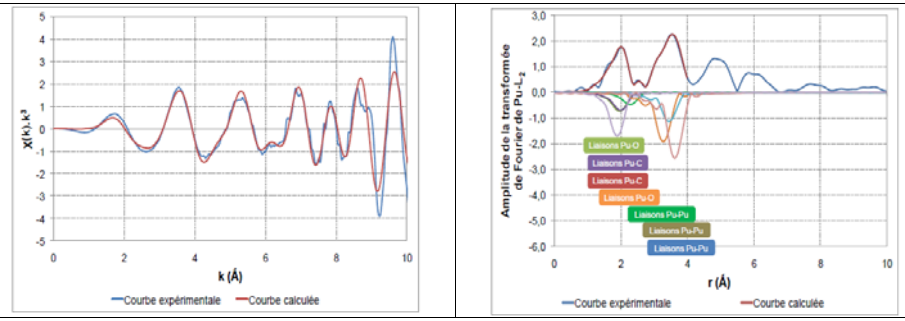

Fig 4: experimental data (-) and fit (-) obtained on PuO2+ C sample reduced during 4 hours

References

[1] Y. Suzuki *et al.*, J. Nucl. Sci. Technol., 18(1981)61.
[2] C. Ganguly, Nucl. Technol., 105(1994)346.
[3] R. B. Matthews *et al.*, Nucl. Technol., 63(1983)9.
[4] C. Ganguly *et al.*, J. Nucl. Mater., 158(1988)159.

ESRF	**Experiment title:** Comparative investigation of the uranium complexation onto γ-Al_2O_3 by means of FT-IR and EXAFS spectroscopy	**Experiment number:** CH-3205
Beamline: BM20	**Date of experiment:** from: Nov 28 2010 to: Dec 1 2010	**Date of report:** 4/20/2011
Shifts: 9	**Local contact(s):** André Rossberg (rossberg@esrf.fr)	*Received at ESRF:*

Names and affiliations of applicants (* indicates experimentalists):

Katharina Mueller, Harald Foerstendorf, Katharina Gückel, André Rossberg, A. C. Scheinost

Forschungszentrum Dresden-Rossendorf, Institute of Radiochemistry, P.O. Box 51 01 19,

Report:

For a better understanding of the sorption mechanisms of uranium(VI) on solid alumina oxide (γ-Al_2O_3) phases, structural information on a molecular level of the surface complexes is needed. In our recent comprehensive studies on γ-Al_2O_3, the formation of different surface complexes as a function of different surface loadings was found between the actinyl ions and the solid phase using in situ infrared spectroscopy. From the spectral data with increasing U(VI) concentration at the alumina-water interface, monomeric and oligomeric surface complexes and the formation of a surface precipitate was deduced. Furthermore, the data evidence the contribution of atmoshperic carbonate during surface complexation reactions. However, because of overlapping vibrational bands in the obtained IR spectra, possibly generated by the aqueous species and the surface precipitate, further information of the molecular structures is required. In particular, a confirmation of the vibrational spectroscopic findings of surface precipitation and polymerization at different U(VI) loading rates of the solid phase was a main goal of the EXAFS experiments.

Therefore, a series of batch samples of sorbed U(VI) onto γ-$Al(OH)_3$ was prepared in presence and absence of atmospheric carbonate, showing different degree of U(VI) loading. These samples were expected to reflect the different stages of the sorption processes in analogy to the IR spectra.

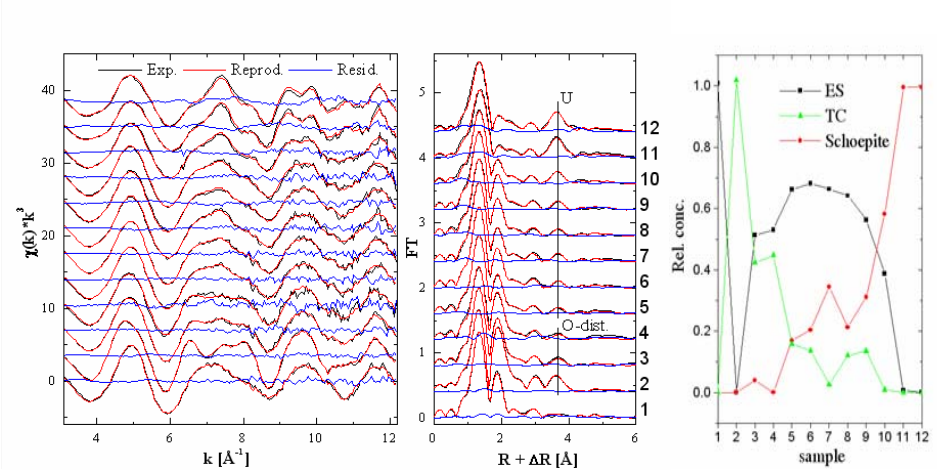

Fig. 1: EXAFS spectra (left panel) and the corresponding Fourier transforms (FT) (middle panel) of the batch samples of U(VI) on γ-Al_2O_3 and reference spectra with their FA reproduction and residuals. Composition of the three components in the samples obtained by FA (right panel). References: sample 1 - mononuclear edge sharing complex (ES), sample 2 - aq. $UO_2(CO_3)_3^{4-}$ complex, sample 12 - meta-Schoepite. The samples in between are the investigated γ-Al_2O_3 sorption samples while the sample number increases with the U(VI) loading. The line in the FT shows special features/interactions: "U" - uranium, "O-dist." distal oxygen atom of a bidentalely coordinated carboxylic group.

RESULTS

The samples provided EXAFS spectra of a sufficiently high quality for factor analysis (FA)(*1*). By taking only the γ-Al_2O_3 sorption samples 3-11 three components were found by FA. We tested several reference spectra from the data pool for describing the spectra of the sorption samples. Only by including the spectra of the mononuclear edge sharing (ES) surface complex, the aqueous $UO2(CO3)_3^{4-}$ complex and meta-Schoepite the number of FA detected components does not increases and the reproduction of the data is sufficient (Fig. 1). The succesful set of reference spectra enables the quantification of the species for each sorption sample by iterative target testing (Fig. 1, right) (*1*). In samples 3 and 4 a sorbed ternary carbonato complex (TC) is detected. All γ-Al_2O_3 samples contain the ES complex, except for the sample with the highest U(VI) loading (sample 11, Fig. 1, right). With inreasing U(VI) loading surface precipitation of meta-Schoepite occures.

The ES complex is obviously dominant at low U(VI) loading rates as confirmed by IR spectra recorded during the first minutes after induced sorption. The cabonate interaction in case of the TC complex was also confirmed by IR spectroscopy. The observation of the "development" of the surface precipitate (schoepite), that is formed at the highest U(VI) accumulation at the alumina-water interface in pure form (sample 11, Fig. 1, right), is in line with the results from IR spectroscopy. Interestingly the EXAFS shell fit structural parameter observed for the ES and TC complex are in line for those observed for the corresponding U(VI)-ferrihydrite sorption complexes (*2*).

REFERENCES

1. A. Rossberg, T. Reich, G. Bernhard, *Analytical and Bioanalytical Chemistry* **376**, 631 (2003).
2. A. Rossberg *et al.*, *Environmental Science & Technology* **43**, 1400 (2009).

ESRF

ESRF	**Experiment title:** Complexation between uranium(VI) and rhenium(VII) in an hydrophobic ionic liquid	**Experiment number**: CH3206
Beamline: BM20	**Date of experiment**: from: 25/09/2010 to: 28/09/2010	**Date of report**: 26/01/2011
Shifts: 9	**Local contact(s)**: Andre Rossberg	*Received at ESRF:*

Names and affiliations of applicants (* indicates experimentalists):

C. Gaillard[1]*, I. Billard[2]*, A. Ouadi[2]*

[1] Institut de Physique Nucléaire de Lyon, CNRS/IN2P2, Université de Lyon, France.
[2] Institut Pluridisciplaire Hubert Curien, CNRS/IN2P3, Université de Strasbourg, France.

Report:

We aim at determining by EXAFS the stoechiometry and structure of the complexes formed between UO_2^{2+} and ReO_4^- in hydrophobic ionic liquids. ReO_4^- is used here as the stable chemical surrogate of TcO_4^-, which is an abundant fission product. Those two ions are known to have weak interactions in water, but our first studies have shown that they form complexes in ionic liquids. The characterisation of those species, which have never been evidenced in a liquid medium, will constitute a basis for our further investigation of the mechanism of extraction of UO_2^{2+} and TcO_4^- by tributylphosphate in an ionic liquid.

Solutions containing different [Re(VII)]/[U(VI)] ratio were made (R, from zero to 10), in two hygroscopic ionic liquids, C_4mimTf_2N and Bu_3MeNTf_2N, and in acetonitrile, the latter for comparison purpose between a conventional molecular solvent and an ionic liquid. All solutions were dried before their measurements, to be sure that water molecules will not interfere in the U-Re complexation phenomenon that we want to observe.
Measurements were led at the ROBL beamline using a Si(111) monochromator. During the experiment a total of nine samples were measured at the U-L_3 edge (17166 eV) in transmission mode (calibration with a Y foil at 17038 eV) and when it was possible, at the Re L_3-edge (10535 eV) in fluorescence mode (calibration with a Zn foil at 9659 eV). In this report, we will focus on results obtained at the U edge.

Figure 1 displays the Fourier-transforms of EXAFS spectra obtained at the U L_3-edge for solutions made in two solvents (an ionic liquid Me_3BuNTf_2N and acetonitrile), containing different [Re(VII)]/[U(VI)] ratio.

Surprisingly, no U-Re contribution could be observed on the FT spectra. According to data available in the literature, we could expect the presence of this contribution at a distance (on the FT, i.e. non corrected distance) between 3.8 and 4 Å. Nevertheless, data available are for solid compounds and not liquid state compounds, for which distances may be longer. In this case, we would be at the limit of the EXAFS technique.

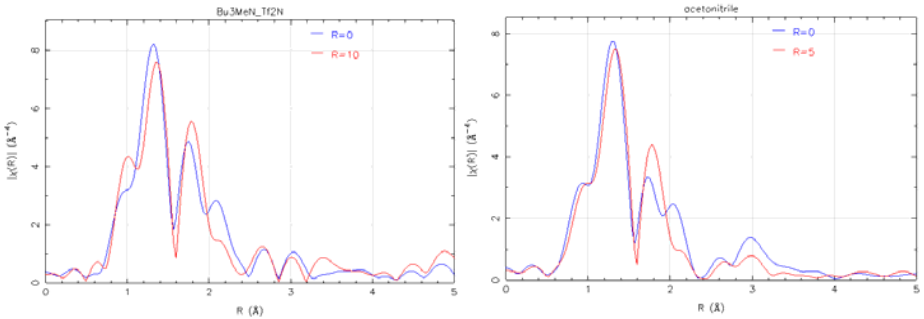

Figure 1: Fourier transforms of spectra obtained at the U-L_3 edge: evolution of the U environment as a function of the rhenium (VII) concentration (R = [Re(VII)]/[U(VI)]) in two solvents, an ionic liquidMe_3BuNTf_2N (left) and acetonitrile (right).

In both solvents, it is clear that adding rhenium to the uranyl solutions entails a change in the equatorial coordination sphere (contribution between 1.6 and 2.2 Å on the FT). Fit of the spectra reveals a significant shortening of the U-O_{eq} distance upon addition of rhenium (VII): in the ionic liquid Bu_3MeNTf_2N, it goes from 2.43 Å (R = 0) to 2.37 Å (R = 10). The former value, obtained for an uranyl salt dissolved in the dry ionic liquid, is consistent with previous measurements obtained in other ionic liquids [1, 2]. In dried acetonitrile, uranium is surrounded by MeCN molecules, and thus, its equatorial shell is composed of nitrogen atoms, found by the fit at a distance of 2.47 Å. After addition of rhenium (VII) at a high ratio, uranium is found coordinated by O atoms at a distance of 2.38 Å. It must be noticed here that EXAFS does not allowed a direct discrimination between N and O atoms, but this can be done according to the equatorial distances found by the fit.

As a conclusion, those measurements allowed us to confirm results obtained by other techniques, and in particular UV-vis. spectroscopy, showing that there is a complexation between U(VI) and Re(VII) in ionic liquids. Even though we could not determine the complexes stoechiometry of the species formed, we could get useful information on the environment of uranyl. In particular, it seems that the complexation between the two ions occurs at the same extend in an ionic liquid and in a conventional molecular solvent. Those results will be part of an article which is currently being written.

References:

[1] C. Gaillard, A. Chaumont, I. Billard, C. Hennig, A. Ouadi, G. Wipff *Inorg. Chem.* **2007**, 46, 4815.
[2] C. Gaillard, A. Chaumont, I. Billard, C. Hennig, A. Ouadi, S. Georg, G. Wipff *Inorg. Chem.* **2010**, 49, 6484.

ESRF	**Experiment title:** EXAFS Study of the Sorption of Np(V) on Opalinus Clay	**Experiment number:** EC-424
Beamline: BM20	**Date of experiment:** from: 03/04/2009 to: 06/04/2009	**Date of report:** 28/10/2009
Shifts: 9	**Local contact(s):** André ROSSBERG	*Received at ESRF:*

Names and affiliations of applicants (* indicates experimentalists):
Samer AMAYRI*, Daniel FRÖHLICH*, Jakob DREBERT*, Tobias REICH*
Institute of Nuclear Chemistry, Johannes Gutenberg-Universität Mainz,
Fritz-Strassmann-Weg 2, 55099 Mainz, Germany

Report:

The sorption of Np(V) on Opalinus clay (OPA) (from Mont Terri, Switzerland) has been investigated as a function of pH in the absence and presence of ambient CO_2 in different background electrolytes such as 0.1 M $NaClO_4$ (pH 8.5), OPA pore water (pH=7.6) [1] and saturated calcite solution (pH 8.5). Six samples with different amounts of Np(V) sorbed were prepared from a 23.5 mM Np(V) stock solution of ^{237}Np. The stock solution had been purified from traces of ^{239}Pu and ^{233}Pa. Aerobic/anaerobic OPA powder (600 mg) was suspended in 40 mL background electrolyte. Aerobic OPA powder was prepared in air and anaerobic OPA powder was prepared under inert gas atmosphere from two different OPA bore cores, respectively.

The pH was adjusted using NaOH and $HClO_4$. Samples 1 and 3 were prepared under ambient air ($p_{CO2}=10^{-3.5}$ atm) at pH 8.5 in saturated calcite and 0.1 M $NaClO_4$ solution, respectively. Sample 2 was prepared under anaerobic conditions with a higher p_{CO2} of $10^{-2.3}$ atm in saturated calcite solution at pH 8.5. Samples 4 and 5 were prepared in the abcence of ambient CO_2 (Ar-atmosphere glovebox) in 0.1 M $NaClO_4$ at pH 8.5 and sample 6 in OPA pore water at pH 7.6 (see Table 1). We can distinguish between three groups of samples according to background electrolyte. i) saturated calcite solution (samples 1,2), ii) 0.1 M $NaClO_4$ (samples 3-5), iii) pore water (sample 6).

After shaking the OPA suspensions for 72 hours, aliquots of 15µL the Np(V) stock solution (pH 3.90) were added (pH change less than 0.3) with immediate readjustment of the pH. The total neptunium concentration in each sample was $8.8\cdot10^{-6}$ mol/L. After a contact time of 60 hours, the solid and liquid phases were separated by centrifugation at 100.000 g for 1h. The neptunium uptake was determined by measuring the neptunium concentration in solution by liquid scintillation counting and γ-spectroscopy using the γ-lines at 29.37 and 86.48 keV. The solid residues were loaded without drying into standard Perspex sample holders (5x16x3 mm^3) with Kapton windows for EXAFS analysis. The neptunium uptake of the samples as measured by γ-spectroscopy was between 52 and 121 ppm (Table 1).

The EXAFS spectra were collected at the Np L_{III}-edge (17625 eV) at room temperature in fluorescence mode using a 13-element Ge solid-state detector. The EXAFS analysis was performed with the software packages EXAFSPAK [2] and FEFF8.20 [3]. The scattering phases and amplitudes were calculated using the crystal structures of $NaNpO_2(CO_3)$ [4] and $(UO_2)_2SiO_4\cdot2H_2O$ [5], where U was replaced by Np to model a possible Np-Si/Al interaction with the OPA surface. Figure 1 shows the raw Np L_{III}-edge k^3-weighted EXAFS data, the best theoretical model, and the corresponding Fourier transforms of all samples 1-6. As can be seen from Fig. 1, in all samples the oxidation state (V) of Np was dominating. The reduction of Np(V) to Np(IV) under anaerobic conditions could not be confirm (possible oxidation during transportation). Samples 2, 4 and 6 of anaerobic OPA prepared in different background electrolytes show similar EXAFS spectra and have a different EXAFS pattern compared to samples 1, 3, 5 of aerobic OPA.

Table 1. Summary of the wet-paste OPA samples prepared at $8.8\cdot10^{-6}$ M Np(V) for EXAFS measurements.

Sample	OPA	CO_2/Ar	pH	Electrolyte	Np loading / ppm	Eh/mV
1	aerobic	$p_{CO2}=10^{-3.5}$ atm	8.5	Sat. $CaCO_3$	91	382
2	anaerobic	$p_{CO2}=10^{-2.3}$ atm	8.5	Sat. $CaCO_3$	109	131
3	aerobic	$p_{CO2}=10^{-3.5}$ atm	8.5	0.1 M $NaClO_4$	108	388
4	anaerobic	Ar-atmosph.	8.5	0.1 M $NaClO_4$	121	135
5	aerobic	Ar-atmosph.	8.5	0.1 M $NaClO_4$	110	386
6	anaerobic	Ar-atmosph.	7.6	OPA pore water	52	132

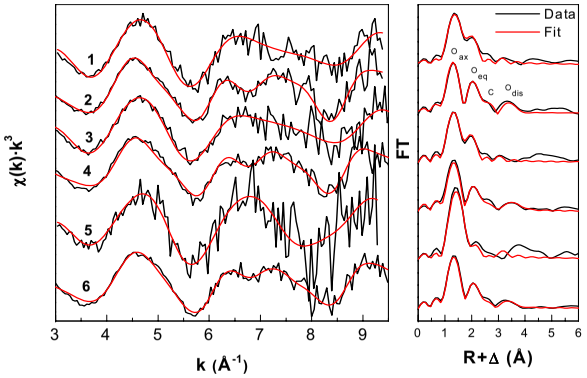

Figure 1. Np L_{III}-edge k^3-weighted EXAFS spectra (left) and the corresponding Fourier transform magnitudes (right) of samples 1-6.

Sample	2 O_{ax}	5 O_{eq}	2 C^d		2 O_{dis}		ΔE_0/eV	Error
	R	R	N[c]	R	N[c]	R		
1	1.85	2.46					-8.1	0.64
2	1.83	2.52	2.4	2.98	2.4	4.25	-8.9	0.51
3	1.83	2.45					-10.3	0.87
4	1.85	2.54	2.5	3.00	2.5	4.26	-6.6	0.38
5	1.86	2.41					-9.2	3.60
6	1.85	2.51	1.9	3.00	1.9	4.24	-9.5	0.33
[a]$NpO_2(H_2O)_4^+$	1.82	2.49						
[b]$NpO_2(CO_3)_3^{5-}$	1.86	2.53	2.7	2.98	3.0	4.22		

Table 2 summarizes the structural parameters derived from the EXAFS fits. The neptunium coordination shells and bond distances of samples 2, 4, and 6 are consistent with the formation of a Np(V) carbonato species at the OPA surface. The average Np-O_{eq} bond distance of samples 1, 3 and 5 is somewhat shorter than in the Np(V) aquo ion (see Tab. 2). This could indicate inner-sphere sorption of a Np(V) at the OPA surface. Due to a poor signal-to-noise ratio in the spectrum of sample 5, only axial, with slightly negative Debye-Waller factor σ^2 (-0.0002), and equatorial oxygen coordination shells of Np, O_{ax} and O_{eq}, respectively, could be analyzed.

Table 2. EXAFS structural parameters for sorption samples 1-6. Coordination numbers for $O_{ax,}$ and O_{eq} were held constant during the fit. c) Coordination numbers for C and $O_{dis,}$ were linked together and adjusted as one parameter during the fit. The average value of the Debye Waller factors σ^2 for O_{ax}, O_{eq}, and O_{dis} were 0.0026 Å^2, 0.011 Å^2, and 0.008 Å^2, respectively. d) Debye-Waller factor σ^2 for C was held constant at 0.003 Å. Distances R are given in Å and Debye-Waller factors σ^2 in Å^2 ($\Delta R= \pm 0.02$ Å, $\Delta\sigma^2= 0.001$ Å^2). Comparison with literature: a) ref. 6, b) ref 7.

Acknowledgement
This work was supported by the German Bundesministerium für Wirtschaft und Technologie (Project 02E10166). We acknowledge the ESRF for provision of synchrotron beam time and thank A. Roßberg, C. Hennig, H. Funke, and A. Scheinost from Forschungszentrum Dresden-Rossendorf for assistance during the EXAFS measurements.

References

[1] R.L. Van Loon et al., J. of Contam. Hydrol. 61 (2003) 73.
[2] G. N. George, I.J. Pickering, EXAFSPAK – A suite of computer programs for analysis of X-ray absorption spectra, SSRL (2000).
[3] A. L. Ankudinov et al., Phys. Rev. B 65 (2002) 104107.
[4] Yu. F. Volkov et. al., Radiokhimiya 21 (1979) 668.
[5] F. Demartin et al., Acta Cryst. C 48 (1992) 1.
[6] T. Reich et al., Radiochim. Acta 88 (2000) 633.
[7] D. L. Clark et al., J. Am. Chem. Soc. 118 (1996) 2089.

ESRF	**Experiment title:** EXAFS study of Neptunium binding mechanism to cementitious materials	**Experiment number:** EC-425
Beamline: BM-20	**Date of experiment:** **from:** 26/06/2009 **to:** 30/06/2009	**Date of report:** 19/08/2009
Shifts: 12	**Local contact(s):** Dr. André Rossberg	*Received at ESRF:*

Names and affiliations of applicants (* indicates experimentalists):
X. Gaona*, R. Daehn*, J. Tits*, D. Kunz* and E. Wieland
Laboratory for Waste Management, Paul Scherrer Institut, Villigen PSI, Switzerland

Report:

Cementitious materials will be used for the construction of the engineered barrier in repositories for long-lived intermediate level wastes (ILW), which may contain significant amounts of ^{237}Np ($t_{1/2} = 2.14 \cdot 10^6$ y). Predicting the long-term behaviour of Np in a cement-based repository requires an adequate understanding of its interaction with the main phases of cement. Several Np redox states are expected under these conditions, although the corresponding stability fields and the binding mechanisms to cement are still poorly understood. The objectives of the project were: a) to study the aqueous speciation of Np(V/VI) under hyper-alkaline conditions; b) to assess the molecular environment of Np(IV/V/VI) sorbed onto calcium silicate hydrates (C-S-H) and cement. Determination of the stability field of the aqueous species is essential prior to sorption studies, while C-S-H phases are the main constituent of cement.

Results:

Aqueous speciation of Np(V/VI) under hyper-alkaline conditions

EXAFS measurements were performed on two aqueous samples (S1 and S2) containing $2.8 \cdot 10^{-3}$ M Np(V) tracer. The hyper-alkaline matrix was provided by tetramethylammonium hydroxide (TMAOH, pH 13.5) to avoid the undesired precipitation of Na/K neptunates. The carbonate impurities of TMAOH led to a final carbonate concentration (at pH = 13.5) of ca. $2 \cdot 10^{-3}$ M. An oxidizing agent (NaOCl $5 \cdot 10^{-3}$ M) was added to sample S2.

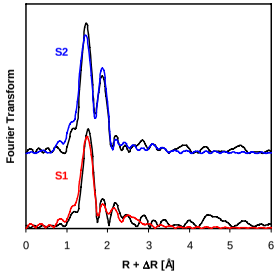

Fig. 1. *Fourier-transformed Np L_{III}-edge EXAFS for samples S1 and S2. Black lines: experimental; blue/red lines: fit*

Fig. 1 shows the Fourier-transformed k^3-weighted Np L_{III}-edge EXAFS at pH 13.5 in the absence (S1) and presence (S2) of NaOCl. EXAFS fitting of both samples shows significant structural differences caused by the presence of NaOCl. A larger Np-O_{ax} distance and splitting of the equatorial oxygen shell characterize sample S1 (Table 1). A backscattering contribution from neighboring carbon was introduced ($R_{Np\text{-}C}$ = 3.06±0.04 Å), although its presence cannot be unambiguously ascertained. Nevertheless, this assumption is in line with the study of Neck et al. [1], which showed the formation of the Np(V) ternary compound $NpO_2(OH)(CO_3)_2^{4-}$ under similar experimental conditions using UV-vis spectroscopy. A rather short Np-O_{ax} distance ($R_{Np\text{-}Oax}$ = 1.80±0.01 Å) was observed for sample S2. The shorter distance in the sample compared to the axial oxygen distance of Np(V) in sample S1 is attributed to the formation of Np(VI) in the presence of the strong oxidizing agent NaOCl. The distance of the four equatorial oxygen atoms in this sample was determined to be $R_{Np\text{-}Oeq}$ = 2.27±0.01 Å. This distance is much shorter than those reported in the literature for Np(VI)-O_{eq} distances where O belonged either to water (R = 2.34 – 2.41 Å) or to sulphate (R = 2.51 Å). This evidence, together with the analogy with U(VI), suggest the presence of OH groups in the equatorial shell, and therefore the formation of the $NpO_2(OH)_4^{2-}$ species. Np(VII/VI) EXAFS studies conducted by Williams et al. [2] in NaOH 1M, as well as theoretical calculations performed by Bolvin et al. [3] for the species $NpO_2(OH)_4^{2-}$ reported Np-O distances in good agreement with those obtained in this study.

Sample	Np-O_{ax}	Np-O_{eq}	Np-C
S1	N = 2 (s) r = 1.86 ± 0.01 Å σ^2 = 0.0021 ± 0.0008	N_{eq1} = 2.3 ± 2.2 r_{eq1} = 2.26 ± 0.05 Å σ^2 = 0.009 ± 0.011 N_{eq2} = 4 (s) r_{eq2} = 2.45 ± 0.04 Å σ^2 = 0.01 ± 0.05	N_C = 2.1 (s) $r_{Np\text{-}C}$ = 3.06 ± 0.04 Å σ^2 = 0.003 (s)
S2	N = 2 (s) r = 1.80 ± 0.01 Å σ^2 = 0.0010 ± 0.0004	N = 4.2 (s) r = 2.27 ± 0.01 Å σ^2 = 0.005 ± 0.001	

Table 1. *Structural information derived from the EXAFS analysis of samples S1 and S2.*

No thermodynamic data have been selected in the NEA thermodynamic series [4] for Np(VI) species forming under hyper-alkaline conditions. The predominance diagram shown in Fig. 2 was calculated with NEA TDB for Np, complemented with log*β^o for $NpO_2(OH)_3^-$ and $NpO_2(OH)_4^{2-}$ species in analogy with U(VI). The experimental pH and E_H conditions determined for the samples S1 and S2 are indicated in Fig.2. The proposed stability fields agree very well with the predicted transition from Np(V) to Np(VI) as observed in this study. This work provides spectroscopic evidences for the formation of Np(VI) hydroxo species under controlled [CO_3^{2-}], E_H and pH conditions, which is essential for further improvements of the thermodynamic properties of Np(VI).

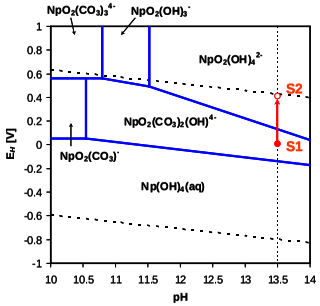

Fig. 2. *Np predominance diagram calculated for 10 < pH < 14 and -1V < E_H < +1V.*

Assessment of Np(IV/V/VI) sorption species on C-S-H phases and cement

C-S-H and cement suspensions were equilibrated with $8 \cdot 10^{-5}$M < [Np] < $1 \cdot 10^{-4}$M in a glovebox ([CO_2], [O_2] < 2 ppm). Samples were conditioned to obtain three different redox states of Np (starting redox states): a) Np(IV) tracer in $Na_2S_2O_4$ (reducing agent); b) Np(V) tracer; c) Np(V) tracer in NaOCl (oxidizing agent, expected to promote the formation of Np(VI)). The E_H of all suspensions was monitored during equilibration. The Np(V) samples prepared in the absence of NaOCl showed a significant decrease of E_H (0.3/0.1V → -0.1/-0.3V), suggesting the predominance of Np(IV) (Fig. 2). The Np-doped C-S-H/cement wet pastes were sealed with a double layer of Kapton foils and encapsulated in two additional plastic containments. The samples remained under air-atmosphere for 7 days prior to the measurements at the beamline due to legal regulations in conjunction with the transport of radioactive samples.

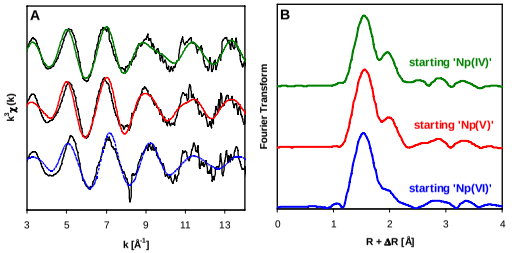

Fig. 3. *EXAFS spectra (A) and Fourier-transformed EXAFS for Np(IV), Np(V) and Np(VI) sorbed on C-S-H (Ca/Si = 1.0).*

Axial and equatorial oxygen atoms had to be considered in the fitting of all samples (Fig. 3 and Table 2). Acceptable fits for the Np(IV) and Np(V) samples were only obtained by including both O_{ax}- and O_{eq}-shells, and either setting N_{Oax} or σ^2_{Oax}. Setting σ^2_{Oax} provided slightly lower R-factors, resulting in N_{Oax} of 1.2 - 1.4. The latter finding could indicate the presence of Np(IV/V) mixtures in these samples rather than presence of pure Np(IV) or Np(V) species, respectively, in line with the study of Denecke et al. [5]. Thus, one may assume that Np(IV) was present in both samples, i.e., the ones starting with Np(IV) and Np(V), and that Np(IV) oxidized to Np(V) during sample transport. This finding suggests that Np(IV) was also present in those sorption samples starting with Np(V), and further that particular precautions (liquid N_2, air tight transport) should be taken in subsequent campaigns. Under oxidizing conditions in presence of NaOCl short Np-O_{ax} and Np-O_{eq} distances were observed, thus indicating the formation of sorbed Np(VI) species.

Sample	Np-O_{ax}	Np-O_{eq}	R-factor
start Np(IV)	N = 1.2 ± 0.2 r = 1.87 ± 0.01 Å σ^2 = 0.001 (s)	N_{eq} = 5.1 ± 0.7 r_{eq} = 2.34 ± 0.02 Å σ^2 = 0.010 ± 0.003	0.059
start Np(V)	N = 2(s) r = 1.87 ± 0.01 Å σ^2 = 0.003 ± 0.001	N_{eq} = 6.1 ± 0.8 r_{eq} = 2.30 ± 0.01 Å σ^2 = 0.011 ± 0.003	0.078
start Np(VI)	N = 2 (s) r = 1.82 ± 0.01 Å σ^2 = 0.004 ± 0.001	N = 5.5 ± 0.8 r = 2.21 ± 0.01 Å σ^2 = 0.009 ± 0.002	0.094

(s): parameters fixed in the fitting process

Table 2. *Structural information derived from the EXAFS analysis of Np-doped C-S-H samples.*

References

[1] Neck et al. (1997). Radiochim. Acta, 77, 167-175; **[2]** Williams et al. (2001). J. Am. Chem. Soc., 123, 4346-4347; **[3]** Bolvin et al. (2001). J. Phys. Chem. A, 105, 11441-11445; **[4]** Guillaumont et al. (2003). NEA Thermodynamic Series. Elsevier; **[5]** Denecke et al. (2005). Talanta, 65, 1008-1014.

ESRF	**Experiment title:** Am(III) sorption on montmorillonite	**Experiment number:** EC-541
Beamline: BM 20	**Date of experiment:** from: 25/11/2009 to 30/11/2009	**Date of report:** 13/12/10
Shifts: 15	**Local contact(s):** Dr. Andreas Scheinost	*Received at ESRF:*
Names and affiliations of applicants (* indicates experimentalists): Maria Marques Fernandes*, Rainer Daehn*, Bart Baeyens*, M. H. Bradbury Laboratory for Waste Management (LES), Paul Scherrer Institut, 5232 Villigen, Switzerland,		

Report:

The safety case for radioactive waste repositories is, to a large extend based on the physical and chemical retention of radionuclides on clay minerals which are important constituents in both the man-made engineered barriers and in argillaceous host rock formations. The presence of carbonate, one of the most important inorganic ligands for lanthanide and actinide ions in groundwater and clay porewaters, can have a significant influence on their sorption behaviour on clay minerals. Previous macroscopic sorption experiments and modelling suggest the formation of Am(III) carbonate complexes at the montmorillonite surface (Marques Fernandes et al., 2007). The aim of this work is to improve the mechanistic understanding at the molecular level of the uptake of Am(III) onto montmorillonite in the absence and the presence of dissolved carbonate.

Preliminary results

The Am(III) loaded montmorillonite films were measured at the L_{III} edges of Am(III) (18510 eV) and in fluorescence mode. EXAFS spectra were analyzed and fitted using the IFEFFIT software package. Backscattering phases and amplitudes were obtained from FEFF8.0 calculations. The multiple scattering paths (MS) related to the bidentate coordination of the carbonate group was included into the fit. The parameters R, N and σ^2 of the scattering paths Am-O_{dist}, Am-O_{dist}-C and Am-C-O_{dist}-C were linked together during the fitting process.

Sorption of Am(III) on montmorillonite

Montmorillonite samples with different Am(III) loadings were prepared in the absence (pH=8) and in the presence of carbonate (equilibrium with the atmospheric $pCO_2 = 10^{-3.5}$ bar at pH~9.3). In addition the solubility liming phase $NaAm(CO_3)_2$ was measured as a reference compound. The experimental conditions used for the preparation of the EXAFS clay samples A, B and C are summarized in Table 1. EXAFS measurements were performed on Am(III) loaded self supporting STx montmorillonite films.

Table 1. EXAFS clay samples description: S/L ratio = $2 g \cdot l^{-1}$, background electrolyte 0.1 M $NaClO_4$

Sample	pH	pCO_2 (bar)	$[^{243}Am(III)]_i$ (M)	$^{243}Am(III)$ sorbed ($mmol \cdot kg^{-1}$)	log R_d ($L \cdot kg^{-1}$)
A	8.0	-----	$2.09 \cdot 10^{-06}$	2.78	4.85
B	9.3	$10^{-3.5}$	$5.90 \cdot 10^{-06}$	2.74	3.80
C	9.3	$10^{-3.5}$	$2.09 \cdot 10^{-06}$	8.32	4.46

Fig. 1a shows the Am L_{III} edge k^3-weighted FT of all the Am(III) samples. The spectra obtained for the samples prepared in the presence and absence of carbonate clearly show different features (Fig. 1a). All the measured carbonate samples show additional peaks in the FT at R~3.8 Å (R+ΔR). The similarity of the FT spectra of the clay sample C and the reference compound clearly shows that in case of sample C surface precipitation occurred. This is in a good agreement with the increased Rd value of 4.46 obtained for sample C.

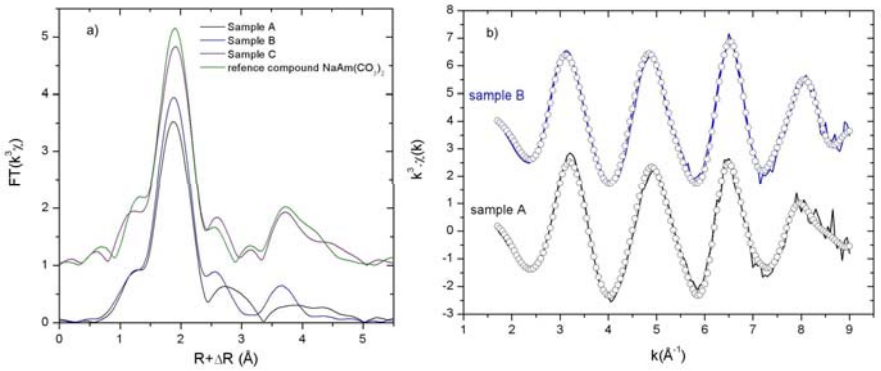

Figs. 1. a) Fourier Transforms of experimental EXAFS spectra measured for the Am(III) sorption samples A to C and the reference compound $NaAm(CO_3)_2$; b) experimental (solid lines) and fitted (symbols) k^3-weighted EXAFS data for the Am(III) samples A and B.

EXAFS spectra of the samples A and B were fitted in the *k*-space and the obtained fits are shown in Fig. 1b (symbols). The results of the data analysis are summarized in Table 2.

The EXAFS parameters obtained by fitting the spectra of the carbonate free sample are consistent with bond lengths from Am-O and Am-Si/Al backscattering pairs. The identification of Am-Al/Si distances is a clear indication that Am(III) forms inner sphere complexes at the STx surface. However, additional EXAFS measurements on carbonate free Am(III) clay samples prepared under different pH and loading

conditions are necessary to derive a reliable structural model for inner sphere complexation of Am(III) at the montmorillonite surface.

The EXAFS parameters obtained by fitting the spectra of the sample B (in equilibrium with atmospheric pCO_2) are consistent with the formation of 1-2 Am(III) carbonate complexes at the montmorillonite surface. No Am-C shell was necessary to reproduce the EXAFS spectrum. However fitting a weak backscatter such as carbon in our system might be difficult, since the backscattering amplitude produced 1 C (z = 6) is much weaker than the amplitude produced by one Si/Al shell (z =13/14) originating from the montmorillonite surface. The most reliable structural evidence for the formation of bidentate Am(III) carbonate complexes at the montmorillonite surface is the identification of the distal oxygen O_{dist} shell of the carbonate ligand (4.28 Å) and the associated multiple scattering of U-C-O_{dis} (4.28 Å) and U-C-O_{dist}-C (4.28 Å).

The evaluation of the $NaAm(CO_3)_2$ solid phase spectra and of the Am(III) loaded clay film C is still in progress.

Table 2. Structural parameters for the Am(III) loaded montmorillonite films derived from the EXAFS analysis.

Sample	Shell	CN	R (Å)	σ^2 [Å^2]	ΔE_0 [eV]
A	Am-O	8 (1)	2.46(1)	0.013(2)	7.83
	Am-Si_1/Al_1	1.1(3)	3.20(2)	0.007*	
	Am-Si_2/Al_2	1.2(5)	3.75(3)	0.01*	
	Am-Si_3/Al_3	5(2)	4.72(2)	0.013(6)	
B	Am-O	7.09	2.46	0.010	10.93
	Am-Si	1.75	3.23	0.010	
	Am-O_{dist}	1.53	4.28	0.005*	
	Am-O_{dist}-C	3.06	4.28	0.005	
	Am-C-O_{dist}-C	1.53	4.28	0.005	

Note: CN: coordination number; R: distance; σ^2: Debye-Waller factor; *: value fixed during the fit; number in parentheses represents the errors in the last digit.

Reference:

Marques Fernandes, M., Baeyens, B., and Bradbury, M. H., 2007. The influence of carbonate complexation on lanthanide/actinide sorption on montmorillonite. *Radiochim. Acta* **96**, 691-698.

ESRF	**Experiment title:** EXAFS Study of Plutonium Sorption on Opalinus Clay	**Experiment number:** EC-616
Beamline: BM20	**Date of experiment:** from: 17/07/2010 to: 20/07/2010	**Date of report:** 10/02/2011
Shifts: 9	**Local contact(s):** André ROSSBERG	*Received at ESRF:*

Names and affiliations of applicants (* indicates experimentalists):
Samer AMAYRI*, Jakob DREBERT*, Ugras KAPLAN*, Tobias REICH*
Institute of Nuclear Chemistry, Johannes Gutenberg-Universität Mainz,
Fritz-Strassmann-Weg 2, 55099 Mainz, Germany

Report:

The sorption of Plutonium (Pu) on Opalinus clay (OPA from Mont Terri, Switzerland) has been investigated as a function of Pu oxidation state (III, IV, VI) at pH 7.6 in the absence and presence of ambient CO_2 in different background electrolytes (0.1 M $NaClO_4$ and OPA pore water). Two samples with Pu(IV) and Pu(VI) were prepared in synthetic pore water (PW) [1] under ambient air conditions. Four samples with Pu(III) and Pu(IV) were prepared under Ar atmosphere (glove box) in 0.1 M $NaClO_4$ and PW (see Table 1). The ^{239}Pu(VI) stock solution had been purified from its decay products and ^{241}Am using anion exchange chromatography. The trivalent and tetravalent oxidation states of Pu were obtained from the purified Pu(VI) stock solution by potentiostatic electrolysis. The oxidation state purity was verified by UV/vis spectroscopy at the characteristic absorption bands at 600 nm for Pu(III) and at 470 nm for Pu(IV). Aerobic (BHE-241) or anaerobic (BHE-24/2) OPA powder (180 mg) was suspended in 30 mL background electrolyte. Aerobic OPA powder was prepared in air and anaerobic OPA powder was prepared under Ar atmosphere. The pH was adjusted using NaOH and $HClO_4$. After shaking the OPA suspensions for 72 hours, aliquots from the corresponding Pu stock solution (Pu(III), Pu(IV) or Pu(VI)) were added with immediate readjustment of the pH to 7.6. The total Pu concentration in each sample was ~10^{-5} mol/L. After a contact time of 60 hours, the solid and liquid phases were separated by centrifugation at 108,000 g for 1 h. The Pu uptake was determined by measuring the Pu concentration in solution by liquid scintillation counting (LSC). The Pu loading in all samples was about 372 ppm (Table 1). The solid residues were dried for 3 days under ambient CO_2 (samples 1 and 2) or Ar atmosphere (samples 3-6), respectively. Then all powders were grinded and loaded into a polyethylene sample holder (SH-01c). The EXAFS spectra were collected at the Pu L_{III}-edge (18070 eV) at 15 K in fluorescence mode using a 13-element Ge solid-state detector. The EXAFS analysis was performed with the software packages EXAFSPAK [2] and FEFF8.20 [3]. The scattering phases and amplitudes were calculated using the crystal structures of $(UO_2)_2SiO_4{\cdot}2H_2O$ [4] and $Eu_{1.3}Fe_{0.7}O_{6.3}Ti_{2.0}$ [5], where U and Eu were replaced by Pu to model possible Pu-Si/Al and Pu-Fe interactions with the OPA surface.

Table 1. Summary of the OPA samples prepared at 10^{-5} M Pu for EXAFS measurements.

Sample	Pu oxd. state	OPA Powder	Atmosphere	pH	Electrolyte	Pu loading (ppm)	Eh/mV (SHE)
Pu-1	VI	aerobic	ambient air	7.62	OPA PW	375	+236
Pu-2	IV	aerobic	ambient air	7.60	OPA PW	375	+237
Pu-3	IV	anaerobic	Ar	7.63	OPA PW	370	-59
Pu-4	III	anaerobic	Ar	7.61	OPA PW	370	-58
Pu-5	IV	anaerobic	Ar	7.61	0.1 M $NaClO_4$	372	-73
Pu-6	III	anaerobic	Ar	7.60	0.1 M $NaClO_4$	372	-63

Figure 1 shows the raw Pu L_{III}-edge k^3-weighted EXAFS data, the theoretical model, and the corresponding Fourier transforms of samples Pu-1-6.

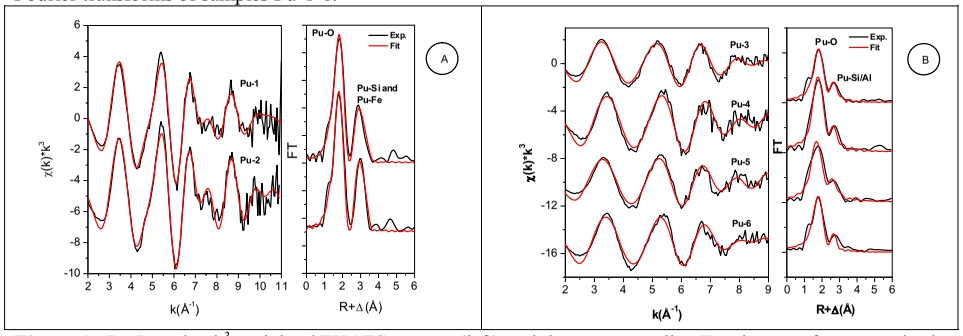

Figure 1. Pu L_{III}-edge k^3-weighted EXAFS spectra (left) and the corresponding Fourier transform magnitudes (right) of samples Pu-1-2 (A), samples Pu-3-6 (B).

As can be seen from Fig. 1, the EXAFS spectra of samples prepared under ambient CO_2 conditions (Pu-1-2) are different from those of samples Pu-3-6 (in the k range 6-9 $Å^{-1}$). The Fourier transform magnitude of Pu-1-2 show an additional peak due to Pu-Fe coordination at 3.46 Å. All samples have in commen a Al/Si coordination shell at about 3.14 Å and an O coordination shell at about 2.34 Å (except Pu-3). The structural parameters derived from the EXAFS fits are summarized in Tab. 2.

Table 2. EXAFS structural parameters for sorption samples Pu-1-6 ($\Delta R = \pm 0.02$ Å, $\Delta\sigma^2 = \pm 0.001$ $Å^2$).

Sample	Pu-O			Pu-Si/Al			Pu-Fe			ΔE_0	Red.
	N	R(Å)	$\sigma^2(Å^2)$	N	R(Å)	$\sigma^2(Å^2)$	N	R(Å)	$\sigma^2(Å^2)$	(eV)	error
Pu-1	8.8	2.34	0.013	2	3.13	0.004	2	3.46	0.006	-9.5	0.21
Pu-2	8.6	2.34	0.012	2	3.13	0.004	2	3.46	0.005	-10.2	0.22
Pu-3	8.4	2.40	0.021	2.3	3.17	0.008				-12.4	0.12
Pu-4	9.9	2.34	0.020	2	3.14	0.007				-11.2	0.36
Pu-5	11.1	2.34	0.026	2	3.14	0.007				-13.7	0.11
Pu-6	9.5	2.36	0.022	2	3.15	0.007				-11.5	0.14
$Pu(OH)_4$(am.) [6]		2.32									

The coordination numbers for Si/Al and Fe were held constant during the fit. The Pu-O distance in all samples (except samples Pu-3 and Pu-6) agrees with those of $Pu(OH)_4$(am) [6]. The detection of Pu-Al/Si interactions in all samples is indicative of inner-sphere sorption of Pu(IV) on the clay minerals present in OPA. Pu L_{III}-edge XANES Spectra (not shown) confirmed that in all samples Pu(IV) is the dominating oxidation state, independent on the initial Pu oxidation state (Pu(III), Pu(IV) or Pu(VI)) and the aerobic / anaerobic conditions during sample preparation. Also, the Background electrolyte does not influence the speciation of Pu sorbed on OPA. This result is in good agreement with a previous XAFS study on the sorption of Pu(III) and Pu(IV) onto kaolinite [7].

Acknowledgement
This work was supported by the German Bundesministerium für Wirtschaft und Technologie (Project 02E10166). We acknowledge the ESRF for provision of synchrotron beam time and thank the experimental support during the EXAFS measurements by the ROBL group members (A. Roßberg, A. Scheinost, C. Henning and D. Banerjee) from Helmholtz-Zentrum Dresden-Rossendorf (HZDR).

References

[1] R.L. Van Loon et al., J. of Contam. Hydrol. 61 (2003) 73.
[2] G.N. George and I.J. Pickering, SSRL (2000).
[3] A.L. Ankudinov et al., Phys. Rev. B 65 (2002) 104107.
[4] F. Demartin et al., Acta Cryst. C 48 (1992) 1.
[5] E. Chtoun et al., Annales de Chimie, 26(3) (2001) 27.
[6] J. Rothe et al., Inorg. Chem. 43 (2004) 4708.
[7] T. Reich et al., AIP Conf. Proc. 882 (2007) 179.

ESRF	**Experiment title:** EXAFS study of Np(IV/V/VI) binding mechanisms to cementitious materials	**Experiment number:** EC-617
Beamline: BM-20	**Date of experiment:** **from: 30/04/2010 to: 05/05/2010**	**Date of report:** 25/08/2010
Shifts: 15	**Local contact(s):** Dr. Andreas Scheinost	*Received at ESRF:*

Names and affiliations of applicants (* indicates experimentalists):
X. Gaona*, R. Daehn*, J. Tits*, D. Kunz* and E. Wieland
Laboratory for Waste Management, Paul Scherrer Institut, Villigen PSI, Switzerland

Report:

Cementitious materials will be used for the construction of the engineered barrier in repositories for long-lived intermediate level wastes (ILW), which may contain significant amounts of ^{237}Np ($t_{1/2} = 2.14 \cdot 10^6$ y). Predicting the long-term behaviour of Np in a cement-based repository requires a sufficiently detailed understanding of its interaction with the main phases of cement. Several Np redox states are expected under these conditions, although the corresponding stability fields and the binding mechanisms to cement are still poorly understood. The objectives of the project were: a) to assess the molecular environment of Np(IV/V) sorbed onto calcium silicate hydrates (C-S-H) and cement; b) to evaluate the stability field of Np(VI) within the pH range 10-14, and to assess its molecular environment when sorbed onto C-S-H phases and cement.

Results:

Sorption of Np(IV) onto C-S-H phases and cement

EXAFS measurements were performed on wet-pastes of C-S-H phases and cement doped with about 10000 ppm of Np(IV) tracer and equilibrated for 2 months in a N_2-filled glovebox. Four types of C-S-H phases with different Ca:Si ratio were prepared (0.7, 1.0, 1.6 and 1.0 in alkali-rich artificial cement pore water of pH = 13.3), representing different degradation steps of cement. Very reducing conditions were generated by $5 \cdot 10^{-3}$M $Na_2S_2O_4$. An additional sample of C-S-H with Ca:Si = 1.0 was prepared in absence of $Na_2S_2O_4$, in order to check the stability of unbuffered Np(IV) in C-S-H systems. As a lesson learnt from the previous campaign (see experiment EC-425), the samples were kept in liquid N_2 for the transport and storage during the measurements. The cryostat available at ROBL was used for all measurements (liquid-He temperature).

The transport and storage of Np(IV) samples in liquid N_2 was found to avoid oxidation to Np(V). Once left at room temperature and presence of air, the oxidation of Np(IV) took place within few hours. No differences in the EXAFS spectra were observed for Np(IV) samples prepared in presence and absence of $Na_2S_2O_4$, despite the unavoidable O_2-traces present in the glovebox. This observation indicates a strong stabilization of Np(IV) by C-S-H phases, in agreement with the very high distribution coefficients (R_d) determined in wet chemistry experiments (10^5-10^6 L·kg^{-1}).

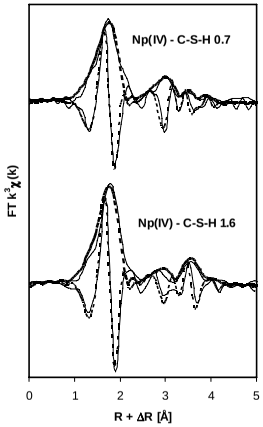

Fig. 1. *Experimental and theoretical Fourier transforms (modulus and imaginary parts) of Np(IV) sorbed on C-S-H 0.7 and 1.6.*

The principal component analysis (PCA) carried out using spectra of Np(IV)-doped C-S-H phases in $\chi(k)$, $k\chi(k)$, $k^2\chi(k)$, $k^3\chi(k)$ and energy spaces clearly indicates that only 2 components are needed to explain the spectra of all samples. The comparison of these compounds in ITFA mode with the original spectra strongly correlates them with Np(IV)-doped C-S-H 0.7 and 1.6. Linear combinations of these two "species" were found to satisfactorily explain EXAFS spectra of Np(IV) sorbed in C-S-H phases with Ca:Si ratio = 1.0, therefore allowing a mechanistic interpretation of Np(IV) uptake by C-S-H phases within the whole degradation sequence of cement. The Fourier-transformed k^3-weighted Np L_{III}-edge EXAFS (experimental and fits) for these samples are shown in Fig. 1. The resulting structural parameters are listed in Table 1. This information suggests an incorporation mechanism where Np(IV) (very likely) is bound in the interlayer of the C-S-H structure.

Sorption of Np(V) and Np(VI) onto C-S-H phases and cement

EXAFS measurements of Np(V) and Np(VI) were performed on weted-pastes, which were prepared in the same way as Np(IV) doped samples. No redox buffer was added to Np(V)-doped C-S-H and cement samples, whereas $5 \cdot 10^{-3}$M NaOCl was used for the preparation of the Np(VI) doped samples.

In contrast to Np(IV), the EXAFS spectra of Np(V) and Np(VI) provided only qualitative indications of an incorporation mechanism, mainly based on the identification of neighboring Si-atoms. Structural parameters determined for C-S-H samples of Ca:Si = 0.7 and 1.6 doped with either Np(V) or Np(VI) are given in Table 2. The Np(V/VI)-Si distances determined from the analysis of the EXAFS data significantly agree with those expected for Si-atoms mono- and di-coordinated to Np, and further they are in line with observations made on U(VI) in C-S-H environments (Macé et al., 2010; Harfouche et al., 2006). In contrast to Np(IV/V), the coordination environment of Np(VI) taken up by C-S-H phases seems to depend not only on the Ca:Si ratio but also on pH. Fig. 2 compares the Radial Structure Functions for samples of Np(VI)-doped C-S-H 0.7 (pH=10.1), 1.0 (pH=12.1), 1.6 (pH=12.5), 1.0 ACW (pH=13.3) and cement (pH=13.3). Axial and equatorial Np-O distances ($r_{Np\text{-}Oax}$ and $r_{Np\text{-}Oeq}$) enlarge at lower pH. A similar behavior is to be expected for the transition of $NpO_2(OH)_3^-$ (with one additional coordinated H_2O) and $NpO_2(OH)_4^{2-}$. Analogously to U(VI), this transition (in the aqueous phase) may occur at pH 12-12.5 (Guillaumont et al., 2003).

The study shows that C-S-H phases play an important role in Np(IV/V/VI) immobilization in cementitious materials. Incorporation in the C-S-H structure is regarded as the predominant uptake mechanism.

Sample	Shell	N	R [Å]	σ^2 [Å^2]	ΔE^0 [eV]	R-factor
Np(IV) – C-S-H 0.7	O	6.8 ± 0.8	2.27 ± 0.01	0.010 ± 0.002	5.8	0.068
	Si	5.0 ± 1.5	3.57 ± 0.03	0.009 ± 0.004		
	Ca_1	2.2 ± 0.9	4.05 ± 0.05	0.006*		
	Ca_2	2.1 ± 1.0	4.22 ± 0.05	0.006*		
Np(IV) – C-S-H 1.6	O	7.7 ± 1.2	2.27 ± 0.01	0.009 ± 0.003	5.5	0.090
	Si	3.6 ± 0.7	3.59 ± 0.03	0.009*		
	Ca_1	4.3 ± 1.1	4.12 ± 0.03	0.006*		
	Ca_2	3.3 ± 1.2	4.28 ± 0.05	0.006*		

* parameters fixed in the fit

Table 1. *Structural information derived from the EXAFS analysis of Np(IV)-doped C-S-H samples with Ca:Si = 0.7 and 1.6.*

Sample	Shell	N	R [Å]	σ^2 [Å^2]	ΔE^0 [eV]	R-factor
Np(V) – C-S-H 0.7	O_{ax}	2*	1.88 ± 0.01	0.002 ± 0.001	13.0	0.02
	O_{eq}	5.7 ± 1.0	2.39 ± 0.01	0.014 ± 0.004		
	Si	2.5 ± 1.9	3.21 ± 0.04	0.014 ± 0.011		
Np(V) – C-S-H 1.6	O_{ax}	2*	1.89 ± 0.01	0.002 ± 0.001	12.2	0.01
	O_{eq}	5.5 ± 0.6	2.39 ± 0.01	0.010 ± 0.002		
	Si_1	2.9 ± 0.9	3.24 ± 0.02	0.014*		
	Si_2	1.7 ± 1.5	3.86 ± 0.08	0.014*		
Np(VI) – C-S-H 0.7	O_{ax}	2*	1.79 ± 0.01	0.002 ± 0.001	11.0	0.01
	O_{eq}	4.2 ± 0.4	2.25 ± 0.01	0.005 ± 0.001		
	Si_1	0.5 ± 0.4	3.08 ± 0.04	0.004**		
	Si_2	1.8 ± 0.7	3.56 ± 0.02	0.004***		
	Si_3	1.3 ± 0.8	3.81 ± 0.04	0.004***		
Np(VI) – C-S-H 1.6	O_{ax}	2*	1.85 ± 0.01	0.004 ± 0.001	10.2	0.06
	O_{eq}	3.5 ± 0.8	2.24 ± 0.02	0.007 ± 0.003		
	Si_1	*0.4 ± 0.6*	*3.22 ± 0.11*	*0.004***		
	Si_2	*0.9 ± 1.2*	*3.65 ± 0.11*	*0.004****		
	Si_3	*1.5 ± 1.3*	*3.83 ± 0.08*	*0.004****		

* parameters fixed in the fit
** parameter left originally free. After the first iteration, it was fixed to reduce the uncertainty in N_{Si}
*** parameters defined originally = σ^2_{Si1}. After the first iteration, they were fixed to reduce the uncertainty in N_{Si}

Table 2. *Structural information derived from the EXAFS analysis of Np(V)- and Np(VI)-doped C-S-H samples with Ca:Si = 0.7 and 1.6.*

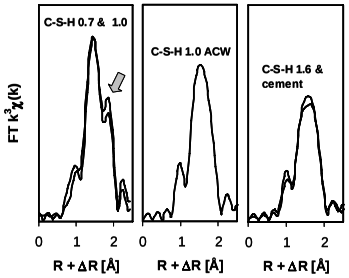

Fig. 2. *Comparison of experimental Radial Structure Functions obtained for Np(VI)-doped C-S-H 0.7, 1.0, 1.0 ACW, 1.6 and cement.*

References

Guillaumont, R., Fanghänel, J., Neck, V., Fuger, J., Palmer, D.A., Grenthe, I., Rand, M.H. (2003) Chemical Thermodynamics 5. Update on the Chemical Thermodynamics of Uranium, Neptunium, Plutonium, Americium and Technetium. NEA OECD, Elsevier

Harfouche, M., Wieland, E., Daehn, R., Fujita, T., Tits, J., Kunz, D., Tsukamoto, M. (2006). EXAFS study of U(VI) uptake by calcium silicate hydrates. Journal of Colloid and Interface Science, 303, 195-204

Macé N., Dähn R., Tits J., Scheinost A., Wieland E. (2010b). EXAFS study of U(VI) sorption on cementitious materials (in preparation)

3.2. Experimental Reports Materials Research

ROBL-CRG	**Experiment title:** Optical properties of planar and lithographic x-ray waveguides	**Experiment number:** 2002670
Beamline: BM 20	**Date of experiment:** from: 01.09.2008 to: 25.02.2009	**Date of report:**
Shifts: 18	**Local contact(s):** Carsten Bähtz	*Received at ROBL:*

Names and affiliations of applicants (* indicates experimentalists):

Matthias Bartels
Institut für Röntgenphysik, Universität Göttingen
Henrike Neubauer
Institut für Röntgenphysik, Universität Göttingen
Sven Philip Krüger
Institut für Röntgenphysik, Universität Göttingen
Tim Salditt
Institut für Röntgenphysik, Universität Göttingen

Report:

3rd generation synchrotron facilities offer high photon flux appropriate for x-ray based imaging such as holography and coherent diffraction imaging. Waveguide optics enable to control coherence properties and to focus the x-ray beam down to the nanometer scale in order to improve the resolution in imaging experiments.
We report on the properties of lithographic and two-component planar x-ray waveguides. The lithographic air/*Si* waveguides are fabricated using electron beam lithography, subsequent Reactive Ion Etching (RIE) and wafer bonding to obtain 10µm x 40nm channel cross-section dimensions minimal. Beam losses of the modes propagating through the waveguide are essentially due to absorption at the air/*Si*-cladding interfaces. Therefore the transmission of the waveguide is intrinsically high.
As already shown previously (*T.Salditt et al.*, PRL **100**, 184801 (2008)) the efficiency of a waveguide can be strongly optimized by placing an appropriate interlayer (*Mo*) between the guiding layer (*C*) and the cladding (*Ge*). The absorption of the evanescent tails of the modes propagating through the guiding layer is significantly reduced while the cladding dampes out the radiative modes. These two-component planar waveguides of 9/18/35nm guiding layer thicknesses are fabricated by Magnetron Sputtering.

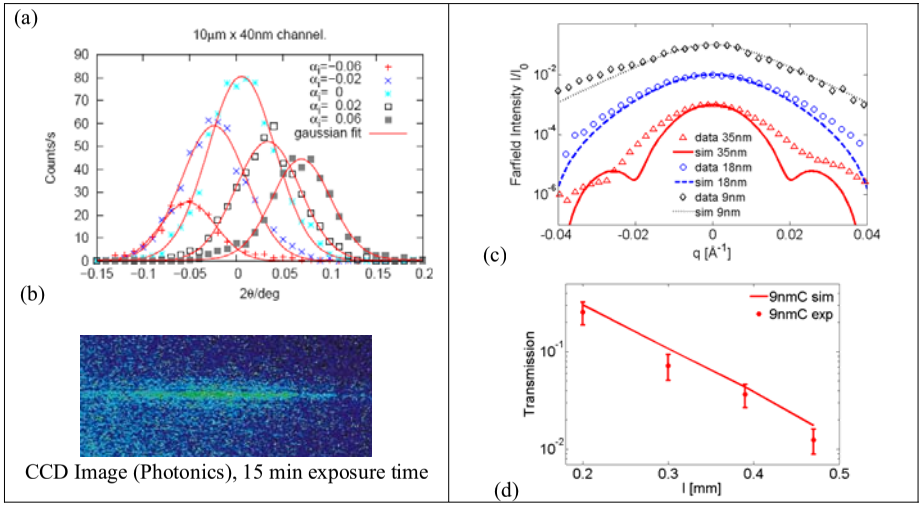

Fig 1: (a) Farfield Intensity of the lithographic waveguide for different angles of incidence α_i , along with Gaussian fits. The maximum positions are found to be at α_f = 0°. (b) CCD image of the farfield of the 10µm x 40nm channel. (c) Farfield intensity of the planar waveguides as a function of q along with simulations. (d): measured and calculated transmission T at E=13.5kev as a function of the waveguide length.

The experiments were performed at the Rossendorf bending magnet beam on a wide range of energies defined by a double-crystal Si(111) monochromator. The beam shape and size was controlled by two collimating Pt-coated mirrors and motorized slits. A flux of 1-3 x 10^7 ph/s impinged on the waveguide entrance at 2 x 0.04mm^2 beam size depending on the energy and ring current. The farfield patterns of the waveguides were measured to obtain the divergence of the beam and therefore resolution properties of the optics in imaging experiments. The maximum of the farfield at different angles of incidence α_i is always found at $2\theta = \alpha_i$ as expected for waveguide properties. The farfield pattern of the planar waveguides are in good agrement with the simulations. The divergence Δq = 0.00255nm of the 9nm*C* mono-modal waveguide is significantly higher than for the 35nm*C* two-modal waveguide (Δq = 0.00147nm), i.e. the numerical aperture of the optics is enhanced. The transmission of the 9nm*C* two-component waveguide depends strongly on the energy *E* and the waveguide length *l*. The measured transmission at *E*=13.5keV reaches *T*=0.256 at *l*=200µm which is 84% of the calculated value (*T*=0.305). The experimental results show that high transmission is obtained for sub-10nm waveguides. A novel generation of lithographic waveguides with air-gap channels capped by wafer bonding was also tested. However, the flux density was seriously compromising these efforts.

ROBL-CRG	**Experiment title:** Influence of ion beam channelling for ripple formation at amorphous-crystalline interface after ion-bombardment	**Experiment number:** 20-02-673
Beamline: BM 20	**Date of experiment:** from: 31.01.09 to: 3.2.09	**Date of report:** 10.05.2009
Shifts: 9	**Local contact(s):** Carsten Baehtz	*Received at ROBL:*

Andreas Biermanns*, Ullrich Pietsch
FB7 - Physik , Universität Siegen, 57068 Siegen, Germany

Antje Hanisch*, Jörg Grenzer
Forschungszentrum Dresden-Rossendorf, Institute of Ion Beam Physics and Materials Research
01314 Dresden, Germany

Report:

With ion beam induced patterning nanostructures such as dot or ripple-like features evolve on solid surfaces via a self-organization process. Certain factors as the beam parameters [1] and the initial roughness [2] highly influence the competing processes of sputtering and surface diffusion during the formation. Our recent experimental findings indicate that also the crystallographic structure of the sample can influence pattern formation in semiconductor materials which is not taken in consideration in hitherto theories [3, 4]. In this experiment at ROBL we studied the role of the crystal orientation, i.e. different lattice planes and their packing density, of the initial surface in the specific case of medium-energy (35keV) Xe^+–induced ripples on Si. For this ion species and energy ripple formation was found on Si(001) surfaces for incidence angles between 55° and 75° off-normal. However, it was so far not adressed if this rather small angular window is related only to the orientation of the surface to the ion beam or to the orientation of the (001) lattice planes before amorphization as well.

In this experiment we studied the ripple formation on silicon surfaces as a function of the miscut angle. We prepared samples with a defined deviation of the surface normal from the [001] direction. The (001) lattice plane of these wafers were tilted by 2°, 5° and 10° towards [110]. All samples were bombarded with Xe ions at an incidence angle ψ of 65° (with respect to the surface normal) at an ion energy of 35 keV at the Forschungszentrum Dresden-Rossendorf. Under these conditions a rippled pattern with a typical wavelength of 150 nm is formed on the surface and at the amorphous-crystalline interface located several tens of nanometers below. The ion-beam projection was orientated parallel, antiparallel or perpendicularly to the miscut direction (Fig. 1) leading to an effective incidence angle with respect to the Si (001) direction between 55° and 75°.

For a set of 9 samples we performed coplanar X-ray diffraction experiments at an X-ray energy 7,8 keV in order to probe the orientation of the ripple pattern with respect to the (001) lattice planes. The incoming X-ray beam was collimated by a set of slits in front of the sample. To achieve sufficient resolution in reciprocal space a combination of slits and an analyser-crystal was used. For all samples we recorded reciprocal space maps (RSM) around the (004) Bragg peak in coplanar scattering geometry.

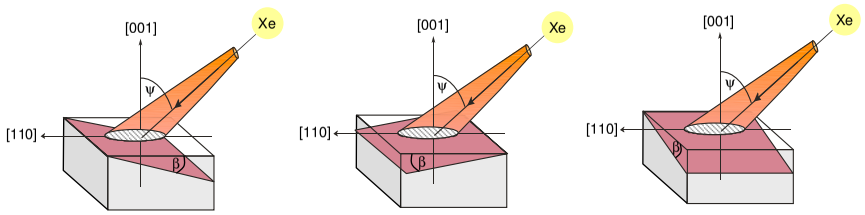

Fig. 1a): ion beam projection parallel to the miscut direction

b) ion beam projection antiparallel to the miscut direction

c) ion beam projection perpendicular to the miscut direction

Fig. 2 shows examples of such maps measured for the three different cases (Fig.1) for the 10° miscut angle. In the RSMs q_z is oriented parallel to the [001] direction. It can be seen that the crystal truncation rod (CTR) which goes parallel to the surface normal is tilted by the miscut angle to q_z and that the satellite peaks which come from the ordered subsurface ripples follow the rotation of the CTR. That means that the ordered nanostructure follows the surface but not the crystal planes. Also, there is no significant difference wether the (001) plane is tilted by +10° (a) or -10° (b), i.e. whether the effective indicence angle in respect to the (001) plane is 55° or 75°, respectively. Preliminary analysis shows that the satellite peaks of all three samples have also the same intensity, equal shape and FWHM indicating a similar shape and degree of ordering of the ripples as on silicon (001) substrates without a miscut. The different shape of the central Bragg peak is an artefact of the resolution function. As the maps were recorded without an analyser crystal for the sake of time, the width of the Bragg peak is strongly influenced by the footprint of the beam on the surface which was different in all three cases due to the miscut. The wavelength determined from the reciprocal maps very well accords with the one extracted from AFM measurements. However, note that the orientation with respect to the crystalline material can not be determined from AFM. In the perpendicular case (c) the miscut cannot be seen in the map because the X-ray beam goes across it.

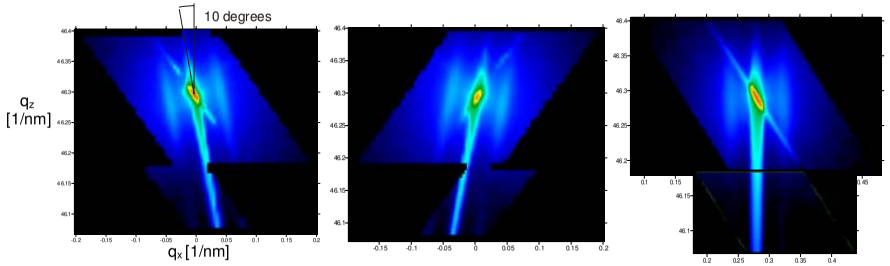

Fig. 2: 35keV β=10° parallel ϕ=0°

35keV β=10° antiparallel ϕ=0°

35keV β=10° perpendicular ϕ=0°

The results indicate that in the case of medium energy ion bombardment with rather heavy ions, the formation of a periodic ripple pattern is rather related to the incidence angle with respect to the surface than to the lattice planes.

[1] T.K.Chini et al. *"Energy dependent wavelength of the ion induced nanoscale ripple"*, Phys. Rev. B. **66**, 153404 (2002)
[2] P.Karmakar et al. *"Role of initial surface roughness on ion induced surface morphology"*, Appl. Phys. Lett. **93**, 103102 (2008)
[3] J. Grenzer et al. *"Ripple structures on surfaces and underlying crystalline layers in ion beam irradiated Si wafers"*, Phys. stat. sol., accepted (2009)
[4]J.Munoz-Garcia et al., "*Coupling of morphology to surface transport in ion-beam irradiated surfaces: Oblique incidence"*, Phys. Rev. B **78**, 205408 (2008)

ROBL-CRG	**Experiment title:** Thermal stability of nanostructures in the Ti-Al-Si-N and Cr-Al-Si-N nanocomposites	**Experiment number**: 20-02/675
Beamline: BM 20	**Date of experiment**: from: 28/01/09 to: 31/01/09	**Date of report**: 08.07.2009
Shifts: 9	**Local contact(s)**: Carsten Baehtz	*Received at ROBL:*

Names and affiliations of applicants (* indicates experimentalists):

Milan Dopita*, Mykhailo Motylenko*, Christina Wuestefeld*, David Rafaja

TU Bergakademie Freiberg, Institute of Materials Science, Gustav-Zeuner-Str. 5, 09599 Freiberg, Germany

Report:

Changes in the microstructure of the $Ti_{0.50}Al_{0.50}N$ coatings due to their high-temperature treatment in vacuum were investigated by in-situ high-temperature measurements at ROBL beamline BM20. The samples were deposited by using cathodic arc evaporation (CAE) at two different bias voltages, U_B = -40 V and U_B = -80 V. Preliminary laboratory experiments revealed differences in the phase composition of the samples. $Ti_{0.50}Al_{0.50}N$ deposited at U_B = -40 V contained fcc-(Ti,Al)N as a single nanocrystalline phase. $Ti_{0.50}Al_{0.50}N$ deposited at U_B = -80 V contained fcc-(Ti,Al)N as the dominant phase and wurtzitic w-AlN as a minor phase. The crystallite size was about 7 nm and 3.5 nm for U_B = -40 V and U_B = -80 V. HRTEM experiments have shown that AlN was grown hetero-epitaxially on fcc-(Ti,Al)N. The main goal of the in-situ synchrotron experiments was to investigate the development of the phase composition in the $Ti_{0.50}Al_{0.50}N$ coatings and the changes in the stress-free lattice parameters and in the microstrain of fcc-(Ti,Al)N with increasing temperature up to 1140°C. Because of the expected spinodal decomposition, the coatings were cooled to approx. 110°C after each high-temperature measurement and measured again. The results of the in-situ experiments are summarised in Fig. 1. The originally single-phase $Ti_{0.50}Al_{0.50}N$ coating remained single-phase up to approx. 660°C. In this temperature range, the stress-free lattice parameter increased slightly as driven by thermal expansion. After cooling the sample from 660°C to 110°C, the stress-free lattice returned to the starting value. After heating the sample to 885°C, the metastable Al-rich fcc-(Al,Ti)N formed. Its amount increased during the annealing time (150 min) up to approx. 13 mol %. Concurrently, thermodynamically stable w-AlN developed at 885°C. During the annealing at 885°C, the mole fraction of w-AlN reached nearly 5 %. The onset of the decomposition of fcc-(Ti,Al)N into fcc-(Al,Ti)N and w-AlN was accompanied with an increase of the stress-free lattice parameter of fcc-(Ti,Al)N as observed after cooling the sample and with an increase of the microstrain in the fcc-(Ti,Al)N phase. The increase of the stress-free lattice parameter confirmed a disappearance of Al from the host structure of fcc-(Ti,Al)N; the increase of the microstrain is an evidence of the formation of local strain fields at the interfaces between the decomposed fcc-(Ti,Al)N and the Al-rich phases. During annealing at 1140°C, the metastable Al-rich fcc-(Al,Ti)N dissolved almost completely and the coating consisted of nearly Al-free fcc- (Ti,Al)N (according to its stress-free lattice parameter) and w-AlN. During the last cooling from 1140°C to 90°C, the sample decomposed almost completely into w-AlN (45 mol %) and Al-free fcc-TiN (50 mol %).

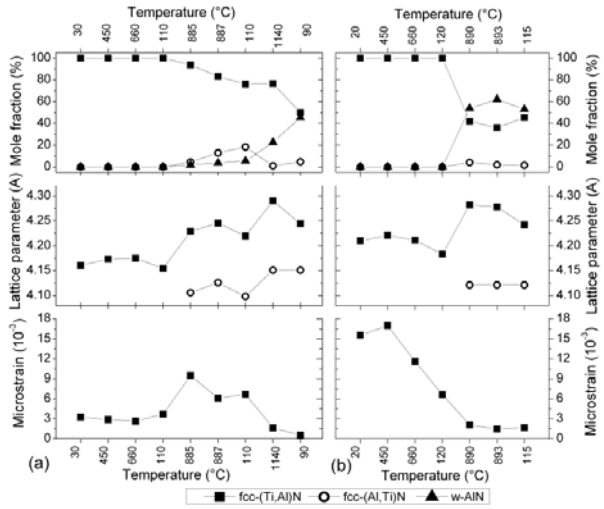

Figure 1: Phase evolution, stress-free lattice parameter and microstrain during annealing of the $Ti_{0.50}Al_{0.50}N$ coatings deposited at U_B=-40V (a) and U_B=-80V (b).

Only traces of the Al-rich fcc-(Al,Ti)N phase (5mol %) were observed. In the dual-phase coating deposited at U_B = -80 V, the de-composition of fcc-(Ti,Al)N into the Ti-rich fcc-(Ti,Al)N and w-AlN was much faster than in the coating deposited at U_B = -40 V. Approx. 50 mol % w-AlN formed already at 890°C. The disappearance of Al from the host structure of fcc-(Ti,Al)N was confirmed by a large stress-free lattice parameter that was observed after cooling the sample from 893°C to 115°C. The microstrain, which is an indicator of the intrinsic strain fields in the coatings, decreased continuously upon heating. Usually, large intrinsic strains are considered to increase the hardness of the thin film nanocomposites. In this particular case, both improved high-temperature stability and a higher high-temperature hardness are expected for the originally single-phase coatings than for the dual-phase coatings. Our in-situ high-temperature synchrotron measurements done on CAE (Ti,Al,Si)N coatings have shown that the addition of Si improves further the high-temperature stability of the microstructure of the coatings.

ROBL-CRG	**Experiment title:** GISAXS study of self organized metallic islands and nanowires on rippled substrates	**Experiment number:** **20-02-676**
Beamline: BM 20	**Date of experiment:** from: 01/07/2009 to: 05/07/2009	**Date of report:** 06/11/2009
Shifts: 12	**Local contact(s):** Nicole Jeutter	*Received at ROBL:*

Names and affiliations of applicants (* indicates experimentalists):

G. Abrasonis* and Gy. J. Kovacs*

Institute of Ion Beam Physics and Materials Research, Forschungszentrum Dresden-Rossendorf, PO BOX 51 01, 01314 Dresden Germany

T. W. H. Oates

I.F.M., University of Linkoping, S-581 83 Linkoeping, Sweden

Report:

Self-organization of Ag nanoparticles on ion beam pre-patterned Si surfaces has been investigated by means of grazing incidence small angle x-ray scattering (GISAXS). The periodic surface roughness undulations have been prepared by oblique incidence ion beam sputtering. Figure 1 shows the atomic force surface image and the corresponding 2D GISAXS image recoreded with the x-ray beam direction parrallel to the ripples. Two streaks in the GISAXS pattern are observed. Position of their maximum on the scattering vector q_y axis is inversely proportional to the ripple period which is ~31 nm. Left streak shows higher intensity than the right one reflecting the assymetric cross-sectional ripple shape [1].

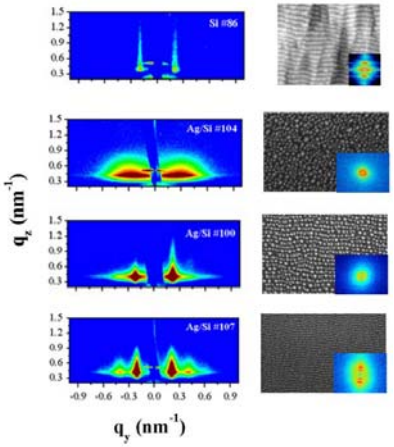

Figure 1. 2D GISAXS images (left column) and correspondind surface micrographs (right column) with their fast fourier transforms (insets) of the Si surface with ripples (first row), Ag nanoparticles on non-patterned Si surface (second row), Ag nanoparticles (third row) and Ag nanowires (fourth row) on ion beam pre-patterned Si surfaces.

When Ag thin film is grown on the pre-patterned surface by physical vapour deposition, alligned nanoparticle or nanowire arrays are obtained depending on the growth conditions (see scanning electron microscopy micrographs in Figure 1). These morphologies are reflected in corresponding GISAXS patterns (see Figure 1) which show strong intensity streaks suggesting strong correlations in the direction perpendicular to the ripples. The presence of a 2nd peak (and 3rd order peak for the nanowires) points out the paracrystalline ordering [1,2]. Ag nanoparticles grown on non-prepatterned Si surfaces show two broad intensity lobes (see Figure 1) suggesting rather diffuse spatial correlations. This underlines the influence of the pre-patterning on the Ag nanoparticle growth thermodynamics and/or kinetics [4]. Note, that the streak assymetry intensity of aligned Ag nanoparticle GISAXS is inversed in relation to that of the underlying Si ripples. This is most probalby related to the growth of Ag nanoparticles on the ripple slope and their oblate (or prolate) shape. The understanding of such behaviour needs further studies.

In-situ experiments of the de-wetting of thin obliquely deposited Ni films on pre-patterned substrates could not be carried out due to technical problems related with the sample re-alignement which is needed after each heating step. However, preliminarly results indicate that thin Ni films show correlated roughness with the underlying Si ripple pattern while upon heating splitting occurs in the temperature range of ~400-500°C. The de-wetted film shows signatures of correlated nanoparticle arrays similar to those observed for the ex-situ grown Ag films.

1. D. Carbone, A. Biermanns, B. Ziberi, F. Frost, O. Plantevin, U. Pietsch and T. H. Metzger, J. Phys.: Condens. Matter **21**, 224007 (2009).
2. R. Lazzari, J. Appl. Cryst. **35**, 406 (2002)
3. R. Lazzari, F. Leroy, G. Renaud, Phys. Rev. B **76**, 125411 (2007).
4. T.W.H. Oates, A. Keller, S. Facsko, A. Muecklich, Plasmonics, **2**, 47 (2007).

	Experiment title: **Self -assembled Fe and FePt nanoparticles in yttria-stabilized zirconia after iron-platinum implantation**	**Experiment number**: 20-02-677
Beamline: BM20	**Date of experiment**: from: 20.06.2009 to: 23.06.2009	**Date of report**: 12.01.2010
Shifts: **9**	**Local contact(s)**: Dr. N. Jeutter	*Received at ESRF:*

Names and affiliations of applicants (* indicates experimentalists):

Dr. A. Shalimov*

Forschungszenrtum Dresden – Rossendorf,

Institute of Ion Beam Physics and Material Research

01328 Dresden, Bautzner Landstr. 400.

Report:

Series of experiments aiming the fabrication and characterization of Fe and FePt magnetic nanoparticles has been performed within the DFG Project PO 1275/2-1 "SEMAN". The current proposal was dedicated for structural investigation of Fe and FePt nanoparticles embedded in yttria stabilized zirconia (YSZ) as a result of Fe and FePt self-assembling, where Fe and Pt ions were doped by means of ion implantation at energies of 110 and 325 keV respectively.

The first part of the application assumed the investigation of secondary phases in YSZ crystals implanted with Fe only. The range of fluences of implanted Fe^+ ions was broadened in respect to initially planned from $1\times10^{14}\ldots1\times10^{16}$ (cm^{-2}) up to $1\times10^{14}\ldots3\times10^{17}$ (cm^{-2}).

The longitudinal $2\theta/\omega$ and transverse ω-scans in double- and triple crystal diffraction mode were performed for all samples in order to reveal the presence of magnetically active Fe-based secondary phases. No additional reflections from pure iron or iron oxides were found for the samples implanted with the fluences of $1\times10^{14}\ldots3\times10^{15}$ (cm^{-2}). High resolution scanning of the reciprocal space close to the vicinity of reciprocal lattice of YSZ substrate did not resolve significant increase of x-ray diffuse scattering with an increase of ion fluence. This result can be caused by the creation of solid YSZ:Fe solution which is possible in the case of low-fluence implantation. Another reason of the reflections absence of Fe (Fe_xO_y) phases is the amorphous structure of the inclusions. The samples implanted with the higher fluences of $1\times10^{16}\ldots3\times10^{17}$ (cm^{-2}) represent diffraction peaks from α-Fe, γ-Fe as well as from oxide-rich (Fe_xO_y) phase.

The x-ray diffraction study of these samples is in good agreement with Mössbauer spectroscopy performed at FZD. Combination of the experimental results obtained at ROBL and in-house research exhibits a variety of possible phases created in YSZ crystals after high-fluence Fe implantation. Moreover, it was found that Fe nanoparticles possess the Fe-core/ Fe_xO_y -shell architecture where the shell thickness is strongly dependent on the size of the nanoparticles. The results of the experiments are submitted to the Journal of Applied Physics.

The second set of samples examined during the beamtime consists of YSZ crystals implanted with Fe and Co ions with overlapping ion distribution profiles at the depth of 55 nm. Although the ferromagnetic response of those samples was relatively strong (much stronger then in case of YSZ:Fe), the expected FePt (or any other ferromagnetic) phase has not been detected using x-ray diffraction. Such a confusing result forced us to attest, for a presence of contaminations, also the back, non-implanted side of specimens. It has been found that the backsides of substrates were contaminated with Fe giving the reflections of bcc iron (magnetic phase). Rough estimation of contaminations' volume made us convinced that iron presented at the non-implanted side of the samples is a main source of the observed ferromagnetism. Afterwards it was found that contaminations, most probably, were introduced by metallic clamps employed for the sample holding during the implantation of this particular set of samples. The non-implanted side of YSZ:Fe samples described early was also examined. Contaminations were not found in those samples. In order to avoid such situations in future, the list of recommendations for technical personnel and experimentalists involved to the research has been worked out.

	Experiment title:	Experiment number:
	Structural investigation of Co-B ferromagnetic nanoparticles in ZnO single crystals	20-02-678
Beamline:	**Date of experiment**: from: 17.06.2009 to: 20.06.2009	**Date of report**: 12.01.2010
Shifts: 9	**Local contact(s)**: Dr. N. Jeutter	*Received at ESRF:*

Names and affiliations of applicants (* indicates experimentalists):

Dr. A. Shalimov*

Forschungszenrtum Dresden – Rossendorf,

Institute of Ion Beam Physics and Material Research

01328 Dresden, Bautzner Landstr. 400.

Report:

Series of ZnO single crystals implanted with Co and B have been characterized by synchrotron radiation x-ray diffraction technique at ROBL. These experiments partially represent one of the research topics of Nanofunctional Films Group at FZD, namely, development of magnetically active semiconductimg materials.
The ZnO substrates were implanted with B ions and with Co ions with energies 30keV and 80 keV respectively. The fluences of implanted Co were chosen as 8×10^{16} and 16×10^{16} (cm^{-2}). The dose of B ions has been varied from 5×10^{15} up to 32×10^{16} cm^{-2} for different samples. According to the aim of the application it was necessary to identify the origin of magnetism in these samples. Such a source supposed to be represented by magnetic Co-based secondary phases.
Using coplanar x-ray diffraction technique in a wide range of angles, we performed set of measurements which did not reveal presence of additional crystalline phases, except of ZnO host material. We would note that in the case of nanoparticles self-organization, the concentration of Co-inclusions should be sufficient for their detection, similarly to MgO:Fe systems, where the doses of implanted ions where equal to those studied in the current proposal. Absence of diffraction pattern from secondary (Co-B)-based phases, leads us to a conclusion that those inclusions are in the amorphous state. High-resolution diffraction of the ZnO substrates proves an enhanced diffuse scattering near the reciprocal lattice points of ZnO. Using the relations of Huang and Stockes – Willson scatterings the average size of nanoparticles was estimated. We have found that dimensions of (Co-B) – inclusions are in the range from 10 to 40 nm. The size of nanoparticles increases with an increasing of B fluence being in good agreement with SQUID measurements. At the present state, the results of the experiments performed at ROBL, as well as at FZD, are in preparation for publishing.
In addition to the measurements of Co-B implanted ZnO, the structural investigations of Fe implanted GaN have been performed. The results of these structural measurements show the correlation between structural and magnetic properties of ion implanted GaN:Fe. It was concluded that spinodal decomposition is the preliminary stage before the formation of precipitates. The results of this experiment jointed with the data of magnetic and spectroscopic investigations are submitted to Physical Review B.

ROBL-CRG	**Experiment title:** ***In-situ* XRD and Electrical Resistivity Study of the Phase Transformations in Ni-Ti Shape Memory Alloys (SMA)**	**Experiment number:** **20_02_679**
Beamline: BM 20	**Date of experiment:** from: 23.01.2009 to: 27.01.2009	**Date of report:** 28.02.2009
Shifts: 12	**Local contact(s):** Dr. Carsten Baetz	*Received at ROBL:* *01.03.2009*

Names and affiliations of applicants (* indicates experimentalists):

F.M. Braz Fernandes*, K. K. Mahesh*, R.J.C. Silva*: CENIMAT-Centro de Investigação de Materiais, Campus da FCT/UNL, 2829-516 Monte de Caparica, PORTUGAL
Rui M.S. Martins, J. Borany*: FZR, ROBL-CRG at ESRF, B.P. 220, F-38043, Grenoble, FRANCE

REPORT:

In situ XRD has been used by the authors to study the structural changes during (i) the crystallization of Ni-Ti thin films [1], (ii) the growth of Ni-Ti thin films by sputtering [2-11], and (ii) the transformation characteristics of bulk N-Ti subject to thermomechanical treatments [12-16]. The phase transformations of Ni-Ti SMA can also be investigated by measuring some physical properties such as electrical resistivity (ER) as a function of temperature. During cooling of Ni-Ti SMA from B2-phase, the resistivity value decreases linearly with the temperature down to R_s , where R-phase self-accommodated (by twinning) starts to be formed. Twinning in an alloy matrix results in electron scattering, which in turn leads to the increase of the ER [17]. Additional cooling below R_f promotes the continuous increase of rhombohedral distortion angle of the R-phase. It is assumed that this rhombohedral distortion is the reason for a further increase of ER (between R_f and M_s). Below M_s, this distortion is relaxed by the R-phase transforming to monoclinic B19' martensite, giving a gradual decrease of ER.

EXPERIMENTAL

A new chamber, based on the Be dome furnace, enables heating and cooling between -100 and 150°C. The chamber was mounted on the Phi-circle of the 6-circle goniometer of ROBL beamline. The sample is contacted with 4 springs at the corners for resistivity measurements. This mounting makes possible the access in nearly all scattering directions; at least, there is no restriction for GIXRD and θ/2θ scans even for angles up to 2θ = 60°. The temperature was measured with a Shell-TC (below the sample). The chamber can be flushed with nitrogen or helium, or evacuated. Two samples were tested: one Ni-Ti thin films deposited on TiN buffer layers and another one deposited on Si(100) oxidized. In both cases the transformation sequence during cooling will be B2 => R-phase and R-phase => B19'.
The following samples (S23 and S32) from previous campaigns have been studied for in situ XRD characterization simultaneously with ER measurement.

sample	*Power applied to the 2nd magnetron (W)*				*Substrate*			
	NiTi	*Ti*	*Hf*	*Cu*	Si oxidized	Si (100)	MgO (100)	MgO (111)
S23	40	20			X			

Sample	*TiN deposition: ratio Ar/N2*	*Substrate bias (V)*		*Deposition (min.)*						*Annealing (min.)*	
		TiN deposition	Ni-Ti *deposition*	*TiN (on top of Si wafer)*	*NiTi 1st layer*	*TiN 1st inter-mediate*	*NiTi 2nd layer*	*TiN 2nd inter-mediate*	*NiTi 3rd layer*	*TiN (on top of Si wafer)*	*After last deposition of NiTi*
S32	10/2.5	-30	0	15	120	-	-	-	-	28	60

RESULTS AND DISCUSSION

Only results for the sample S23 are shown. Results for S32 are still being processed.

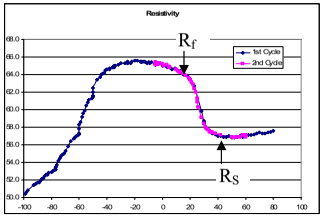

Fig. 1 – Electrical resistivity measurements during 2 consecutive cooling cycles showing the good reproducibility of the results (sample 23).

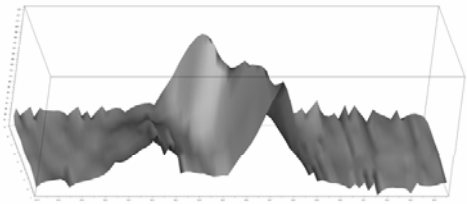

Fig. 2 – In situ XRD during cooling, showing the splitting of the B2 (110) peak, giving the (211) and (300) of the R-phase (back to forth in the 3-D plot) for the sample 23.

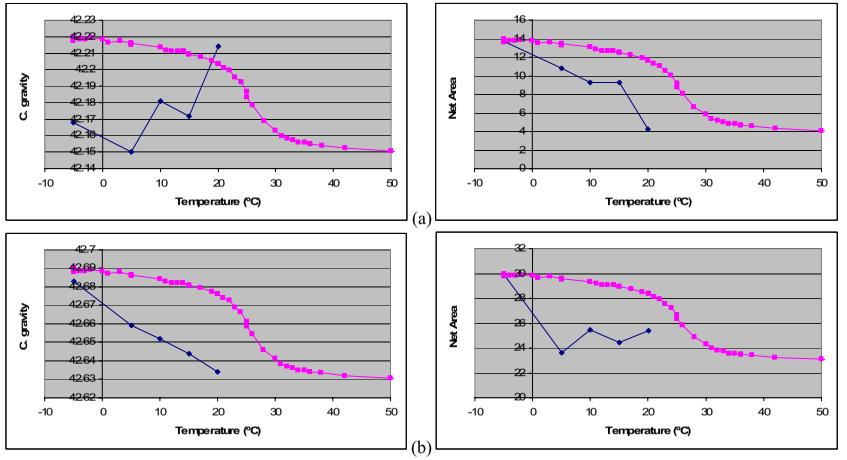

Fig. 3 – Variation of the peak position and net area for (a) (211) and (b) (300) of the R-phase represented in blue. In cyan it is represented the variation of the electrical resistivity (in an arbitrary scale) as a function of the temperature for the sample 23.

CONCLUSIONS

- The simultaneous measurement of the electrical resistivity and XRD during thermal cycles allows establishing a direct correlation between features of electrical resistivity variation and structural changes.
- It is usually assumed in the published literature [1] that, during cooling, the B2 to R-phase transformation shows a significant electrical resistivity increase associated to (i) formation of R-phase from R_s to R_f, followed by (ii) increasing rhombohedral distortion (with no further R-phase formation). Data presented in left-hand graphs of Fig. 3 (a) and (b) confirm that the rhombohedral distortion is notorious (variation of the peak position of (211) and (300) from R-phase) when cooling below the temperature usually identified as R_f. But data presented in right-hand graphs of Fig. 3 (a) and (b) show that the net areas of both R-phase peaks (211) and (300) are still increasing during the last step of the electrical resisitivity increase. These results suggest that, besides a significant rhombohedral distortion below R_f, there is still new R-phase formation.

Reference

[1] V. Novák, P. Šittner, G.N. Dayananda, F.M. Braz-Fernandes, K. K. Mahesh. *Materials Science and Engineering A* 481–482 (2008) 127–133.

	Experiment title: In-situ investigation of the dewetting process of thin iron film in the CNT growth process	**Experiment number:** **20_02_682**
Beamline: BM 20	**Date of experiment:** from: 21.4.2009-28.4.2009	**Date of report:** 3.2.2011
Shifts: 18	**Local contact(s):** Dr. Carsten Baehtz (baehtz@esrf.fr)	*Received at ROBL:*

Names and affiliations of applicants (* indicates experimentalists):

C. Baehtz, T. Wirth[1)], B. C. Bayer[1)]

Helmholtz-Zentrum Dresden-Rossendorf, Institute of Ion Beam Physics and Materials Research, P.O.B. 510119, 01314 Dresden, Germany
1) Centre for Advanced Photonics and Electronics, University of Cambridge, 9 JJ Thompson Avenue, Cambridge CB3 0FA, UK

Results

Carbon nanotubes (CNTs) can be grown from gaseous precursors by the use of metal nanoparticles as catalysts. These catalyst particles are commonly prepared by dewetting of metal thin films at elevated temperature under hydrogen atmosphere (to reduce thin oxide layers).[1] The size of the resulting particles strongly depends on the film thickness of the pristine material (approx factor 3, see report 20-02-671). The system under investigation is Fe, due to Fe being the most commonly used nanotube catalyst.[2,3]

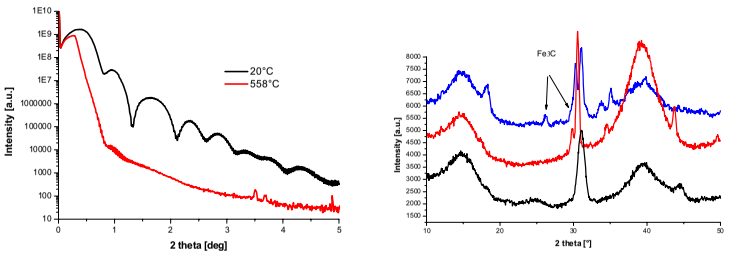

Fig. 1, left: XRR curve of the pristine material and the spitted film. Right: XRD pattern of the catalyst at different stages of the reaction; before (black line, after heating (red line and during CNT growth.

The pristine material is pure α-Fe in the thin film (shown in Fig. 1 right side, black line) with an amorphous oxide layer seen by an additional oszillation in the XRR curve in Fig. 1 left side, on a Si-wafer with a 200 nm SiO_2 buffer layer. By heating the film splits and a phase transformations into a mixture of α- and γ-Fe (Fig.1, right side red line) as catalyst are observed. When applying H_2C_2 as carbon source gas this α/γ-ratio is shifted towards the γ-Fe phase. The formation of CNTs starts immediately (signal at 18° 2theta in Fig. 1, right hand, blue line) and additionally crystalline Fe_3C is observed. The growth parameters were 560°C surface temperature, 170 mbar pressure by 30 scccm Ar, 10 sccm H_2 and 1 sccm H_2C_2 gas flow.

We succeeded in establishing that the carbide is not necessary for CNT growth by growing CNTs only from metallic Fe, when carbide formation was very extensivly avoided. But further time resolved experiments are needed to elucidate the question, if the carbide is also an active catalyst or only a side product.The reaction itself shows a very high yield of CNTs, as shown in Fig.2.

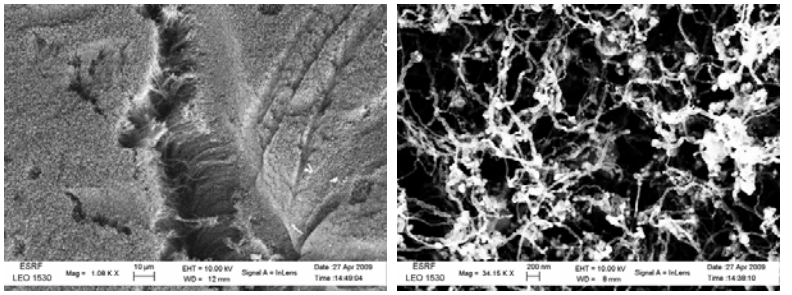

Fig.2: SEM picture of the CNT grown with fe-catalyst.

The preparation of the results for publication is in progress.

References

[1] Mattevi et al. J. Phys. Chem. C 112, 12207 (2008).
[2] Wirth et al. ACS Nano 3, 3560 (2009).
[3] Hofmann et al. J. Phys. Chem. C 113, 1648 (2009).

ROBL-CRG	**Experiment title:** Anisotropic strain-distribution in ion-beam irradiated silicon	**Experiment number:** 20-02-683
Beamline: BM 20	**Date of experiment:** from: 05.07.09 to: 10.07.09	**Date of report:** 01.02.2010
Shifts: 12	**Local contact(s):** Carsten Baehtz	*Received at ROBL:*

Andreas Biermanns*, Ullrich Pietsch
FB7 - Physik , Universität Siegen, 57068 Siegen, Germany

Antje Hanisch*, Jörg Grenzer
Forschungszentrum Dresden-Rossendorf, Institute of Ion Beam Physics and Materials Research
01314 Dresden, Germany

Report:

Many properties of surfaces and interfaces can be modified by controlling their roughness. Among them are electrical, optical or magnetic properties. One process to tune surface roughness in a controlled manner is ion beam sputtering (IBS). By IBS, nanopatterns in the form of wave-like rippled structures on solid surfaces can be achieved by ion beam bombardment under oblique incidence [1]. Whereas in the low ion energy region the ion beam is usually provided by a compact, broad beam ion source that delivers a homogeneous ion flux with several cm in diameter, a rather small ion beam (diameter ~1cm) provided by an ion implanter has to be used in the latter case. In order to achieve a homogeneous irradiation of the whole sample surface, the small beam is scanned across the sample surface. In a previous work we found an anisotropic defect concentration in the region of the amorphous-crystalline interface in medium-energy Xe beam induced ripple patterns on Si(001) [2]. It was proposed that the aforementioned scanning process of an across the tilted sample creates an anisotropic defect distribution.

Aim of the present experiment at ROBL was to study the ion beam induced strain and defect distribution in samples irradiated with different ion beam "shapes" (figure 1, text below). For this experiment, 1x1 cm² Si(001) substrates with no intentional miscut were irradiated at room temperature with Xe^+ ions with a kinetic energy of 25keV and an incidence angles of θ=70° (ripple patterns form on the surface) and θ=80° (no ripple patterns form). The projection of the ion beam on the substrate was parallel to the [110] direction. The ion-irradiation was done using a Danfysik 1050 Low Energy Ion Implanter in the Forschungszentrum Dresden-Rossendorf. In normal operation, the ion beam with a mean diameter of 15mm was swept over an square area of 45x45mm² with the tilted sample located in the centre. As proposed in the previous work the projection of the homogeneous ion beam onto the sample surface may lead to an inhomogeneous beam-profile in the plane of the sample surface (case '1:1' in fig. 1). In addition, samples were prepared increasing the sweeping amplitude by a factor of $\cos(\theta)^{-1}$ parallel or perpendicular to the tilting-direction (cases '2:1' and '1:2' in fig. 1).

With those prepared samples we performed coplanar X-ray diffraction experiments at an X-ray energy 8 keV. The incoming X-ray beam was collimated by a set of slits in front of the sample. To achieve sufficient resolution in reciprocal space a combination of slits and an analyser-crystal was used. We measured reciprocal space maps (RSM) around the asymmetric Si (113) reflection, making an angle of 25.2° with respect to the Si (001) surface. To probe an ion beam induced asymmetry, measurements have been performed with the incidence x-ray beam either parallel or perpendicular to the ion-beam direction. In addition, high resolution measurements of the symmetric Si (004) and the forbidden Si (002) reflection have been performed.

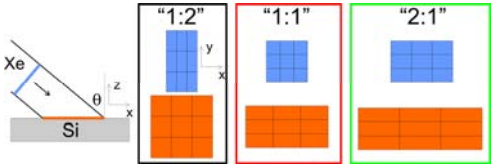

Figure 1: Scheme of the three different implantation conditions. Varying the shape of the ion beam perpendicular to it's direction changes the final symmetry in the surface plane of the sample inclined by the angle θ.

As example, figure 2 shows measured reciprocal space maps for the sample irradiated by 70° in the "1:2" configuration, either with the inplane scattering component parallel (left) or perpendicular (right) to the projection of the ion beam on the surface. Due to the periodic ripple pattern in the crystalline material, the left RSM shows satellite peaks around the Si (113) reflection measuring a wavelength λ=105nm of the periodic pattern. Interestingly, the intensity of the satellite peaks is not symmetric, exhibiting a slightly increased intensity on the smaller q_x side.
In addition, the intensity distribution along the crystal truncation rod is asymmetric too, exhibiting an increased intensity at the smaller q_z side (fig. 3). The same asymmetry was found around the symmetric (004) reflection. In combination, the measurements indicate the presence of a tensile strain in the crystalline region, created by the ion beam bombardment. However, no strong asymmetry could be found in the inplane-direction perpendicular to the ripples (fig. 2, right). A possible reason is that the (expected) small asymmetry becomes amplified by the presence of the satellite peaks, whereas the signal to noise ratio is too large if no satellite peaks are present. Detailed analysis will be subject to further evaluation of the data.

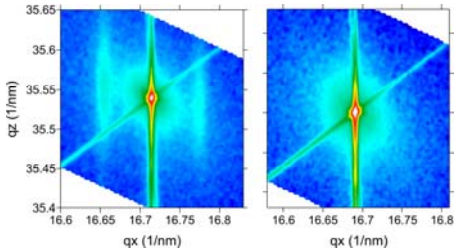

Figure 2: Reciprocal space maps around the asymmetric Si (113) and (1-13) reflection of a sample irradiated by 25keV Xe ions. If the direction of the x-ray beam is parallel to the direction of the ripple pattern on the surface (left), sattelite peaks measure the wavelength of the nanostructures (here, λ=105nm). The intensity distribution is slightly asymmetric towards smaller |q| values, indicating expansion due to the ion implantation.

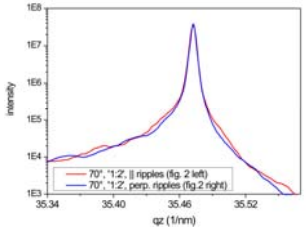

Figure 3: cut along the crystal truncation rods in fig. 2. The asymmetry indicates expansion of the lattice planes perpendicular to the surface

[1] W. L. Chan and E. Chason, J. Appl. Phys. **101**, 121301 (2007)
[2] A. Biermanns, U. Pietsch, J. Grenzer, A. Hanisch, S. Facsko, G. Carbone and T.H. Metzger, J. Appl. Phys. **104**, 044312 (2008),

ROBL-CRG	**Experiment title:** Thermal stability and interface interactions in the TM-Al-N (TM = Ti, Cr) thin film nanocomposites	**Experiment number**: 20-02-684
Beamline: BM 20	**Date of experiment**: from: 21/10/09 to: 27/10/09	**Date of report**:
Shifts: 18	**Local contact(s)**: Carsten Baehtz	*Received at ROBL:*

Names and affiliations of applicants (* indicates experimentalists):

Milan Dopita*, Mykhailo Motylenko*, Christina Wuestefeld*, David Rafaja

*TU Bergakademie Freiberg, Institute of Materials Science, Gustav-Zeuner-Str. 5, 09599 Freiberg, Germany

Report:

The development of the microstructure of $Ti_{1-x}Al_xN$ coatings during their treatment at elevated temperatures in vacuum was investigated by in-situ high temperature glancing angle X-ray diffraction (HT-GAXRD) experiments performed at ROBL BM 20. The samples were deposited using cathodic arc evaporation (CAE) at [Ti]/[Al] ratios between 60:40 and 33:67 and at bias voltages (U_B) ranging from -40 to -120 V. Preliminary laboratory experiments revealed that the initial microstructure, especially the phase composition in the as-deposited state, was modified via [Ti]/[Al] ratio and U_B [1]. At low U_B, fcc-(Ti,Al)N formed as a single phase up to x≤0.5. In contrast, the coatings deposited at high U_B contained fcc-(Ti,Al)N as major phase and AlN as minor phase. Our previous in-situ characterisation of the microstructure evolution of $Ti_{0.5}Al_{0.5}N$ coatings deposited at U_B=-40 V and U_B=-80 V during annealing at ROBL BM 20 (proposal numer; 20-02-675) revealed differences in the thermal stability of the coatings depending on the initial microstructure [2]. The main goal of the continuation of the previous study (20-02-675) was the investigation of the microstructure development during annealing for a wider range of chemical compositions (x=0.4, 0.5, 0.6, 0.67) and bias voltages (U_B=-40 V, U_B=-80 V and U_B=-120 V). Thus in-situ synchrotron HT-GAXRD experiments were done at 450℃, 650℃ and 850 ℃ as well as at 100℃ after each annealing step. From the analysis of the GAXRD patterns, the phase composition as well as the macroscopic lattice strain and the stress-free lattice parameter of the fcc-(Ti,Al)N phase were determined for all investigated temperatures. The results obtained from the GAXRD experiments are shown in figure 1 for the $Ti_{0.6}Al_{0.4}N$ coatings deposited at U_B = -40 V and -120 V. The analysis of the stress-free lattice parameter of the fcc-(Ti,Al)N phase (a_0) of the originally single-phase $Ti_{0.6}Al_{0.4}N$ coating (Fig. 1a) showed an increase of a_0 at 450℃ and 650℃ due to thermal expansion. After cooling from 650℃ to 100℃ a_0 returned to its starting value indicating that the coating remained single-phase up to 650℃. During annealing at 850℃, diffraction lines of w-AlN and fcc-AlN appeared in the GAXRD pattern. Rietveld analysis using the MAUD programme [3] yielded ~30 mol % fcc-AlN and ~10 mol % w-AlN. This onset of the decomposition was accompanied with an increase of both a_0 and macroscopic lattice strain in the fcc-(Ti,Al)N phase. Further annealing at 850℃ for ~100 min did not change the phase composition significantly. After cooling to 100℃, a_0 was smaller than 0.42418 nm, which is the lattice parameter of TiN. This indicated that some of Al was still incorporated in the fcc-(Ti,Al)N host structure; the coating consisted of ~60 mol% $Ti_{0.9}Al_{0.1}N$, ~30 mol% fcc-AlN and ~10 mol% w-AlN. In contrast to the originally single-phase coating (U_B=-40V), already ~ 30 mol% of w-AlN were formed and only ~10 mol% fcc-AlN could be observed in the dual-phase coating (U_B=-120 V) at 850℃. Further annealing at 850℃ did not change the phase composition. The analysis of a_0 after the 850℃ annealing step revealed that Al from fcc-(Ti,Al)N in the dual-phase coating $Ti_{0.6}Al_{0.4}N$ (U_B=-80V (not shown) and U_B= -120V (Fig. 1b)) segregated after 850℃ completely from the fcc-(Ti,Al)N host structure, because a_0 observed at 100℃ corresponds to Al-free fcc-TiN. The fraction of w-AlN and fcc-AlN in the $Ti_{0.6}Al_{0.4}N$ coating deposited at U_B=-80V was for both phases ~20 mol% and lay between the AlN fractions observed in the coatings deposited at U_B= -40V and U_B= -120V. The same tendency of the fraction of the decomposition products was observed in other investigated coatings.

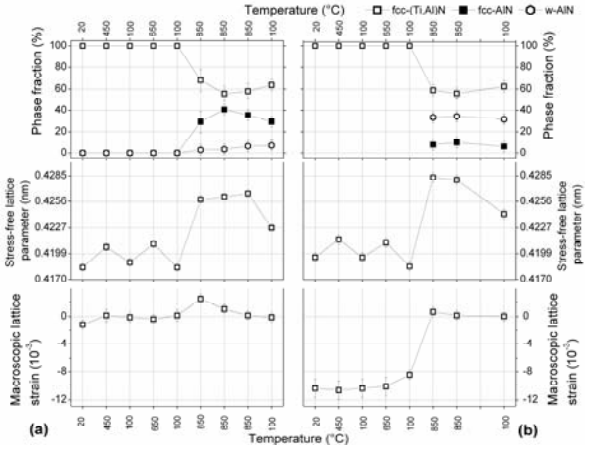

Figure 1: Evolution of the phase composition, stress-free lattice parameter of the fcc-(Ti,Al)N phase and macroscopic lattice strain of the fcc-(Ti,Al)N phase during annealing of $Ti_{0.6}Al_{0.4}N$ coatings deposited at U_B=-40 V (a) and U_B=-120 V (b).

[1] Ch. Wüstefeld, D. Rafaja, V. Klemm, C. Michotte, M. Kathrein, Surf. Coat. Technol. (2010), doi: 10.1016/j.surfcoat.2010.07.057.
[2] D. Rafaja, C. Wüstefeld, C. Bähtz, V. Klemm, M. Dopita, M. Motylenko, C. Michotte, M. Kathrein, Metal. Mater. Trans. A (2010), DOI: 10.1007/s11661-010-0204-8
[3] L. Lutterotti, D. Chateigner, S. Ferrari, J. Ricote, Thin Solid Films 450, (2004), 34-41.

	Experiment title: GISAXS study of self-organized multilayers of carbon encapsulated transition metal nanoparticles	Experiment number: 20-02-685
Beamline: BM20	**Date of experiment:** from: 28/08/2009 to: 01/09/2009	**Date of report:** 18/05/2010
Shifts: 12	Local contact(s): Nicole Jeutter	*Received at ESRF:*

Names and affiliations of applicants (* indicates experimentalists):

Gintautas Abrasonis*[1], Thomas W. H. Oates*[2], Gy. J. Kovacs*[1], Matthias Krause[1], Andrius Martinavičius[1,†]

[1]*Institute of Ion Beam Physics and Materials Research, P .O. Box 510119, Forschungszentrum Dresden-Rossendorf, 01314 Dresden, Germany.*

[3]*Linköpings Universitet, 58183 Linköping, Sweden.*

[†]*participated in the experiments, but is not listed in the application for the beamtime*

Report:

Self-organized nanostructures in C:Ni nanocomposite thin films have been investigated *ex-situ* by means of grazing-incidence small-angle x-ray scattering (GISAXS). Films were grown by ionized physical vapour deposition (iPVD) in the form of pulsed filtered cathodic vacuum arc. This approach provides a flux of depositing species in the form of hyperthermal (~10-100 eV) ions whose energy and direction can be easily controlled by an electromagnetic field. During thin film growth, atomic displacements are caused by impacting energetic ions, resulting in phase separation in an advancing surface layer. No additional thermal sample heating has been applied thus suppressing any considerable surface diffusion of ad-atoms.

The transmission electron microscopy (TEM) and GISAXS results of C:Ni films grown at various conditions are summarized in Figure 1. Deposition normal to the substrate surface results in an alternating carbon-rich and nickel-rich layered structure. The undulations of Ni concentrations within each layer are correlated to the metal distribution in adjacent layers which indicates that the nanoparticle nucleation is dependent on the morphology of the underlying layer. This demonstrates that after an initial growth period, the 'active' layer switches to an oscillatory mode which results in the emergence of a periodic precipitation pattern. It must be noted that any considerable surface diffusivity destroys the periodic pattern formation and results in the growth of columnar Ni rich nanoparticles.

Ion impacts off-normal to the surface tilt the alternating carbon rich and nickel layers (Figure 1 (c)-(h)). *The metal nanopatterns no longer align with the advancing surface, but with the incoming ions.* At the very beginning of the deposition process a few precipitate layers form parallel to the substrate surface before the layers tilt. An increase of Ni content and ion energy results in a decrease of the tilt angle and an increase of the pattern period. After tilting the sample, the fast Fourier transform (FFT) of the TEM images exhibit rotational rather than mirror symmetry. GISAXS images from a macroscopic sample region (~5mm^2) closely resemble the upper part of the FFT patterns of the local area probed by TEM, confirming that the observed asymmetries are a global property of the material. A comparison of the fast fourrier filtered TEM images and GISAXS one can conclude that the structure consists of two composition modulation waves represented by two spots in GISAXS patterns – one 'moves' during the film growht roughly towards the ions and the other one with a significanlty lower amplitude in the direction perpendicular to the incident ions. In addition, GISAXS at different in-plane angles (now shown here) shows that the density correlations become symmetric and significantly weaker when approaching the plane which is perpendicular to the plane of incoming ions and sample surface normal.

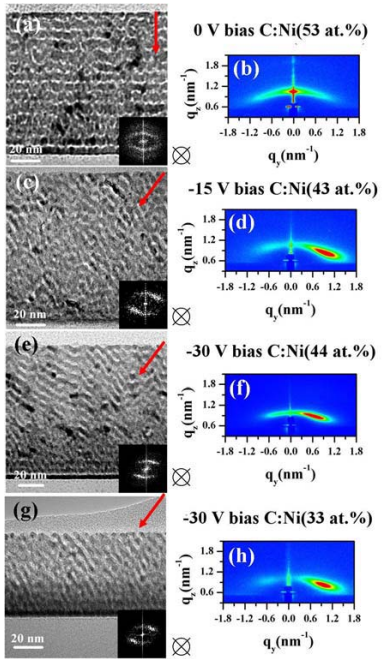

Figure 1. C:Ni film morphologies by TEM (left column) and GISAXS (right column) Growth parameters are indicated on the corresponding panels. The red arrows on the TEM images schematically indicate the incoming ion direction. The insets are FFTs of the corresponding X-TEM images. The crossed circles indicate the direction of the x-ray beam for the corresponding GISAXS measurements (extracted from Ref. [1]).

GISAXS in combinations with TEM has allowed us to establish a dependence of the nanopattern morphology on the film composition, ion energy and incidence angle, and demonstrate a method for controlling the nanopatterning. From the fundamental point of view this study shows that phase separation processes at the nanoscale may be externally controlled

by controlling the velocity and proportion of the depositing species. The approach is generally applicable to all ionized physical vapour deposition techniques and a large range of nanocomposite systems. This opens new prospects in controlled bottom-up synthesis of nanostructured composite materials or even of sculpted complex encapsulated 3D nanostructures such as chevrons or helices if the ion incidence angle is changed during the growth. A publication has been prepared and is under consideration in the Journal of Applied Physics.

In-situ heating experiments could not be carried out due to technical problems related with the sample alignement. The optimized procedure was established to carry out ex-situ measurements. However, the remaining time was sufficient for ex-situ GISAXS experiments only.

[1] G. Abrasonis, T. W. H. Oates, Gy. J. Kovács, J. Grenzer, P. O. Å. Persson, K. H. H. Heinig, A. Martinavičius, N. Jeutter, C. Baehtz, M. Tucker, M. M. M. Bilek, W. Möller, "Nanoscale precipitation patterns in carbon-nickel nanocomposite thin films: period and tilt control via ion energy and deposition angle", J. Appl. Phys. *submitted* .

ROBL-CRG	**Experiment title:** Structural diagnostic of metal doped transparent oxides and germanium employed at photonic, magneto-optical and magnetic applications.	**Experiment number:** 20-02-686
Beamline: BM 20	**Date of experiment:** from: 18.11. 2009 to: 21.11.2009	**Date of report:** 8.07.2010
Shifts: 9	**Local contact(s):** Dr. N. Jeutter	*Received at ROBL:*

Names and affiliations of applicants (* indicates experimentalists):

Dr. A. Shalimov *
Dr. M. O. Liedke *
L. Li *

Forschungszentrum Dresden-Rosendorf,
Institute of Ion Beam Physics and Materials Research,
FWIN

Report:

During the experiment, the structural properties of FePt magnetic nanoparticles embedded in MgO matrix have been examined as a function of ion beam fluence, and high-temperature annealing regime.

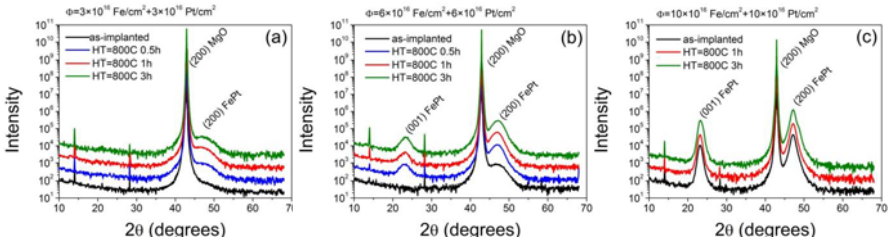

Fig.1. Diffraction patterns (2θ/θ scans) of MgO crystals implanted with Fe^+ and Pt^+ with the fluencies: (a) – 3×10^{16} cm^{-2}, (b) – 6×10^{16} cm^{-2}, (c) – 10×10^{16} cm^{-2}. Annealing regimes are indicated in legends.

Diffraction peaks arising from fcc FePt phase with a lattice parameter of a=3.58(2) Å were observed for all investigated samples. It was found that the nanoparticles size increase with an increase of ion fluencies, as well after high-temperature annealing: from 3.6 to 4.7 nm for $(3+3)\times10^{16}$ (Fe+Pt)/cm^2, from 5.3 to 7.8 nm for $(6+6)\times10^{16}$ (Fe+Pt)/cm^2; from 3.6 to 4.7 nm for $(3+3)\times10^{16}$ (Fe+Pt)/cm^2, and from 19 to 20 nm for $(10+10)\times10^{16}$ (Fe+Pt)/cm^2. Summarizing this part we found that an optimum for creation of isolated nanoparticles with at least partial chemical ordering, low-current implantation of 6×10^{16}Fe/cm^2 and 6×10^{16}Pt/cm^2 as well as 1h annealing at 800°C has to be performed. Possible origin of the suppressed formation of the L_{10} phase is stoichiometric imbalance between metallic Fe and Pt or the cubic surrounding of the clusters.

P-type doped Ge(100) single crystal wafers were implanted with 100 keV Mn ions to a fluence of 1×10^{16} cm^{-2}, which corresponds to a peak concentration of 2% Mn. The samples were held at 300 °C during implantation to avoid amorphization. The SR-XRD 2θ/θ scan confirms the formation of Mn_5Ge_3 nanomagnets. As shown in Fig. 2, beside the main peaks from Ge(004) and Ge(002), the diffraction peaks of Mn_5Ge_3 (111), (002), (310), (222) and (004) are clearly visible.

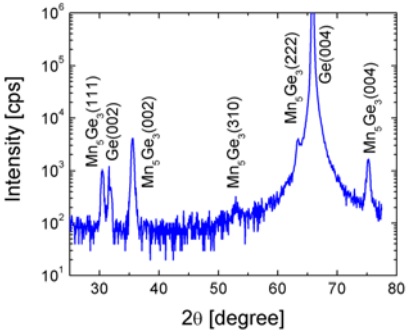

Fig.2. Diffraction pattern of Mn implanted Ge.

Moreover, it was found that low-temperature implanted Ge accompanied with millisecond PLA does not cause the secondary phase formation giving the possibility to production of diluted magnetic semiconductors.

Al doped ZnO films were grown on fused silica substrates by magnetron sputtering using different target concentrations of Al (0-4 wt %) at substrate temperatures Ts ranging from RT to 500°C. 2θ/θ measurements confirmed a dominant c-axis texture in films grown below the optimum Ts. For higher temperatures this preferred orientation is lost and crystallite size decreases. At high Al concentrations and Ts the films become electrically insulating which is accompanied by a strongly disordered film structure. Within the framework of this experiment no secondary phases other then wurtzite ZnO could be identified.

ROBL-CRG	**Experiment title:** Structural investigations of SiO_2/Cr/NiFe/FeMn/Cr multilayers representing unusual exchange bias properties.	**Experiment number**: 20-02-687
Beamline: BM 20	**Date of experiment**: from: 21.11. 2009 to: 24.11.2009	**Date of report**: 8.07.2010
Shifts: 9	**Local contact(s)**: Dr. N. Jeutter	*Received at ROBL:*

Names and affiliations of applicants (* indicates experimentalists):
Dr. A. Shalimov *
Dr. M. O. Liedke *
L. Li *

Forschungszentrum Dresden-Rosendorf,
Institute of Ion Beam Physics and Materials Research,
FWIN

Report:

The structural characterization of multilayered magnetic structures of SiO_2/Cr/FeNi/FeMn/Cr and SiO_2/Cu/FeMn/FeNi/Cr has been performed using coplanar and non-coplanar synchrotron x-ray diffraction techniques. According to the aim of experiment, the investigations were subjected to the grain size and strain state analysis of ultrathin permalloy films grown on Cr buffer layers of different thicknesses, where the strong variation of exchange bias has been observed by means of magneto-optical Kerr effect. Grazing incidence diffraction (GID) was employed for the study of in-plane size of FeNi grains, since the crystalline quality of the layers was supposed to play a decisive role in magnetic behavior.

Taking into account high complexity of the measurements and inhomogeneous quality of the samples, the experiment can be considered as a partially successful. It has been found that samples with ultrathin Cr (Cu) buffer layer (< 2 nm) being of enormously pure crystalline quality, representing randomly oriented small grains. Due to those reasons, the intensity of the diffracted beam was extremely low. Nevertheless, the samples possessing 10 nm thickness Cr buffer layer provide better crystalline quality of the following permalloy film as compared to ones grown on thinner or without buffer layers (e.g. Fig 1). The average grain size of about 6-7 nm was calculated using the diffraction peak width. Therefore, the strong influence of buffer layer on the quality of permalloy has been confirmed.

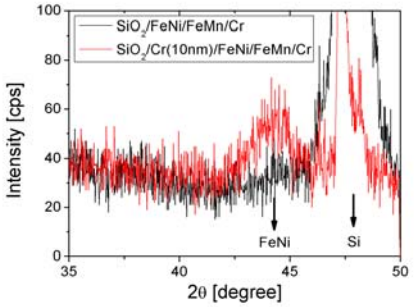

Fig. 1. GID pattern of magnetic multilayered structures representing the better crystalline quality of permalloy film grown on 10 nm Cr buffer layer.

In addition, magnetic structures of as-grown Al_2O_3/Mo/Pt/Co/Pt representing the change of magnetic anisotropy after implantation with Ga^+ have been investigated. On the present stage, x-ray diffraction patterns are being interpreted by self-developed numerical code for an analysis of $2\theta/\theta$ scans and rocking curves allowing determination of strain distribution and static Debye – Waller profile in multilayered systems.

	Experiment title: In-situ investigation of the behavior of Fe catalyst during the CNT formation	**Experiment number:** **20_02_688**
Beamline: BM 20	**Date of experiment:** from: 17.2.2010-23.2.2010	**Date of report:** 26.1.2011
Shifts: 18	**Local contact(s):** Dr. Carsten Baehtz (baehtz@esrf.fr)	*Received at ROBL:*

Names and affiliations of applicants (* indicates experimentalists):
C. Baehtz, T. Wirth[1)], B. C. Bayer[1)]

Helmholtz-Zentrum Dresden-Rossendorf, Institute of Ion Beam Physics and Materials Research, P.O.B. 510119, 01314 Dresden, Germany
1) Centre for Advanced Photonics and Electronics, University of Cambridge, 9 JJ Thompson Avenue, Cambridge CB3 0FA, UK

Results

Carbon nanotubes (CNTs) are promising candidates as interconnects for future microelectronic devices.[1] One challenging question is how to growth CNTs on conductive supports which are often reactive in the high temperature, reactive gas atmospheres used in carbon nanotube growth. Such supports (e.g. Ta, TiN, $CoSi_2$) may also interact with the metallic catalyst particles from which the CNTs nucleate.[2,3] Therefore the phase formation and behaviour of the complete support-catalyst-CNT system is of interest. TiN with Fe as catalyst show during reaction the formation of TiO_2 from only minute gas contaminations. Means to avoid this are for example plasma pre-treatment [2], where the effect of this on structure was studied by in-situ XRD. Tantalum as conducting buffer shows under these conditions also the formation of Tantalum oxide as well as tantalum carbide. Cobalt silicide [3] in contrast seems to offer strongly improved chemical and structural stability.

Publication of the results are in preparation.

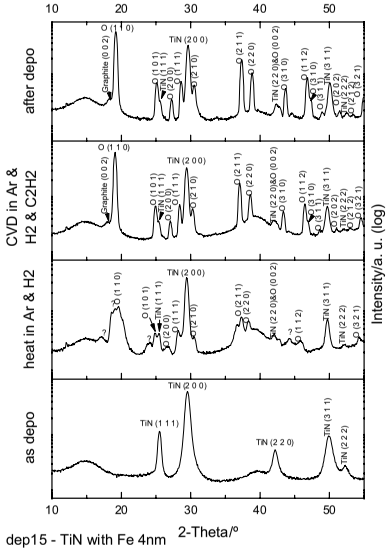

Fig.1: Phase evolution of TiN during CNT growth.

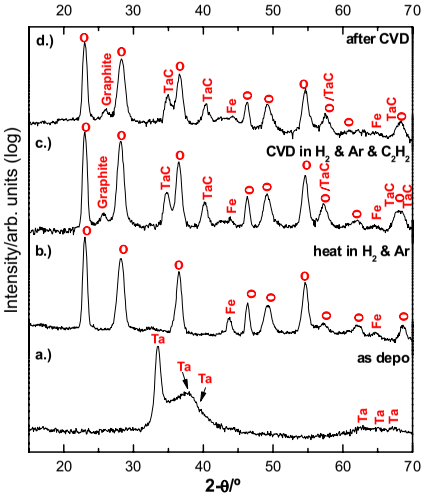

Fig. 2: Phase evolution of Ta during Fe catalysed CNT growth. Data is rescaled for 1.541 Å wavelength.

References

[1] Robertson et al. Diamond Relat. Mater. 18, 957 (2009)
[2] Esconjauregui at al. Appl. Phys. Lett. 95, 173115 (2009)
[3] Zhang et al. J. Appl. Phys. 108, 024311 (2010).

ROBL-CRG	**Experiment title:** Determination of Point Defect Concentrations in Nano-crystalline Pt	**Experiment number**: 20-02/691
Beamline: BM 20	**Date of experiment**: from: 24-02-2010 to: 01-03-2010	**Date of report**: 16-08-2010
Shifts: 15	**Local contact(s)**: Carsten Baehtz	*Received at ROBL:*

Names and affiliations of applicants (* indicates experimentalists):
W. Gruber[1]*, S. Chakravarty[1]*, H. Schmidt[1]*, C. Baehtz[2]*

[1]TU Clausthal, Institut für Metallurgie, AG Materialphysik, Germany
[2]Forschungszentrum Rossendorf, Germany

Nano-crystalline metals are generally in a non-equilibrium state after preparation by e.g. magnetron sputtering. The aim of this work was to explore the modification of non-equilibrium point defect concentrations (PDC) and residual stresses during isothermal annealing of nano-crystalline Pt films. The out-of-plane lattice parameter, a, and the thickness, L, of a 40 nm film were measured by XRD (Bragg-Brentano) and XRR, respectively, as a function of annealing time at 130, 200, 300 and 400 °C in an in-situ vacuum furnace at 10^{-6} mbar. In addition, GI-XRD (0.34 °) measurements were done.

For analysis it is assumed that $a(t, T) = a_0 + \Delta a_{th}(T) + \Delta a_{mis}(T) + \Delta a_i(t, T)$, where a_0 is the lattice parameter in the as-deposited state, Δa_{th} is the modification of the lattice parameter due to thermal expansion, Δa_{mis} due to stress resulting from thermal mismatch between substrate (SiO_2) and Pt film and Δa_i due to intrinsic stress, resulting from the production of the film by sputtering. Further, $L(t, T) = L_0 + \Delta L_{th}(T) + \Delta L_{mis}(T) + \Delta L_i(t, T) + \Delta L_V(t, T)$, ΔL_j (j = 0, th, mis, i), are the corresponding quantities of the film thickness and ΔL_V is the thickness change due to a modification in PDC, which becomes not visible in lattice constant changes in first approximation. Note that the determined experimental resolution of the method, given by the maximum error limits of $\sigma(\Delta L/L) < 5 \times 10^{-4}$ and $\sigma(\Delta a/a) < 1 \times 10^{-4}$ is better than initially expected, allowing to determine changes in PDC of about 1×10^{-3}. The modification of PDC as function of time and temperature can be obtained by simply using the formula $\Delta c = \Delta L_V/L_0 = (L-L_0)/L_0 - (a-a_0)/a_0$ (Fig.1(a)).

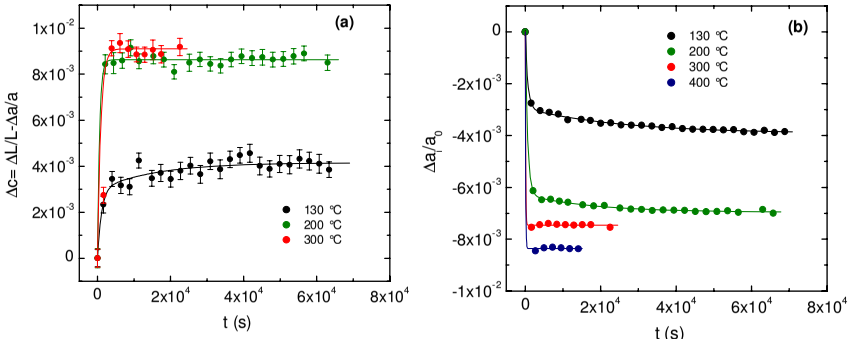

Fig. 1 *Modification of* ***(a)*** *point defect concentration and* ***(b)*** *intrinsic strain as a function of annealing time. The lines are a guide for the eye. The error limits in* ***(b)*** *are smaller than the dots.*

As obvious, for all temperatures we observe a drastic increase of Δc as a function of annealing time, however limited to the first hour of annealing. This can tentatively be interpreted by a process connected with the formation of free volumes, e.g. vacancies during annealing. This is in contrast to initial assumptions, where a reduction of Δc is expected due to vacancy annihilation. A preliminary idea to explain the results is that vacancies are formed to counterbalance the development of stresses during heating to elevated temperatures (see below). A possible influence of an oxide layer forming at the surface is currently discarded by high resolution XPS measurements.

From analysis of a(t,T) closer information on strain modifications can be derived. It is assumed that strain modifications resulting from thermal expansion, Δa_{th}, and thermal mismatch, Δa_{mis}, are time-independent. Detailed analysis (not plotted) shows that during heating up to 400 °C we are in the thermo-elastic range, resulting in the formation of more compressive stresses. Consequently, the observed time-dependence is attributed to the modification of intrinsic strains $\Delta a_i(t, T)$ (see Fig. 1(b)). For T > 200 °C the increase in Δa_i takes place during the first 30 min of annealing (the actual time resolution of the experiment). However, for T ≤ 200, the process slows down and becomes visible on a time scale of several hours. The extraction of characteristic time constants is in progress. Further insight into the modification of stresses was gathered from GI-XRD measurements. The discussion is omitted here due to space limitations.

In conclusion, we demonstrated the feasibility of our method for the determination of PDC. For T ≤ 200 °C a sufficient resolution can be achieved in order to quantify strain modifications as a function of annealing time. For PDC this can also be achieved for lower temperatures and/or faster data acquisition.

ROBL-CRG	**Experiment title:** Microstructure and interface interactions in Cr/ta-C multilayer thin films	**Experiment number**: 20-02-692
Beamline: BM 20	**Date of experiment**: from: 31/03/2010 to: 06/04/2010	**Date of report**: 28/01/2011
Shifts: 18	**Local contact(s)**: Dr. Carsten Baehtz	*Received at ROBL:*

Names and affiliations of applicants (* indicates experimentalists):
Ulrike Ratayski*, Torsten Schucknecht *, Christian Schimpf*, David Rafaja
* TU Bergakademie Freiberg, Institute of Materials Science, Gustav-Zeuner-Str. 5, 09599 Freiberg, Germany

Report:

Microstructure development and the interdiffusion in Cr/ta-C multilayers during the heat treatment in vacuum were investigated using in-situ high temperature glancing angle X-ray diffraction (HT-GAXRD) and high temperature small angle X-ray (HT-SAXS) experiments performed at ROBL BM 20. The multilayers were deposited using a combined DC arc/laser arc technique, in which the Cr layers were deposited using the DC arc and the ta-C layers using the laser arc. The energy of the carbon ions was set to approximately 25 eV, 200 eV and 500 eV. Previous laboratory experiments showed that the carbon ion energy influences primarily the amount of sp^3 bounds in ta-C layers and the roughness of the Cr/ta-C interfaces. The main goal of the in-situ synchrotron experiments was to investigate the development of chromium carbides at the Cr/ta-C interfaces supported by the diffusion of carbon at higher temperatures. Within the Cr-C system, three stable carbides exist with narrow homogeneity ranges, which may work as diffusion barriers at higher temperatures. The samples were successively heated between 200°C and 600°C in steps of 100°C. The measurements were carried out after cooling the samples to 100°C to interrupt the carbon diffusion. The HT-GAXRD measurements showed the existence of the crystalline bcc Cr phase in all samples, whereas the carbon was amorphous. The sample with the carbon ion energy of 500 eV showed an additional peak corresponding to nanocrystalline chromium carbide. A more detailed in situ phase analysis was not possible because of the similar peak positions of all three Cr carbides. HT-XRR measurements showed that the carbon layer thickness decreased from 10.4 nm to 5.6 nm with increasing carbon ion energy, whereas the Cr layer thickness remained constant at approximately 10 nm. The heat treatment of the Cr/ta-C coatings at 200°C showed a recovery of the multilayer structure. The sample deposited using the highest carbon ion energy of 500 eV contained an additional layer with the thickness of about 2-3 nm, which might be related to the presence of a Cr carbide layer at the Cr/ta-C interface caused by a higher penetration of the C species into the Cr layer. Furthermore, this thin layer grows with increasing heat treatment to 5 nm at 200°C, which is related to the diffusion of carbon. The heat treatments at temperatures above 200°C resulted in a strong increase in the interface roughness for all Cr/ta-C multilayers. This confirmed a strong diffusion of carbon. The multilayer structure degraded for heat treatments at temperatures above 400°C. However, the degradation of the Cr/ta-C coating deposited at about 500 eV with strongly intermixed interfaces was less pronounced as compared to the other multilayers, which confirms the suggestion of the existence of one of the chromium carbides acting as diffusion barrier. The HT-SAXS measurements done on the multilayer deposited using 25 eV showed a roughness replication. The replication disappeared for the sample deposited using the highest carbon ion energy. Furthermore, the roughness replication decreased with increasing temperature of the heat treatment that corresponds to the increase in interface roughness.

ROBL-CRG	**Experiment title:** Simultaneous XRD and Electrical Resistivity Measurements of the phase transitions in Co-Ni-Ga ferromagnetic shape memory alloy system	**Experiment number:** 20-02-693
Beamline: BM 20	**Date of experiment:** From:14-06-2010 to: 19-06-2010	**Date of report:** 24.01.2011
Shifts: 15	**Local contact(s):** Carsten Baehtz, Nicole Jeuter	*Received at ROBL:*

Names and affiliations of applicants (* indicates experimentalists):

C.M. Craciunescu*, F.M. Braz Fernandes*, K. K. Mahesh*: CENIMAT-Centro de Investigação de Materiais, Campus da FCT/UNL, 2829-516 Monte de Caparica, PORTUGAL

Carsten Baehtz *,Nicole Jeuter*: FZD, P.O. Box 510119, 01314 Dresden, GERMANY

Report:

The experiments have been performed on bulk Co_2NiGa samples in three states: quenched, deformed and quenched, and quenched and stabilized at 350ºC. The in situ X ray scans were performed along with ER measurements in the temperature range where the phase transformations occur. The tests have been done in the beryllium dome, with the electric resistance vs temperature (ER) measurements performed using a Keythley 2010 multimeter. The heating and cooling was performed between – 100 and + 200°C. The shape memory alloys were insulated using kapton foil from the heating device. The beam size used for the experiments and focused on the sample had to be limited due the contacts for the ER measurement device. Thus, corroborated with larger grain sizes for the investigated alloys, it is possible that only particular crystallographic orientations have been observed.

EXPERIMENTAL

The results recorded for the quenched sample are shown in figure 1. Apparently, it is difficult to observe a phase transition from the spectra detailed in fig. 1a. This appears in contrast with the expected Martensite and Austenite peaks reflecting the martenstic phase transition on heating and on cooling. A further analysis of the (110)M peak intensity in figure 1b, based on ER measurements durring heating and cooling indicates that the phase transition actually exists, but is dificult to distinguish since the (111)γ and (110)M peak are coincident. Adjustments and tests of the ER equipment for thicker samples allowed the observation of the relative change of the electric resistance (as the average ER result for the stabilized temperature recorded during a XRD scan- fig.1 c) only on heating, but the result appears to be consistent with the one based on the analysis of the (111)γ and (110)M peak height. There was no significant influence of deformation on the structure at RT and at 200 °C, as it also results from fig. 2, but is was not possible to detect the phase transition in the materials, a result consistent with preliminary experiments.

Conclusions

The comparison with experimental results obtained using a Brucker XRD equipment and the results recorded at ESRF suggests that the large grains that resulted after quenching had orientations that did not allow us to observe the phase transition related to the A(110) peak. The restrictions related to the beam spot due to the presence of the contacts of the ER device only alowed us to focus on a limited surface, most likely on grains with other orientation. For this reason it is possible that only the martensite peak M(110) superposed on the γ (111) could be used to observe the phase transition.

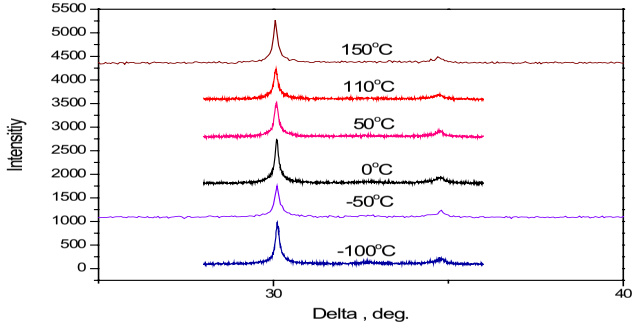

a. In situ XRD of the Co_2NiGa in the quenched state

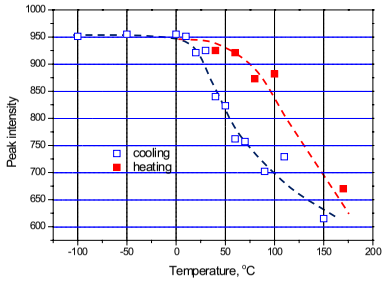

b. Max intensity of overlapping (110)M and (111)γ peak intensity

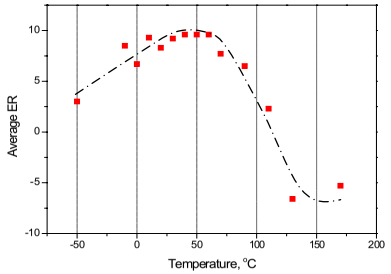

a. Average ER values vs temperature data

Fig. 1 In situ XRD and ER results of CoNiGa samples in the quenched state

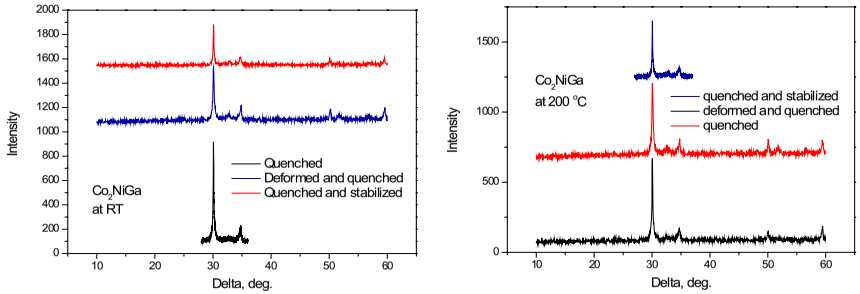

Fig. 2 In situ XRD of Co_2NiGa samples in the quenched, deformed and quenched and quenched and stabilized state

ROBL-CRG	**Experiment title:** In-situ synchrotron X-ray diffraction studies of the crystallization and hydrogen sorption properties of rapidly quenched Mg-Ni-Y-(Cu) alloys	**Experiment number:** **20-02-694**
Beamline: BM 20	**Date of experiment:** from: 6.4.2010-13.4.2010	**Date of report:** 01.09.2010
Shifts: 18	**Local contact(s):** Dr. Carsten Baehtz (baehtz@esrf.fr)	*Received at ROBL:*

Names and affiliations of applicants (* indicates experimentalists):

Lars Röntzsch*[1)], Siarhei Kalinichenka*[2)]

1) Fraunhofer Institute for Manufacturing Technology and Applied Materials Research, Winterbergstraße 28, 01277 Dresden, Germany
2) Institute for Materials Science, Dresden University of Technology, Helmholtzstraße 7, 01069 Dresden, Germany

Results

The Mg-Cu-Ni-Y alloys exhibit good hydrogen storage properties which makes these materials especially attractive for solid-state hydrogen [1]. However, the phase transformation during crystallization and hydrogen (de)sorption of Mg-based alloys have remained largely undetermined experimentally.
The aim of the in-situ diffraction study at the Rossendorf beamline ESRF-BM20 was to investiagte the crystal phase formation processes during thermal annealing of the amorphous as-spun Mg-Cu-Ni-Y alloys, and furthermore, the desorption of hydrogeneted ribbons under vacuum.

Recrystallization behavior

The recrystallization behavior of melt-spun amorphous Mg-Ni-Cu-Y was studied under different atmospheres (Ar, H_2 and vacuum). The SR-XRD results were compared with the corresponding results obtained by DSC measurement (Fig. 1). Fig 2 shows the evolution of the in-situ SR-XRD of melt-spun $Mg_{85}Cu_5Ni_5Y_5$ at different temperatures under argon atmosphere (for this system the effect of the different atmospheres was not significant). The incident X-ray beam with an X-ray wavelength of 1.05 Å was used for this investigations.
The crystallization of the amorphous structure starts with nucleation and growth of Mg and Mg_2Cu grains at 150°C. The XRD data also shows that at 200°C the formation of MgY occurs. The final composition of the sample at 250° is Mg, MgY and Mg_2Cu. It is interesting that no metallic Ni or Ni-phases diffraction peaks can be observed. The reason for this finding could be explained by forming of Ni-substituted Mg_2Cu [2].
The results of recrystallization behavior of melt-spun Mg-Ni-Y provide imortant information regarding the activation of as-spun ribbons.

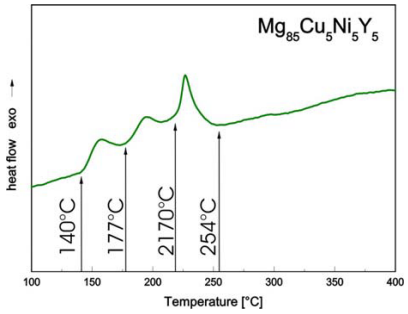

Fig. 1: DSC curve of melt-spun $Mg_{85}Cu_5Ni_5Y_5$ (5 K/min, Ar).

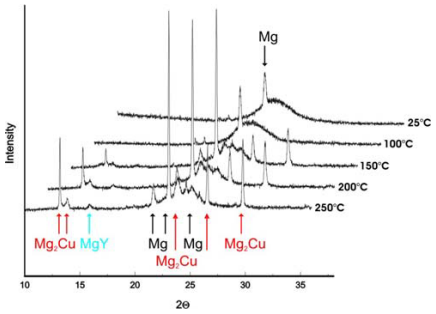

Fig. 2: Evolution of the in-situ SR-XRD pattern of the as spun $Mg_{85}Cu_5Ni_5Y_5$.

Heat treatment of hydrogenated Mg-Cu-Ni-Y ribbon under vacuum in the stainless steel dome designed with Kapton windows.
The evolution of the in situ SR-XRD patterns of the as-spun and hydrogenated $Mg_{85}Cu_5Ni_5Y_5$ during vacuum thermal decomposition at 200 °C (10^{-2} mbar) is presented in Fig. 3. The X-ray diffraction pattern at t=0 min represents the X-ray diffraction pattern of hydrogenated samples at ambient temperature.
During the dehydrogenation of $Mg_{85}Cu_5Ni_5Y_5$ several processes can be identified: decomposition of the hydride phases according to Eqns. (1) to (4) and transformation of $MgCu_2$ to Mg_2Cu according to Eq. 5. It must be noted, that these dehydrogenation reactions take place simultaneously.

$$MgH_2 \longrightarrow Mg + H_2 \quad (1)$$
$$Mg_2NiH_4 \longrightarrow Mg_2Ni + 2\,H_2 \quad (2)$$
$$Mg_2NiH_{0.3} \longrightarrow Mg_2Ni + 0.15\,H_2 \quad (3)$$
$$2\,YH_3 \longrightarrow 2\,YH_2 + H_2 \quad (4)$$
$$2\,Mg_2Cu + 3H_2 \longrightarrow 3\,MgH_2 + MgCu_2 \quad (5)$$

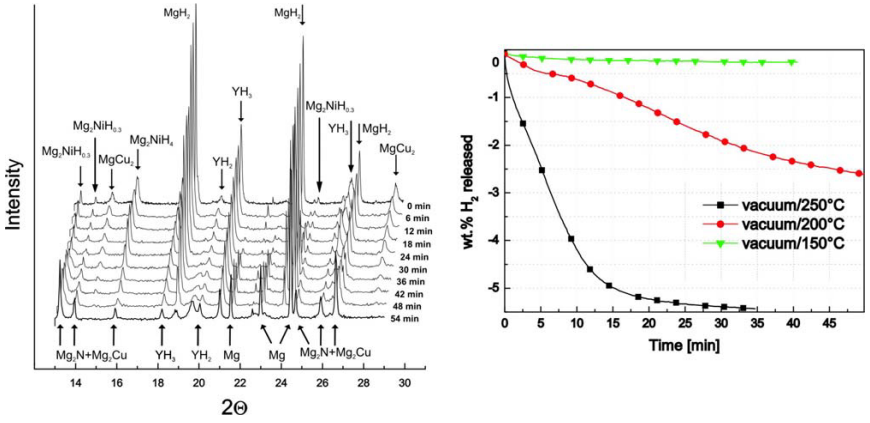

Fig. 3. The evolution of the in situ synchrotron XRD pattern of melt-spun and hydrogenated $Mg_{85}Cu_5Ni_5Y_5$ during its isothermal dehydrogenation at 200°C and at a pressure of 10^{-2} mbar H_2.

After dehydrogenation five phases have been observed in the material: Mg, Mg_2Ni, Mg_2Cu, YH_2 and YH_3. These XRD results of the dehydrogenated sample are similar to literature data, e.g. for $Mg_{60}Ni_{10}Cu_{30}$ prepared by ball milling [3]. It is also evident that the transformation of YH_3 into YH_2 is the slowest step of the reaction and even after 54 minutes at 200°C a residual amount of YH_3 can be observed in the diffraction pattern.

Conclusion

In order to understand the crystallization behavior and the dehydrogenation reactions of the melt-spun Mg-Cu-Ni-Y, the recrystallization and desorption properties were studied by in-situ synchrotron X-ray diffraction performed at the Rossendorf Beamline (BM20) of the ESRF.
Particularly, the results of desorption mechanisms of hydrogenated $Mg_{85}Cu_5Ni_5Y_5$ reveal interesting differences between Mg-Cu-Ni-Y alloy and the recently investigated systems [4, 5]. The SR-XRD results indicated that the dehydrogenation of the hydride phases and the transformation of $MgCu_2$ to Mg_2Cu take place at the same time and no formarion of hydrogen transfer phase was observed.
The results of these investigations have been already presented at International Symposium on Metal-Hydrogen Systems 2010 and submitted for publishing in the Journal of Alloys and Compounds [1].

References

[1] S. Kalinichenka, L. Röntzsch, C. Baehtz, Th. Weißgärber and B. Kieback, Hydrogen desorption kinetics of melt-spun and hydrogenated Mg-based alloys using in situ synchrotron X-ray diffraction and TGA, submitted to J. Alloys Compds.

[2] P. Damaudery, M. Pezat and B. Darriet, Effect of substituting copper for nickel on hydrogen storage in magnesium–nickel (Mg_2Ni), J. Less-Common Met. **92** (1983) 199.

[3] C. Milanese, A. Girella, G. Bruni, P. Cofrancesco, V. Berbenni, P. Matteazzi, A. Marini, Mg-Ni-Cu mixtures for hydrogen storage: A kinetic study, Intermetallics **18** (2010) 203.

[4] S. Kalinichenka, L. Rontzsch, C. Baehtz, B. Kieback, Hydrogen desorption kinetics of melt-spun and hydrogenated $Mg_{90}Ni_{10}$ and $Mg_{80}Ni_{10}Y_{10}$ using in-situ synchrotron, X-ray diffraction and thermogravimetry, J. Alloys Compds. **496** (2010) 608.

[5] S. Kalinichenka, L. Röntzsch, B. Kieback, Structural and hydrogen storage properties of melt-spun Mg–Ni–Y alloys, Intl. J. Hydrogen Energy **34** (2009) 7749.

ROBL-CRG	**Experiment title:** **Temperature dependent crystallization and ordering of Ge NCs in a SiO_2 matrix**	**Experiment number:** **20-02-695**
Beamline: BM 20	**Date of experiment:** from: 6.05.2010 to: 11.05.2010	**Date of report:** 14.02.2011
Shifts: 15	**Local contact(s):** Dr. N.M. Jeutter	*Received at ROBL:* 17.02.2011

Names and affiliations of applicants (* indicates experimentalists):

M. Zschintzsch*, N.M. Jeutter*, J. von Borany*

Forschungszentrum Dresden-Rossendorf e.V., Institute for Ion Beam Physics and Materials Research, PO Box 51 01 19, D-01314 Dresden, Germany

Report:

Promising materials for new generations of light emitters or solar cells are based on semiconductor nanocrystals (NCs). The optical properties are highly linked to their size, crystallinity and location within a matrix. A successful method to get uniformly sized NCs is the use of multilayer (ML) structures [1,2]. In a series of ongoing studies (20-02-658, -667, -674), during this ROBL experiment $(Ge\text{-}SiO_2/\ SiO_2)^{50x}$ ML are investigated. The simultaneous deposition of $Ge+SiO_2$ by reactive magnetron sputtering from Ge and Si targets in the dc mode uses a certain process window for the oxygen partial pressure [4]. Samples, prepared at FZD beforehand, differ with respect to deposition temperatures, ML period thicknesses and the Ge/SiO_2 ratios. The variation of the stoichiometry was quantified by Rutherford Backscattering Spectrometry (RBS) prior to the beam time.

At the ROBL beamline the samples were *ex-situ* stepwise annealed in a separate UHV oven (base pressure low 10^{-8} mbar range) between 500 – 800°C (ΔT = 50K), in between characterized with x-ray (λ = 1.24 Å) scattering and diffraction. In the following the results of one representative sample are presented: substrate Si(001), deposition temperature T = 425°C, ML period thickness 5.8 nm, and Ge to SiO_2 ratio 1:2. The SiO_2 separation layers thickness amounts to 1.0 nm.

As shown in fig. 1, after deposition and annelings up to 600°C, only the broad Ge near-order peak at about 2θ = 22° appears in the GiXRD pattern (Scherrer size ~ 1.5 nm). The crystallisation of Ge starts at 650°C indicated by Ge(111) peak narrowing and the appearance of the Ge(220) and Ge(311) reflections. For annealing temperatures > 650°C, the peaks are characterized by the superposition of two contributions from Ge NCs of different sizes. Subsequent electron microscopy investigations reveal the existance of small Ge NCs in the ML (4 nm as visible in TEM fig. 3) and bigger NCs with sizes between 30 - 150 nm at the surface (SEM in fig. 4). After annealing at 800°C the crystallisation of Ge is completed as proofed by Raman spectroscopy.

In the XRR pattern (fig. 2), the partial coverage of surface with Ge NCs leads to a dip in the spectra at very low angles (grey rectangle). This can be interpreted as a second critical angle for SiO_2 which originates from the part of the surface not covered by Ge NCs. Furthermore, with increasing temperatures the 1st order ML peak is shifted to a larger angel which indicates a slight decrease of the ML period thickness due to ongoing Ge redistribution from the ML towards the surface.

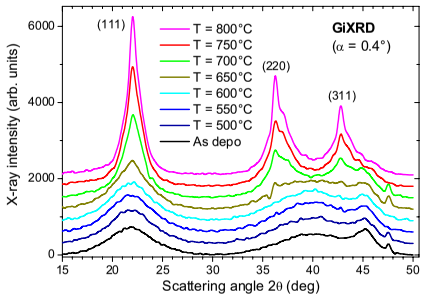

Fig. 1: *Ge NCs formation confirmed by grazing incidence X-ray diffraction (GiXRD, α = 0.4°)*

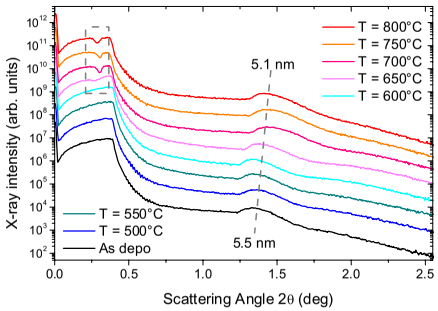

Fig. 2: *XRR reveals growth of Ge NC on surface and decrease of Ge-SiO_2-multilayer period.*

The TEM picture in fig. 3 reveals that the ML structure is still visible for the first layers, but with increasing distance to the Si substrate it seems to be washed out. In contrast XRR shows still a multilayer peak for the annealed samples so that there must be a density variation with a fixed length, which maybe ca nnot resolved in TEM. In the inset in fig. 3 and in fig. 4 the size, crystallinity and even the facetts of the Ge NCs on top of the multilayer are visible.

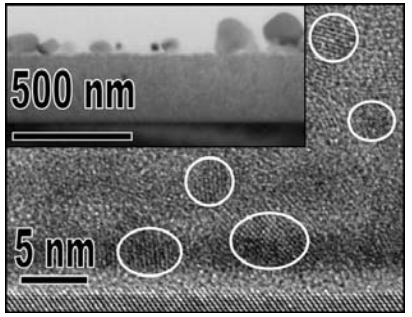

Fig. 3: *Ex-situ TEM pictures show Ge NCs in and on top (inset) of the multilayer*

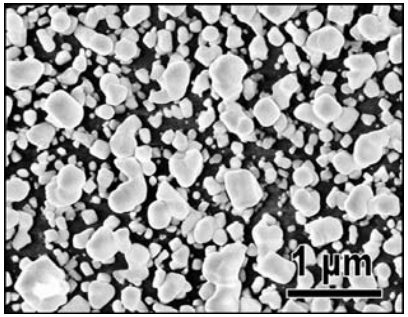

Fig. 4: *Ex-situ SEM show Ge NCs on top of the surface.*

From the data evaluation of the complete sample set the following conclusions can be derived:

(1) the Ge crystallization temperature in $(Ge+SiO_2)/SiO_2$ ML is considerably (~ 150°C) higher than in $GeOx/SiO_2$ ML, where Ge NCs are formed already at 550°C,

(2) the Ge NC size (2-10 nm) can be well tailored by the Ge containing ML sub-layer thickness and temperature,

(3) the formation of a high density of larger Ge NCs (30 – 100 nm) at the surface becomes more pronounced with increasing Ge to SiO_2 ratio and decreasing deposition temperature.

References:

[1] S. Foss et al., Thin Solid Films **515**, 6381 (2007)

[2] M.Buljan et al. Phys.Rev.B **79**, 035310, (2009), and Nanotechnology **20**, 085612 (2009).

[3] M.Zschintsch et al., Journal of Applied Physics **107**, 034306 (2010)

	Experiment title: **Grain growth induced by focused ion beam irradiation in thin magnetic films**	Experiment number: 20-02-696
Beamline: BM20	**Date of experiment:** from: 08-06-2010 to: 14-06-2010	**Date of report:** 26-01-2011
Shifts: 17	**Local contact(s):** Dr. Nicole Martha Jeutter	*Received at ESRF:*

Jörg Grenzer*, Olga Roshchupkina*
Helmholtz-Zentrum Dresden-Rossendorf, Institute of Ion Beam Physics and Materials Research
01314 Dresden, Germany

Report:

Over the last decade there is a rise of interest in fabrication and study of nanometer size magnetic elements that are widely used for magnetic recording media. Combination of focused ion beam with lithography (FIB lithography) can be used as a comprehensive tool for magnetic nanostructuring. Previous studies have demonstrated that FIB irradiation of thin metallic films induces significant grain growth and modifies the magnetic properties[1-2]. However in order to use FIB irradiation for nanostructuring one needs high Ga^+ ion fluences up to 2000µC/cm^2, leading to irradiation times of about 5 up to 98 hours for the area size of 0.4x0.4mm^2. As a result due to the small irradiated areas produced by FIB irradiation CRL beryllium lenses were applied to focus the beam down to 20µm.

The aim of this experiment was to study the structure of magnetic metallic films after 30keV Ga^+ FIB irradiation by the EXAFS measurements. The main advantage of the EXAFS analysis is precise short-range order structural information. Such information in combination with XRD data is needed for understanding weather any relationship between the structure and magnetic properties takes place. We have investigated a series of 50nm thick permalloy ($Ni_{80}Fe_{20}$) films irradiated with different Ga^+ ion fluences.

Prior to the EXAFS measurements an XRD analysis was performed. A set of rocking curves and in-plane rotation measurements using a position sensitive detector were carried out. From the rocking curve measurements we found out that fluences up to 1000µC/cm^2 modify the material and induce the crystalline growth (from 13nm for the non-irradiated sample up to 23nm for the sample irradiated with 1000µC/cm^2). The in-plane rotation measurements have demonstrated an increased ordering towards a (111) texture of the material induced by irradiation. The magnetic properties were measured via MOKE magnetometry and demonstrate degradation with increasing the ion fluence.

Integral raw XAS spectra of the Fe *K* (figure 1), Ni *K* (figure 2) and Ga *K* (figure 3) absorption edges of the permalloy film before (black) and after (red) irradiation are presented. Due to the fact that in the investigated permalloy film the lattice positions are randomly occupied by Fe or Ni and the low signal-to-noise ratio at the Fe edge (Fig.1) the date of the Fe *K* edge were not further taken into account. Subsequently, analysis of the EXAFS data was performed only for Ni *K* (Fig.2*)* and Ga *K* (Fig.3) edges. The measurements were first smoothed and a background subtraction was performed using ATHENA software. The data refinement was further performed using ARTEMIS software based on the FEFF6 code. Figure 4 demonstrates the extracted experimental EXAFS function $\chi(k)$ weighted to the wave number k^2 for Ni *K* edge of samples irradiated with 735µC/cm^2 and 1000µC/cm^2 fluences. The red line corresponds to the simulation. The simulation didn't show any distinguishable difference in parameters since no significant changes are observed in extracted EXAFS function χ(k) for the Ni *K* edge. The Ni *K* edge fits demonstrate negligible deviations of the lattice parameter from its nominal value of 3.55 Å as well as very small atom displacements within the simulation errors at different irradiation fluences. The fitting performed for the Ga *K* edge requires a model being not attached to a fixed crystallographic symmetry (an almost amorphous material case).

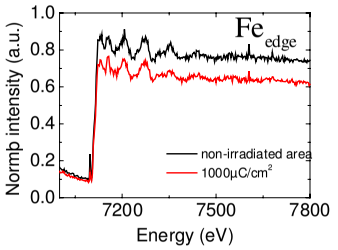

Figure 1. Normalized integral raw XAS spectra of the Fe *K* absorption edge of the permalloy film before (black) and after (red) irradiation.

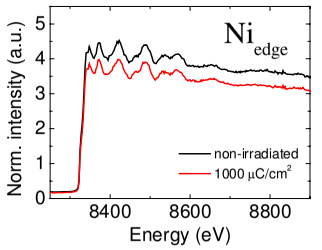

Figure 2. Normalized integral raw XAS spectra of the Ni *K* absorption edge of the permalloy film before (black) and after (red) irradiation

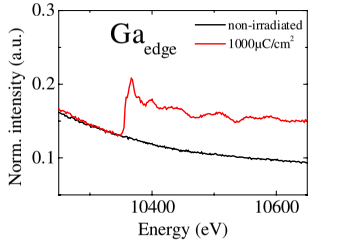

Figure 3. Normalized integral raw XAS spectra of the Ga *K* absorption edge of the permalloy film before (black) and after (red) irradiation.

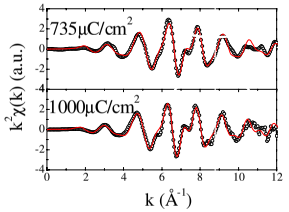

Figure 4. Extracted experimental EXAFS function χ(k) of the samples irradiated with 735µC/cm^2 and 1000µC/cm^2 weighted by k^2 at the Ni *K* edge.

Our investigations let us propose the following: FIB irradiation modifies the material and leads to a further material crystallization and to an incorporation of Ga^+ ions, however the simulation of the EXAFS data for the Ga *K* edge demonstrates that Ga atoms are not incorporated in perfect fcc cells but may remain outside, e.g. in the grain boundaries.

References

[1] C.M. Park and J. A. Bain., J. of Appl. Phys. 91, 6830 (2002).
[2] W.M. Kaminsky et al., Appl. Phys. Lett. 78, 1589 (2001).
[3] O. Roshchupkina, J. Grenzer, M. Fritzsche, J. Fassbender, DPG Regensburg 2010, DS 36.2.
[4] O. Roshchupkina, J. Grenzer, M. Fritzsche, J. Fassbender, XTOP 2010, B59.

	Experiment title: Hydrogen loading of thin films	**Experiment number:** 20-02/697
Beamline: BM 20	**Date of experiment:** from: 21.07.2010 to: 28.07.2010	**Date of report:** 24.08.2010
Shifts: 21	**Local contact(s):** Dr. Carsten Bähtz	*Received at ESRF:*

Names and affiliations of applicants (* indicates experimentalists):

Stefan Wagner*[,1], Helmut Uchida*[,1], Astrid Pundt[1]
Martin Vlach*[,2], Marian Vlcek*[,2], Frantricek Lukac*[,2], Jakub Cizek[2]

[1]Institute for Materials Physics, University of Göttingen, 37077 Göttingen, Germany
[2]Faculty of Mathematics and Physics, Charles University, 18000 Praha 8, Czech Republic

Report:

Physical properties of matter change when the system dimension is reduced to the nano-size. Especially, nano-sized systems have different phase boundaries in phase diagrams and different mechanisms of phase precipitation. To study the impact of both microstructure and mechanical stress contributions on the thermodynamics of nano-sized systems, in the present test-series of experiments at BM 20 we investigated different metal-hydrogen thin film systems with different initial microstructures and film thicknesses in the range from 30 to 300 nm. Fibre textured, nanocrystalline and epitaxial Palladium thin films as well as fibre textured Magnesium thin films were stepwise electrochemical charged or dischared with hydrogen. The subsequent change of the out-of-plane lattice parameters and the occurrence of hydride phases were monitored in Bragg-Geometry. For successful measurements an inert gas atmosphre (Argon/N_2) and fast XRD measurements (approx. 1 min per scan) appeared mandatory.
Epitaxial as well as nanocrystalline Palladium films prepared at 673 K on sapphire (0001) substrates were shown to reveal initially very smooth surface conditions, as thickness fringes around the (111) Bragg-Peak appeared (Fig. 1). From the oscillation period of the fringes and their damping the films thickness T and the near surface lattice distortion (surface roughness σ) can be determined [1] (Parameters in Fig. 1 at $c_H = 0$: T = 85.02 nm, σ = 0.0025 nm) . Next to the out-of-plane expansion, during hydrogen charging and hydride formation the thickness fringes allow to monitor the films surface roughness evolution - a technique, that is conventionally only applicable in XRR geometry. The example of an 85 nm epitaxial Pd film on sapphire in Fig. 1 shows that the surface roughness increases with the precipitation of the hydride phase, suppressing the thickness fringes when the film is loaded up to a hydrogen concentration of $c_H = 0.13$ H/Pd. However, during subsequent discharging the thickness fringes reversibly return. Subsequent loading to $c_H = 0.45$ H/Pd, on the other hand, irreversibly changes the surface condidtions, as the thickness fringes do not return after a further unloading step. According to our interpretation this irreversible change in the surface roughness reflects on the lattice matching during hydride precipitation – initially coherent hydrides are formed, elastically straining the metal lattice, while above a certain hydrogen concentration the precipitates become incoherent by the emission of misfit dislocation. These dislocations cause irreversible steps on the films surface. Interestingly, this change is not coupled to the thin film phase boundary.
In Fig. 2 the lattice parameter evolution and the occurance of the hydride phase in 300 nm thick Pd films with different microstructures are shown. From the figure clear differences in the initial stress states of the films and differences of their phase boundaries appear, approaching the bulk values with increasing epitaxy quality of the films. Furthermore, the initial slopes Δa/a of the lattice parameters in the solid solution region (α-phase) differ strongly (0.153 for nanocrystalline Pd, 0.104 for epitaxial Pd). This behaviour is in good agreement with calculations of the theoretically expected out-of-plane expansion of thin films that are clamped on elastically hard substrates. [2] The palladium film on silicon detached from the substrate in the two phase field. The accompanied strong reduction in mechanical stress resulted in a lattice relaxation, clearly visible in the continously increasing hydride (β-phase) lattice paramater.
Magnesium hydride is served as a promising candidate for hydrogen storage applications. However, Griessen et al. [3] state that it is not possible to completely hydride Mg thin films with more than 100 nm thickness due to the formation of a surface hydride blocking layer. In contrary, our test measurements at BM 20 revealed that hydride formation is possible for Mg-film thickness up to 188 nm, and that the thickness of the hydride layer can be tuned by proper loading condidtions. In Fig. 3 the appearance of the hydride peak in a 188 nm thick Mg film is shown. The hydrogen concentration at the onset of hydride peak visibilty strongly depends on the applied loading current.

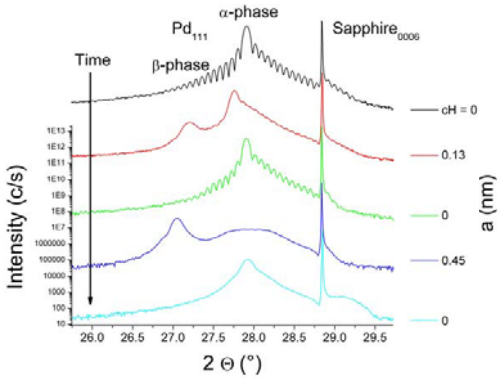

Fig. 1: Thickness Fringes and phase evlution of 85 nm epitaxial PdH_c on sapphire.

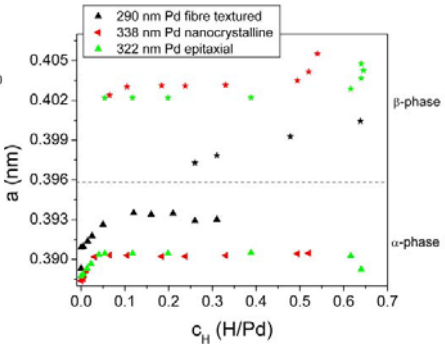

Fig. 2: Lattice parameter and phase evolution of PdH_c thin films with different microstructures.

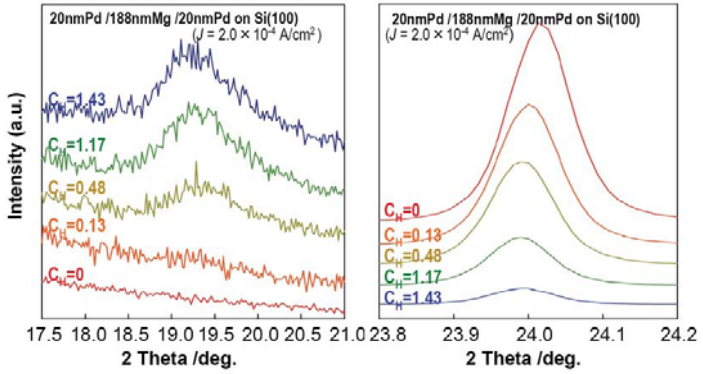

Fig. 3: Hydride formation in a 188 nm Mg thin film. Left side: MgH_2-peak, right side: α-peak.

[1] Zolotoyabko, E.: J. Appl. Cryst. (1998), 31, 241.
[2] Pundt, A: Annu. Rev. Mat. Res. (2006), 36, 555.
[3] Baldi, A. et al., Appl. Phys. Lett.(2005), 95, 071903.

ROBL-CRG	**Experiment title:** GISAXS study of the secondary phase morphology in transparent conductive oxide thin films	**Experiment number**: 20-02-698
Beamline: BM 20	**Date of experiment**: from: 17-11-2010 to: 20-11-2010	**Date of report**: 08-02-2011
Shifts: 9	**Local contact(s)**: Dr. Carsten Baehtz	*Received at ROBL:*

Names and affiliations of applicants (* indicates experimentalists):

G. Abrasonis*[1], M. Vinnichenko*[1], S. Brunken*[2], K. Ellmer[2]

[1] *Institute of Ion Beam Physics and Materials Research, Helmholtz Zentrum Dresden-Rossendorf (HZDR), P .O. Box 510119, 01314 Dresden, Germany*
[2] *Institute Solar Fuels, Helmholtz Zentrum Berlin (HZB), Hahn-Meitner-Platz 1, 14109 Berlin, Germany*

Report:

A proper understanding of secondary phase formation and their influence on the free electron generation and transport is of crucial importance for establishing performance limits of transparent conductive oxides (TCOs). Therefore, these experiments were aimed at checking the applicability of synchrotron based x-ray diffraction (XRD) and grazing-incidence small-angle x-ray scattering (GISAX) for this purpose. The focus was on Al-doped ZnO (AZO) and Nb-doped TiO_2 (TNO), while certain experiments were carried out for Ga-doped ZnO (GZO).

The AZO films were deposited in HZDR by reactive pulsed magnetron sputtering using metallic Zn-Al targets (Al concentration of 4.7 and 8.7 at. %.) at different temperatures (T_S=200-400 °C). Film grown on amorphous fused silica substrates were compared to those grown on single crystal Al_2O_3 (0001) substrates. The GZO films were grown at HZB epitaxially on ZnO (0001) substrates at elevated temperatures using DC sputtering of ceramic ZnO-Ga_2O_3 targets. The TNO samples (HZB) were grown on glass substrates at RT using reactive magnetron sputtering.

Electrically insulating and high-resistivity AZO films with the thickness in the range of 200-400 nm were selected for these experiments. The films deposited at T_S>300 °C exhibit Al concentration 16-20 at. % and are electrically insulating. The film grown at T_S=200 °C had Al concentration of 8 at. % and relatively high electrical resistivity. The GZO films had Ga concentration in the range of 3 at.% and had lower electrical resistivity compared to AZO.

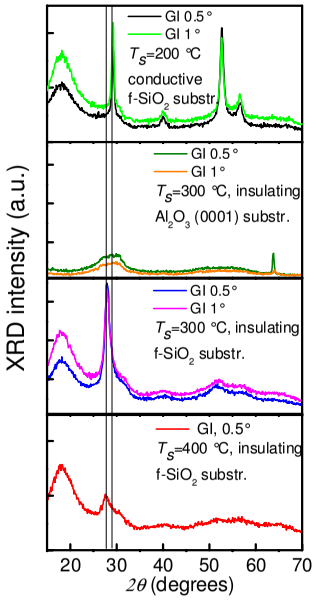

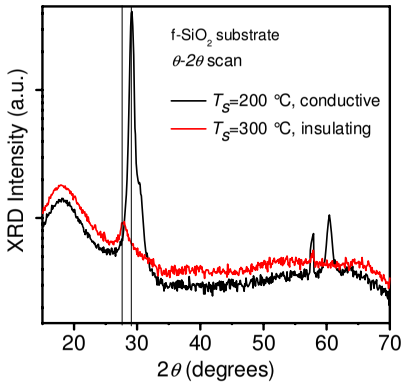

Figure 1. XRD patterns of AZO films grown at different conditions measured in grazing incidence (left, linear scale) and θ-2θ (right, logarithmic scale) geometry.

In the case of the AZO films, it is clearly observed that the insulating samples with a high aluminum concentration (16-20 at.%) have much broader and weaker XRD peaks compared to a conductive film (8 at. % of Al) (see Fig. 1). The broad peak below ~20° is attributed to the amorhous fused silica substrate. Preliminary analysis shows that the line at 28.97° observed for the conductive sample is associated with the ZnO (0002) diffraction. The distinct line at 27.68° is observed only in insulating films and is interpreted as a diffraction from the new $(ZnO)_3Al_2O_3$ secondary phase in agreement with previous study where θ-2θ scans using Cu $K\alpha$ wavelength were performed for similar AZO films (*Vinnichenko et al, APL 96, 141907 (2010)*). In addition to the earlier measurements, it has been found that:

1) intensity of this diffraction line drops dramaticall while changing from GI to θ-2θ geometry that points to a strongly disordered nano-crystalline structure of these films;
2) the films grown on sapphire show much weaker diffraction from this phase even in GI compared to AZO film grown on fused silica at identical conditions;

3) deposition of AZO films at the epitaxial substrate does not prevent formation of this phase, but its amount seems to be comparable with amount of nanocrystaline ZnO in this case.

XRD of GZO and TNO shows only ZnO and TiO_2-related peaks, respectively.

GISAX measurements even of the smoothest (rughness of 2 nm) insulating AZO films showed that the contribution from the surface roughness is dominating the signal. This means that the contribution from inhomogneities is much smaller than from the surface roughness.

Finally, it is shown that synchrotron-based XRD of AZO films is a useful tool for determination of secondary phase formation, however, GISAX measurements of this system does not provide additional information in this case.

	Experiment title:	Experiment number:
	Grain growth induced by focused ion beam irradiation in thin magnetic films	20-02-700
Beamline: BM20	**Date of experiment:** from: 08-09-2010 to: 15-09-2010	**Date of report:** 26-01-2011
Shifts:21	**Local contact(s):** Dr. Carsten Baehtz	*Received at ESRF:*

Jörg Grenzer*, Olga Roshchupkina*
Helmholtz-Zentrum Dresden-Rossendorf, Institute of Ion Beam Physics and Materials Research
01314 Dresden, Germany

Report:

This experiment is a continuation of the experiment № 20-02-696.

Previously it was demonstrated that nanoscale patterning can be performed using focused ion beam (FIB) techniques combined with lithography. Such a combination is known as FIB irradiation and is similar to standard implantation. FIB irradiation source differs from a standard ion implanter in a very small beam size of ~10nm in diameter and in a very high beam current density of ~ 12.7A/cm^2. Both beam size and beam current density can lead to difference in interaction of the ion beam with the matter changing both structural and magnetic properties. As a result detailed structural investigations of both irradiation cases are of great importance to understand the processes that take place while irradiation. In previous studies by C.M. Park and J.A. Bain (Ref. 1) it was demonstrated that FIB irradiation of permalloy films under certain conditions induces a significant grain growth. W.M. Kaminsky and co-authors (Ref. 2) have shown that FIB irradiation causes a degradation of magnetic properties with increasing the Ga^+ ion fluence.

In this experiment we have studied the structure of magnetic metallic films irradiated with Ga^+ ions by a standard implanter at the energy of 30keV. The main goal of this experiment was EXAFS measurements providing precise local structural information. Such information in combination with XRD data is needed for understanding the difference between FIB irradiation and standard implantation, in particular which parameters play the main role while irradiation. We have investigated a series of 50nm thick permalloy ($Ni_{80}Fe_{20}$) films irradiated with different Ga^+ ion fluences (the fluences were similar to the FIB irradiated samples).

Prior to the EXAFS measurements an XRD analysis was performed. A set of rocking curves using a position sensitive detector were carried out at the laboratory setup. From the rocking curve measurements we have estimated the crystallites size showing a growth at higher fluences (from 13nm for the non-irradiated sample up to 19nm for the sample irradiated with 1000μC/cm^2). Moreover the rocking curves have demonstrated an increased ordering towards the (111) texture of the material induced by irradiation. MOKE magnetometry measurements demonstrate degradation of the magnetic properties with increasing ion fluence. Both results demonstrate similarity to the FIB irradiated samples.

Integral raw XAS spectra of the Fe *K* (Fig. 1) and Ni *K* (Fig. 2) absorption edges of the permalloy film for the samples irradiated with 1000μC/cm^2 (black) and 4000μC/cm^2 (red) fluences are presented. Figure 3 demonstrates Ga *K* edge for the samples irradiated with 400μC/cm^2 (blue) and 4000μC/cm^2 (red).Due to the fact that in the investigated permalloy film the lattice positions are randomly occupied by Fe or Ni and the low signal-to-noise ratio at the Fe edge (Fig.1) the data of the Fe *K* edge were not further taken into account. As a result the EXAFS data analysis was performed only for Ni *K* (Fig.2) and Ga *K* (Fig.3) edges. The measurements were first smoothed and a background subtraction was performed using ATHENA software. The data refinement was further performed using ARTEMIS software based on the FEFF6 code. Figure 4 demonstrates the extracted experimental EXAFS function $\chi(k)$ weighted to the wave number k^2 for Ni *K* edge of samples irradiated with 1000μC/cm^2 and 4000μC/cm^2 fluences. The red line corresponds to the simulation. Since no significant changes are observed in extracted EXAFS function χ(k) for different irradiation doses for the Ni *K* edge the corresponding simulation didn't show any distinguishable difference in parameters. The Ni *K* edge fits demonstrate negligible deviations of the lattice parameter from its nominal value of 3.55 Å as well as very small atom displacements within the simulation errors at different irradiation fluences. The fitting performed for the Ga *K* edge requires a model being not attached to a fixed crystallographic symmetry (an almost amorphous material case). Both fitting results are similar to the FIB irradiation.

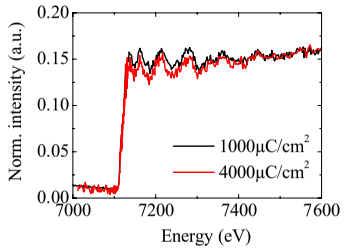

Figure 1. Normalized integral raw XAS spectra of the Fe *K* absorption edge of the permalloy film irradiated with 1000μC/cm^2 (black) and 4000μC/cm^2 (red) fluence.

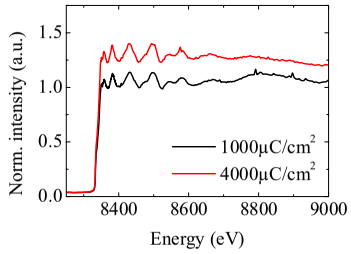

Figure 2. Normalized integral raw XAS spectra of the Ni *K* absorption edge of the permalloy film irradiated with 1000μC/cm^2 (black) and 4000μC/cm^2 (red) fluence.

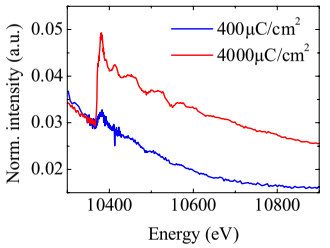

Figure 3. Normalized integral raw XAS spectra of the Ga *K* absorption edge of the permalloy film irradiated with 400μC/cm^2 (blue) and 4000μC/cm^2 (red) fluence.

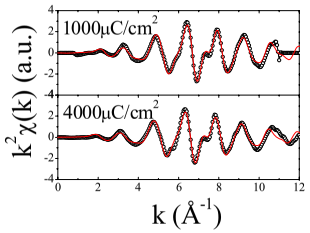

Figure 4. Extracted experimental EXAFS function χ(k) of the samples irradiated with 1000μC/cm2 and 4000μC/cm2 weighted by k^2 at the Ni *K* edge.

Our investigations let us propose the following: standard implantation modifies the material and leads to a further material crystallization and to an incorporation of Ga^+ ions, however the simulation of the EXAFS data for the Ga *K* edge demonstrates that Ga atoms are not incorporated in perfect fcc cells but may remain outside, e.g. in the grain boundaries. As a conclusion standard implantation demonstrates similar behaviour in comparison to the FIB irradiation.

References

[1] C.M. Park and J. A. Bain., J. of Appl. Phys. 91, 6830 (2002).
[2] W.M. Kaminsky et al., Appl. Phys. Lett. 78, 1589 (2001).
[3] O. Roshchupkina, J. Grenzer, M. Fritzsche, J. Fassbender, DPG Regensburg 2010, DS 36.2.
[4] O. Roshchupkina, J. Grenzer, M. Fritzsche, J. Fassbender, XTOP 2010, B59.

	Experiment title: In situ study of lithium insertion-deinsertion in lithium rich layered oxide.	Experiment number: 20-02-706
Beamline: BM20	**Date of experiment**: from: 23/10/2010 to: 26/10/2010	**Date of report**: 27/01/2011
Shifts: 9	**Local contact(s)**: Carsten Baehtz	*Received at ESRF:*

Names and affiliations of applicants (* indicates experimentalists):

J.-F. Colin*, L. Simonin*, J.-F. Martin*, L. Daniel*, C. Bourbon*

Commissariat à l'Energie Atomique et aux Energies Alternatives, Grenoble.

Report:

The goal of this experiment was to study the mechanism of lithium insertion-deinsertion in a high capacity electrode material : $Li_{1.2}Ni_{0.2}Mn_{0.6}O_2$. We aimed to get more information on the origin of the extra capacity observed during the first charge and which cannot be explained by the oxidation of metals to tetravalent state.

For this purpose we cycled this material in a pouch cell containing lithium as counter electrode. During this cycling, difffractogramms were taken in a transmission mode every 3 minutes at the energy of 25 keV and using an image plate detector. This allowed us to collect 900 diffractogramms along the first 1.5 cycle, giving us a high time resolution.

The whole pattern matching refinement was carried out every ten patterns to follow the structural changes. Each result was then attributed to one voltage. These results are provided in figure 1

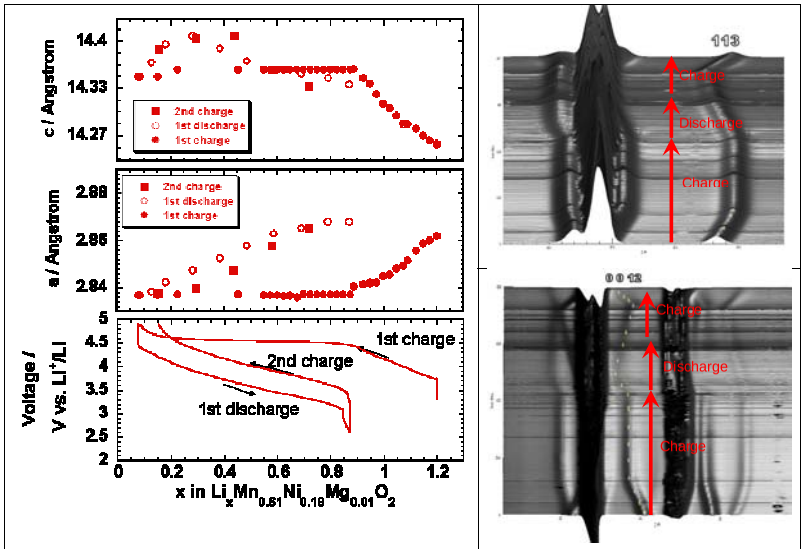

Fig. 1 : Evolution of cell parameters related to electrochemical curve and evolution of caracteristic reflexions

As one can observe, during the first step of the charge, the cell parameters evolve linearly as well as the potential. This is attributed to the oxidation of metals which gives smaller ionic radii explaining the decrease of a and b parameters, and to the lesser content of the lithium layer that lead to a diminishing screening effect between the oxygen of the metals layers and then to an increase of the c parameter.

When the potential reach the high voltage plateau, no further evolution of cell parameters is observed. This would be expected for a biphasic process, but surprisingly no new phase is observable. Then we can suppose the second phase is amorphous or so close from the first one that we can not distinguish them simply. An analysis of the FHWM is under progress do determine if the peak broadening observed can be due to this second phase.

However after this first charge, we observe a completely different mechanism, allthough the a and b parameters come back to values close from the starting one during the discharge, indicating the reduction of the metals, the c parameter does not show a reversible behaviour. This new mechanism is reversible during the second charge with almost no hysteresis. This

would mean, that the first charge acts as an activation which creates a new structure. This structure would then be cycle reversibly.

During this measurement campaign we also took an *ex situ* pattern of the starting compound in a capillary geometry, to be able to refine the complex structure of this compound where metallic cationic site are occupied by 3 different atoms. Coupled with an ex situ neutron measurement, it allowed us to refine the repartition of the cations in the layers giving us a reliable starting point for further refinement on cycled compounds. We particularly observed a statistic ordering of metals decresing the symmetry from R $\bar{3}$ m to C 2/m with cell parameters a=4.961Å, b=8.588 Å, c=5.038 Å, β=109.30°, and a 3.85 % Ni/Li exchange in the lithium layers (fig.2) .

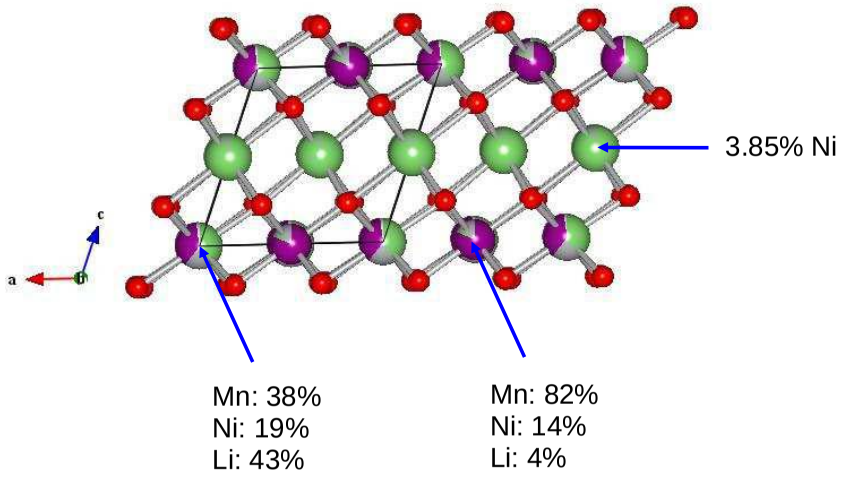

Fig. 2 : Structure of the starting compound and repartition of the metals

To summarize, this study allowed us to enlight an activation step at high voltage in this material and to obtain more information on the starting compound. The caracterization of the compound at the end of the charge is still to be done and it would certainly require new experiment (*ex situ* neutron diffraction has already been carried out).

ESRF	**Experiment title: Unknown crystal structures of selected uranyl sulfates: solution from the high resolution powder data combined with EXAFS spectroscopy**	**Experiment number**: CH-3085
Beamline:	**Date of experiment**: from: 14. 5. 2010 to: 18. 5. 2010	**Date of report**: 16. 12. 2010
Shifts: 12	**Local contact(s)**: Dr. Carsten Baehtz	*Received at ESRF:*

Names and affiliations of applicants (* indicates experimentalists):

Jakub Plášil*, National Museum, Václavské nám. 68, Prague 1, 11579, Czech Republic

Michal Hušák*, Institute of Chemical Technology, Technická 5, Prague 6, 16628, Czech Republic

Jan Rohlíček*, Institute of Chemical Technology, Technická 5, Prague 6, 16628, Czech Republic

Report:

The main objective of the research was to collect high-resolution powder diffraction data on selected uranyl sulfate minerals to provide more structural information on their unknown crystal structures. We have collected data for 3 natural uranyl sulfates – jáchymovite, johannite and rabejacite. They were chosen from the broader selection, but else phases were found to be not quite stable after grinding.

There are considerable difficulties arising from the complexity of the crystal structures of these phases and for dominant U-scattering power. For these reasons the data obtained from the experimental setting of the beamline BM-20 are not sufficient for solving the structures of jáchymovite (found to be a mixture of two phases, probably) and rabejacite, ab-initio. However, the new unit-cell parameters for both phases are proposed and currently are under evaluation. In case of johannite, the Rietveld refinement of its crystal structure was carried out, regarding Mg contents entering the cationic site instead of Cu. Results are acceptable and will be published along with the chemical/structural characterization of johannite samples from different environments (Plášil et al. in prep.).

Besides these three phases, an additional set of samples were measured. The set consists of UO_2^{2+} containing natural phases (J. Plášil), two minerals from the Cu-Se system (J. Plášil) and two samples of pharmaceutical phases (Dr. Hušák). Most promising results carried out an diffraction experiment on the naturally occurring $U(HAsO_4)_2(H_2O)_4$ (Fig. 1).

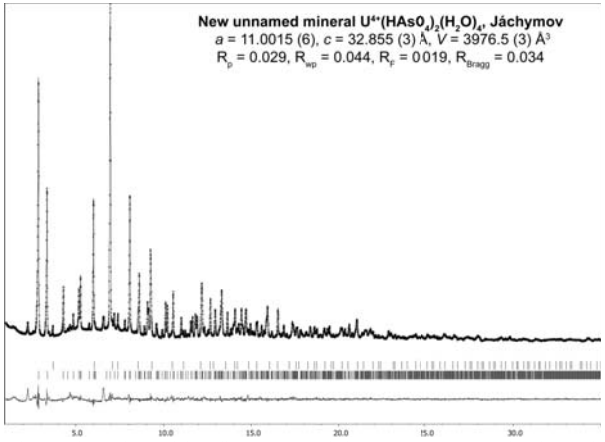

Fig. 1. The final plot from the Rietveld refinement of the new unnamed mineral from Jáchymov, Czech Republic. The data were collected from the mixture, consisting mainly of the new mineral, arsenolite (Bragg reflections bars above those belonging to new mineral) and else, unidentified mineral phase (positive maxima in the difference plot).

The proposal for approval this phase as a new mineral is now prepared to be submitted to the CNMNC of the International Mineralogical Association. Powder diffraction data were further collected for widenmannite, an unique Pb-UO_2^{2+} carbonate. Its crystal structure is now under evaluation (in combination with PED/TEM). The crystal structure of flavine2 (10-Methylisoalloxazine 5-oxide), one of the pharmaceutical phases measured, has been published yet in Acta Crystallographica E (Rohlíček et al. 2010):

The title compound [systematic name: 10-methylbenzo[g]-pteridine-2,4(3H,10H)-dione 5-oxide], $C_{11}H_8N_4O_3$, consists of a large rigid isoalloxazine group which is approximately planar (r.m.s. deviation = 0.037 Å). In the crystal, intermolecular N–H···O hydrogen bonds link the molecules into centrosymmetric dimers. Dimers related by translation along the *c* axis form stacks through π–π interactions [centroid–centroid distances = 3.560 (5) and 3.542 (5) Å]. Weak intermolecular C–H···O interactions further consolidate the crystal packing.

References

Plášil J., Škoda R., Dušek M., Fejfarová K., Hloušek J., Sejkora J., Meisser N., Škácha P. and Čejka J. (in prep.): Johannite from different localities: A chemical and X-ray diffraction study. To be submitted to Journal of Geosciences.

Rohlíček J., Cibulka R., Cibulková J., Maixner J. and Hušák M. (2010): 10-Methylisoalloxazine 5-oxide from synchrotron powder diffraction data. Acta Crystallographica E66, o3350–3351.

ESRF	**Experiment title:** **Nucleation conditions for diamond nanocrystals in amorphous silica matrix**	**Experiment number:** HS-3849
Beamline: BM20	**Date of experiment:** from: 15.4.2009 to: 21.4.2009	**Date of report:** 27.8.2009
Shifts: 18	**Local contact(s):** Carsten Baehtz	*Received at ESRF:*

Names and affiliations of applicants (* indicates experimentalists):

*Maja Buljan, Department of Condensed Matter Physics, Charles University in Prague, Czech Republic and Ruđer Bošković Insitute Zagreb, Croatia

*Jörg Grenzer, Forschungszentrum Dresden Roßendorf, Germany

*Václav Holý, Department of Condensed Matter Physics, Charles University in Prague, Czech Republic

Report:

The aim of the beamtime was to investigate the crystallization of carbon nanoclusters in-situ during annealing of C-implanted amorphous silica layers in forming gas (mixture of Ar and H). However, we found that the diffraction peaks of crystalline carbon inclusions (diamond inclusions, fcc-carbon or simple-cubic carbon) are not measurable, since they were covered by an intense background due to the scattering from amorphous silica. Therefore we decided to study the spatial arrangement of Ge nanocrystals in silica, using grazing-incidence small-angle x-ray scattering (GISAXS).

Introducing regularity in the spatial arrangement of Ge quantum dots (QDs) is proven to affect their properties; in particular, collective QDs vibrations appear a distribution of their sizes is much narrower [1]. Moreover, the wavefunctions of carriers confined in periodically arranged quantum wells may overlap creating minibands of eigenenergies with broad optoelectronical applications.

The formation of regularly ordered QDs arrays is usually obtained during the growth of crystalline multilayers (MLs) [2,3] where the mismatch of the lattice parameters causes elastic forces which induce QDs ordering. Some very recent studies [4] showed the possibility of the production of spatially correlated Ge QDs also in amorphous MLs, where the ordering is achieved by the interplay of diffusion and surface morphology mechanisms. However, in such systems, regions with ordered dots appear in small, randomly oriented domains, and only ordering of the positions of next neighbors in QD arrays (short-range ordering) can be achieved.

In the reported beamtime we have investigated the growth of Ge QDs in $(Ge+SiO_2)/SiO_2$ multilayers after ion beam irradiation under oblique incidence angle (ϕ_{irr}= 60 deg*)*. The irradiation is used for induction of regular ordering of QDs, which are nucleate along the rods in irradiation direction [4]. We have performed series of reflectivity, diffraction and grazing incidence small angle X-ray scattering (GISAXS) measurements of the system consisting of 20 $(Ge+SiO_2)/SiO_2$ bi-layers deposited on Si(111) substrate. The purpose of the measurements was investigation of temperature dependence of structural properties of the irradiated multilayer and of the crystalline quality of the formed QDs. Therefore, the measurements were taken before after and during the in-situ annealing in vacuum in temperature range from 200-900^{o}C. GISAXS maps of the multilayer measured during annealing treatment are shown in Fig.1. All maps taken on ML annealed below 800^{o}C show presence of tilted Bragg sheets. The tilt angle ($\phi_{tilt} = 90 - \phi_{irr}$) correspond to formation of QDs which are correlated along the irradiation direction. For annealing temperature higher than 700^{o}C, the Bragg-sheets are not visible in GISAXS maps showing destruction of the multilayer structure and regular QDs ordering.

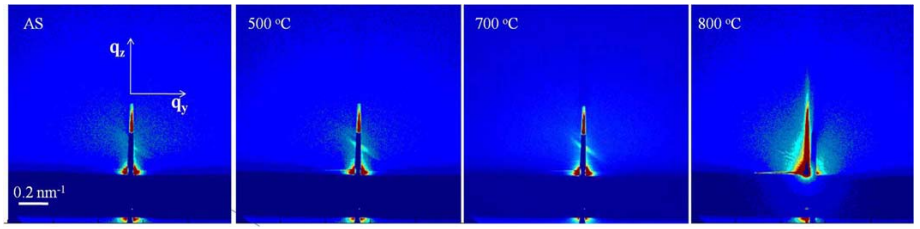

Fig.1. GISAXS maps measured on the irradiated (Ge+SiO2)/SiO2 multilayer during in-situ annealing. The incident X-ray beam was set perpendicular to the plane of the irradiation.

In the following, we are going to analyze the GISAXS data. We have formulated a model describing the ordering of the QDs along the ion tracks and we are dealing with numerical fitting of the GISAXS data to this model.

[1] M. Buljan, U.V. Desnica, G. Dražić, M. Ivanda, N. Radić, P. Dubček, K. Salamon, S. Bernstorff, V. Holy Nanotechnology **20**, 085612 (2009)
[2] G. Springholz, V. Holy, M. Pinczolits, and G. Bauer, Science **282**, 734 (1998).
[3] M. Buljan, U. V. Desnica, M. Ivanda, N. Radić, P. Dubček, G. Dražić, K. Salamon, S. Bernstorff, and V. Holý, Phys. Rev. B **79**, 035310 (2009).
[4] M. Buljan, I. Bogdanović-Radović, M. Karlušić, U.V. Desnica, G. Dražić, N. Radić, P. Dubček, K. Salamon, S. Bernstorff, V. Holy Appl. Phys. Lett. **95**, 063104 (2009)

ESRF	**Experiment title:** "HRXRD characterization of MOCVD-grown GaN layers on 4H, 6H 001 SiC substrates with AlGaN/GaN heterostructures as a buffer layer".	**Experiment number**: HS-3850
Beamline: BM 20	**Date of experiment**: from: 10 July 2009 to: 14 July 2009	**Date of report**: 03-02-2010
Shifts: 12	**Local contact(s)**: Dr. Nicole M. Jeutter	*Received at ROBL:*
Names and affiliations of applicants (* indicates experimentalists): Jarosław Gaca, Marek Wojcik, Krystyna Mazur Institute of Electronic Materials Technology, Warsaw, Poland		

Report:

The properties of SiC applied as a substrate for III-N compound epitaxy allow to utilize it for high-power devices, working in high-temperature and resistant to the action of the electromagnetic field. This is the source of great interest in an epitaxial growth of Al(Ga)N/GaN/In(Ga)N heterostructures on both 4H and 6H SiC substrates. The problem consists in finding the appropriate buffer layers to grown good quality Al(Ga)N/GaN/In(Ga)N heterostructures. The objective of the project was to work out the undestructive method of characterization of the above mentioned buffer layers and heterostructures based on X-ray diffraction. To this end the measured rocking and reflectometric curves were compared to the ones simulated by means of a computer program based on a Darwin version of X-ray diffraction theory [1]. Because of the small volume of the investigated III-N layers the synchrotron radiation proved to be necessary to properly determine the chemical composition and interplanar spacing profiles especially in the interface region of succeeding layers.

At the first stage of the experiment the rocking curves were collected at the vicinity of the 002 GaN reflection for Al(Ga)N/GaN heterostructures grown on 4H and 6H 001 SiC substrates by MOCVD technique [2]. The sample of such experimental and simulated rocking curves for heterostructure deposited on 6H SiC substrate are presented in Fig. 1. The investigated heterostructures have been designed so that to enable the assessment of the influence of the substrate and buffer type, thickness of AlN layer and the level of the doping of the AlGaN layer on the their crystalline quality.

At the second stage of the experiment the strain was induced in 1μm thick GaN layer by means of the Ar ion implantation. It was found that strained layer was created within the GaN one, with lattice constant greater then that for GaN, and that the relative lattice misfit $\Delta a/a$ between these two layers, measured in the growth direction as a function of implanted dose of Ar ions proved to be linear for doses less then 1.0E+15, Fig. 2. The increase of the implanted dose beyond that value does not bring about the increase of the lattice deformation in the growth direction. These results may be employed to accomplish the postgrowth engineering of the interface profiles in AlN/GaN/AlGaN hetrostrructures.

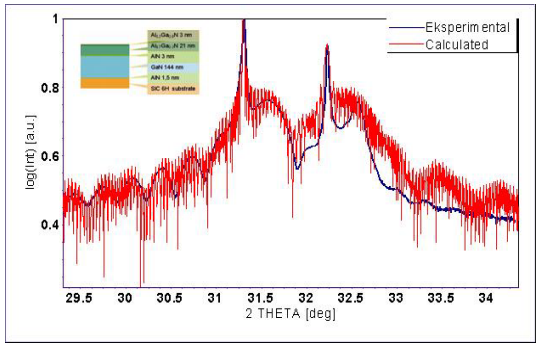

Fig. I. Experimental and simulated rocking curves for the heterostructure presented in the inset. The experimental data were collected at the ESRF BM 20 with wavelength λ=0.139997nm

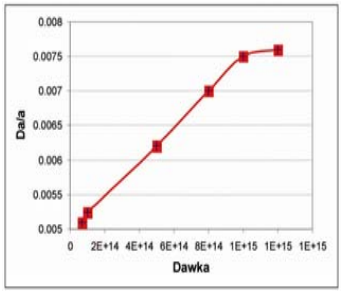

Fig. 2. The lattice misfit Δa/a between the ion-implantation damaged and non-damaged layers as a function of the implanted dose of Ar ions.

At the third stage of the experiment the study of the degree of crystalline and chemical perfection of AlN/GaN heterostructures consisting of ultra-thin GaN quantum wells (QWs) separated by AlN barriers, grown on the top of AlN buffer layers with thickness ranging from 100 nm to 220 nm have been investigated.

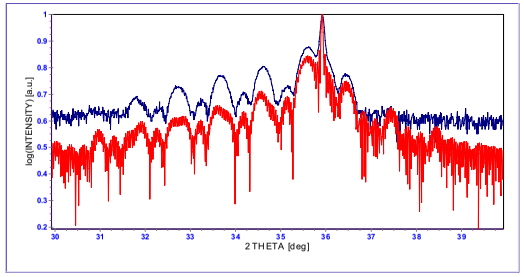

Fig 3. The experimental and simulated HRXRD diffraction 002 profiles for AlN/GaN heterostructures obtained by means of synchrotron radiation ESRF Grenoble, (logaritmic scale θ/2θ scan mode)

It has been found, that in the volume of GaN well, no relaxation occurred i.e. both AlN and GaN layers have the same in-plane lattice parameter as the underlying buffer layer. It means that GaN QWs are compressed to match the lattice constant of AlN. This means that applied buffer layers actually are effective substrates for the two-dimensional growth. The structure quality of AlN/GaN heterostructures have been confirmed by the satisfactory match between the measured and simulated diffraction and reflectometric profiles. The values of correlation length of columnar crystallites and the strain normal to the surface has been determined by applying the pseudo-Voit fit of 002 AlN and heterostructure reflections. The strain plotted versus correlation length normal to the surface turned out to be a monotonically decreasing function.

References

[1] A. Jasik, A. Wnuk, J. Gaca, M. Wójcik, A. Wójcik-Jedlińska, J. Muszalski, W. Strupiński, J. of Cryst. Growth 311 (2009) 4423– 4432

[2] P. Caban, K. Kosciewicz, W. Strupinski, J. Szmidt K. Pagowska, R. Ratajczak, M. Wojcik, J. Gaca, A. Turos, Materials Science Forum Vols. 615-617 (2009) pp 939-942

ESRF	**Experiment title:** Investigation of Fe-rich phases in (Ga,Fe)N:Mg by x-ray diffraction	**Experiment number:** HS-4246
Beamline: BM 20	**Date of experiment:** from: 08/12/2010 to:14/12/2010	**Date of report:** 24/01/2011
Shifts: 18	**Local contact(s):** Carsten Baehtz	*Received at ROBL:*

Names and affiliations of applicants (* indicates experimentalists):

A. Navarro-Quezada[*1],T. Devillers[*1],M. Rovezzi[1], E. Wintersberger[*1], A. Bonnani[1] and G. Bauer[1]

[1] Institut fur Halbleiterphysik, Johannes Kepler Universitaet Linz, Altenbergerstrasse 69, A-4040 Linz, Austria

Report:

(Ga,Fe)N is a nanocomposite material system, in which the existence of nanoscale regions or crystals containing a large density of magnetic cations exhibiting high Curie temperature, account for its ferromagnetic behaviour. The aggregation of these magnetic cations depends strongly on the fabrication conditions and also on co-doping with shallow impurities. While the influence of co-doping with donors (e.g. Si) has been already studied, the influence of co-doping with acceptors (e.g. Mg) is yet not clear. In order to obtain a conclusive picture on the orientation, composition, and structure of the different observed nanocrystals, annealing experiments and a set of reciprocal space mapping (RSM) measurements were performed.

For this purpose 4 samples fabricated at different growth temperatures and containing different Fe_xN nanocrystals were carefully studied using coplanar diffraction at different annealing temperatures (from 100 to 800°C) in a N_2 atmosphere at 800 mbar. RSM of each sample prior and after annealing were acquired at different sample orientations to obtain information on the topotaxial relationship of the nanocrystals to the host matrix.

In figure1 we show the effect of annealing on the Fe-rich phases. The phases observed in the as-grown sample (peaks 2 and 3) are ε-Fe_3N (002) and (111), respectively. After annealing this phase is reoriented as (110) along the growth direction (peak 1). Peak 4 is identifed as GaN(003), peak 5 probably belongs to a Fe_3C alloy and peak 6 is identified as $Fe_{0.7}Ga_{0.3}$.

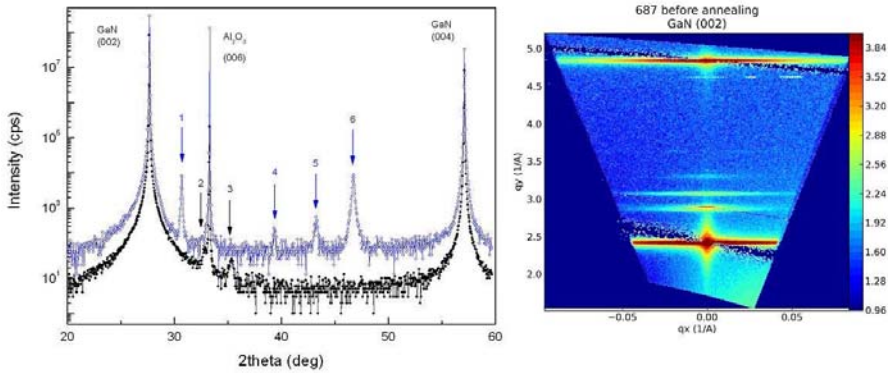

Fig 1. (left) SXRD spectra of the sample grown at 850°C prior (black) and after annealing (blue). The numbers indicate the phases present and described in the text. **(right)** RSM of the as-grown sample.

On the right side of figure 1 the RSM of the as-grown sample is shown. One can clearly distinguish the GaN (002) and (004) peaks, the Al_2O_3 (006) peak and the two ε-Fe_3N nanocrystal peaks close to the substrate diffraction. RSM at asymmetric directions were acquiered to find their orientation along the in-plane direction of GaN. From this we found that the annealed ε-Fe_3N nanocrystals orient in GaN as follows: $[110]_{Fe3N}$II$[001]_{GaN}$ and $[221]_{Fe3N}$II$[101]_{GaN}$, and that the $Fe_{0.7}Ga_{0.3}$ nanocrystals, observed also after annealing, lie with $[102]_{FeGa}$II$[001]_{GaN}$ and $[201]_{FeGa}$II$[101]_{GaN}$ and have an hexagonal lattice structure with a six-fold symmetry. Unfortunately most of the GaN and substrate asymmetric diffractions lie along the expected asymmetric diffractions of the nanocrystals, screening the contribution these last. Therefore, only some of the asymmetric diffractions could be observed. The same procedure was applied to all samples, gathering a full set of data which is currently still under analysis. The measurements during this beamtime will be very helpful to know the orientation of these Fe-rich nanocrystals in GaN, which might be related to the magnetic properties of the layers. The results obtained during this beamtime will be submitted for publication.

References: [1] A. Bonanni et al., *Phys. Rev. Lett.* **101** (2008).

[2] M. Rovezzi et al., *Phys. Rev. B* **79** 195209 (2009)

ESRF	**Experiment title:** Temperature dependence of lattice parameters of langasite single crystals ($La_3Ga_5SiO_{14}$)	**Experiment number:** MA-645
Beamline: BM 20	**Date of experiment:** from: 18/02/2009 to: 21/02/2009	**Date of report:** 15/12/2009
Shifts: 9	**Local contact(s):** Dr. Nicole Jeutter	*Received at ESRF:*

Names and affiliations of applicants (* indicates experimentalists):

Dr. Kräußlich, Jürgen * [1)]
Zastrau, Ulf * [1)]
Höfer, Sebastian * [1)]
Dr. Baehtz, Carsten *
Dr. Jeutter, Nicole *
Prof. E. Förster [1)]

[1)] Friedrich Schiller University of Jena
Institute of Optics and Quantumelectronics
Max-Wien-Platz 1
07743 Jena
Gemany

Report **16/12/2009**

Temperature dependence of lattice parameters of langasite single crystals ($La_3Ga_5SiO_{14}$)

J. Kräußlich, S. Höfer, U. Zastrau, C. Baehtz

Aims of the experimental and scientific background

Due to its outstanding piezoelectric properties, langasite ($La_3Ga_5SiO_{14}$) is a very suitable material for high-effective SAW filters in modern information and communication technology. Currently, it is possible to grow large langasite single crystals up to 3 inches in diameter [1,2]. Further potential applications using langasite single crystals are focused to pressure or temperature sensor devices operating at high temperatures up to 1200°C. The high-temperature applications presume that the langasite does not show any phase transformation before melting at about 1475°C. For the characterisation of the high temperature behaviour a precise knowledge of the thermal expansion is required.

Experimental method

Using the X-ray diffraction we measured the temperature dependence of the two significant lattice parameter ***a*(T)** and ***c*(T)** of the trigonale langasite single crystals belonging to crystallographic space group P321. With a specially prepared substrate orientation (Fig. 1, 2) it is possible to measure the two parameters ***a*(T)** and ***c*(T)** independently of each other and from the same single crystal area. The asymmetric reflections (000 6) and (10 -1-1 0) are well suitable to determine the lattice parameters ***a*** and ***c***, independently of each other. With the Bragg angle $\Theta_{(hkil)}(T)$ which has to be measured we have the relation:

$$(1) \quad \lambda = 2d_{(hkil)}(T)\cdot\sin(\Theta_{(hkil)}(T)) \rightarrow 2d_{(hkil)}(T) \rightarrow \boldsymbol{a}(T) \text{ bzw. } \boldsymbol{c}(T)$$

The measurements were carried out using the new material research goniometer of the CRG[1] Beamline ROBL[2] located at the bending magnet BM20 of the ESRF[3] in Grenoble. The goniometer was equipped with an evacuable high-temperature chamber, which permits in-plane and out-of-plane measurements because of its spherical beryllium dom. Temperatures up to 1400°C are attainable. All our measurements were realized with a X-ray wavelength $\lambda = 0.15407(5)$ nm.

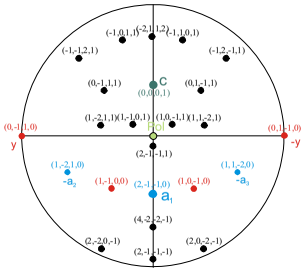

Fig. 1: Stereographic projection of the trigonal langasite. The pole and orientation is given by a temperature reduced influence surface. The four-indexing is used because of the threefold symmetry.

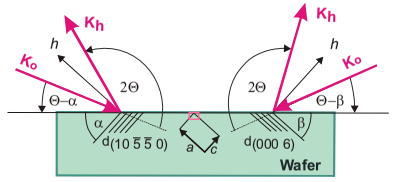

Fig. 2: Schematic for the X-ray diffraction measurement of ***a*(T)** and ***c*(T)** independently of each other and from the same single crystal area □. $\alpha + \beta = 90°$.

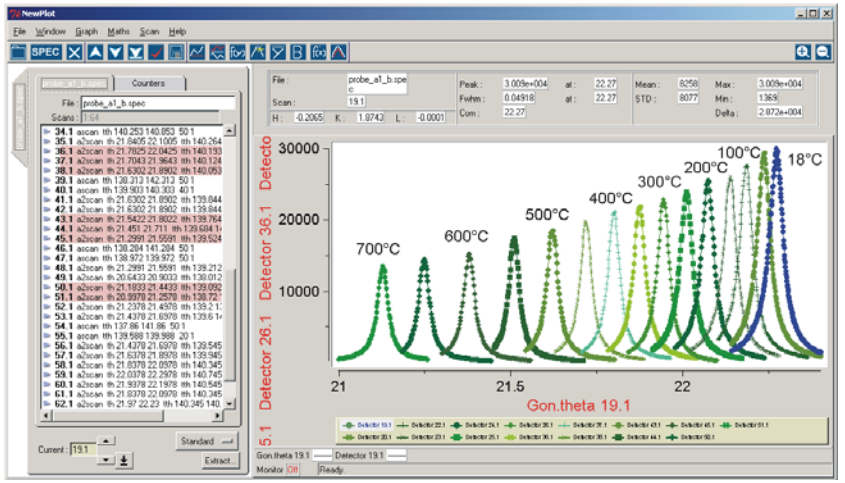

[1] **C**ollaborating **R**esearch **G**roup
[2] **Ro**ssendorf **B**eam**l**ine (Forschungszentrum Dresden Rossendorf)
[3] **E**uropean **S**ynchrotron **R**adiation **F**acility

Fig. 3: X-ray diffraction rocking curves of the asymmetric (10-5-5 0)-reflection in dependence of the sample temperature. The decreasing of the intensity with the increasing of the temperature is to be due to the Debye-Waller factor.

Results

The lattice parameters ***a*** and ***c*** of the trigonal langasite single crystals determined from the measured Bragg angle Θ(T) are plotted against the temperature (Fig. 4 and 5). Their nonlinear behaviour can be described well with equations of second order.
It should be note that measurements at temperatures above 800°C could not be realized because the single crystal sample became instable regarding its shape.

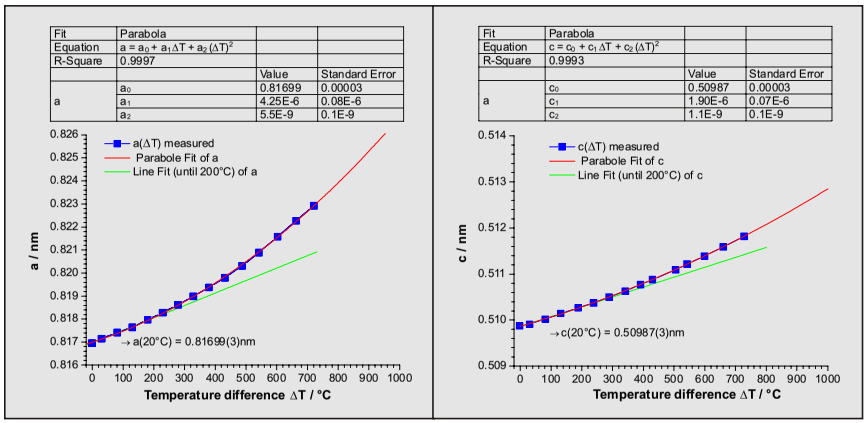

Fig. 4: The lattice parameter ***a*** and ***c*** of the langasite single crystals plotted against the temperature difference ΔT=T-20°C

For temperatures T expressed in °C, we have the following relation of the temperature-dependent lattice parameters ***a*** and ***c***

$$(2) \qquad \begin{aligned} \boldsymbol{a}(T\text{-}20) &= \boldsymbol{a}_{20°C}\left(1+\alpha_{11}(T\text{-}20)+\beta_{11}(T\text{-}20)^2\right) \\ \boldsymbol{c}(T\text{-}20) &= \boldsymbol{c}_{20°C}\left(1+\alpha_{33}(T\text{-}20)+\beta_{33}(T\text{-}20)^2\right) \end{aligned}$$

α_{ii} , β_{ii} - linear and quadratic coefficient of thermal expansion, respectively
$\boldsymbol{a}_{20°C}$, $\boldsymbol{c}_{20°}$ - lattice parameter ***a*** and ***c*** for 20°C, respectively

The numeric values of the linear and quadratic thermal expansion coefficients obtained from the best fit are given in Table 1.

Thermal expansion of langasite single crystals ($La_3Ga_5SiO_{14}$)		
lattice parameter at 20°C	$\boldsymbol{a}_{20°C}$ = 0.81699(3)nm	$\boldsymbol{c}_{20°C}$ = 0.50987(3)nm
linear thermal expansion coefficient	α_{11} = 5.20(8)·10^{-6} K^{-1}	α_{33} = 3.72(8)·10^{-6} K^{-1}
quadratic thermal expansion coefficient	β_{11} = 6.7(1) 10^{-9} K^{-2}	β_{33} = 1.1(1) 10^{-9} K^{-2}

Table 1: Parameter of the thermal expansion of langasite single crystals

We thank all members of the ROBL beamline team, especially Dr. C. Baehtz and Dr. N. Jeutter for all the helpful support during the time executing this experiment.

References

[1] S.Uda, O.Buzanov: "Growth of a 3'' Langasite crystal with clear faceting"; Journal of Crystal Growth **211 (2000) 318-324**
[2] S. Uda, S.-Q. Wang, N. Konishi, H. Inaba and J. Harada: Growth technology of piezoelectric Langasite single crystal; Journal of Crystal Growth **275 (2005) 251-258**
[3] W. Matz, N. Schell, G. Bernhardt, F. Prokert, T. Reich, J. Claussner, W. Oehme, E. Eichhorn, M. Betzl, D. Pröhl, U. Strach, R. Reicherl, M. Denecke and H. Nitsche: ROBL – a CGR beamline for radiochemistry and materials research at the ESRF, J. Synchrotron Rad. **6** 1076 (1999)

ESRF	**Experiment title:** Combined in-situ XRD and Electrical Resistivity Study of the Phase Transformations in Ni-Ti SMA	**Experiment number:** MA- 895
Beamline: BM 20	**Date of experiment:** from: 12.02.2010 to: 16.02.2010	**Date of report:** 27.02.2011
Shifts: 12	**Local contact(s):** Carsten Baehtz, Nicole Martha JEUTTER	*Received at ESRF:* **27.02.2011**

Names and affiliations of applicants (* indicates experimentalists):

F.M. Braz Fernandes*, Rui J. C. Silva*, K. K. Mahesh*: CENIMAT/I3N-Centro de Investigação de Materiais, Campus da FCT/UNL, 2829-516 Monte de Caparica, PORTUGAL
J. von Borany*, Carsten Baehtz*, Nicole Jeuter*: FZD, P.O. Box 510119, 01314 Dresden, GERMANY

REPORT:

The proposal for the experimental session was drafted with a view to approach a combination of characterization techniques, wherein, the acquisition of the X-ray diffraction (XRD) and the electrical resistivity (ER) measurement will be made during the thermal induced phase transformations in Ni-Ti shape memory alloys (SMAs).

Specimen were mounted on the 6-circle goniometer. ER measurement was carried out by employing HL5500 Hall system. Electrical probes are contacted with the specimen in Vander Pauw configuration as shown in Fig. 1. X-ray energy is set to 11.5keV.

Samples S32 (Ni-Ti thin film (~ 720 nm thick) on SiO_2/Si(100) from ME-1087, April, 2005) and S23 (Ni-Ti thin film (~ 800 nm thick) on SiO_2/Si(110) from ME-936, Feb, 2005) specimens were tested. During the periods of experiments with both the specimens, unexpected beam instabilities had come across together with alignment of the optics of the beamline. Hence, the experiments with both specimens remained inconclusive.

On the final day, when the beam was stable and optics was set, sample S40 (Ni-Ti thin film ~ 1450 nm thick, on MgO(110), from ME1255, Feb, 2006) was chosen for the study. The specimen was heated to 100ºC. XRD scanning were performed in the range $25^\circ < 2\theta < 34^\circ$ at selected temperatures to track the phase transformation until -99ºC. Again, while heating, diffractions were registered in the predetermined temperatures. Simultaneously, ER values were noted both while cooling and heating. In Fig. 2, XRD profiles obtained at selected temperatures while cooling and, ER profile both while cooling and heating are shown. From the XRD profiles, it can be observed that the diffractograms corresponding to the temperatures while cooling from 70 to 40 ºC possess a single peak at $2\theta = 29.2^\circ$ attributed to B2(110). For the diffractogram obtained at 20 ºC, this peak splits into R(112), at $2\theta = 29.1^\circ$, and R(300), at $2\theta = 29.4^\circ$. Together with this, other peaks also appear corresponding to M-phase. As the cooling is continued below – 30 ºC, the diffractograms are found to possess the peaks corresponding to M-phase.

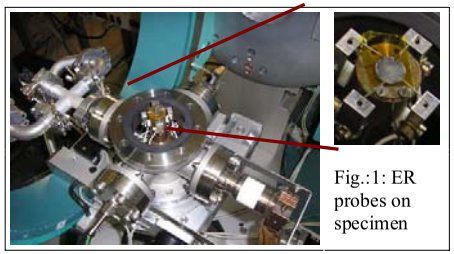

Fig.:1: ER probes on specimen

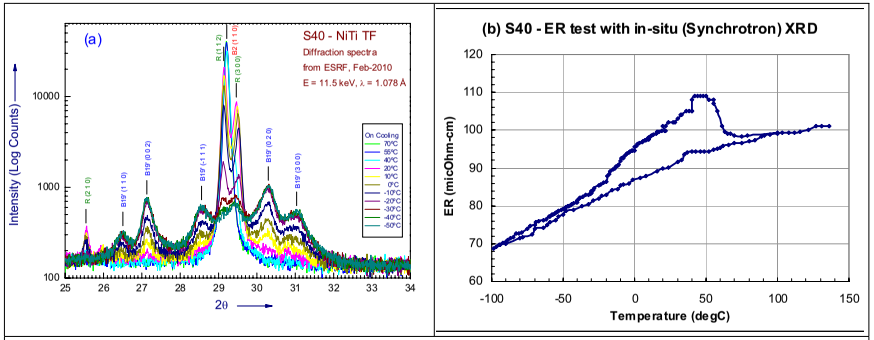

Fig. 2: (a) XRD profiles obtained at selected temperatures while cooling and, (b) ER profile both while cooling and heating

In the ER profile shown in Fig. 2(b), as the temperature is decreased, ER is observed to decrease followed by increase around 60 ºC associated with A→R phase transformation. On further cooling, the ER increases to have a plateau corresponding, followed by a decrease with cooling associated with R→M phase transformation. While heating, ER is increased with increase in temperature up to around 30 ºC followed by a sudden increase corresponding to M→A phase transformation.

In Fig. 3, main parameters, such as, (a) full width at half measure (FWHM) and (b) Integrated Area (IA), obtained from the diffractogram peaks corresponding to B2(110), R(112), R(300) and R(210) are presented. It is observed that the peaks corresponding to R-phase can be traced even at temperature of 40ºC. When the phase transformation nature in the ER profile is compared with the XRD profiles, it is clear that ER detects R-phase transformation well before, than by XRD, at around 60 ºC and R→M phase is observed around 40 ºC. Further, the presence of A-phase is not observed below 10ºC. From IA observation in Fig. 3(b), R-phase is found to be more prominent in the temperature range between 20 and – 10 ºC. In the ER curve, R-phase transformation is more prominent in the temperature range between 55 and 40 ºC.

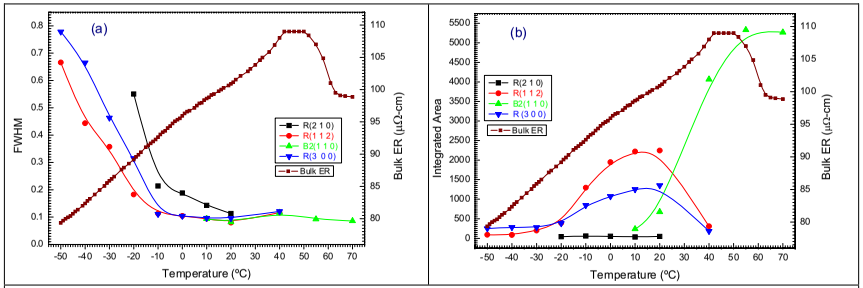

Fig. 3: (a) Full Width at Half Maximum (FWHM) and (b) Integrated Area values obtained from the diffractogram peaks corresponding to B2(110), R(112), R(300) and R(210) while cooling.

Conclusions

From the above observations, it can be concluded that ER technique is more sensitive to the early stages of the phase transformations. However, with the information from the XRD profiles, quantitative estimation of the presence of phases over a temperature range can be made. It is foreseen that the combined analyses of the data obtained would lead to quantitative input into the knowledge of the phase transformation behaviour in Ni-Ti shape memory alloys.

ESRF	**Experiment title:** In-situ time-resolved diffraction of phase formation during annealing of amorphous and hydrogenated Mg-Ni-Y alloys	**Experiment number:** MA – 896
Beamline: BM20	**Date of experiment:** from: 18.09.2010 to: 22.09.2010	**Date of report:** 03.03.2010
Shifts: 9	**Local contact(s):** Dr. Carsten Bähtz (carsten.baehtz@esrf.fr)	*Received at ESRF:*

Names and affiliations of applicants (* indicates experimentalists):

Lars Röntzsch* (Fraunhofer Institute for Manufacturing Technology and Applied Materials Research, Winterbergstraße 28, 01277 Dresden, Germany)

Siarhei Kalinichenka* (Institute for Materials Science, Dresden University of Technology, Helmholtzstraße 7, 01069 Dresden, Germany)

Report:

The main part of the results reviewed in the present report has been already published in the Journal of Alloys and Compounds [1]. During the experiments at BM20 two rapid solidificated magnesium-rich alloys ($Mg_{90}Ni_{10}$ and $Mg_{80}Ni_{10}Y_{10}$) were investigated. As it was shown recently [2] this systems are very suitable for the reversible solid-state storage of hydrogen, but detailed understanding of recrystallization of amorphous phase as well as of sorption mechanisms is needed. For this reason the main focus of investigations at BM20 was set on the recrystallization behavior of the melt-spun alloys and on the study of the desorption properties of hydrogenated alloys using in-situ synchrotron X-ray diffraction. The incident X-ray beam with an X-ray wavelength of 1.05Å was used for investigation in the scanning range of the diffraction angle between 10° and 35° (2Θ) in reflection geometry.

Recrystallization behavior of melt-spun amorphous Mg-Ni and Mg-Ni-Y

The recrystallization behavior of melt-spun amorphous Mg-Ni and Mg-Ni-Y was studied under different atmospheres (Ar, H_2 and vacuum). The SR-XRD results were compared with the corresponding results obtained by DSC measurement (Fig. 1). Fig 2. shows the evolution of the in-situ SR-XRD of melt-spun Mg-Ni at different temperatures under argon atmosphere. The recrystallization of the amorphous structure starts with nucleation and growth of Mg grains at 125°C. The metastable cubic Mg_6Ni Phase already occurs at 125°C and is decomposed at TA > 200°C into Mg and Mg_2Ni [3,4]. For this system the effect of the different atmospheres was not significant. The result of recrystallization behavior of melt-spun Mg-Ni-Y is more complicated and will be published later.

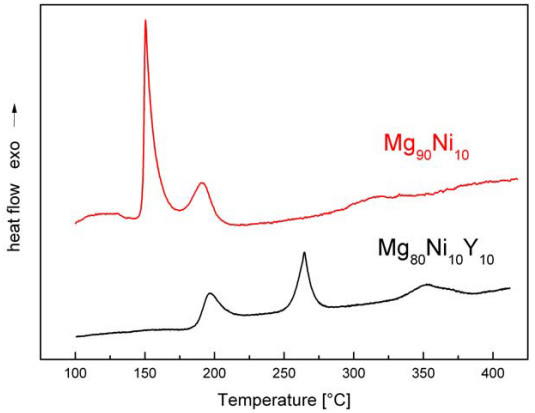

Fig. 1 DSC curves of melt-spun $Mg_{90}Ni_{10}$ and $Mg_{80}Ni_{10}Y_{10}$ (5 K/min, argon).

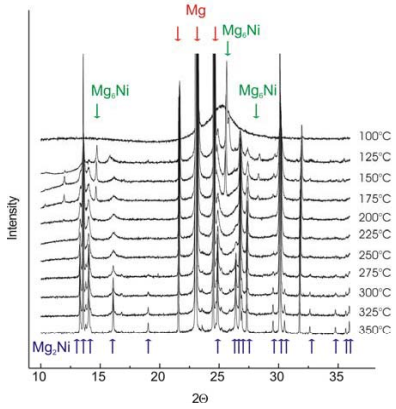

Fig. 2 Evolution of the in-situ SR-XRD pattern of the as spun $Mg_{90}Ni_{10}$

Heat treatment of hydrogenated Mg-Ni and Mg-Ni-Y ribbons under vacuum in the Be-dome annealing chamber

Fig. 3 shows the evolution of the in-situ SR-XRD pattern of the as spun and hydrogenated $Mg_{90}Ni_{10}$ during its vacuum thermal decomposition at 200°C. The X-ray diffraction pattern at t=0 min represents the X-ray diffraction pattern of hydrogenated $Mg_{90}Ni_{10}$ at ambient temperature. The heating to 200°C was carried out within the first 4 minutes. During the dehydrogenation of $Mg_{90}Ni_{10}$ two separate processes were identified: desorption of Mg_2NiH_4 to $Mg_2NiH_{0.3}$ and desorption of MgH_2 in the presence of $Mg_2NiH_{0.3}$. The reaction rates are rather different: the dehydrogenation rates for High-Temperature- and Low-Temperature-Mg_2NiH_4 at 200°C in vacuum (10^{-2} mbar) are in the range of 0.2 wt.% H_2/min while for MgH_2 it could be calculated as 0.1 wt.% H_2/min [1]. The improved kinetics of hydrogen desorption for Mg-Ni can be explained by the presence of $Mg_2NiH_{0.3}$ as the active catalyst phase. Unexpectedly, in-situ SR-XRD investigations of the thermal decomposition of $Mg_{80}Ni_{10}Y_{10}$ revealed that no formation of $Mg_2NiH_{0.3}$ is observed in this case during the dehydrogenation (Fig. 4). The reason for this behaviour may be explained by the fact that yttrium can be solved in Mg_2Ni causing a lattice parameter expansion. For more detailed results, including the results of Rietveld analysis (phase abundance and lattice parameters) and TGA results please see [1].

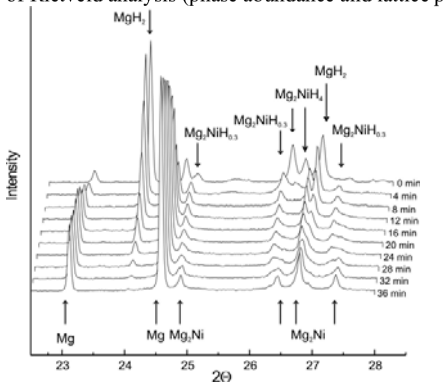

Fig. 3: Evolution of the in-situ SR-XRD pattern of the as spun and hydrogenated $Mg_{90}Ni_{10}$ during its vacuum thermal decomposition at 200°C (pressure: 10^{-2} mbar).

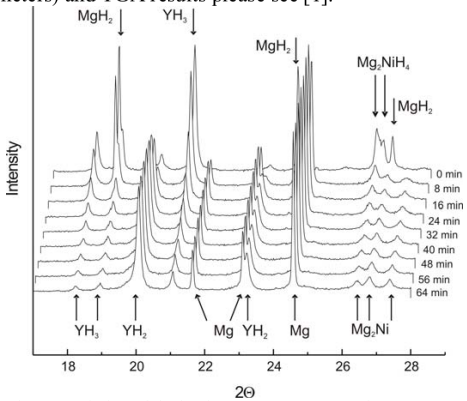

Fig. 4: Evolution of the in-situ SR-XRD pattern of hydrogenated $Mg_{80}Ni_{10}Y_{10}$ during its vacuum thermal decomposition at 200°C (pressure: 10^{-2} mbar).

Conclusion

In order to understand the phase transformations and the dehydrogenation reactions of the melt-spun Mg-Ni(-Y), the recrystallization and desorption properties were studied by in-situ synchrotron X-ray diffraction performed at the Rossendorf Beamline (BM20) of the ESRF.
Primarily, the results of desorption mechanisms of hydrogenated Mg-Ni and Mg-Ni-Y reveal interesting differences in the investigated systems (Fig. 3 and 4). It was found that the kinetics of H-desorption is controlled by the two-step hydrogen desorption process in case of Mg-Ni. In the case of $Mg_{80}Ni_{10}Y_{10}$ no formation of the $Mg_2NiH_{0.3}$ phase was observed
The results of these investigations have been published in the Journal of Alloys and Compounds [1].

Acknowledgement

The authors would like to acknowledge financial support of the European Synchrotron Radiation Facility.

References

[1] S. Kalinichenka, L. Rontzsch, C. Baehtz, B. Kieback, Hydrogen desorption kinetics of melt-spun and hydrogenated $Mg_{90}Ni_{10}$ and $Mg_{80}Ni_{10}Y_{10}$ using in-situ synchrotron, X-ray diffraction and thermogravimetry, *J Alloys Comp*, In Press, Accepted Manuscript, Available online 24 February 2010, ISSN 0925-8388, DOI: 10.1016/j.jallcom.2010.02.128 .

[2] S. Kalinichenka, L. Röntzsch, B. Kieback, Structural and hydrogen storage properties of melt-spun Mg–Ni–Y alloys, Intl.J. Hydrogen Energy 34 (2009) 7749.

[3] T. Spassov, St. Todorova, V. Petkov, Kinetics of Mg6Ni nanocrystallization in amorphous Mg83Ni17, Journal of Non-Crystalline Solids, Volume 355, Issue 1, 1 (2009) 1

[4] A. Teresiak, M. Uhlemann, J. Thomas, A. Gebert, The metastable Mg~6Ni phase—Thermal behaviour, crystal structure and hydrogen reactivity of the rapidly quenched alloy, *J Alloys Comp*, Volume 475, Issues 1-2, 5 (2009) 191.

ESRF	**Experiment title:** Concurrent Effect of Melt-spinning and Severe Plastic Deformation on Shape Memory Alloy Ribbons by Simultaneous XRD and Electrical Resistivity Measurements	**Experiment number:** MA- 1019
Beamline: BM 20	**Date of experiment:** from: **19.06.2010** to: **22.06.2010**	**Date of report:** 31.01.2010
Shifts: 9	**Local contact(s):** **Carsten Baehtz, Nicole Jeuter**	*Received at ESRF:* **dd.mm.yyyy**

Names and affiliations of applicants (* indicates experimentalists):
C.M. Craciunescu*, F.M. Braz Fernandes*, K. K. Mahesh*: CENIMAT-Centro de Investigação de Materiais, Campus da FCT/UNL, 2829-516 Monte de Caparica, PORTUGAL
Carsten Baehtz *, Nicole Jeuter*: FZD, P.O. Box 510119, 01314 Dresden, GERMANY

REPORT:

The experiments have been performed on the TiNiCu shape memory alloy ribbons, in the as cast (AC), severely deformed: as mild (MSPD) and very (VSPD) deformed, and VSPD and annealed (VSPDA) state. The experiments were made in the beryllium dome, with the electric resistance vs temperature (ER) measurements performed using a Keythley 2010 multimeter. The heating and cooling was performed between – 100 and + 150 ^{o}C. The shape memory alloy ribbons have been mounted on silicon wafers and insulated using kapton foil. Not all the experiments on ER were successful, but it has been proven that the equipment can be use in conjunction with the XRD to identify the onset of the phase transition and to adjust the temperature interval between two measurements according to the development of the phase transition.

EXPERIMENTAL

The results for the TiNiCu ribbon in the AC state are shown in fig.1. A single cubic (B2)→ orthorhombic (B19) reversible phase transition is detected on heating and cooling, for both the XRD and the ER spectra. The results are in the expected behavior of the TiNiCu ribbons in the high Cu compositional range.
The MSPD samples also show the B2→ orthorhombic B19 phase transition, but the ER signal is noisier (fig. 2 a-b). Based on the ER signal, there is no major difference between the as cast and MSPD state, in terms of the phase transition.
The influence of the severe plastic deformation based on RT scans is detailed in fig. 3a-c. The ER results are not reliable, in part for the fact that the samples are small (in width) ribbons and it is difficult to provide an adequate contact for the four probe measurement.

Conclusions

The use of the simultaneous XRD and ER measurements proved to be a usefull tool for the investigation of the shape memory alloy ribbons. One of the reasons for the noise that appeared amplified by the degree of inhomogenties on the surface of the investigated samples, in the transformation temperature range, can be related to the relative movement between the ribbon samples and the ER connecting pins. The deformed samples have rougher surface and relative slipping between the ER contacts and the sample can occur in a discontinuous manner.

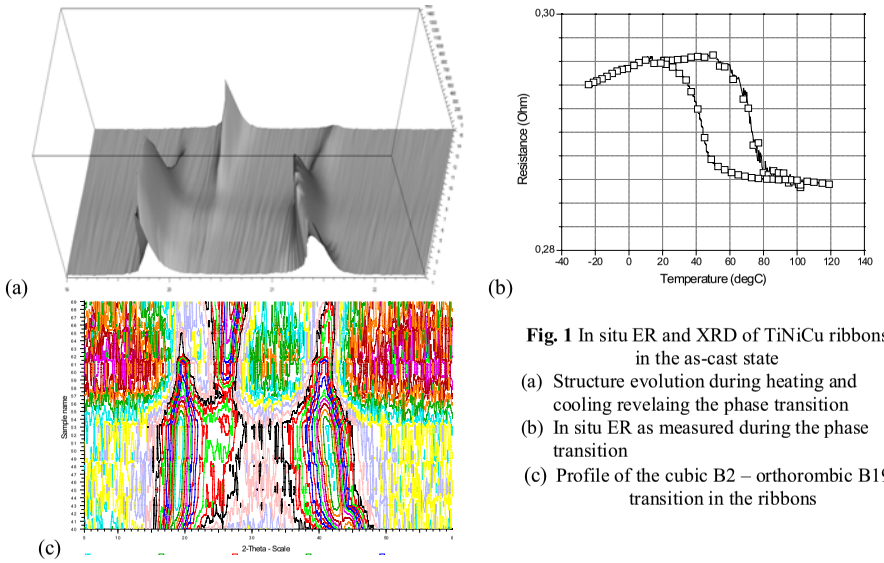

Fig. 1 In situ ER and XRD of TiNiCu ribbons in the as-cast state
(a) Structure evolution during heating and cooling revelaing the phase transition
(b) In situ ER as measured during the phase transition
(c) Profile of the cubic B2 – orthorombic B19 transition in the ribbons

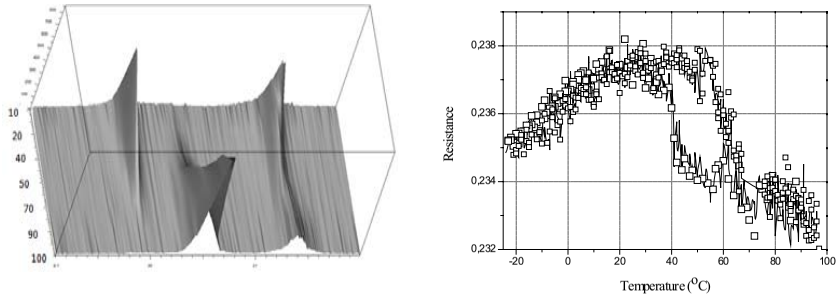

Fig. 2 In situ XRD (left) and ER(right) vs temperature scans for the as MSPD sample

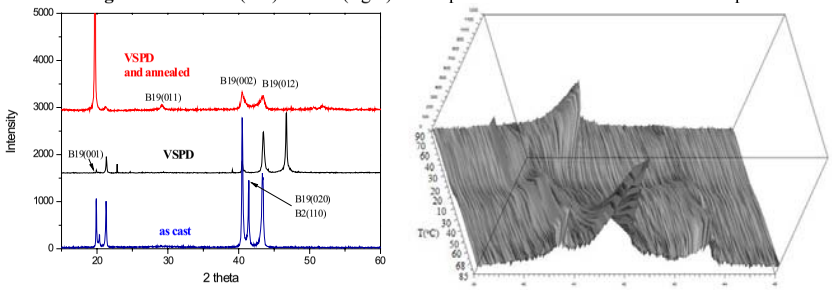

(a) influence of deformation and annealing for the AC, VSPD and VSPDA samples
(b) structural evolution during heating and cooling of the VSPDA sample

Fig. 3 Structural changes as a function of the deformation state for the Ti-Ni-Cu ribbons

ESRF	**Experiment title:** Microstructure design of electrodeposited GMR multilayers via annealing	**Experiment number:** MA-1148
Beamline: BM20	**Date of experiment:** from: 16.12.2010 to: 20.12.2010	**Date of report:** 28.01.2011
Shifts: 12	**Local contact(s):** Carsten Baehtz	*Received at ESRF:*

Names and affiliations of applicants (* indicates experimentalists):

Torsten Schucknecht*, Ulrike Ratayski*, Christian Schimpf*, David Rafaja

TU Bergakademie Freiberg, Institute of Materials Science, Gustav-Zeuner-Str. 5, 09599 Freiberg, Germany

Report:

The aim of the experiment was the in situ investigation of the effect of the thermal treatment on the microstructure of electrodeposited (ED) Co/Cu multilayers (MLs) with GMR effect. A series of samples with constant layer thickness was deposited using the single bath method under different current densities. The current density is expected to affect strongly the amount of copper codeposited during the deposition of cobalt and consequently the microstructure of the ED MLs. As in situ methods, symmetrical WAXS and EXAFS were used. WAXS described the microstructure evolution during annealing; EXAFS revealed details on intermixing of the codeposited species.

The isothermal WAXS measurements showed a high thermal stability of the ED MLs up to 200°C. In samples prepared at high current densities, copper segregated after annealing at temperatures exceeding 350°C as seen on the formation of a distinct diffraction line from Cu in Fig. 1a. This was accompanied by an improvement of the multilayer satellites these samples. The samples deposited at low current densities contained hdp Co, which disappeared during the annealing up to 500°C (Fig. 1b) and did not occurred more upon cooling.

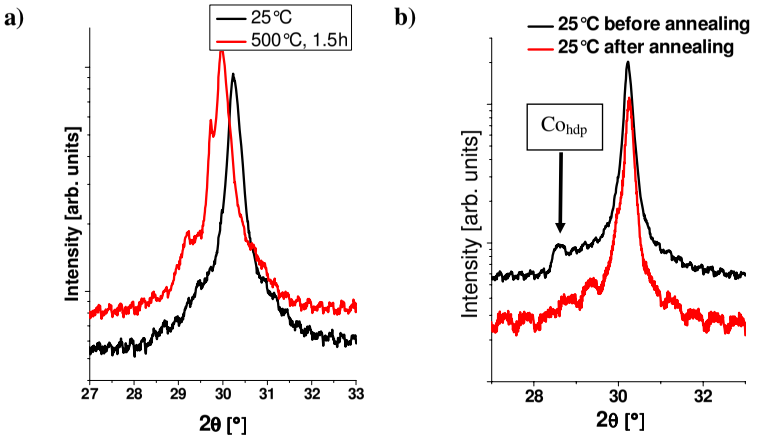

Fig. 1: a) sample deposited using a high current density in the initial state (black) and after 85 minutes at 500°C (red) – the shift of the peaks is due to the thermal expansion b) sample deposited at low current density before (black) and after (red) the heat treatment, the arrow indicates the position of the (100)-Co$_{hdp}$ The periodic, wavelike intensities are an artefact of the line detector.

Selected samples were subjected to EXAFS measurements. The intention of these measurements was to describe the local chemical environment of Co and to identify the intermixing or decomposition effects. All samples were measured at the Co-Kβ edge (7700 eV). The background absorption $\mu_0(E)$ has been removed using the *Athena* program; the Fourier transform $\chi(E)$of the absorption fine structure was loaded into the *Artemis* program. Both programs are included in the IFeffit package. The analysis of the data was done using the 'model for doped materials' explained by B. Ravel at the 2001 EXAFS workshop [1]. This model calculates the intermixing parameter *x*. Several other parameters like the relative displacements ΔR of the first neighbours of the absorbing Co atom were used for refinement as well. The resulting fits are shown in Fig. 2. In the sample deposited at high current density (j = 84 mA/cm²), Co is surrounded mainly by Co (x = 0.14). Due to a larger atomic radius of Cu as compared to Co, Cu atoms are shifted in outward direction with respect to the original cell. An opposite shift was observed for Co. The annealing leads to an intermixing of Co and Cu until a random distribution around the Co absorber is achieved (x = 0.57). The intermixing is expected to occur as substitutional occupation of the Wyckoff positions of the fcc cell by Co and Cu, which can be the cause of the vanishing displacement

(ΔR) of Co and Cu for the annealed sample. Lower current deposition density (j = 16 mA/cm²) leads to enhanced intermixing of Co and Cu ($x = 0.32$). The opposite displacement of Co and Cu persists.

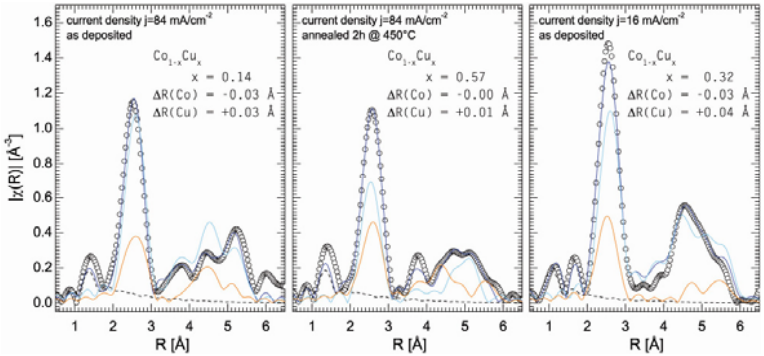

Fig. 2: Results of the fitting of EXAFS spectra measured for Co-Cu multilayers deposited at high deposition current density, the same sample after annealing and a sample deposited at low deposition current density. Results are given in the text. The dots represent experimental data, blue line the resulting fit, cyan line the Co contribution, orange line the Cu contribution and dashed line the background

[1] http://leonardo.phys.washington.edu/~ravel/talks/course/notes.pdf

ESRF	**Experiment title:** Influence of codoping on nanocrystal formation in GaFeN	**Experiment number:** SI-1797
Beamline: BM 20	**Date of experiment:** from: 25/02/2009 to:03/03/09	**Date of report:** 30/09/2009
Shifts: 12	**Local contact(s):** Nicole Jeutter	*Received at ROBL:*

Names and affiliations of applicants (* indicates experimentalists):
R.T. Lechner*[1], V. Holy[2], A. Bonnani[1] and G. Bauer[1]

[1] Institut fuer Halbleiterphysik, Johannes Kepler Universitaet Linz, Altenbergerstrasse 69, A-4040 Linz, Austria
[2] Charles University, Faculty of Mathematics and Physics, Ke Karlovu 5, 12116 Prague, Czech Republic

Report:

Transition metal doped III-V compounds offer an unprecedented opportunity to explore ferromagnetism in semiconductors. Because ferromagnetic spin-spin interactions are mediated by holes in the valence band, changing the Fermi level using co-doping, can directly manipulate the magnetic ordering. The Fermi energy can even control the aggregation of magnetic ions, providing a new route to self-organization of magnetic nanostructures in a semiconductor host [1].

Recent work on GaFeN samples codoped with Si has given evidence of the possibility of Fermi-level engineering in this material system [2]. The co-doping of GaFeN with acceptors is of great interest due to the fact that acceptor impurities like Mg increase the density of holes. It is believed that these holes change the charge state of the iron-ions from Fe^{3+} to Fe^{4+}. The increased electrostatic repulsion of the Fe^{4+} ions should hinder the formation of both coherent Fe-rich inclusions in the GaN lattice as well as the growth of Fe-rich precipitates. Furthermore a systematic study of the influence of growth temperature on the precipitation of the Fe-rich phases observed in GaFeN is desired. For this purpose two GaFeN samples series were measured in coplanar geometry at BM20 using a photon energy of 10 keV. Long radial scans from 5° to 40° in $\omega/2\theta$ were performed on each sample. In first series in Fig. 1(a) only the substrate temperature during growth was varied.

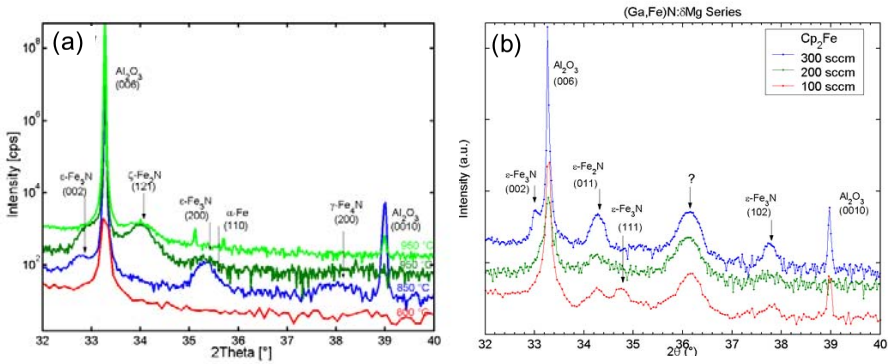

Fig. 1: (a) Radial ($\omega/2\theta$) scans of GaFeN samples as a function of growth temperature**. (b)** XRD spectra of a GaFeN:Mg sample series with constant Mg flux, but varying Fe flux.

The sample grown at 850°C shows two diffraction peaks from the ferromagnetic (FM) wurzite ε-Fe_3N, which had already been reported before [3, Exp.Rep. SI-1633]. One additional peak, however, could be detected, which can be related to the γ'-Fe_4N phase. This is an evidence that FeN precipititates can be formed in different crystallographic phases, whereas the formation process can be influenced by adjusting the growth conditions, such as the substrate temperature. At 800°C no indication of precipitate formation is observed, where as at 950°C only one precipitate peak is observed related to the ζ-Fe_2N phase. This phase had not been observed in a previous experiments.

In the second series the temperature (950°C) and the flux of the co-dopant Mg was kept constant, and only the Fe flux was altered (see Fig. 1 (b)). In this way, different Mg co-doping levels during the precipitate formation could be realised. We have evidenve that the formation of Fe precipitates is not hinderd by the co-doping with Mg as for the case of Si co-doping. Actually, Mg even *enhances* the formation of precipitates even at very low Fe source flows of 100 sccm. This will be a topic for detailed future investigations. One diffraction peak could not yet be identified, but is most probably related to an Fe-Mg alloy. The measurements on the influence of growth temperature performed during beam time SI1797 are under analysis and will soon be submitted for publication.

References: [1] T. Dietl, Nature Materials **5**, 673 (2006).
[2] M. Rovezzi *et al.* Phys. Rev. B. **79,** 195209(2009)
[3] A. Bonnani et al., Phys.Rev.Lett **101**, 135502 (2008)

ESRF	**Experiment title:** **Investigation of Ge quantum dots ordering in Ge+SiO2 multilayers**	**Experiment number:** SI-1980
Beamline: BM20	**Date of experiment:** from: 09.12.2010 to: 14.12.2010	**Date of report:** 17.02.2010
Shifts: 18	**Local contact(s):** Nicole Jeuter	*Received at ESRF:*

Names and affiliations of applicants (* indicates experimentalists):

*Maja Buljan, Department of Condensed Matter Physics, Charles University in Prague, Czech Republic and Ruđer Bošković Insitute Zagreb, Croatia
*Nikola Radić, Ruđer Bošković Institute Zagreb, Croatia
*Jörg Grenzer, Forschungszentrum Dresden Roßendorf, Germany
*Václav Holý, Department of Condensed Matter Physics, Charles University in Prague, Czech Republic

Report:

In our previous works [1,2] we have investigated the nucleation, growth and crystallization of Ge nanoclusters in amorphous SiO_2 matrix. We have demonstrated that originally amorphous Ge clusters crystallize during post growth annealing creating crystalline quantum dots. Moreover, in Ge+SiO_2/SiO_2 multilayers we found that the positions of the quantum dots are correlated creating a well developed rhombohedral lattice. We have explained this self-organization process by the influence of the morphology of the growing surface on the diffusion of Ge adatoms during the growth.

In order to prove this idea, we have investigated in-situ the nucleation and growth of Ge nanoclusters in Ge+SiO_2/SiO_2 multilayers deposited on quasiperiodically corrugated surfaces. The substrates were produced by the ion beam erosion of Si(100) wafers creating quasiperiodic ripples, the AFM image of the ripples is shown in Fig. 1. We have chosen the parameters of the ion erosion so that the resulting ripple period (19±2) nm was close to the "intrinsic" distance of Ge nanoclusters on a flat substrate.

The rippled Si surface was used as a substrate for the deposition of the Ge+SiO_2/SiO_2 multilayer. We deposited 5 bilayers Ge+SiO_2/SiO_2 using dual (AC/DC) magnetron sputtering, the substrate temperature was 400°C and the Ge:SiO_2 molar ratio was approximately 75:25 in the mixed layers. After the deposition of each bi-layer we measured a grazing incidence small angle X-ray scattering (GISAXS) intensity map. The probing x-ray beam was directed parallel to the ripples direction, so that the intensity distribution measured in the reciprocal plane perpendicular to the primary beam reflects a spatial correlation of the ripple positions and the influence of the periodicity of the ripples on the correlation of the positions of the growing Ge nanoclusters .

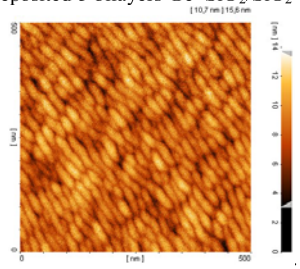

GISAXS maps were measured for two incidence angles of the probing beam, i.e. at the critical angle and slightly above it. In the former case we see mainly scattering from the surface, while in the latter the beam penetrates into the deposited film (Fig. 2). All maps exhibit strong lateral satellites stemming from the ripple periodicity, these satellite maxima are elongated vertically and their height along q_z is inversely proportional to the ripple depth. The strongest satellites are visible for the substrate and their periodicity corresponds to the ripple period of 19 nm. The GISAXS maps taken with the critical incidence angle after the growth of individual bilayers (Fig. 2(a)) are rather similar to that of a naked rippled substrate, which indicates that the morphology of the rippled substrate is replicated during the growth. The surface of each newly deposited layer contains ripples with a very similar geometrical arrangement. However, the degree of spatial correlation between ripple positions decreases during the deposition, since the lateral satellites become less pronounced.

For the examination of the inner structure of the film, the probing beam with a higher incidence angle was used (Fig. 2(b)). The resulting GISAXS maps exhibit vertical satellite maxima indicating that the local morphologies of the interfaces of different layers are correlated. This correlation might be described as a roughness correlation using standard models, or as a correlation of the positions of Ge nanoclusters. A detailed numerical comparison of the measured intensity distributions with the intensities following from these two structural models is necessary in order to confirm unambiguously the presence of the correlation of the positions of the nanoclusters induced by the ripples underneath, this work is underway.

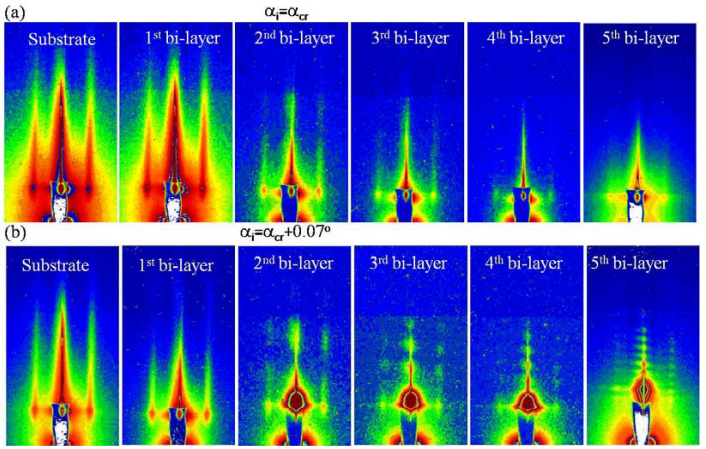

Fig.2. GISAXS maps measured in-situ during deposition of (Ge+SiO_2)/SiO_2 multilayer. (a) The surface contribution, the incidence angle equals critical angle, (b) the contribution coming mainly from the film volume, the incidence angle of probing beam was slightly above the critical angle.

After the deposition the film was annealed in vacuum up to 800°C and the GISAXS maps were measured in-situ after each 100°C step in the annealing sequence starting from 600°C (Fig. 3). All maps are very similar showing that the layers keep their morphology during the annealing. With increasing annealing temperature, the overall GISAXS intensity increases indicating that the contrast in the electron densities in the clusters and the surrounding increases.

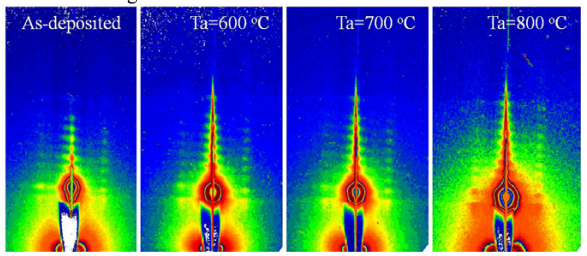

Fig.3. GISAXS maps measured in-situ during annealing of the deposited multilayer.

[1] M. Buljan et al., Phys. Rev. B **79**, 035310 (2009).
[2] M. Buljan et al., Nanotechnology **20**, 085612 (2009).
[3] A. Keller, R. Cuerno, S. Facsko, W. Moller, Phys. Rev. B **79**, 115347 (2009).

ESRF	**Experiment title:** In-situ x-ray diffraction investigation of growth of ferromagnetic clusters in (Ga,Mn)N epitaxial layers	**Experiment number:** SI-1981
Beamline: BM 20	**Date of experiment:** from: 23/09/2009 to:03/00/09	**Date of report:** 24/02/2010
Shifts: 18	**Local contact(s):** Nicole Jeutter	*Received at ROBL:*

Names and affiliations of applicants (* indicates experimentalists):
R.T. Lechner*[1], A. Bonnani[1] and G. Bauer[1]

[1] Institut fuer Halbleiterphysik, Johannes Kepler Universitaet Linz, Altenbergerstrasse 69, A-4040 Linz, Austria

Report:

In contrast to (Ga,Fe)N, very little is known about (Ga,Mn)N. No attention has been paid so far to a possible growth of incoherent precipitates of other Mn-rich phases, which might affect the magnetic performance of prospective spintronic devices. We have hints that by increasing the concentration of the magnetic ions through the samples series, regions rich in Mn but coherent with the surrounding GaN matrix start to emerge.

Recently the fabrication (Ga,As)Mn layers with MnAs nanocrystals, for spintronic applications (e.g. spin-battery effect [1]), has been achieved through annealing of the dilute (Ga,Mn)As layers at temperatures ranging from 500 to 700°C[2].

For this purpose, two dilute samples of (Ga,TM)N (with TM=Mn, Fe) capped with Si_3N_4, were first measured in coplanar geometry at BM20 using a photon energy of 10 keV. Long radial scans from 10° to 45° in $\omega/2\theta$ were performed on each sample. Once it was established that the samples were dilute (*i.e.* did not present any secondary phases), they were annealed up to 900°C using the beryllium dome under nitrogen atmosphere and keeping a constant pressure of 200 mbar, in order to promote the aggregation of the TM ions.

The temperature was rapidly increased from 22 to 500°C, where long radial scans were taken after realigning with the GaN(002) peak. The samples were then heated up to 900°C, realigning after each 100°C step and taking long radial scans for each temperature step. However, no evidence of second phases formation during the entire annealing procedure was observed neither for the Fe nor the Mn doped GaN layers as can be seen in Fig. 1a).

The next step was to anneal samples containing secondary phases, in order to observe phase transformations and stability of the phases.

On Fig. 1b) we show the effect of annealing on (Ga,Fe)N layers containing different Fe-rich secondary phases.

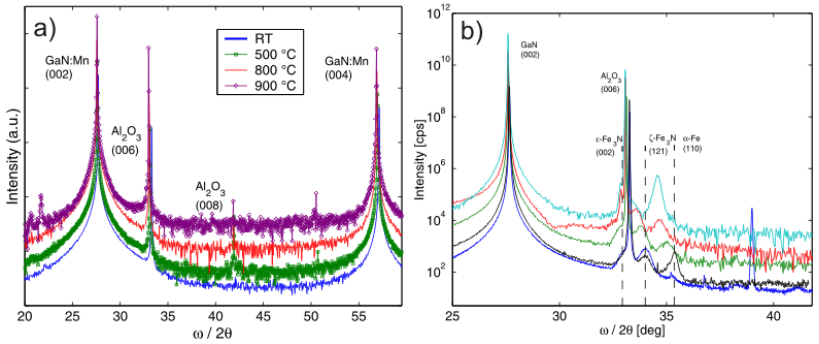

Fig 1. Annealing experiments on a) a (Ga,Mn)N dilute sample, and b) on a (Ga,Fe)N sample containing Fe-rich secondary phases.

As can be seen from fig.1 the most stable phase is ζ-Fe_2N, as it remains during the whole annealing process. The formation of α-Fe after annealing can be explained by the loss of nitrogen due to the heating, which promotes the formation of this Fe pure phase.

The measurements on the effect of annealing on the Fe_xN phases observed in (Ga,Fe)N performed during this beam time are under analysis and will soon be submitted for publication. Important parameters such as the change in lattice parameters (*d*-spacing) of the different phases, can be easily obtained from the obtained measurements.

References:

[1] P.Nam-Hai et al. *Nature* 07879 (2009).

[2] M. Tanaka et al. *Properties and Functionalities of MnAs/III–V Hybrid and Composite Structures,* Elsevier (2009).